



TECHNISCHE UNIVERSITÄT MÜNCHEN  
FAKULTÄT FÜR ELEKTRO- UND INFORMATIONSTECHNIK  
HEINZ NIXDORF-LEHRSTUHL FÜR MEDIZINISCHE ELEKTRONIK

# Highly Integrated Multichannel CMOS Sensor Systems for Micro-Physiological High-Content Screening Applications

MARKUS HEFELE

Vollständiger Abdruck der von der Fakultät für Elektrotechnik und Informationstechnik der Technischen Universität München zur Erlangung des akademischen Grades eines

Doktor-Ingenieurs (Dr.-Ing.)


genehmigten Dissertation.

Vorsitzender: Prof. Dr.-Ing. Ralf Brederlow  
Prüfer der Dissertation 1. Prof. Dr. rer. nat. habil. Bernhard Wolf  
2. Prof. Dr. rer. nat. Franz Kreupl

Die Dissertation wurde am 22.10.2020 bei der Technischen Universität München eingereicht und durch die Fakultät für Elektrotechnik und Informationstechnik am 01.03.2021 angenommen.

© 2020 Markus Hefe

<http://mediatum.ub.tum.de/?id=1574623>

**Excluding images provided by third-parties**, this work is licensed under a Creative Commons Attribution 4.0 International License (CC-BY). Images by third-parties are explicitly marked in their figure caption as such. Permission to use these external images within this thesis was kindly granted by the copyright owners. Reusing these images for other purposes might require the permission of the respective copyright holders. To avoid confusion, all images that fall under the above CC-BY license are explicitly marked in the caption with the label “”. **Images that do not bear this label are not covered by the above mentioned CC-BY license!** For full license text of the CC-BY see:

<https://creativecommons.org/licenses/by/4.0>



# Contents

<b>Title</b>	<b>ii</b>
<b>Contents</b>	<b>vi</b>
<b>Acknowledgement</b>	<b>vii</b>
<b>Abstract</b>	<b>ix</b>
<b>Zusammenfassung</b>	<b>xi</b>
<b>1 Introduction</b>	<b>1</b>
1.1 Bio-Medical Test Systems . . . . .	1
1.2 Sensors . . . . .	4
1.2.1 Bio-hybrid Sensors . . . . .	4
1.3 Goals . . . . .	5
1.3.1 Challenges . . . . .	6
<b>2 State of the Art</b>	<b>9</b>
2.1 Label-Free High Throughput Biological Screening Systems . . . . .	9
2.1.1 Commercial systems . . . . .	9
2.1.1.1 Epic . . . . .	9
2.1.1.2 xCELLigence . . . . .	10
2.1.1.3 Seahorse XF Analyzer . . . . .	10
2.1.1.4 CalScreener . . . . .	11
2.1.1.5 IMOLA . . . . .	12
2.1.1.6 zenCELL owl . . . . .	12
2.1.2 Research systems . . . . .	13
2.1.2.1 Oxygen BioSensor . . . . .	14
2.1.2.2 LAPS based Microphysiometer . . . . .	14
2.1.2.3 Lens-free optical screening system . . . . .	14
2.1.2.4 TUMscreen . . . . .	14
2.1.2.5 MicroLA . . . . .	15
2.1.2.6 Intelligent Microplate Reader (IMR) . . . . .	15
2.1.3 Summary of available systems . . . . .	15
2.2 Oxygen Sensors . . . . .	17
2.2.1 Amperometric Oxygen Sensors . . . . .	17
2.2.2 Optical Oxygen Sensors . . . . .	18
2.3 pH-Sensors . . . . .	18
2.3.1 Glass Electrode . . . . .	18
2.3.2 Optical Sensors . . . . .	19
2.3.3 Metal oxide Sensors . . . . .	19

2.3.4	pHit Scanner . . . . .	20
2.3.5	LAPS . . . . .	20
2.3.6	Ion Sensitive Field-Effect-Transistor (ISFET) . . . . .	21
2.3.6.1	REFFET . . . . .	22
2.3.6.2	O <sub>2</sub> FET . . . . .	22
2.3.6.3	CVFET . . . . .	23
2.3.6.4	CHEMFET . . . . .	23
2.3.6.5	Heated ISFET . . . . .	23
2.3.6.6	ISFETs for cell culture monitoring . . . . .	23
2.3.6.7	ISFET Readout . . . . .	24
2.3.6.8	Commercially available ISFETs . . . . .	25
2.4	Miniature Reference Electrode . . . . .	29
2.4.1	Palladium-Hydride Electrode . . . . .	30
2.5	Impedance Spectroscopy . . . . .	31
2.5.1	Bio Impedance Spectroscopy . . . . .	31
2.5.2	Commercially Available Impedance Spectrometers . . . . .	32
2.5.3	Research on impedance spectroscopy circuits . . . . .	33
2.6	Sensors for the Multi-Well-Plate . . . . .	33
<b>3</b>	<b>Material, Methods and Technology</b>	<b>35</b>
3.1	Overview . . . . .	35
3.2	Chemicals . . . . .	35
3.2.1	pH buffers . . . . .	35
3.2.2	O <sub>2</sub> references . . . . .	35
3.3	Measurement Equipment . . . . .	35
3.3.1	IVIUM CompactStat.h - Potentiostat . . . . .	37
3.3.2	PalmSens4 - Potentiostat . . . . .	37
3.3.3	Fibox . . . . .	37
3.3.4	Keysight E4980A - LCR-Meter . . . . .	39
3.3.5	Keithley 2401 - Source measure unit . . . . .	39
3.3.6	B1500A Semiconductor Device Parameter Analyzer . . . . .	39
3.4	Electrodes . . . . .	40
3.4.1	Reference and pH Electrode . . . . .	40
3.4.2	PdH-Electrode . . . . .	40
3.4.3	commercial ISFETs . . . . .	42
3.4.4	ISFET-Simulator . . . . .	42
3.5	Test Setups . . . . .	44
3.5.1	Automated Fluidic Package Test . . . . .	44
3.5.1.1	Generation 1 . . . . .	44
3.5.1.2	Generation 2 . . . . .	44
3.5.2	Waferprober . . . . .	45
3.5.3	Thermo cabinets . . . . .	47
3.6	Sensor Chips . . . . .	47
3.6.1	Layouts . . . . .	47
3.6.1.1	Generation 1 - DOE . . . . .	47
3.6.1.2	Gen2 - improved process . . . . .	48
3.6.2	Packaging . . . . .	50
3.6.3	Temperature Sensor . . . . .	51

3.6.4	TUM Sensor-Chip . . . . .	52
3.7	Conventions . . . . .	53
3.7.1	ISFET voltages and currents: $V_{sg}$ , $V_{sd}$ and $I_{sd}$ . . . . .	53
<b>4</b>	<b>Electronics</b>	<b>55</b>
4.1	Source-Drain-Follower . . . . .	55
4.2	DemoBoard . . . . .	56
4.2.1	Specifications . . . . .	56
4.2.2	Circuit Design . . . . .	56
4.2.3	O2FET readout . . . . .	57
4.2.4	Software . . . . .	57
4.2.4.1	Domain specific language . . . . .	59
4.2.4.2	User GUI . . . . .	60
4.2.5	Performance . . . . .	60
4.3	Stand-alone impedance analyser . . . . .	61
4.4	Integrated mixed-signal-frontend . . . . .	62
4.4.1	Specifications . . . . .	62
4.4.2	Operating principle . . . . .	63
4.4.2.1	ISFET readout . . . . .	63
4.4.2.2	Impedance spectroscopy . . . . .	66
4.4.2.3	RTD readout . . . . .	69
4.4.2.4	Battery voltage measurement . . . . .	69
4.4.3	Software . . . . .	70
4.4.3.1	I2C-interface . . . . .	70
4.4.4	Stand-alone front-end . . . . .	71
4.4.5	Multi-Chip-Module integration with sensor . . . . .	72
4.4.6	Measurement Performance . . . . .	72
4.4.6.1	ISFET Measurements . . . . .	72
4.4.6.2	High resolution ADC mode . . . . .	74
4.4.6.3	Temperature stability . . . . .	76
4.4.6.4	Impedance Measurements . . . . .	77
4.4.7	Discussion of MSP430FR2355 AFE . . . . .	82
4.4.7.1	ISFET readout . . . . .	83
4.4.7.2	Parameter Sweep . . . . .	84
4.4.7.3	Impedance spectroscopy . . . . .	84
4.5	Electro-chemical multi-well-plate . . . . .	87
4.5.1	2x2 experimental module . . . . .	87
4.5.2	Contactless Electro-Chemical Multi-Well-Plate . . . . .	88
4.5.3	Contactless Electro-Chemical Multi-Well-Plate, rev 2 . . . . .	88
4.5.4	Receiver . . . . .	92
4.5.5	Software . . . . .	94
4.5.6	Electrical tests . . . . .	94
4.5.6.1	Battery Lifetime . . . . .	94
4.5.6.2	NFC . . . . .	97
4.5.6.3	Data Transmission . . . . .	97
4.5.7	Architecture . . . . .	98

4.6	Auxiliary Software . . . . .	99
4.6.1	MSP. elegans . . . . .	99
4.6.1.1	Problem . . . . .	100
4.6.1.2	Concept . . . . .	100
4.6.1.3	Limitations of MSP. elegans . . . . .	101
<b>5</b>	<b>Results and Discussion</b>	<b>103</b>
5.1	Temperature Measurement . . . . .	103
5.2	PdH electrode . . . . .	105
5.3	ISFETs . . . . .	106
5.3.1	Parameter Sweep . . . . .	108
5.3.2	O2FET . . . . .	109
5.4	Cell Culture Measurements with the Plate . . . . .	111
5.5	IDES . . . . .	113
5.6	Thermally referenced ISFET . . . . .	114
<b>6</b>	<b>Conclusion and Outlook</b>	<b>119</b>
6.1	Future improvements and research opportunities . . . . .	119
6.1.1	AFE with ADuCM355 . . . . .	119
6.1.2	Industrial and Consumer Applications for ISFETs . . . . .	122
6.1.3	Sensor research . . . . .	122
6.1.4	Recycling and Waste Management . . . . .	122
	<b>Appendix</b>	<b>123</b>
<b>A</b>	<b>MWP Communication Protocol</b>	<b>125</b>
<b>B</b>	<b>MSP430FR2355 front-end register structure</b>	<b>131</b>
<b>C</b>	<b>Total harmonic distortion calculation</b>	<b>135</b>
<b>D</b>	<b>Schematics</b>	<b>137</b>
D.1	DemoBoard . . . . .	137
D.2	Standalone Impedance Analyzer . . . . .	147
D.3	Integrated Front-end . . . . .	149
D.4	Contactless Multi-well-plate . . . . .	151
<b>E</b>	<b>Eurosensors 2020 conference entry</b>	<b>155</b>
	<b>Publications</b>	<b>159</b>
	<b>Bibliography</b>	<b>161</b>

# Acknowledgement

I would like to thank Prof. Bernhard Wolf for the interesting topic, the many productive discussions, his patience and the possibility to realize this work. I would also like to thank Prof. Franz Kreupl and Prof. Ralf Brederlow for their support and help throughout these nearly four years. I would like to specially thank Ernst Müllner for his help and discussions with and on ISFETs and integrated electronics and some bureaucracy stuff. I would like to thank Texas Instruments for the great support for this whole project. I would like to thank Sebastian Meier and Christian Pfeffer for the good cooperative work on this and related projects and wish them the best success for their own PhD-thesis.

Furthermore I'd like to thank all the employees/members/students of HES, LBE, LME, LSE, LTE, TI and ZEITlab for their help, cooperation and good working climate, notably: Anika Kwiatkowski and Margarete Remm for helping me handling the nasty chemical stuff. Martin Brischwein and Alfred Michelfelder for their help with cell culture experiments. Wolfgang Pielock and Karl Demmel for manufacturing all my weird fixtures, adapters, fluidics, etc. based on sketchy drawings. And: Iris Artinger, Syed Muhammad Ibad Ur Rahman Bukhari, Helmut Bumberger, Giacomo Calabrese, Bettina Cutrupia, Stefan Dirr, Eugen Egel, Werner Emer, Rainer Emling, Niklas Fauth, Ingrid Franz, Tobias Fritz, Hamza Ben Ghazala, Andrew Giebfried, Helmut Grothe, Moritz Jung, Daniel Kaindl, Maik Kaufmann, Sebastian Kiesel, Christoph Klösters, Mohamed Amine Kthiri, Michael Lueders, Andreas Lösel, Elisabetta Mahmutovic, Rene Nauthe, Florian Neveu, Umidjon Nurmetov, Helmut Rinck, Sargam Sharma, Max Stelzer, Scott Summerfelt, Michael Szelong, Bernhard Ziegltrum, Gražvydas Žiemys.

I would like to thank the German Federal Agency for Technical Relief (THW) for their THW services, as they are a perfect opportunity to write on a thesis: Hours in an Autobahn parking lot without much distraction or possibilities for procrastination. I would also like to thank the German Academic Scholarship Foundation for their kind support. Nevertheless, I thank my voluntary editors (rvs, Helena, jj), helping me diminishing typos and bad grammar. Finally, I would like to thank my family for their everlasting support.





# Abstract

The investigation of living cells is an important part of biological and medical research. They can be used as transducer to screen drugs and other substances. For that purpose their metabolism must be monitored. Most recent approaches use different sensors to measure metabolites and morphology in automated test stands. However, these systems are complex to operate and expensive, partly due to the sensor systems used.

For this thesis a compact and economic sensor system is developed. It is based on a standard form factor of so called multi-well-plates for high-content cell culture handling. To ease handling the unit is completely wireless. This requires ultra compact and low-power electronics.

The used sensors are ISFET-based and can measure pH, dissolved oxygen and bio-impedance. They were developed in parallel by a semiconductor manufacturer. The sensors were tested and characterized and these results were fed back to the process development. For this purpose an automated fluidic test stand for the sensors was constructed. A new type of ISFET readout was developed based on a standard mixed-signal microcontroller. This circuit is flexible in its operation parameters, compact and cost-effective while providing the required resolution, accuracy and energy conservation. Also basic impedance spectroscopy measurement capabilities were implemented with this circuit.

An architecture concept for the sensor-equipped wireless multi-well-plate based on the readout electronics is presented which simplifies PCB-layout and reduces manufacturing cost. It is manufacturable with standard assembly processes and able to read 24 independent sensors each with up to four ISFETs and one impedance electrode on the area of a standard multi-well-plate.

Different tests were performed with the electronics and sensors to verify their proper operation. The tests ranged from electronic dry testing over chemical tests with the sensors to basic cell culture experiments.

Finally a new ISFET concept is proposed to perform absolute pH measurement without the need of a reference electrode. The reference electrode is the most difficult part to be integrated in semiconductor processes and can also cause trouble for biological applications because it can leak silver, which is cytotoxic. The new method uses the pH and temperature dependence of the sensing layer in conjunction with a built-in heater. The viability of this principle was successfully demonstrated with a test chip.

With the help of the methods and technologies developed in this thesis, better medicament screening systems and in general electrochemical sensor systems can be built.



# Zusammenfassung

Die Untersuchung biologischer Zellen ist ein wichtiger Teil der biologischen und medizinischen Forschung. Sie können als Transducer für das Screening von Medikamenten und anderen Substanzen verwendet werden. Zu diesem Zweck muss ihr Stoffwechsel überwacht werden. Die aktuellsten Verfahren verwenden verschiedene Sensoren zur Messung von Metaboliten und Morphologie in automatisierten Systemen. Diese sind jedoch komplex zu bedienen und teuer, teilweise aufgrund der verwendeten Sensorsysteme.

Ziel dieser Arbeit ist es ein kompaktes und kostengünstiges Sensorsystem auf der Basis des Standardformfaktors von sogenannten Multi-Well-Platten für die Handhabung von vielen Zellkulturen zu entwickeln. Um den Einsatz zu erleichtern ist die Einheit vollständig kabellos. Dies erfordert eine sehr kompakte und stromsparende Elektronik.

Die verwendeten Sensoren sind ISFET-basiert und können pH-Wert, gelösten Sauerstoff und Bioimpedanz messen und wurden parallel von einem Halbleiterhersteller entwickelt. Sie wurden getestet und charakterisiert und diese Ergebnisse wurden in die Prozessentwicklung zurückgeführt. Zu diesem Zweck wurde ein automatisierter fluidischer Prüfstand für die Sensoren aufgebaut. Eine neuartige ISFET-Ansterelektronik wurde auf der Grundlage eines standard Mixed-Signal Mikrocontrollers entwickelt. Diese Schaltung ist flexibel in ihren Betriebsparametern, kompakt und kostengünstig und bietet gleichzeitig die erforderliche Auflösung, Genauigkeit und Energieeinsparung. Die Schaltung kann auch einfache Impedanzspektren messen.

Es wird ein auf der Ausleseelektronik basierendes Architekturkonzept für die drahtlose Multi-Well-Platte vorgestellt, welches das PCB-Layout vereinfacht und die Produktionskosten verringert. Es ist mit Standardprozessen herstellbar und in der Lage 24 unabhängige Sensoren mit jeweils bis zu vier ISFETs und einer Impedanzelektrode auf der Fläche einer normalen Multi-Well-Platte auszulesen.

Verschiedene Tests mit der Elektronik und den Sensoren wurden durchgeführt, um deren ordnungsgemäße Funktion zu überprüfen. Diese reichten von elektronischen Trockenversuchen über die Erprobung mit Testmedien bis hin zu einfachen Zellkulturexperimenten.

Desweiteren wird noch ein neues ISFET-Konzept gezeigt um absolute pH-Messungen ohne eine Referenzelektrode durchzuführen. Die Referenzelektrode ist der am schwierigsten in Halbleiterprozesse zu integrierende Teil und kann auch für biologische Anwendungen Probleme bereiten, da zytotoxisches Silber austreten kann. Die neue Methode nutzt die pH- und Temperaturabhängigkeit der Sensorschicht in Verbindung mit einem Heizelement. Die Nutzbarkeit dieses Prinzips wurde erfolgreich mit einem Testchip demonstriert.

Mit Hilfe der in dieser Arbeit entwickelten Methoden und Technologien können bessere Arzneimittel-Screening-Systeme und allgemein elektrochemische Sensorsysteme gebaut werden.



# 1 Introduction

This thesis aims to develop and improve sensor systems to monitor biological cells. These monitoring systems are important for the development of new drugs and therapies and can also provide biological and medical research with new tools.

## 1.1 Bio-Medical Test Systems

Bio-medical testing of medicaments on cell cultures is a relatively young research technique compared to the history of medicament application. The latter dates back some thousand years [1] while systematic tests on cell cultures were first conducted in the 1950s e.g. by Eagle and Foley [2, 3]. Testing on cells allows a more controlled environment than testing in animals. It can be also more efficient [4] as the cell cultures can be provisioned relatively easy and do not take much room compared to setups with animals. Using cell cultures is also more ethical than harming animals [4], although there is a little catch with FBS<sup>1</sup> [5].

So called Multi-well-plates are often used in these experiments or assays to hold cell cultures. They have about the size of a post card with a few centimetres height, are made out of polystyrene and contain several cavities also called wells. These can take up a cell culture each. Three different multi-well-plates are depicted in Fig. 1.1. There are plates with 6, 24, 96, 384 or even 1536 cavities. The more wells, the more experiments can be

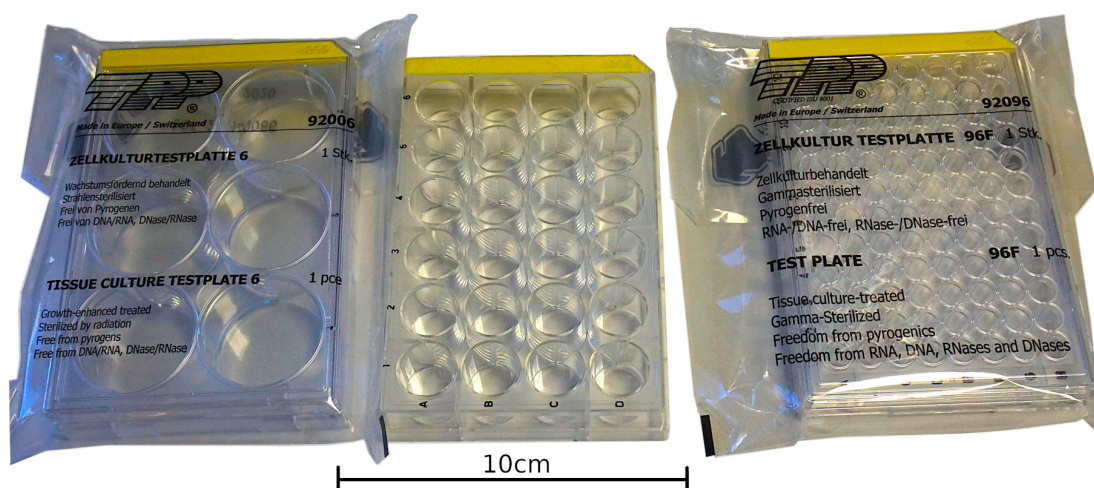



Figure 1.1: Photograph of different standard multi-well-plates for biological applications. From left to right: A 6-well-plate, a 24-well-plate and a 96-well-plate. The 6- and 96-well-plates are still packaged sterile. 

<sup>1)</sup> Fetal bovine serum, needed for most cell cultures and extracted from bovine fetuses.

## Introduction

run at the same time. Normally a cover is also supplied to prevent airborne contamination and make them stackable. With these plates lot of experiments can be run in parallel. This is necessary because there are many potential error sources in biological experiments. Therefore the experiment should be run several times to generate significant statistics. The plates are ideal for that, they are compact and can hold all required experiment runs at once. There are machines available, like pipetting robots, that *process* the plates automatically.

These cell cultures are subject of some study and therefore need to be monitored. There is a broad range of different experiments possible: Testing new substances for toxicity [6, 7], testing the effect of a new potential medicament in general [8, 9], or as part of personalized medicine [10, 11, 12], environmental monitoring [9, 13], etc.

To achieve that the vitality of the cells needs to be assessed somehow. One of the oldest methods is optical observation with a classical microscope to count the amount of living cells [8]. There is also a possibility to use a so called electronic Coulter counter. But this is a very coarse parameter for vitality. It can also be interesting to see if the cells loose adhesion, change their shape or dissolve. But this either requires lots of manual work or advanced image processing algorithms that were just recently developed to obtain quantitative information. Also subtle changes in cell metabolism are not always visible in their appearance. Optical setups are also often expensive due to the optics, especially the lenses [14]. These systems are also quite large and not easy to integrate [15].

Therefore other methods were developed to obtain more information from the cells. They can be distinguished into two classes: methods using a label and label-free methods. A label is here an additional substance that is introduced into the cell culture specifically for the measurement. This could be a dye that is metabolized and the metabolite has different colour. By measuring *the colour*, which can be done with well established photometric methods, the metabolic rate can be determined. A disadvantage of such methods is that they can disturb the cells [9, 16, 15]. Some of them are even poisonous, e.g. the MSDS from Sigma-Aldrich for Methylthiazolyldiphenyl-tetrazolium bromide (also called MTT, CAS: 298-93-1) states it to be “Suspected of causing genetic defects” (GHS H341) [17].

These are so called “endpoint assays”, because they terminate the culture and are therefore not usable for continuous observation. MTT is put into the culture at a defined point in time and incubated for some time. Then the culture is lysated and stored for the reagent products to fully dissolve. After that the result is read with an optical meter (exemplary description of the workflow in [18]). To obtain kinetic data this assay needs to be repeated several times with different delays between start and addition of the MTT. This is tedious work and error prone as for each data point a new assay needs to be started [18] with the chance for some mishap. Therefore the time resolution is often low, in the range of half an hour steps. To avoid this problems and obtain higher resolution kinetic data label-free methods were developed [16]. They measure metabolites or cell parameters without disturbing the cell culture even allowing the recording of real-time kinetic data.

There are different ways to obtain this data: The cells’ metabolism produces protons resulting in the acidification of the cell culture media, in other words a drop of the pH [19]. They also use up oxygen when aerobic metabolic paths are active resulting in a decreased concentration in the media [16]. Depending on their vitality cells grow in form of a layer on the well bottom, either tightly attached to their neighbours or they become spherical and get detached from other cells [20]. Nearly all metabolism is driven by an exothermic

reaction which always generates some heat which can be measured [21, 22]. By evaluation of these parameters the state and vitality of the cells can be assessed in real-time.

That way the effect of different chemicals, drugs or other environmental factors on the cells can be observed. As cells and organisms are very complex systems such a systemic approach of monitoring the metabolism with multiple parameters is advantageous to assess the effect on the cell [16, 23]. Earlier approaches that focused on the DNA, which was believed to be the only determining factor of a cells behaviour, were not successful [24]. It is also important to consider the environment of the cell as well as cell-cell interactions [23].

Monitoring the cells with such methods is comparable to a test bench or test stand widely used in engineering since decades. To check a system it is placed in a precisely controlled environment equipped with sensors and actuators to stimulate the device-under-test and measure its behaviour. This ensures reproducibility, eases debugging and provides safety. Nobody would even dare to think to test new brakes on a car at 200 km/h on the highway. Instead the car is strapped to a test stand with rollers, securely fixed, hooked up with lots of sensors and then automatically tested, while the experimenters watch from behind bulletproof windows, ready to safely abort the test if something fails. Only after these tests are successful the car is put to a street.

For biological *devices-under-test* however, there are only some rudimentary test benches available. They often measure only one parameter of the cells, they are complex in operation, big and in any case very expensive. Therefore they are mostly used in research. An exemplary schematic of the structure of such a test stand is depicted in Fig. 1.2 and available current systems are described in Section 2.1. It is also important to mention that

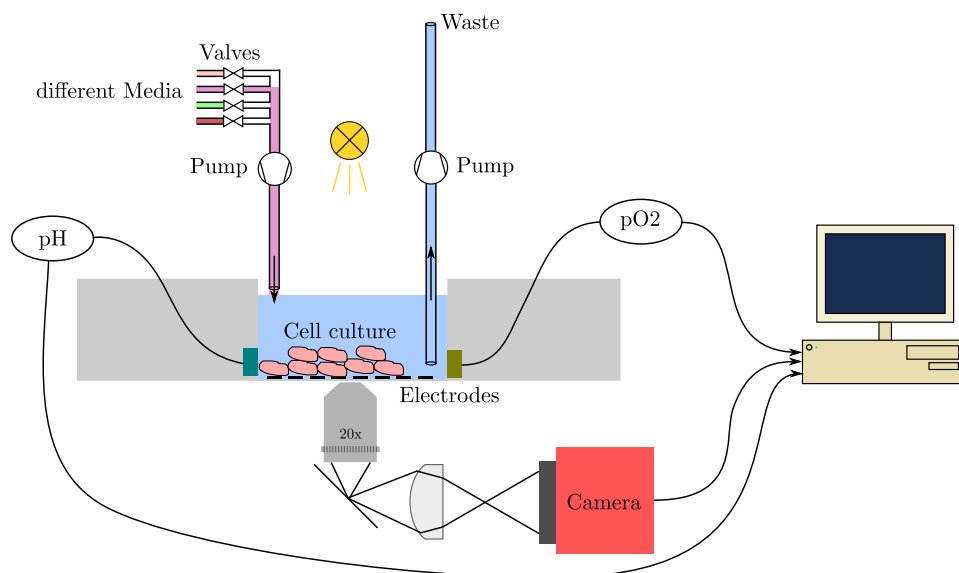



Figure 1.2: Principle of a test-bench for biological cells. A cell culture is placed in a basin equipped with different sensors for pH, oxygen and electrodes for impedance measurements. There is a transparent bottom through which the cells can be observed with a microscope. All data is collected by a computer system. A fluidic system exchanges the medium and can also introduce different substances. (redrawn after [9]) 

such systems need to be capable to conduct multiple assays preferably in parallel. This is due to the nature of biological experiments: There are many error sources that can lead to

wrong results like contamination with mould spores from the air or some mishap during preparation and of course the huge complexity of biological systems that still not fully understood. Therefore these assays are repeated several times and evaluated statistically to detect and compensate outliers. Here the use of multi-well-plates aid conducting these tests in parallel. If such a system is then, with these requirements, able to run lots of tests in a short time it is called a *high-throughput* system.

## 1.2 Sensors

Sensors are the interface from the environment to technology. Ever since they have been improved and miniaturized further. Cameras were once bulky and difficult to operate. Same goes with a variety of different environmental sensors for temperature, barometric pressure and humidity. Not to forget navigational sensors like satellite navigation receivers, accelerometers, gyroscopes or magnetic sensors. Today all of them fit into a standard phone.

But electrochemical sensors are a bit special. Industry standard for pH measurement till today is the century old glass electrode (e.g. as defined in DIN EN ISO 10523:2012-04). Due to its structure, miniaturization is not easy. With modern semiconductor technology a new sensor for pH is possible, the ion sensitive field effect transistor (ISFET).

With these ISFET pH-Sensors many new applications become possible which are difficult now due to size or price constraints. The low price, achievable through modern semiconductor manufacturing processes, enable the widespread use. For example in water-quality monitoring networks where sensors could be integrated in every water tap or other appliances connected to the water infrastructure. Broad sensor networks for environmental monitoring can be realized to asses changes in real-time. Smaller sizes allow the use in wearable devices and medical implants. Also, more sensors can be integrated in a device. With a trick, oxygen can also be measured with a slightly modified ISFET, a so called O2FET (see Section 2.3.6.2).

These sensors pose an ideal candidate for the aforementioned multi-well-plates. By measuring pH and dissolved oxygen in direct vicinity of the cell culture their metabolism rate can be quantified and they are small enough to fit in the bottom of each well of a 24-well-plate. Impedance spectroscopy on exposed noble metal electrodes can additionally be used to determine morphological changes of the cells.

Despite their advantages ISFETs are still not widely used. They have still some technical challenges. They can show a large drift, need specialized readout electronics and they also need a reference electrode which is usually the largest part of the sensor (see Section 2.3.6).

### 1.2.1 Bio-hybrid Sensors

A biological organism on the previously described cellular test stand can also be used as sensor [25, 26, 27, 28]. External environmental factors that effect the metabolism of the cells can be detected indirectly through the metabolic sensors. This concept has advantages to classical sensors. It can for example be used for water quality monitoring



[29, 13, 30, 31]. Instead of observing lots of parameters that degrade water quality one can simply monitor the vitality of i.e. algae which will react as soon as the provided water contains any harmful contamination. Then a specialized and therefore accurate but expensive laboratory can take samples and search for the exact cause. A schematic for such a sensor is depicted in Fig. 1.3.

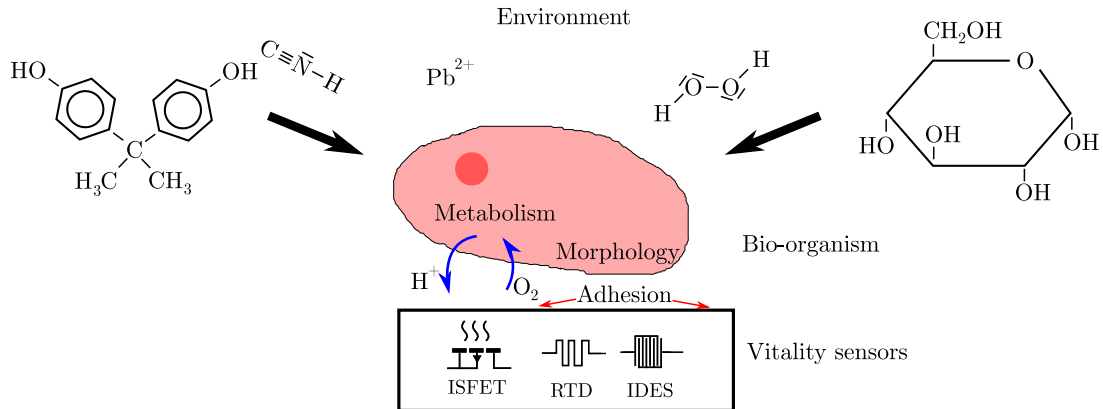



Figure 1.3: Principle of bio-hybrid sensors: A biological component, in this case a living cell, is used as transducer to monitor environmental parameters. When toxic or otherwise harmful substances are present they affect the cells metabolism, in the worst case till death. This metabolite changes can be assessed by the underlying electrical sensor-system which measures in this case the vitality parameters pH, oxygen consumption and morphological changes, here with ISFETs, O<sub>2</sub>FETs and interdigitated electrode structures (IDES). For temperature measurement a RTD can be used. 

## 1.3 Goals

Main goal of this thesis is the creation of a new cell culture test system and the required sensor electronics. The new system shall be more cost effective and easier to use while providing better results through more sensory observations. Such a system can then be used for personalised cancer therapy to identify drugs which specifically affect this patients tumour cells. Main part is a sensor-equipped multi-well-plate (sketch in Fig. 1.4). This to be developed sensor plate should work wirelessly to avoid error prone electrical contacts in a potentially corroding environment due to spilled fluids and to allow easier handling.

The work flow of the system could then look like this: The plate is loaded with cells to test, obtained from the tumour of the patient, and placed into a receptacle inside an incubator. A pipetting robot automatically exchanges the media and administers different drugs for the different samples in parallel. The reaction of the cells is registered by the sensors in the bottom of the wells and transmitted to a data processing system. The physician can now see, for example, which drug effectively killed the cancer cells for this patient and can then use it for the treatment.

This research project aims to reduce some drawbacks of ISFETs electrically through new readout electronics and fusion of multiple sensors to reduce errors and noise. With these sensors a multi-parametric sensor-equipped multi-well-plate for cell culture assays shall be developed with focus on the electrical part of the sensor plate and components necessary for its use. This includes circuits and algorithms to efficiently read the sensors and also to use sensors in such ways to improve their lifetime, accuracy and obtain additional information.

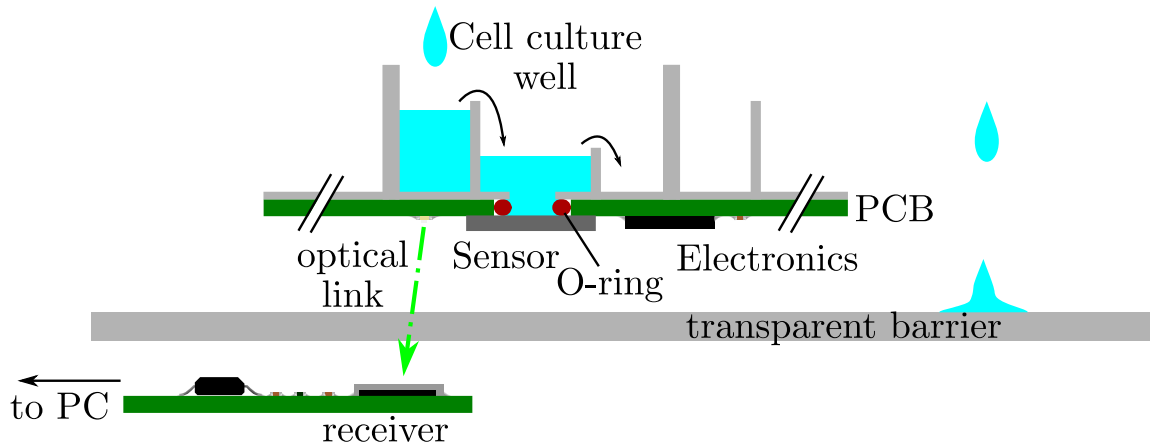



Figure 1.4: Sketch of the sensor-equipped multi-well-plate in side view. The cells are incubated in wells (only one shown). These have three cavities with different height walls. In the left new medium is inserted. In the middle the cell culture resides and from the last the medium is removed. Under each cell culture well is a sensor chip sealed with an o-ring. The required readout electronics is placed entirely on the PCB at the bottom. An optical link is used to transmit the data to a receiver connected to a PC. A transparent barrier (glass, acrylic) is used to shield this receiver from the fluids handled with the plate. 

It also tries to improve the handling and operation of the plates in rough clinical and laboratory environments. Some of the main difficulties include the size constraints of the plate, its wireless operation, the packaging, availability of the sensors and cost effective manufacturability. They are addressed in the following paragraphs in more detail as well as the specification of the plate.

### 1.3.1 Challenges

**Size** The size of a multi-well-plate is standardized (ANSI/SLAS 1-2004) to be 127,76 mm by 85,48 mm. The height is defined in ANSI/SLAS 2-2004 as 14,35 mm. The sensors and the required readout electronics need to be integrated into the plate without exceeding these dimensions too much, where the footprint allows less tolerance than the height. Most pipetting Robots have some clearance between their pipettes and the plate top which allows higher than standard plates. Albeit the spacing between plates in lateral dimensions is very dense. Usually a receptacle with the standard dimensions is used to hold the plate in position. Smaller plates would need an adapter to be held in place securely. Larger plates will not fit and block neighbour slots.

**Manufacturability** The whole system has to be manufacturable with mostly standard processes. Otherwise the economic and cost optimized production of a large amount of these plates is not possible. If the plates are too expensive they wont be used and would therefore be useless. A low price is also required as the plate will likely to be a single use device due to contamination issues. A method to refurbish, sterilize and reuse the plates would in turn add great value and reduce electronic waste.

**Wireless operation** The plate shall send its measurement data wirelessly to a base station and requires energy to operate. There are different technologies to achieve these goals. But they usually have some disadvantages. They are either expensive, complex,

require lots of space or energy, cause interference with the measurements or do not have enough power or bandwidth. Different solutions need to be examined and optimized to fit the requirements for the plate. The wireless operation eases handling and is needed to increase the robustness: In this case the electronics can be completely encapsulated and protected from the potentially wet lab environment. This is especially important for sterilization of the equipment with liquid agents.

**Packaging** As there are fluids involved a thorough and watertight packaging process is required. The fluid with the cell-culture needs to be in touch with the sensors, but the rest of the electronics needs to be sealed. These two conflicting properties need to be satisfied with a suitable construction.

**Sensor availability** The required sensors for this project are still in development. A partner research project in cooperation with a semiconductor manufacturer aims to set up a process to manufacture these sensors. Due to the non-standard process there is a chance for delays due to unforeseen problems. It is therefore useful if the electronics can be adapted to new sensors.



## 2 State of the Art

### 2.1 Label-Free High Throughput Biological Screening Systems

Label-free high-throughput screening systems can incubate cell cultures and then monitor them. They are mainly used to test new candidates for medicaments. They are “high-throughput”, if they can screen lot of samples in parallel. Label-free means, these systems do not require a stain or other helping substance, a so called label, in the cell culture medium to monitor the cells and their metabolism. There are systems with different sensing principles, different time resolution and different levels of automation.

#### 2.1.1 Commercial systems

Currently there are several commercial systems available that provide label free cell culture analysis.

##### 2.1.1.1 Epic

Corning offers a label-free cell culture system called “Epic”, based on evanescent waves [32]. The Corning Epic BT System currently costs 114758,60 € (Sep. 2019) and can analyse special 384-well-plates. This is only the reader without any automated plate handling. The bottom of these plates is equipped with waveguides. They direct the light that is coupled into them close underneath the surface where cell cultures grow upon. The electromagnetic fields from the light extend from the waveguide into the cell culture vessel and can then interact with matter there, the so called evanescent wave. This will also affect the travelling light wave. A mass distribution shift of the cells cause a shift in the wavelength of the light that exits the plate. A spectrometer can then detect this change. This technique requires complex and very expensive optics. The BT series is only a bench top device without any automation. The user places a prepared plate on the reader and gets the results. There used to be a fully automated system with fluid and multi-well-plate handling (see Fig. 2.1) which is no longer sold. This system can then take up several multi-well-plates, place them into an incubator, place a plate on a reader station and handle the fluidics to some extend.

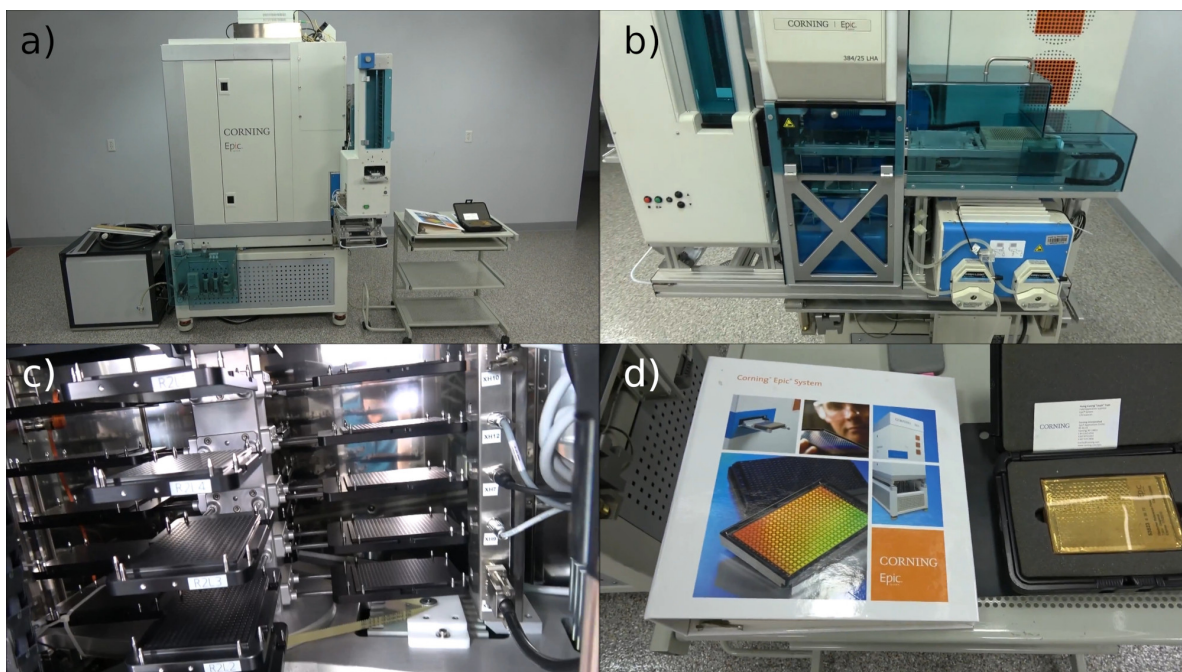


Figure 2.1: Corning Epic system: a) shows a fully automated system with multi-well-plate and fluidics handling. The big box in the middle is an incubator. The small box on the left is the power supply. On the right side of the box a feeder for plates is attached. b) shows the automated plate feeder and fluidics in detail c) shows the interior of the incubator. The plates are stored in a rotatable shelf and can be put onto a reading position by a robot. d) shows an image of the the custom required multi-well-plates. The plate on the left is upside down and shows the waveguide bottom causing a rainbow effect. The plate on the left in the case is for calibration. Adapted from a redistributor's promotional video [33], reproduced with permission from New Life Scientific, Inc. The subfigure designators are added.

### 2.1.1.2 xCELLigence

The xCELLigence series from ACEA Biosciences (now part of Agilent) uses electrical impedance measurement to assess cell culture vitality [34]. It uses special multi-well-plates with interdigitated gold microelectrodes on the well bottom (see Fig. 2.2). The excitation voltage is stated as 22 mV @ 10, 20 and 50 kHz. There are different sized systems available from 16 well to four times 384 wells. Depending on cell morphology, e.g. sparse single cells or a tightly connected cell monolayer, the impedance measured changes indicating how much cells are currently growing on the sensor. ACEA also provides some specialized systems which can additionally measure cell migration. Here a micro-porous membrane divides the well horizontally. On its bottom surface there are gold electrodes. When a cell migrates from the upper half through the membrane and settles on its underside this can be detected with these electrodes. Both chamber halves are filled with different media to potentially trigger the migration. The process can then be monitored in real-time.

### 2.1.1.3 Seahorse XF Analyzer

The Seahorse XF Analyzer series, recently acquired by Agilent, measures both oxygen consumption and acidification of biological assays in multi-well-plates [35]. Fluorescent pH and oxygen sensor dyes immobilized in gel matrices are used as measurement transducers. These fluorescent sensor spots sit on a special cover for the plate on the tip of cones that

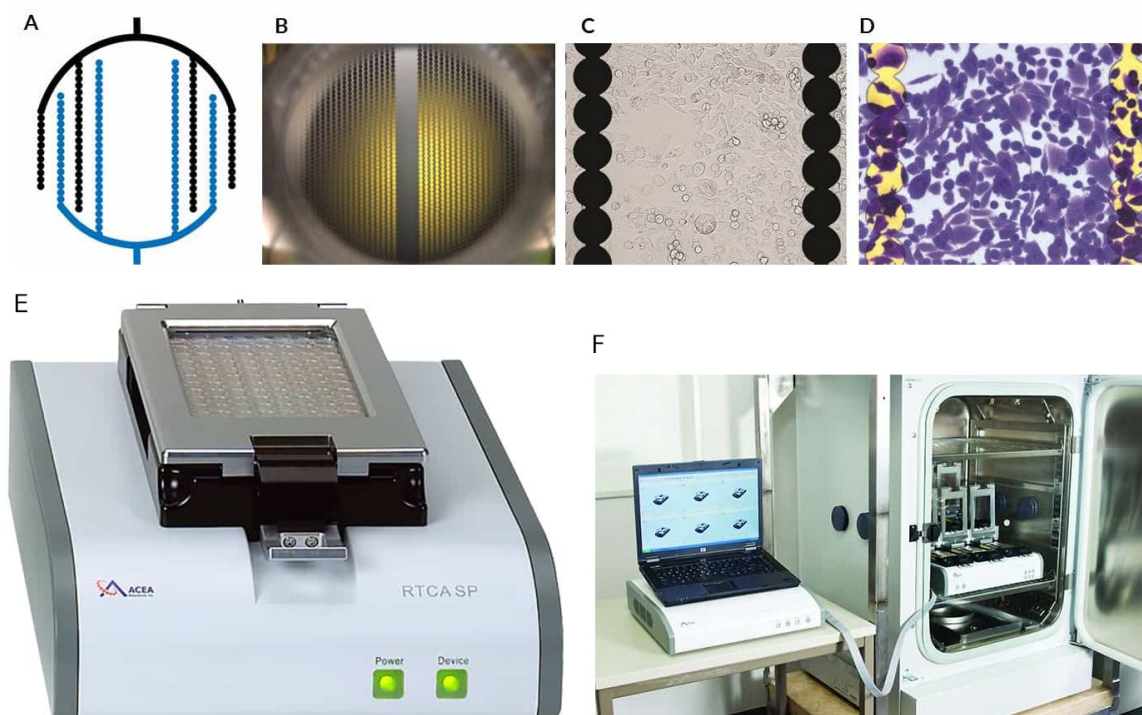


Figure 2.2: Agilent xCELLigence RTCA system: A is a schematic drawing of the interdigitated electrode structure in one well. B is a picture of such a well. C and D show some cells growing between and on the electrodes. E is a reader for such an electrode equipped plate and F shows the system built into an incubator on the right with a control PC on the left. Adapted from ACEA's website [34], rearranged and subfigure designators added. Reproduced with permission from Agilent Technologies, Inc.

are lowered into the cavities. A fibre optic assembly is dipped into these cones from atop to excite the fluorophores and direct the emission to a photodetector. The system also incorporates an incubator to control the temperature and a drug delivery system that can introduce additional substances into the well at a defined time of the experiment to ease pharmaceutical assays (see Fig. 2.3). There is a 24 and a 96 well version available.

#### 2.1.1.4 CalScreener

CalScreener from Symcell measures the heat generated by the cell's metabolism [36, 22]. Nearly all metabolic processes are in sum exothermic and thus generate at least a little heat. This thermal energy can be measured by a very sensitive calorimeter that is integrated into the CalScreener. A cell culture is placed in a well of a special multi-well-plate that is thermally connected with a heat sink through a thermopile sensor. Any excess heat generated inside the well flows to the heat sink. Heat flux through the thermopile generates a voltage that can then be processed. A detection limit of about  $0,1 \mu\text{W}$  is achieved. For comparison: A solution with initially  $10^5$  L6 rat skeletal myoblast cells generate about  $18 \mu\text{W}$  at peak [22]. The system provides 48 wells of which 16 are used as references leaving 32 wells for experiments. The samples need to be put into titanium cups that are then closed with a cover. Additional plastic inserts can be used to ensure a sterile environment. Using the system with automated pipetting systems is therefore not possible. A huge advantage of this approach is its versatility as it can detect nearly any form of metabolism. On the other hand it cannot easily distinguish them.

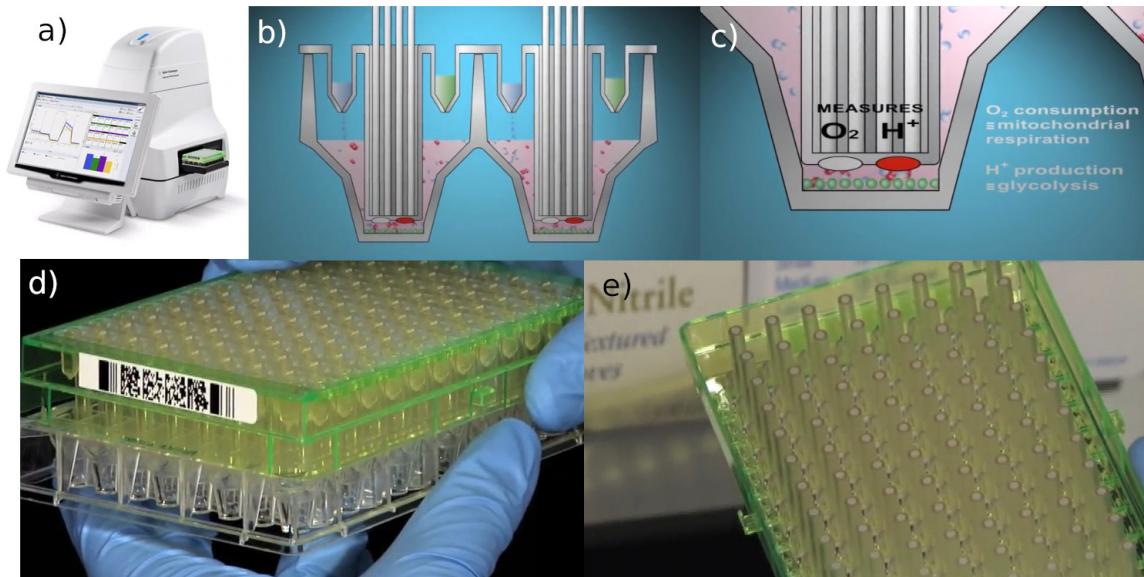


Figure 2.3: Agilent Seahorse XF Analyzer: a) shows the complete analyzer system. On the right side a multi-well-plate is inserted. d) shows this special multi-well-plate. It consists of a bottom part (clear) and a cover (green). e) shows the cover upside down. It has a cone for every well with fluorophores in the tip for oxygen and pH sensing and fiberoptics to guide the light. b) shows a schematic cross-section through the plate. In the bottom the cells are growing. The cone from e) is in the middle. There are also reservoirs for substances that can be added during the assay (blue and green). c) shows a close up from the bottom part of the well. The cone can be pressed down so that the fluorophores (red and white spot) are in close proximity to the cells (green spheres). The cone can also be lifted (not shown here) to allow mixing of the media (light pink). Adapted from Agilent's website [35], rearranged and subfigure designators added. Reproduced with permission from Agilent Technologies, Inc.

### 2.1.1.5 IMOLA

The Intelligent Mobile Lab for in-vitro diagnostics (IMOLA-IVD, see Fig. 2.4) was developed at the Heinz-Nixdorf chair for medical electronics at TUM (Prof. Wolf) and is now commercially distributed by cellasys [37, 13, 38]. It uses a single so called biochip either based on a silicon or ceramics substrate to monitor a living cell culture immobilized on it. The ceramic chips have an interdigitated electrode structure (IDES) for impedance spectroscopy, metal-oxide sensors for pH measurement and an amperometric oxygen sensor. The system integrates the required read-out and processing electronics together with the exchangeable sensor chip and fluidics assembly in one case. For medium control an external standard micro-fluidic pump and valves are required. The system is intended for stationary lab use but can also be operated stand-alone and used in field applications.

### 2.1.1.6 zenCELL owl

innoME offers an optical cell monitoring system called zenCELL owl [39] (see Fig. 2.5). This device can take up a 24-well-plate and monitor the cells with a miniature microscope. The system is very compact and has no mechanics. Multiple cameras with appropriate optics are integrated in the base underneath the place for the multi-well-plate. A light source is mounted over the plate for illumination. The ZenCell is able to capture an image of each well every five minutes, or in longer user defined intervals. Thus the growth and morphological change can be monitored. innoME also provides algorithms for automated





Figure 2.4: Intelligent Mobile Lab (IMOLA): a) shows the IMOLA on the right with a Laptop in the left that is used for data recording and display. b) shows the IMOLA in detail. The inserted biochip is labelled. It is held in place by a fixture. The micro-fluidic connectors and tubing are also visible. Next to the IMOLA there are several flasks with cell culture media being pumped through the chip. Adapted from cellasys' website [37], rearranged and subfigure designators added. Reproduced with permission from cellasys GmbH.

image processing, i.e. to count cells. This system can be used for cyto-toxicity assays or medicament studies.

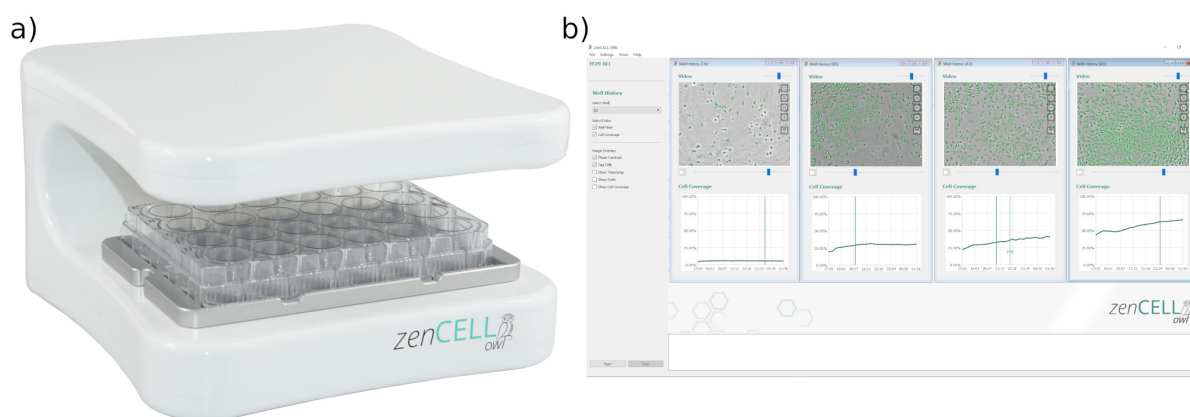


Figure 2.5: zenCELL owl: a) shows the system itself. A 24-well-plate is placed in the zenCELL. Under the plate are the cameras for the cell observation, above is a light source. The device is slightly larger than the multi-well-plate. b) shows a screenshot from the evaluation software. Shown here are four images from different wells. Below them a graph of the cell coverage over time is displayed that is generated by automated image processing algorithms. Images supplied by and reproduced with permission from innoME GmbH [39].

## 2.1.2 Research systems

The previous systems are commercially sold by companies while the systems described in this section are not available on the marked. These were described in various research publications, hence, the denotion “research systems”.

### **2.1.2.1 Oxygen BioSensor**

The Oxygen BioSensor system was proposed by Wodnicka et. al. [18] in 2000 and uses fluorescent oxygen sensors immobilized in multi-well-plates. A standard fluorescence reader is used to measure the fluorescence intensity of the dye which correlates with the oxygen concentration in the wells. The plates are manually put onto the reader for measurement and then stored again in an incubator. If there are cells growing in the well and using up oxygen this is detected as an increased fluorescence intensity. The system was compared to a traditional MTT assay and showed similar results. This article [18] also shows the different work necessary for labelled and label-free assays.

### **2.1.2.2 LAPS based Microphysiometer**

Hu et. al. present a cell screening system that uses a LAPS (see Section 2.3.5) to measure the external acidification rate [40]. Unfortunately this paper lacks a description of the size of the system, especially for the flow-cell which holds the cell culture. Based on the pictures it seems to be about 3 cm in diameter. It is connected to a micro-fluidic system that uses a syringe pump. The flow is stopped periodically to observe the acidification. Afterwards the flow is started again to refresh the medium and restore the baseline. The system shows a good sensitivity and resolution but the electronics is rather large, on the pictures it has a ca. shoe box sized case for one single measurement cell.

### **2.1.2.3 Lens-free optical screening system**

Jin et. al. present a purely optic cell screening system that eliminates the need of costly lenses [14]. They use a standard CMOS image sensor. On top of that a flow cell with a glass bottom is placed which is pumped with fresh media. An RGB-LED is used as illumination from atop. The system uses the shadows cast by the cells on the image sensor to detect and monitor them. Due to their size interference patterns emerge and can be captured by the image sensor. The live and dead cells are counted automatically by an image processing algorithm.

### **2.1.2.4 TUMscreen**

The TUMscreen was designed by Prof. Wolf and developed at the Heinz-Nixdorf chair for medical electronics at TUM [41, 42] to automatically monitor six cell cultures on silicon sensor chips. The chips are equipped with four ISFETs, two O<sub>2</sub>FETs, one REFFET, an amperometric oxygen sensor, a temperature diode and an IDES. The electronic system is built modular. One channel uses at least 13 high-precision differential amplifiers (AMP03), five quad precision opamps (LT1114), a precision isolation amplifier and an isolated DCDC-converter. The whole system has a size of about 0,7 m × 0,7 m × 0,8 m. It uses a fluidic system that is based on tubings and a peristaltic pump. This caused severe problems with air bubbles and contamination that finally lead to the development of a system without those elements, the IMR (see Section 2.1.2.6) [private communication with Prof. Wolf].

### **2.1.2.5 MicroLA**

The MicroLA is a handheld Bio-Sensor device which forms a complete test system that uses a similar bio sensor chip as the IMOLA (see Section 2.1.1.5) but also fully integrates the fluidics and is intended for mobile use [43]. It was developed at TUM (Heinz-Nixdorf chair for medical electronics, Prof. Wolf). The used biochips detect pH, dissolved oxygen and have electrodes for electrical impedance spectroscopy. The system is intended to use yeast cells as transducer to search for potentially toxic substances. Yeast cells are more robust and way easier to handle than human cells. The device's dimension are 16 cm × 4 cm × 12 cm.

### **2.1.2.6 Intelligent Microplate Reader (IMR)**

The IMR was designed by Prof. Wolf and developed at the Heinz-Nixdorf chair for medical electronics at TUM [7, 44] in 2013 for pharma-screening, toxicity tests and personalized cancer therapy as improved successor to the TUMscreen for higher throughput. It combines impedance sensors and optical oxygen and pH sensors to assess cell vitality in special 24-well-plates. With this sensor combination it is able to detect cellular activities for different metabolic paths. The whole system consists of an incubator to keep the cells under test at their preferred temperature. A pipetting robot exchanges the medium in the sensor-multi-well-plate periodically. Different media can be prepared and provided to the robot, e.g. plain cell culture medium and medium with a drug.

The fluorescence sensors are read through an automatic movable microscope which is coupled to a fluorescence reader. The microscope can also be used to capture photos of the cell cultures. The impedance sensors are formed on the glass bottom of the multi-well-plate and are connected with a row of test pins to an impedance spectrometer.

Figure 2.6 shows a picture of the system.

The oxygen and pH sensor output generally has the form of a saw-tooth. Fresh medium has 100 % oxygen saturation and a pH of usually 7,4. The cells metabolism uses up oxygen and produces lactate, decreasing pH over time. The measured values drop slowly and will then again rise with a step once the next pipetting cycle comes. The metabolism rate is proportional to the first derivative of the oxygen and pH signal, excluding the steps caused by media change [45].

## **2.1.3 Summary of available systems**

There are some systems available that can, at least in parts, perform the requested tasks of label-free cellular metabolism monitoring. However, there are lots of drawbacks: These systems are either very expensive or can only be used in specialized laboratories and not in a regular clinic. They are intended for research. Therefore the new system proposed in this thesis shall be relatively cheap and built for mass use and operated by regular MTAs<sup>1</sup>. This requires some robustness of the system. The old standard format of the multi-well-plate is kept as many lab technicians know them and many labs have tools to

---

<sup>1</sup>) Medical technical assistant

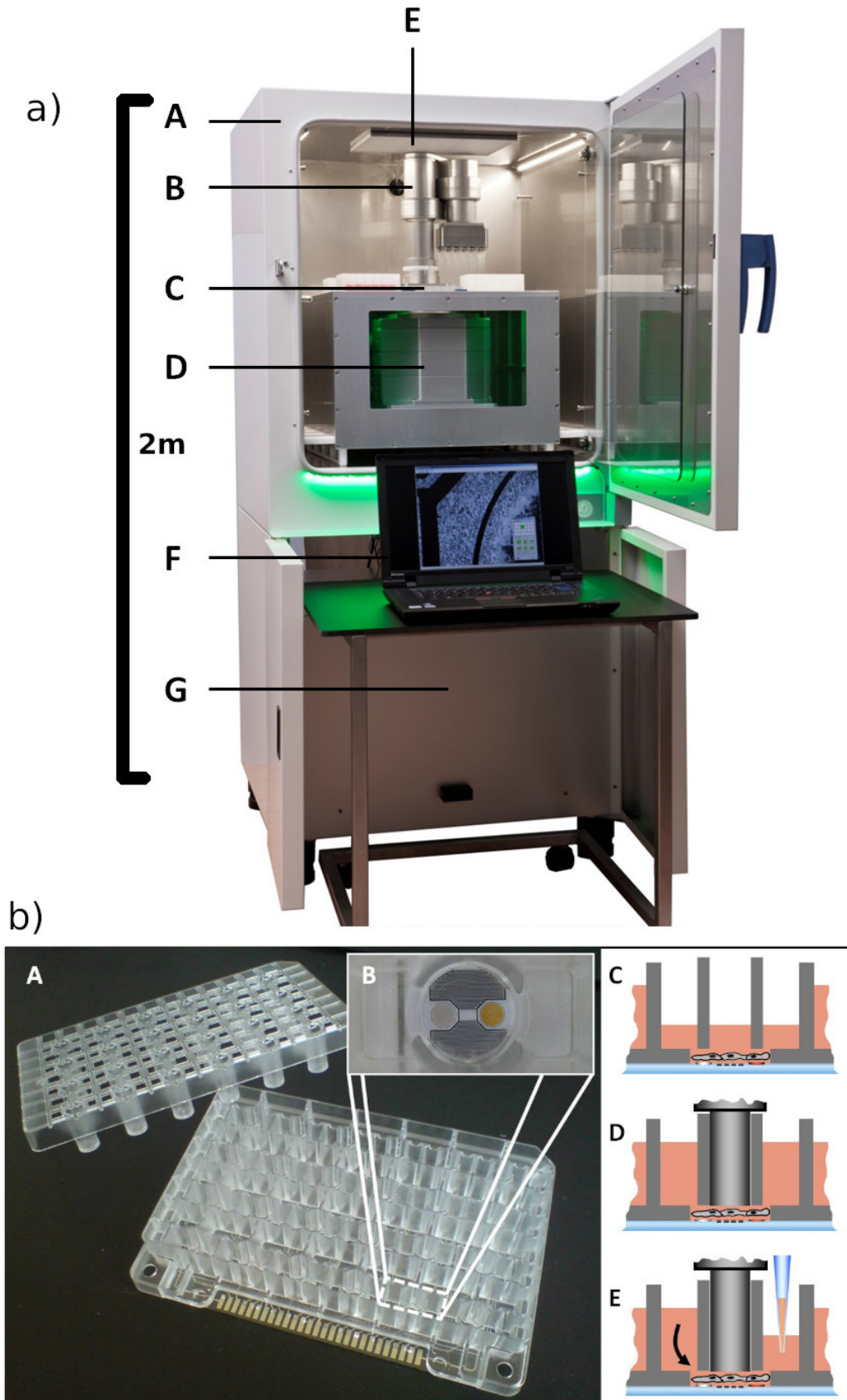


Figure 2.6: The Intelligent Microplate Reader (IMR). a) A: Incubator, B: Pipetting robot, C: Sensorplate, D: Automatic microscope, E: Illumination for microscope, F: Computer for data processing, G: Sensor and control electronics hidden behind cover. b) A: specialized cell culture plate, B: bottom of one well with two optical sensors (white and yellow circle) and electrode structure, C: cross-section through well with cell culture, D: top cover inserted which reduces the volume over the cell culture, E: pipetting medium out of the well which creates a flow through the middle part. Pictures: B.Wolf, former Heinz-Nixdorf chair for medical electronics, TUM, reproduced with permission.

handle them like multi-head pipettes and racks. From former systems it is known that electrical connections to the plate are difficult: Sometimes custom and therefore expensive connectors are needed. Corrosion due to spills can cause contact problems leading to complete failure or even worse to subtle errors that can be misinterpreted as valid results. Therefore the new plate will be wireless.

Monitoring the generated heat of the cells is very unique and interesting but requires also a careful and complex setup to channel the heat flux through the thermopiles. Optical systems are usually very expensive due to the optics, have a rather large power consumption for illumination and require complex algorithms for automatic evaluation. These approaches are therefore omitted. To make the system usable for different applications, metabolism monitoring by detecting metabolites is used. Namely the consumption of oxygen and the extra cellular acidification. Also morphological changes which can be detected by impedance spectroscopy is considered. Sensors for these parameters are likely to be integrated on such a sensor plate.

Next the available sensors for such a task are evaluated with the focus on oxygen and pH sensing as well as on impedance spectroscopy.

## 2.2 Oxygen Sensors

There are lots of ways to detect and measure oxygen. This Section will concentrate on sensors for the measurement of oxygen dissolved in water although some of these sensors can also detect gaseous oxygen. Cells can consume oxygen for their metabolism. Measuring the changing oxygen concentration can therefore be used to deduce the metabolic activity.

### 2.2.1 Amperometric Oxygen Sensors

The class of amperometric sensors reduces oxygen and measures the charge transferred in this redox-reaction. In 1953 Clark et. al. introduced an electrode design that was superior to previous models [46]. It consists of a platinum surface covered by a cellophane membrane. At cathodic potentials versus a reference electrode (e.g.  $-0,6\text{ V}$  vs. Ag/AgCl) oxygen is reduced according to formula 2.1:



The flowing current is proportional to the oxygen concentration in the vicinity of the electrode. The membrane prevents unwanted reactions with other substances in the fluid while not severely disturbing its measurement performance. This made this electrode design superior to previous ones. It is today known as Clark-Electrode.

One disadvantage is the fact that this electrode uses up the oxygen it measures. Due to diffusion limitations it should not be operated continuously.

## 2.2.2 Optical Oxygen Sensors

A different sensor concept is based on fluorescent dyes. Some of them exhibit a property called oxygen quenching. Oxygen can take up the energy of an excited dye molecule and dissipate it without light emission. That way the fluorescence intensity of the dye is reduced in the presence of oxygen. Also the fluorescence lifetime, the time constant of the emission after the end of the excitation, decreases. The Stern-Volmer-Equation describes this phenomena:

$$\frac{I_0}{I} = 1 + K_{sv} \cdot pO_2 = \frac{\tau_0}{\tau} \quad (2.2)$$

Here  $I$  denotes the intensity,  $\tau$  the lifetime, with index 0 these values at zero oxygen,  $pO_2$  the partial oxygen pressure and  $K_{sv}$  a dye dependent factor.

To measure this effect there are different principles. One tries to measure the intensity directly. A disadvantage here are errors due to dirt in the optical path, varying dye amounts and photo-bleaching. A better way is to measure the fluorescence lifetime which is unaffected by any of the aforementioned error sources.

In biological applications there are some error sources as some of the many different molecules in the media can also cause interference with the fluorescent dye [47]. There is a good overview article from Wang and Wolfbeis describing these sensors and their principle in detail [48].

A manufacturer of these dyes and corresponding readout systems is PreSens [49]. They offer dye spots in the form of a small disk with adhesive to be stuck to a transparent vessel wall. The spots can then be read through the wall. Other sensors consist of an optical fibre with the dye on one end. The other end comes with a connector for the reader. PreSens also offers similar probes for pH (see Section 2.3.2) and  $CO_2$ .

## 2.3 pH-Sensors

This section will evaluate different pH sensors that can be used in conjunction with cell cultures. Some metabolic pathways will lead to an output of protons, hence a decrease of pH of the extracellular medium. By monitoring the pH outside of the cells the metabolic rate can be deduced.

### 2.3.1 Glass Electrode

The glass electrode is today one of the most common ways to measure pH. Probably every chemical lab has such an electrode. It uses the fact that two electrolytes on the two sides of a glass membrane cause a potential difference across it proportional to their pH difference. This effect was first observed by Cremer in 1906 [50]. Over the years the construction of the electrode was improved and used for measurements [51, 52]. Their main principle and construction is nearly unchanged over the last century. They consist of a test tube like glass body filled with a reference electrolyte and contacted with an inner electrode. The bottom of this assembly consists of a special glass membrane which is conductive for Li- and Na-ions but impermeable for protons. Due to binding of the protons a measurable

potential difference emerges. With a reference electrode in the outer fluid this can be measured against the inner electrode. The impedance of this electrode configuration is very high (around 1 G $\Omega$ ), so specialized volt-meters are required.

There is a huge variety of different glass electrodes for different applications, environments and precisions available from a multitude of manufacturers. Only a few remarkable and for this thesis relevant examples are described:

**Thermo Scientific Orion 9810 BN** is a “Micro-pH-Electrode” with a 1,3 mm tip designed to measure small volumes, e.g. biological samples [53]. The complete electrode assembly is nevertheless 120 mm long and intended for use through a human operator.

**Unisense pH Microelectrodes** are available with tip sizes down to 10  $\mu\text{m}$  [54]. These electrodes are available with shaft lengths down to 70 mm. They do not have a built-in reference electrode but these are available from the same manufacturer in similar dimensions. The body is based on normal glass pipettes with only the tip having micrometer dimensions. A few centimetres from the tip the body diameter is some millimetres.

There are no commercial glass electrodes available that can be integrated into each well of a multi-well-plate. They are all too large.

### 2.3.2 Optical Sensors

The most commonly known optical pH sensors are dyes either as fluids or adherent to paper strips that change colour according to pH. There are lots of dyes with this property, they can even be extracted from common food like tea and red cabbage. They usually have a pH level at which they switch colours. By combining multiple different dyes a gradual colour change over the whole pH-range can be achieved.

More advanced dyes are used for automated measurements. Those show different fluorescence intensities or lifetimes dependent on pH similar to fluorescent oxygen sensors. A trick is used here to convert the intensity information to an easier measurable time-domain information [55]. The dye is usually confined in a matrix and either suspended at the wall of a transparent vessel. The readout optics is outside of the vessel protected from the liquid inside. Another sensor type uses a rod with the electronics and optics hermetically sealed inside. The matrix with the dye is on the outside and read through a window.

PreSens is a manufacturer of such sensor probes [49] (see also Section 2.2.2).

### 2.3.3 Metal oxide Sensors

There are a variety of different metal oxides which exhibit a pH dependent potential versus a reference electrode [56, 57, 58]. The most commonly used is iridium oxide: It is long known to show good pH sensitivity, stability, bio-compatibility and robustness. There are different manufacturing methods: electrochemical deposition and sputtering yielding slightly different properties of the sensor. This also includes the sensitivity which can be higher than 59 mV/pH [59, 60, 61, 62].

### 2.3.4 pHit Scanner

There used to be a pH meter called pHit Scanner by Senova Systems. It was claimed to be calibration free and using a non-glass sensor. Apparently it also seems not to have a classical reference electrode. It is stated to use a carbon substrate with attached so called analyte sensing modules. To these hydronium ions can reversibly bind when subjected to a voltage. The voltage when this happens is dependent on the concentration of hydronium ions and thus the pH [63, 64, 65, 66]. By scanning the potential at the electrode and measuring the current the pH can be determined. However, this product is no longer available and Senova Systems was acquired by Parker-Hannifin. Parker-Hannifin does not offer pH sensors.

### 2.3.5 LAPS

LAPS is an acronym for light-addressable potentiometric sensor. It was first proposed by Hafeman et. al. in 1988 [67]. It consists of a doped silicon substrate which is covered

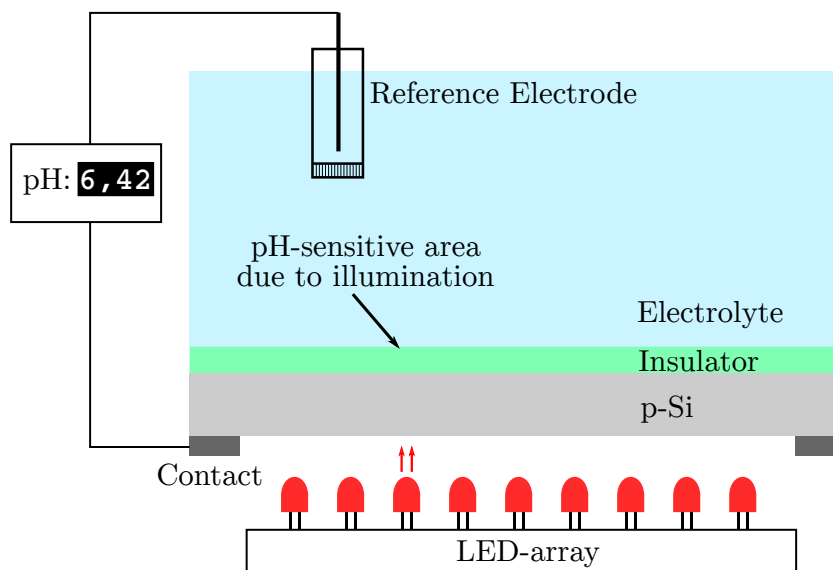



Figure 2.7: Cross-section of a LAPS. On a silicon substrate an insulator e.g.  $\text{SiO}_2$  is grown. The backside of the silicon is locally illuminated with a LED-array. A reference electrode is used to contact the electrolyte above the insulator. The device measures pH only at the illuminated areas. 

with an insulation layer such as  $\text{SiO}_2$  or  $\text{Ta}_2\text{O}_5$ . The bulk substrate is connected with an ohmic contact. On top of the insulator sits the electrolyte to be measured contacted with a reference electrode. The back of the substrate is illuminated by a modulated light source. A schematic cross-section of a LAPS is depicted in Fig. 2.7. When a bias voltage is applied to the reference and the substrate an AC-photocurrent can be observed. For high enough bias voltages the current saturates. For low voltages the current is zero. The bias potential at which the photocurrent reaches its extremes is dependent on pH. This is caused by the surface charge on the insulated layer due to the binding of protons to it which will then influence the depletion layer in the silicon. One operating mode is referred to as “constant current”. Here the current is kept in the middle between zero and saturation current by adjusting the bias voltage. Another mode is “constant voltage”



where the bias is held constant and the current is measured. This allows higher sensitivity and faster response, according to Hu et. al. [40].

This current is only generated in the illuminated area. Therefore spatially resolved pH measurements are possible with this device. Another advantage is its simplicity. It does not need any structures which makes it very simple to manufacture. Also the structure is very flat. Illumination is possible with LEDs or lasers and the light source can be modulated to use a lock-in amplifier.

Molecular Devices uses this device as detector in its immunoassays [68].

### 2.3.6 Ion Sensitive Field-Effect-Transistor (ISFET)

ISFETs were invented by Bergveld [69] and are modified MOSFETs. The gate metallization is omitted and replaced with an electrolyte which is also connected via an (reference-) electrode. Now the  $V_{th}$  of the resulting device reacts to chemical changes of the electrolyte, most notably to pH. Other ions can be detected in a similar fashion as the sensor shows cross-sensitivity [70, 71, 72]. These sensors are very fast with response times in the millisecond range [73, 74].

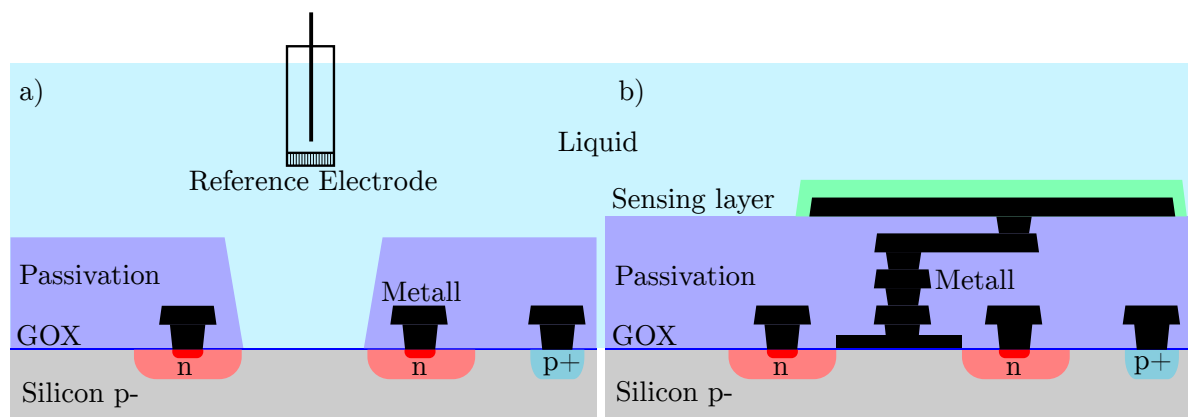


Figure 2.8: Schematic cross-section of two different ISFET designs. a) depicts the classical ISFET as proposed by Bergveld in 1970 [69]. It is based on a MOSFET but without a gate electrode. Instead, the electrolyte forms the gate and is only separated from the channel by the gate oxide GOX. The electrolyte is connected with a reference electrode for a stable bias potential. b) instead shows a so called extended gate ISFET. This is a standard MOSFET with the gate terminal connected to a larger metal plane on the top layer, covered by an oxide or other sensing layer. The potential difference between electrolyte and sensing layer is coupled capacitively to the gate. This design has the huge advantage of CMOS-compatibility. A disadvantage is that charge can be trapped on the floating node, resulting in a changing threshold voltage.



An important detail is the insulator between the channel and the electrolyte. It determines the sensitivity for different ions and is the only protection of the device. Often  $Ta_2O_5$  is used as it shows superior sensitivity, linearity and stability [70, 71, 75, 74].  $SiO_2$  [76] or  $Si_3N_4$  [77] are also often employed as they are widely available in semiconductor fabs. Other Materials include  $Al_2O_3$  [78],  $HfO_2$  [79] and  $WO_3$  [80, 81].

There are two different types: The original open design by Bergveld and the so called floating gate or extended gate ISFET. Here a normal integrated transistor is used and

the gate electrode is connected to a metal plane on the topmost layer of the chip. On top of that the protective passivation layer is used as sensing layer (see Fig. 2.8 for a direct comparison). This approach has the huge advantage of CMOS-compatibility [82]. But there is also the disadvantage of a capacitive voltage divider reducing the trapped charges on the floating node and influence through geometry and nearby fields that cause interference and drift [83, 84, 85]. Therefore some additional efforts need to be taken to compensate that [86].

### 2.3.6.1 REFFET

The ISFET itself still needs a reference electrode to set the electrolyte to a defined potential to measure absolute pH. A way around that is to use an ISFET with no or less pH-Sensitivity, a so called REFFET, together with a normal ISFET. From their difference the absolute pH can be derived [87, 70, 88]. To contact the electrolyte only a pseudo-reference electrode like platinum is required. One way to create a REFFET is to coat an ISFET's sensing surface with a PVC membrane [87]. However, this is no longer a standard semiconductor process. With floating gate ISFETs a similar effect can be achieved through different sized gate electrodes [89].

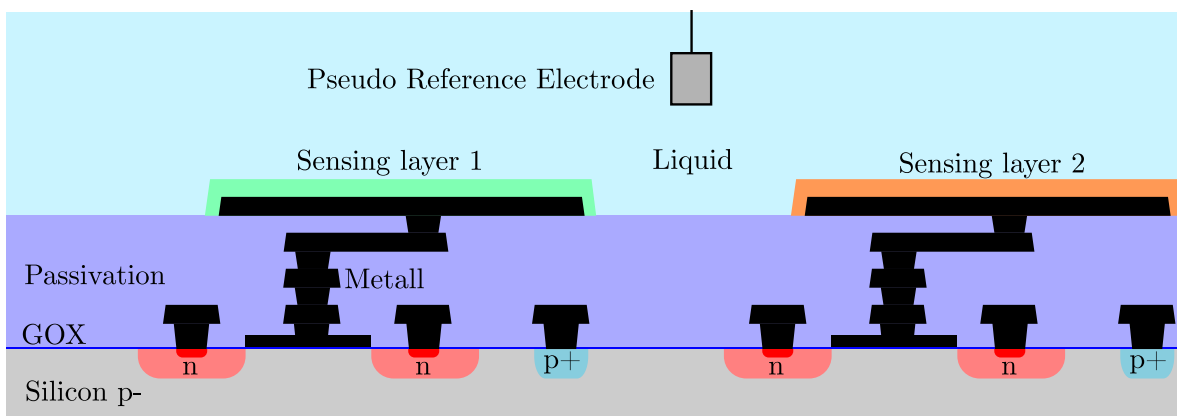


Figure 2.9: Schematic cross-section of an ISFET with REFFET. A REFFET is an ISFET with a modified sensing layer here depicted in orange. Ideally, it should behave the same as sensing layer 1 but without any sensitivity to pH. From the difference of the two FET signals the absolute pH can be calculated even with only a pseudo reference electrode instead of a proper reference. The pseudo reference can be a simple Pt-electrode and be integrated on the same chip which is much more difficult for an Ag/AgCl-electrode.



### 2.3.6.2 O2FET

An O2FET is an extension for an ISFET to measure dissolved oxygen [90, 91, 92]. It uses two additional electrodes, one in the vicinity of the sensing gate insulator (cathode) and one further away (anode). By applying a potential of  $-600\text{ mV}$  (vs. Ag/AgCl) to the cathode oxygen is reduced in the vicinity of the gate and  $\text{OH}^-$  is generated according to equation 2.1. The local increase of pH due to  $\text{OH}^-$  is detected through the ISFET. The change is dependent on the available dissolved oxygen.

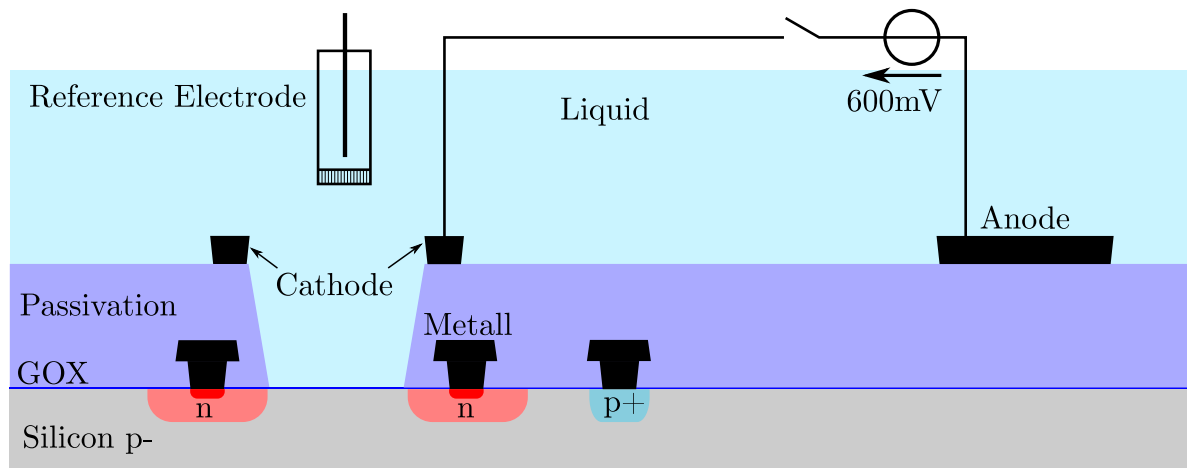



Figure 2.10: Schematic cross-section of an O<sub>2</sub>FET. Basis is an ISFET (see Fig. 2.8). Next to the sensitive gate area is an electrode (e.g. made of Pt), the so called cathode. The corresponding anode is further away. By periodically applying a potential of 600 mV between these electrodes oxygen is reduced at the cathode according to equation 2.1. This reaction produces OH<sup>-</sup> which can then be detected by the ISFET as pH increase. 

### 2.3.6.3 CVFET

The CVFET is the generalized form of the O<sub>2</sub>FET to detect more different substances by applying specific voltage-sweeps to the auxiliary electrodes and start a Analyte dependent and pH-changing redox reaction [93].

### 2.3.6.4 CHEMFET

Another method to detect different substances with an ISFET is to apply an ion-selective membrane on top of the gate area. This device is then called CHEMFET. This way specific ion-concentrations other than H<sup>+</sup> can be measured e.g. K<sup>+</sup>, Na<sup>+</sup> and Ca<sub>2</sub><sup>+</sup> [76, 94, 95, 96]. This principle can also be extended to enzymes and combined with methods from the CVFET to detect more different agents [97, 98].

### 2.3.6.5 Heated ISFET

Toumazou et. al. present an ISFET chip with integrated heating element [99]. The intention of this heater is to facilitate DNA reactions like polymerase chain reaction (PCR). The chip is used for DNA measurements, i.e. virus detection and exploits the liberation of H<sup>+</sup> during PCR. The chip has temperature sensors and a feedback loop to control the temperature and reaches up to 95 °C.

### 2.3.6.6 ISFETs for cell culture monitoring

Bergveld proposed ISFETs from the beginning for cell monitoring, mainly for action potentials of muscle cells [76]. Not quite cell monitoring but somewhat similar is the use of an ISFET to measure pH changes due to dental issues in a patients mouths [100]. Baumann et. al. could show that cells grow on ISFETs which can then be used to read the

extracellular acidification rate to deduce the metabolism [9]. The so called cell monitoring system was intended to study the effect of drugs and other substances on cells. Their sensor chip also included an IDES for impedance spectroscopy to also monitor morphological changes of the cells. They also propose a multi-well-plate with sensor chips in its bottom for high-throughput screening. A later version of that system also uses O2FETs to measure oxygen in close proximity to the pH sensors allowing a better correlation of the signals [91]. Milgrew et. al. build an array of ISFETs on their chip to achieve a spatially resolved pH image of their cell culture and use it for cellular imaging.

### 2.3.6.7 ISFET Readout

ISFET readout is a bit more complex than for other sensor types. External factors like pH affect the  $V_{th}$  of the transistor. This internal property cannot be measured as easy as a resistance for example. There are several ways to extract  $V_{th}$  of a transistor. A usually recommended approach for ISFETs is to keep  $V_{ds}$  and  $I_{ds}$  constant and monitor the required  $V_{gs}$ , where the gate is the electrolyte potential connected through the reference electrode [70, 101]. This method is often called CVCC (constant voltage, constant current).

Assuming a Schichman-Hodges model this results in:  $\Delta V_{gs} \propto \Delta V_{th}$ . With  $\Delta V_{th} \propto \Delta \text{pH}$  this yields  $\Delta V_{gs} \propto \Delta \text{pH}$ . So a direct relation between a measurable voltage and pH is established. There are different realizations for this circuit described in literature and app-notes of manufacturers. A proposed circuit from Optoi Microelectronics (Italy) [102] is depicted in Fig. 2.11.

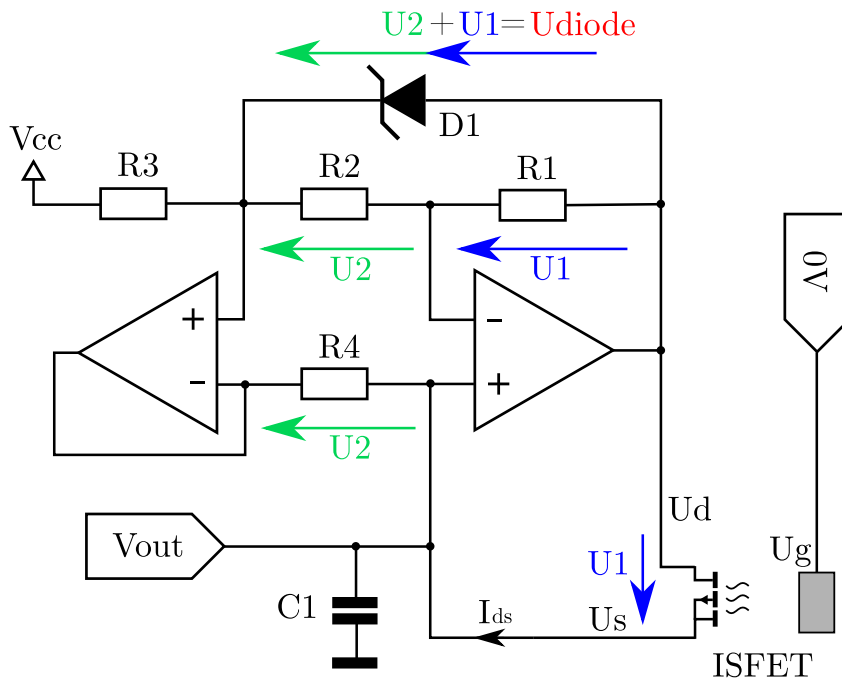



Figure 2.11: Schematic of the ISFET readout circuit proposed by Optoi Microelectronics (Italy) for its sensors (redrawn from [102] and adapted for p-channel).  $R1 = 150 \text{ k}\Omega$ ,  $R2 = 470 \text{ k}\Omega$ ,  $R3 = 10 \text{ k}\Omega$ ,  $R4 = 9,1 \text{ k}\Omega$ ,  $C1 = 470 \text{ pF}$ ,  $D1$ : Bandgap voltage reference diode 1,23 V (e.g. MP5010), OpAmp: e.g. AD8608, AD8674 or equivalent. The circuit keeps  $V_{ds}$  and  $I_{ds}$  constant and outputs  $V_s$ .  $V_g$  is set to a constant level with a reference electrode. 

Moser et. al. present a different other readout circuits [101]: One method is called ISFET-inverter[103]: it is based on a normal CMOS inverter but the input gates are floating. The electrochemical environment couples capacitively to that like in a standard extended gate ISFET. There is a second electrode that also capacitively couples with the floating gate. It is fed with a triangular wave signal and therefore periodically switches the inverter. The switching point is determined by the voltage coupled by the chemical potential. This allows a direct digitization of the ISFET signal.

There are also different other architectures that try to convert the pH-signal to a time signal [104]. This allows for higher density of ISFETs e.g. for pixel sensor arrays.

It is often recommended to set the reference electrode that connects the electrolyte to ground potential [70, 105]. This is justified with the argument that the liquid could be grounded anyway through some other metal part that touches it. However, this can still create a galvanic element between the reference electrode and this other metal leading to a current. This current might disturb and destroy the reference electrode. Therefore, the best solution is to either prevent any other contacts in the liquid or galvanically isolate the complete ISFET circuit in the first place. With galvanic isolation, the reference potential can then be set freely to a value that is favourable for the circuit.

### 2.3.6.8 Commercially available ISFETs

**Sentron** offers ISFETs encapsulated in different form factors and corresponding readout units [106] (see Fig. 2.12). They also provide OEM-circuit modules and denote the sensitivity of their devices with 52 mV/pH. The available readout is modular (ISFET-control, ADC-unit, UART-USB-bridge) and quite expensive (ca. 400 EUR for all three). It does not seem to be adjustable. There are no operating parameters for the ISFETs provided. The probes are also equipped with a temperature sensor and a standard Ag/AgCl-reference electrode.

**Honeywell** offers with its *Durafet* product line ISFET based pH-Sensors for process monitoring. They come with reference electrode and temperature sensor and are only compatible with Honeywell specific readout electronics. There are not much details about the principle and the structure of the FET available on the website [107]. Also there are only a few images available, shown in Fig. 2.13.

**Winsense** Winsense provides ISFETs in different packages and even as bare die or whole wafer. They use silicone nitride as sensing layer and claim a sensitivity of 50 mV/pH. They also provide much information about their FETs and the operating principle, as well as operating conditions ( $V_{DS} = 0,3\text{ V}$ ,  $I_{DS} = 30\text{ }\mu\text{A}$ ) and circuits on their website [108]. The circuit is built discrete and the operating point is fixed using the constant  $V_{ds}$  and  $I_{ds}$  principle. The ISFET has a size of  $1,4\text{ mm} \times 3,5\text{ mm}$ . Its range is denoted as pH 2-12. Also, a temperature sensor is attached to the ISFET. A collage of images from Winsense to its sensor and readout unit is depicted in Fig. 2.14.

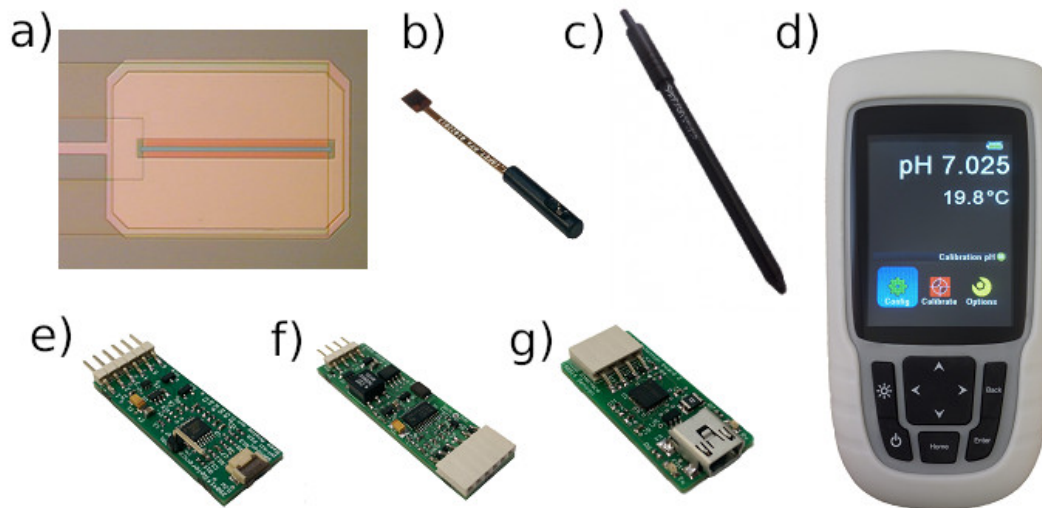


Figure 2.12: Sentron ISFETs: a) microscope image of the ISFET die, unfortunately no dimensions are provided. b) and c) two different form factors of encapsulated ISFET-probes. The actual ISFET is mounted in the bottom tip. c) has also a reference electrode integrated. d) Hand-held pH-meter for electrode c). e) OEM ISFET read-out electronic with analog output. f) OEM ADC-module to digitize the analog output of e). g) OEM UART to USB bridge to connect f) to a computer. All images adapted from Sentron's website [106], rearranged and subfigure designators added. Reproduced with permission from Sentron Europe B.V.

**Microsens** offers among other electro-chemical sensors also ISFETs with  $\text{Ta}_2\text{O}_5$  sensing layer and  $55 \text{ mV/pH}$  sensitivity ([109] and enquiry to Microsens SA). They also provide functionalized devices to detect specific ions like  $\text{K}^+$  and  $\text{NO}_3^-$ . Their readout electronics has a resolution of  $1 \text{ mV}$  at  $1 \text{ SPS}$  and is fully galvanically isolated. It uses the constant current and constant voltage approach and the operation point is fixed to  $V_{ds} = 500 \text{ mV}$  and  $I_{ds} = 100 \mu\text{A}$ . There are electronics for USB-operation and for embedded systems with an UART. The size of the embedded version is  $35 \text{ mm} \times 25 \text{ mm}$ . There are only a few passives on the PCB and two ICs, one being the isolator for the UART and the other being a microcontroller (see Fig. 2.15). However, based on the designators of these two to be U3 and U4 one can assume that there are some more ICs on the underside, i.e. opamps.

**Mettler Toledo** also provides ISFET sensor probes. The information on their website [110] are very sparse and do not reveal a lot about the technology of the FET. They claim to measure the full range pH 0-14 and have a standard reference electrode build into the shaft (see Fig. 2.16 for a drawing). A proprietary electronic from Mettler Toledo is needed to read the sensor. The ISFET control circuit is apparently build into the electrode shaft because the electrode uses a manufacturer specific communication protocol.

**Zimmer and Peacock** do not offer ISFETs but an ISFET-readout based on the ADuCM355-chip called GFET that can read two sensors. Besides the ISFET readout it supports also other electro-chemical principles. Unfortunately, as of September 2020 there is no further documentation or specification available [111].

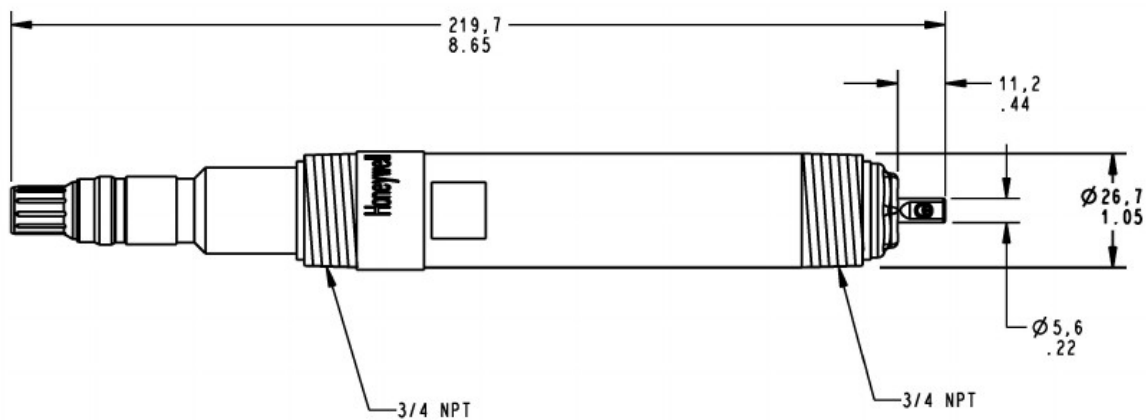
a)



b)



c)



mm  
inches

Figure 2.13: Honeywell DuraFET: a) Different transmitters for Honeywell sensors that can also be used for the DuraFET ISFET probe. b) is an image of a Durafet probe. The sensitive area is on the right end and protected by a cover. On the left is the connector. c) is a technical drawing of a similar probe but this has no cover for the sensitive area which is therefore visible. All images adapted from Honeywell's website [107], rearranged and subfigure designators added. Reproduced with permission from Honeywell.

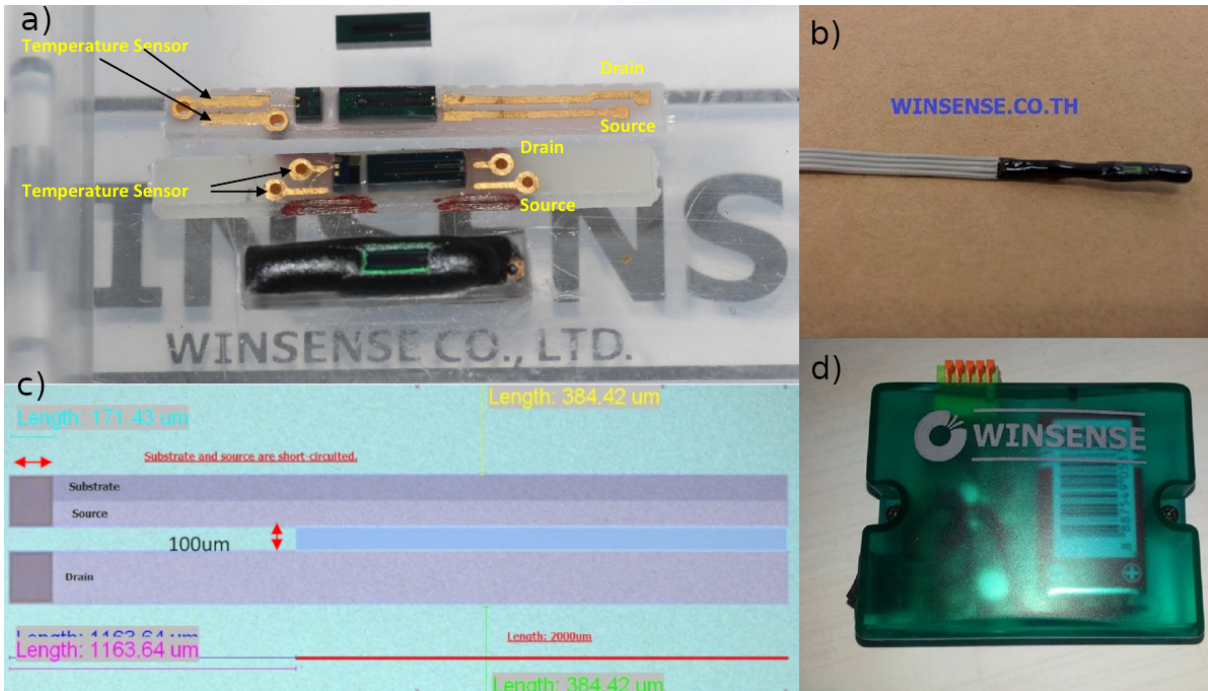


Figure 2.14: Winsense ISFET: a) shows a bare die and two unencapsulated ISFET chips with connectors and an encapsulated one from top to bottom. b) is an ISFET as it is sold with connecting wires. c) shows a microscope image of the actual ISFET with the source and substrate connection on the top and the drain on the bottom. On the left side are the connectors and on the right the ISFET with a channel width of  $2000\ \mu\text{m}$  and a length of  $100\ \mu\text{m}$ . d) shows the readout electronic provided by Winsense. On the top there is a 5-pole connector for the ISFET connection and the analog voltage output. It is powered by a 9V-Battery that can be seen through the translucent case. All images adapted from Winsense's website [108], rearranged and subfigure designators added. Reproduced with permission from Winsense Co., LTD.

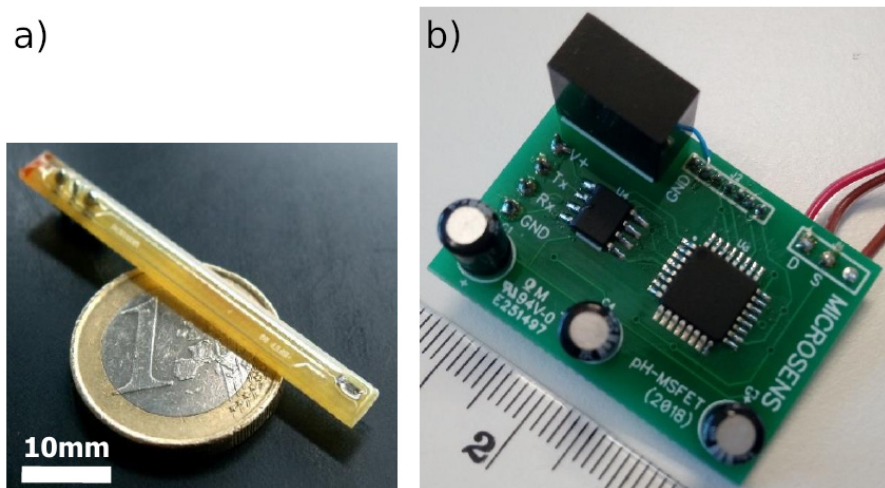


Figure 2.15: Microsens ISFET: a) shows an ISFET, the sensitive area is in the lower right of the image. b) shows one readout electronic from microsens intended for embedded use. The ISFET is connected to the solder terminal on the upper right corner labelled with D and S. The IC on the left is an isolator for UART, the large black box in the top left corner seems to be an isolated DC/DC-converter. The right IC seems to be a microcontroller. The part designators indicate that there might be more ICs on the bottom side of the PCB. All images adapted from Microsens's website [109], rearranged and subfigure designators added. Reproduced with permission of MICROSENS SA, Lausanne, Switzerland.



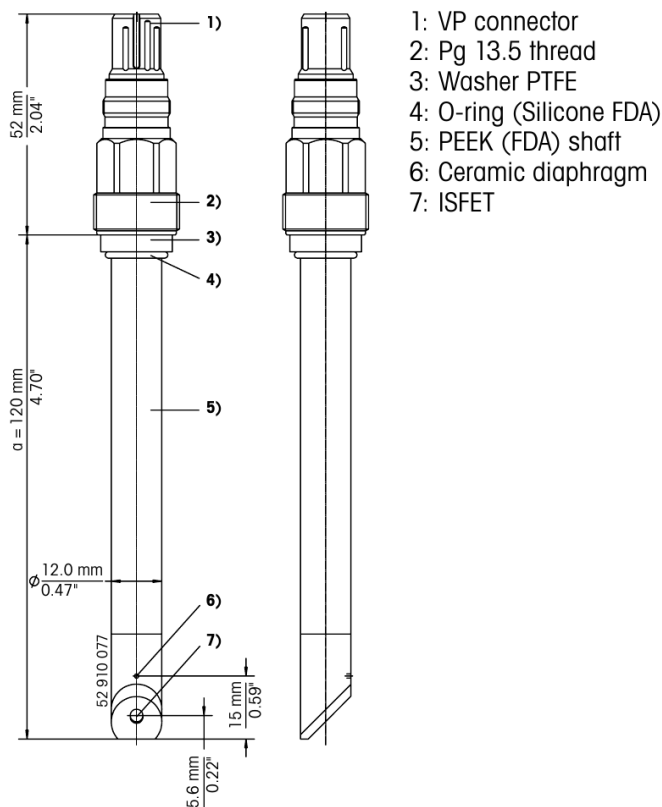


Figure 2.16: Technical drawing of an ISFET-pH-probe by Mettler Toledo. The ISFET itself (7) sits on the bottom tip of the shaft. The diaphragm (6) is the fluid connection for the reference electrode. On the top is a connector (1) for the readout electronics. Drawing adapted from Mettler Toledo instruction manual for their InPro3300-ISFET pH-probe, available on their website [110]. Reproduced with permission from Mettler Toledo GmbH.

## 2.4 Miniature Reference Electrode

A reference electrode is important for ISFET sensors to set the electrolyte to a defined potential. But unfortunately there are not so many solutions having a similar size of an ISFET of only a few millimetres. This is mainly due to the fact that common reference electrodes like the Ag/AgCl electrode need a defined electrolyte to work properly. Here a change in the electrolyte's  $\text{Cl}^-$  concentration will change the potential. The AgCl on the silver may slowly dissolve in the electrolyte. To prevent this the reference electrolyte is saturated with AgCl [112]. To ensure a constant concentration this reference electrolyte needs to be separated well enough from the other electrolyte but still in electrical contact. This is usually done with a salt bridge or a frit, which is a micro-porous material.

There is an electrode from Unisense [54] with a tip down to  $10\ \mu\text{m}$  similar to their pH probe. But the whole electrode is 70 mm long.

Another solution uses a micro-hole in a Si-die for a very low leakage liquid junction. The reference electrolyte is in a cavity of a PCB which is sealed on both sides with a Si-die. One of those has a micro-hole for electrical contact to the surrounding liquid. In the inner electrolyte a silver electrode is used for contact forming an Ag/AgCl-Electrode. This assembly is very small, fits in a PCB and is manufacturable with mostly common semiconductor and PCB processes except for the final assembly [113].

The concept from Comte and Janata is similar [114]: They use an ISFET and build a small well around its sensitive area. This is then filled with agarose gel based on a buffer. A glass capillary is inserted in the gel and the remaining area is sealed with epoxy. The reference transistor can then be used similar to a REFFET. However, this process is all done manually.

Another paper claims to have build a solid state reference electrode with Ag/AgIO<sub>3</sub> and used it for pH measurements together with a Sb<sub>2</sub>O<sub>3</sub> electrode [115, 116]. No further publications about Ag/AgIO<sub>3</sub> as reference electrode could be found. There are however reference electrodes based on iodide/triiodide [117] but these are not solid state and similarly built as Ag/AgCl electrodes.

For bio sensors often planar Ag/AgCl-electrodes are used. One way is to deposit silver and then create an AgCl layer electrochemically on it. It is also possible to print an Ag/AgCl paste on a noble metal electrode [112]. The potential determining Cl<sup>-</sup> concentration in cell culture medium is quite stable, so this results in a stable reference potential [118]. However, silver ions are cytotoxic and will affect the cell culture. It is possible to prevent the spread of silver ions in the medium by covering the electrode with pHEMA<sup>2</sup> [private communication with Walter Wirths].

### **2.4.1 Palladium-Hydride Electrode**

For micro applications also very popular are palladium-hydride electrodes. Sometimes they are entitled reference electrodes [119, 120, 121, 112]. But this is only true as long as the pH of the electrolyte is stable. PdH shows a nearly Nernstian pH dependence of ca. 58 mV/pH [122, 123, 124] making it a good pH-electrode but rendering it useless as reference electrode for pH measurement applications. The electrode is based on palladium, usually in form of a wire or a thin film that is charged with hydrogen. Palladium has the property to take up relatively huge amounts of hydrogen in its lattice forming palladium-hydride (PdH). This charging can be done by electrolysis of water. Thus a reservoir for hydrogen is created. Because of a lower hydrogen pressure in the solution a hydrogen out-flux from Pd occurs changing the composition. The potential is determined by this redox reaction:  $\text{H}^+ + \text{e}^- \rightleftharpoons \text{H}(\text{Pd})$  and therefore by the activity of the hydrogen in PdH. The PdH system has three phases:  $\alpha$ ,  $\beta$  and  $\alpha + \beta$  where the former two are in equilibrium. During the  $\alpha + \beta$  phase the hydrogen activity which affects the potential is only dependent on temperature [124]. The  $\alpha$ - and  $\beta$ -phase only exist at extreme Pd to H ratios so it is very easy to create the required  $\alpha + \beta$ -phase. If the hydrogen content is too low and only the  $\alpha$ -phase exists the potential is no longer stable. In this case the electrode can simply be charged again. As the redox reaction also involves H<sup>+</sup> the potential is also dependent on the activity of H<sup>+</sup> which is by definition the pH. Oxygen present in the solution will consume the out-flowing hydrogen and disturb the potential. A solution to prevent this is to increase the surface of the palladium resulting in the hydrogen outflow to overwhelm the oxygen. An easy way to achieve this is to deposit palladium black which is palladium with a very large surface [123].

---

<sup>2)</sup> Poly(2-hydroxyethyl methacrylate)

## 2.5 Impedance Spectroscopy

Impedance spectroscopy is the measurement of the electrical impedance at different frequencies. The impedance is usually described as a complex value to account for the possible phase shift between voltage and current with sinusoidal signals. For ideal, linear, fundamental circuit elements such as resistances, inductances and capacitances, the impedance is either constant, proportional or indirect proportional with frequency. For more complex RLC-networks different spectra emerge. Most instruments excite the DUT<sup>3</sup> with a constant sinus signal and measure the response, i.e. excite with a voltage and measure the current or the other way round. The spectrum is recorded by scanning different frequencies sequentially. This can be quite time consuming therefore there are methods to use more complex excitation signals to record more frequencies at once, speeding up the measurement [125].

Impedance spectroscopy is used to characterize electronic filters but can also be employed for material science. For example, the state of a battery-cell can be assessed by its impedance spectrum [126, 127]. Another use case for impedance spectroscopy is to measure the vitality of biological cells [128, 129]. This is often referred to as EIS, electrical-impedance spectroscopy, or bio-impedance spectroscopy.

Impedance spectrometry circuits can also be used in combination with an optical interface to read fluorescence sensor probes [55, 130].

### 2.5.1 Bio Impedance Spectroscopy

Biological cells are surrounded by a membrane consisting of lipids. In contrast to ion-containing and therefore conductive cytoplasm, the cell membrane is insulating. The extracellular medium is also conductive. A very simple electrical model to describe the membrane is as a capacitor and the electrolyte as resistor. Depending on cell morphology that is if they form a monolayer with tight connections to their neighbour, or single, unconnected spheroids the capacitive and the resistive components of this model changes. That way the growth and death of a cell culture on a special electrode structure can be monitored by impedance spectroscopy [128] (see Fig. 2.17). Usually a so called Inter Digitated Electrode Structure (IDES) is used. Two electrodes form a structure like the fingers of folded hands but in a plane (Fig. 2.2A and 3.18b show such structures). There is also an effect of the used frequency: At low frequencies around 5 kHz the formation of a tightly connected monolayer can be observed. At high frequencies around 100 kHz the total cell count is reflected by the impedance [129].

There are also approaches to measure capacitance effects of the cells without a direct electrical contact [131]. The sensing electrodes are completely isolated from the cells and the medium, unlike the other bio impedance approaches. The sensing approach is similar to a capacitance meter, e.g. with an oscillator where the sensing capacitance determines the frequency [132].

---

<sup>3)</sup> device under test

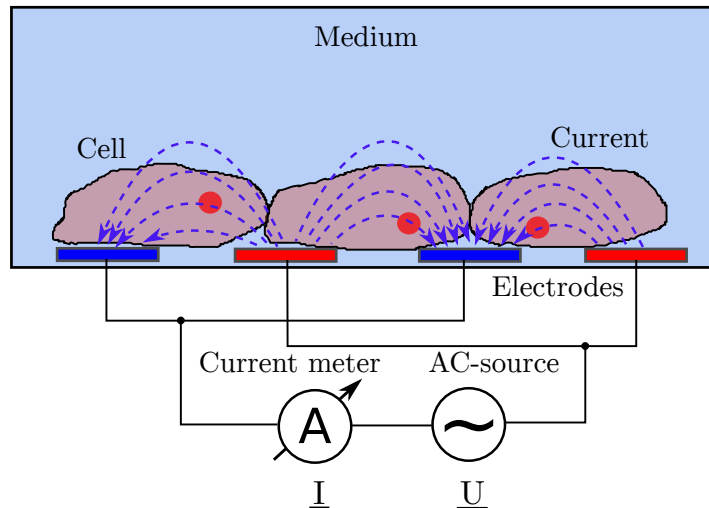



Figure 2.17: Cells on an interdigitated electrode structure (cross-section). The electrode is excited with an AC-voltage  $\underline{U}$  and the current  $\underline{I}$  is measured in phase and amplitude. Depending on cell morphology different paths for the current (blue dashed lines) are available, either between the cells through media or directly through the cells as depicted here. This results in different amplitudes and phases for different frequencies making it possible to detect morphological changes. 

## 2.5.2 Commercially Available Impedance Spectrometers

**Sciospec** offers impedance spectrometers for different applications [133]. They are able to measure from Ohm to GigaOhm and from DC to 10 MHz in two, three and four electrode mode. Sciospec also offers equipment for impedance tomography which can be used for imaging of samples. They also manufacture OEM and custom electronics.

**Ivium** provides a variety of different electrochemical measurement devices. Amid others they come with an impedance measurement mode [134, 135]. They feature a Frequency range from 10  $\mu$ Hz to 3 MHz. There is no specification on impedance measurement accuracy.

**Eliko** features an impedance measurement system which can assess multiple frequencies at once [136]. To achieve this the impedance is excited with a random looking square signal whose frequency domain representation shows strong peaks at different frequencies [137]. A demo system costs about 2200€ and its measurement repeatability is stated as 0,1 %.

**PalmSens** manufactures relatively cheap (3000-4000€, Aug. 2019) impedance spectrometers for 10  $\mu$ Hz to 1 MHz [138, 139]. They also produce OEM-Modules based on the Analog Devices ADuCM355. Accuracy is stated to be better than 1 % of the reading.

**Ametek** manufactures the Solartron 1260A which is featured in many research papers and provides high precision impedance measurements with 0,1 % amplitude and 0,1° phase accuracy [140]. It covers a frequency range from 10  $\mu$ Hz to 32 MHz and is considered as the standard for impedance spectroscopy.

**Analog Devices** offers several integrated circuits specifically designed for impedance analysis such as the AD5933, AD5934, ADuCM350 and ADuCM355. They offer dedicated hardware for the discrete Fourier transform as well as a DDS for the excitation signal and an ADC with preamplifier. The ADuCM series also comes with an integrated ARM-Core and analog front-ends for other electro-chemical measurements. Their frequency range is up to 200 kHz. For some use cases they need some external amplifiers. Their prices range from 8 to 30€.

**OpenEIT** is a project that aims to build a low-cost impedance tomography interface [141]. It is open source and open hardware and based on the ADuCM350. A multiplexer is used to measure impedance between each of up to 32 electrodes. There is no information on resolution and accuracy available. There is a crowdfunding campaign for a first revision of the electronics. A board costs about 300€.

### 2.5.3 Research on impedance spectroscopy circuits

Grassini et. al. present an interesting approach for wide range impedance spectroscopy using a logarithmic amplifier to measure the current through the unknown impedance [142]. This allows the detection of current over several orders of magnitude without the need to switch the input range. Implementing such a range switch with programmable gain amplifiers makes the systems more complex and expensive. The logarithmic transfer function of the amplifier needs then to be compensated in software to calculate the impedance. Excitation is done with a DDS implemented in a microcontroller with integrated DAC. This controller has also an ADC which is used for coherent detection of both excitation and current response of the system. The achievable range is from  $100\ \Omega$  up to  $10\ \text{G}\Omega$  at low frequencies. The frequency can go up to 100 kHz.

Santos and Ramos use a microcontroller with integrated DSP functionality, the dsPIC from Microchip, to measure impedances [143]. Two external ADCs with PGAs are used to capture the voltages across a switchable reference impedance and the DUT which form a voltage divider. An external DDS IC is used for excitation. The DSP functions are used for filtering and to calculate the argument and phase from the ADC samples very fast. The system has a wide range up to 200 kHz and an impedance range from 0,1 to  $10\ \text{k}\Omega$ . Unfortunately the paper lacks some details like the measurement accuracy and a detailed evaluation of the measurement performance.

## 2.6 Sensors for the Multi-Well-Plate

From the available sensors ISFETs seem promising in their ability to detect pH and also with a little modification oxygen. With these parameters oxygen consumption and extra cellular acidification rate can be measured to determine the metabolism of the cell. These sensors can also be produced cheaper than optical systems thanks to semiconductor technology. On the same substrate an IDES can be manufactured for impedance spectroscopy to measure cell adhesion and morphology. Still an integration of lots of these sensors into the confined space of the plate together with the required read-out electronics is needed. The current read-out systems are either too big or too expensive and complex for the plate:

## *State of the Art*

They use either bench-top measurement devices or they need an ASIC. Therefore another solution is required, one that is small but also manufacturable for reasonable prices like a normal PCB with stock components. This is developed in this thesis.

# 3 Material, Methods and Technology

## 3.1 Overview

The mind map (Fig. 3.1 on page 36) gives an overview and shows the different parts of this work and their relations to each other. They are further explained in the following sections and chapters. In chapter 3 all used materials such as chemicals, sensors and test-setups are described. In chapter 4 all developed electronic circuits are described, as well as electronic tests to evaluate their performances. Chapter 5 describes the measurement results regarding the electronics together with the sensors and as part of the wireless multi-well-plate.

## 3.2 Chemicals

### 3.2.1 pH buffers

pH buffers from Merck (Certipur and Titripur) were used to establish known pH values for pH-sensor tests. They are traceable to national and international pH standards and commonly used to calibrate pH meters. Here they are used to simulate pH changes for the ISFET-sensors.

### 3.2.2 O<sub>2</sub> references

PBS (VWR Chemicals) was used to test oxygen sensors. PBS is phosphate buffered saline, a solution with physiological salt concentration and buffered to pH 7,4 with a phosphate buffer system. One part of the solution was bubbled with nitrogen (5N) to remove all dissolved oxygen [144] to create a zero standard. The second part was shaken with air in a bottle to ensure 100 % air saturation with oxygen. A third solution was prepared by bubbling it with pure oxygen (97 % from a medical concentrator), resulting in ca. 450 - 500 % air oxygen saturation. A Fibox 2 from PreSens [49] was used to verify that these procedures were successful. With these solutions the oxygen consumption of cells is simulated to test the sensitivity and accuracy of the O<sub>2</sub>FET oxygen sensors.

## 3.3 Measurement Equipment

This section describes the used commercial measurement systems.

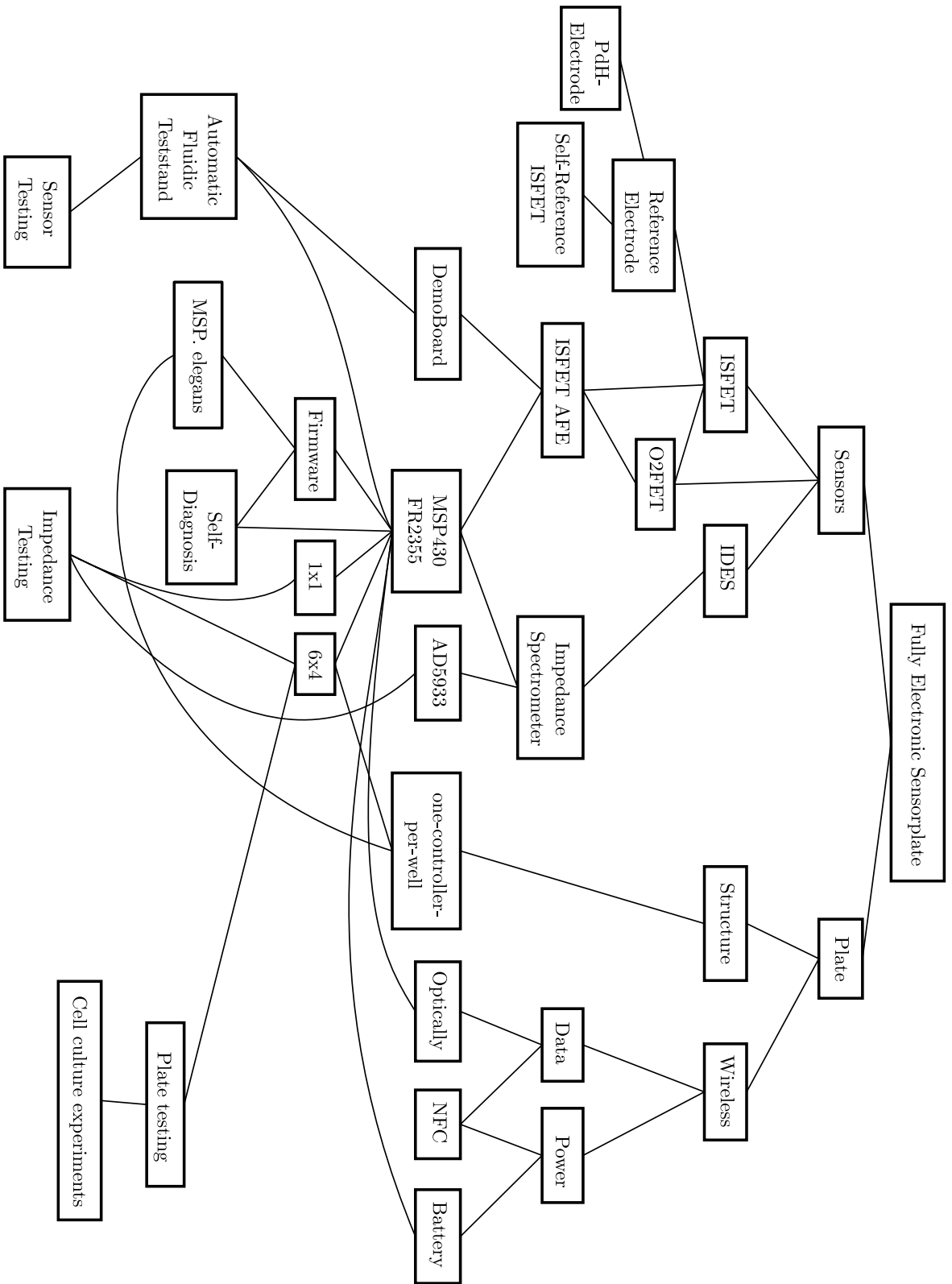


Figure 3.1: Mind map showing the parts of this thesis and their relations to each other.





### 3.3.1 IVIUM CompactStat.h - Potentiostat

The IVIUM CompactStat.h (see Fig. 3.2) is a small USB-powered potentiostat with EIS capability [135]. It provides the usual electro-chemical measurement methods like cyclic voltammetry or chrono-amperometry. Additionally it can perform impedance measurement for frequencies up to 3 MHz. This device is used as reference for the developed impedance spectrometers and to conduct measurements on the PdH-electrode and various other electrochemical tests.

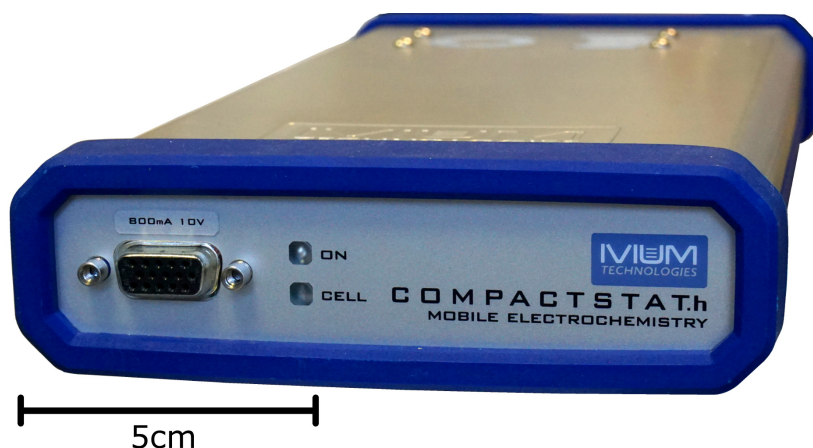



Figure 3.2: Ivium Compactstat.h potentiostat: The electrodes are connected to the 15-pole sub-D connector in the front. In the back (not visible) there is an USB, power and auxiliary connector. 


### 3.3.2 PalmSens4 - Potentiostat

The PalmSens4 (see Fig. 3.3) is a device similar to the IVIUM CompactStat.h for electrochemical measurements and impedance spectroscopy up to 1 MHz [139]. It is cheaper than the IVIUM and has the option for a 8:1 multiplexer. This device was used to test multiple IDES-structures quasi-simultaneously. It also provides a software that allows easy scripting of complex measurement sequences, which is useful to e.g. apply different potentials to sensors to trigger different reactions over time.

### 3.3.3 Fibox

The Fibox (see Fig. 3.4), manufactured by PreSens, is an optical dissolved oxygen meter. It uses a fluorescent dye (see Section 2.2.2) at the end of a optical fibre. This sensor probe can then be dipped into a vessel to measure the oxygen inside. It also supports a temperature sensor for temperature compensation. Data is transmitted via a RS-232 link, otherwise, there is no display. The software to read the data and control the instrument only works under one proprietary operating system. It is also possible to read the values in plain text in the data stream, in case the software does not run. This device is used as reference for dissolved oxygen measurement.



Figure 3.3: PalmSens4: This is a electrochemical measurement device, which is also capable of doing impedance measurements. The electrodes are connected to the cable on the right. On the left side of the device, there is an USB-connector Type-C (not visible). The display shows current parameters and status of the device. 

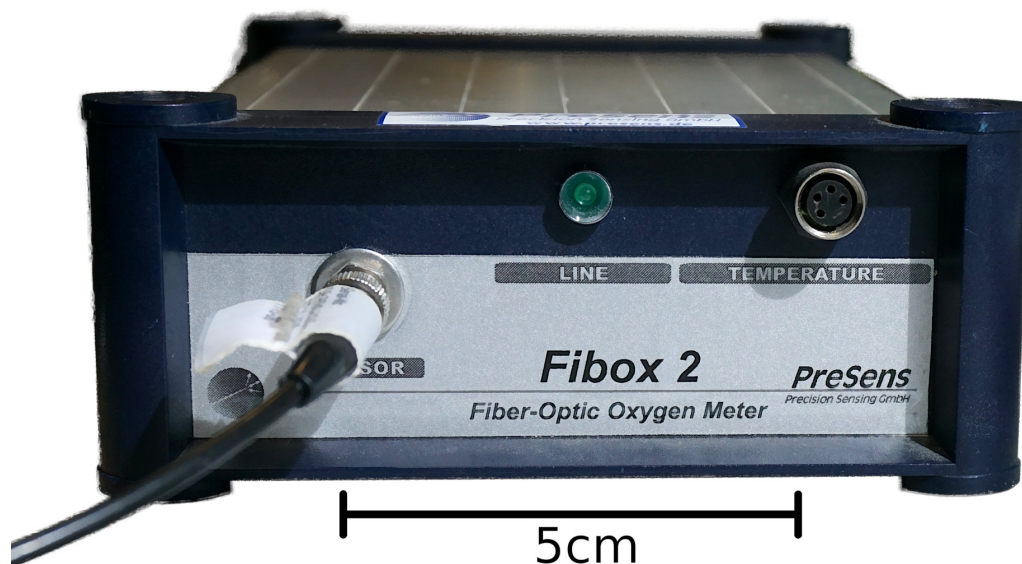



Figure 3.4: PreSens Fibox 2 optical dissolved oxygen meter. A fibre optic with a fluorescent oxygen probe at the end is connected on the left side of the front panel. 

### 3.3.4 Keysight E4980A - LCR-Meter

IDES sensor structures, coils for NFC antennas and various other parts were measured with a Keysight E4980A precision LCR-Meter. This device is stated to have a basic accuracy of 0,05 %. But this figure is not sufficient to describe the whole topic, more details on the measurement performance of this device can be found in the datasheet [145].

### 3.3.5 Keithley 2401 - Source measure unit

Keithley 2401 Source measure units (SMU) (see Fig. 3.5) were used for different measurement purposes, generating bias voltages for ISFET simulation and device characterization. This device can source and sink 20 V and 1 A with a resolution of 5.5 digits [146].

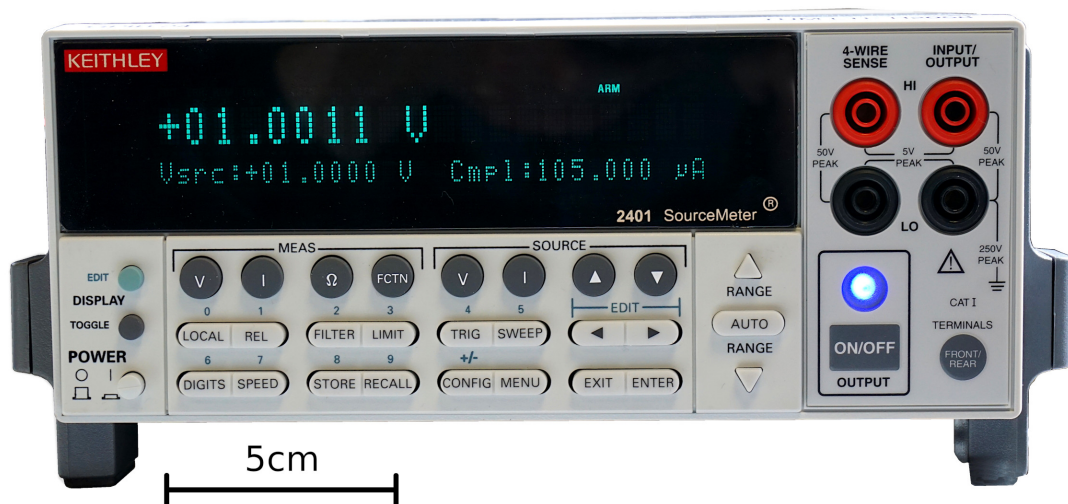


Figure 3.5: Keithley 2401 Source Measure Unit. 

### 3.3.6 B1500A Semiconductor Device Parameter Analyzer

The B1500A Semiconductor Device Parameter Analyzer from Keysight can be equipped with several SMU modules and perform different measurements required to characterize electronic components, such as all kinds of diodes and transistors. It can be programmed to sweep two SMUs, required to measure the typical output characteristics of transistors. This system was used for first tests with the new ISFETs to verify their transistor behaviour and measure leakage. Due to the complex setup with triaxial connectors, inconvenient data export possibilities and work space limitations, this system was not used for further measurements.

## 3.4 Electrodes

### 3.4.1 Reference and pH Electrode

To test the ISFETs a pH-combination-electrode with integrated Ag/AgCl electrode from VWR (catalogue number: 662-1381) was used. Only the reference electrode, that is the outer connector on the coaxial connector, was connected for this measurement. For this electrode a flow-cell assembly with standard IDEX-fittings is available, allowing easy integration into fluidic systems (see. Fig. 3.6). This electrode was also used to measure pH with a standard pH meter.

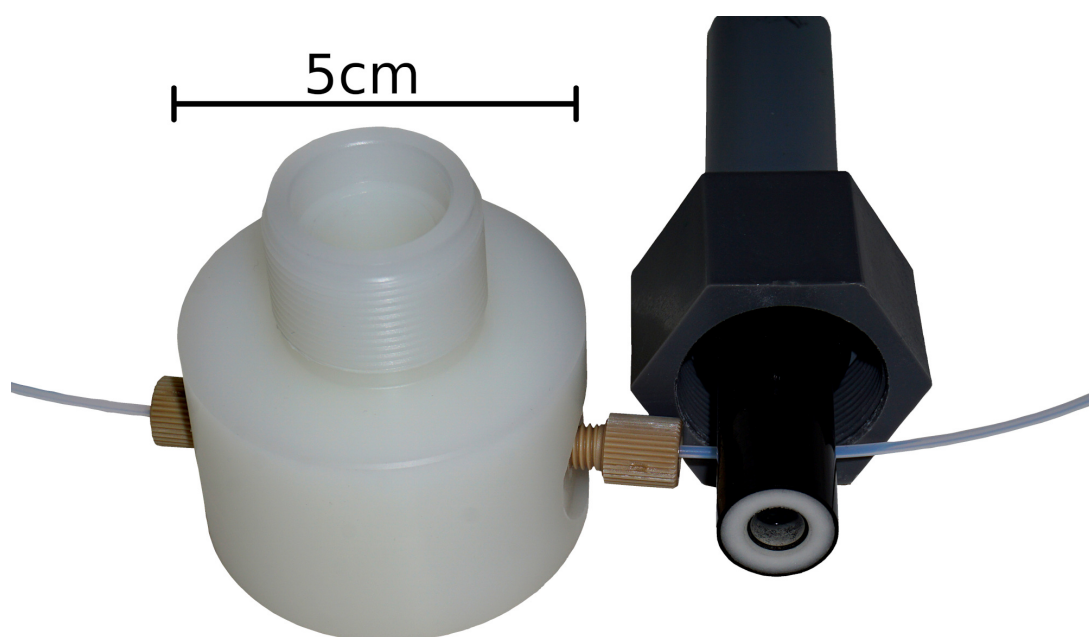



Figure 3.6: This image shows the disassembled electrode: The electrode itself is on the right with the pH sensitive glass membrane in the center and the diaphragm for the reference electrode as concentric white ring around it. The flow through cell is the white cylindrical part on the left. It has a small tube connected to it on either side and a large threaded opening on the top. To use this electrode, it is inserted in the large opening of the white flow-cell and fixed with the sleeve nut. The media is then pumped through the tubing and has contact with the diaphragm and the glass membrane while achieving a minimal dead volume. 

### 3.4.2 PdH-Electrode

Palladium can take up large amounts of hydrogen, forming the alloy PdH. This is reported to show a quite stable, but pH-dependent reference potential (see Section 2.4.1). However, as some publications use it as reference electrode, experiments were conducted if palladium can be used as reference for ISFETs and to obtain more knowledge about their properties. Different electrode types were examined for their performance in the course of a Master's Thesis by Daniel Kaindl [147]. They can be divided in wire based and plate electrodes. Pd-wires with a diameter of 0,2 mm and 25  $\mu\text{m}$  were cut to small pieces and soldered to Cu-wires. The solder joint was protected with Kapton tape or silicone. The wire pieces were dipped into a beaker with the electrolyte and used as working electrode in a three electrode

setup. A platinum electrode is used as counter electrode and an Ag/AgCl-electrode as reference.

Ca. 17 cm of the 25  $\mu\text{m}$  Pd-wire was wound around a PTFE-rod (6 mm diameter) and connected on both ends with two wires each for a four wire resistance measurement. Pd changes its resistance with the hydrogen charging level [148, 149]. Therefore such a thin but long wire was chosen to obtain a resistance value that is easy to measure. The DemoBoard was used to record the resistance values by feeding a current of 200  $\mu\text{A}$  and amplifying the voltage drop with a 10x instrumentation amplifier.

Pd-coated wafer pieces (200 nm Pd on 400 nm TEOS on Si) were broken into pieces about 2 cm by 5 cm and used as plate electrodes. The adhesion of the Pd layer was very low due to a manufacturing issue, therefore sawing was not possible. The wafer-pieces were glued together with a sheet of PTFE with a hole to expose only a defined surface (see Fig. 3.7).

To increase the surface, some electrodes were coated with *palladium black*. This is palladium, grown as a dense forest of very tiny spikes. It does not reflect much light, therefore it appears black. Pd black was deposited electrochemically from a  $\text{H}_2\text{PdCl}_4$  solution with 1% palladium content (mass percent). This solution was prepared from  $\text{PdCl}_2$  powder which was dissolved in HCl (1 mol/L) with some drops of concentrated HCl to aid the dissolution according to [150]. Also experiments were made with adding tiny amounts of lead in form of lead acetate to help the forming of the Pd black structure. The electrochemical deposition was performed at current density of 80  $\text{mA}/\text{cm}^2$  for about three minutes with a graphite anode and the blank Pd-electrode as cathode [147].

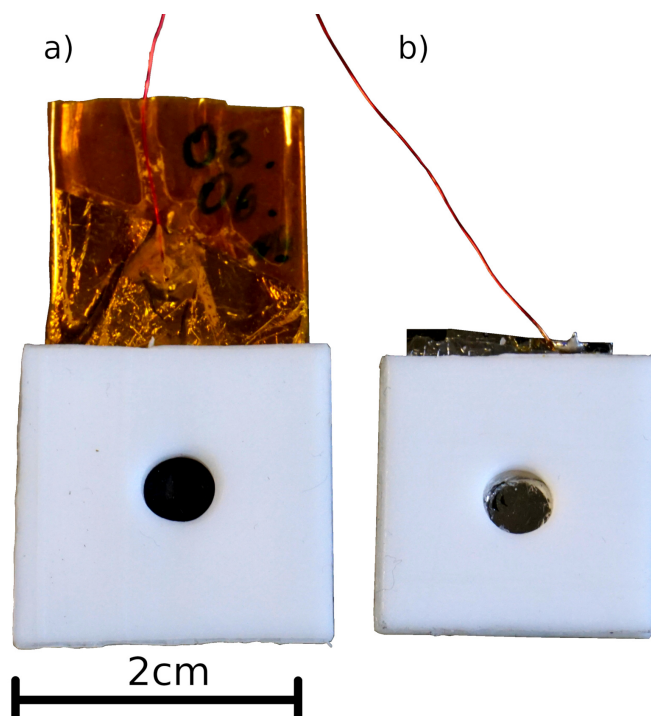



Figure 3.7: Two electrodes used for PdH-electrode experiments. Both consist of a wafer piece with Pd glued onto a PTFE-plate with a hole to define the active surface. A wire is soldered to the Pd for electrical contact. The backside is isolated with silicone. a) shows an electrode with Pd-black deposited, appearing black, while b) has still an unmodified Pd surface which appears silvery. 

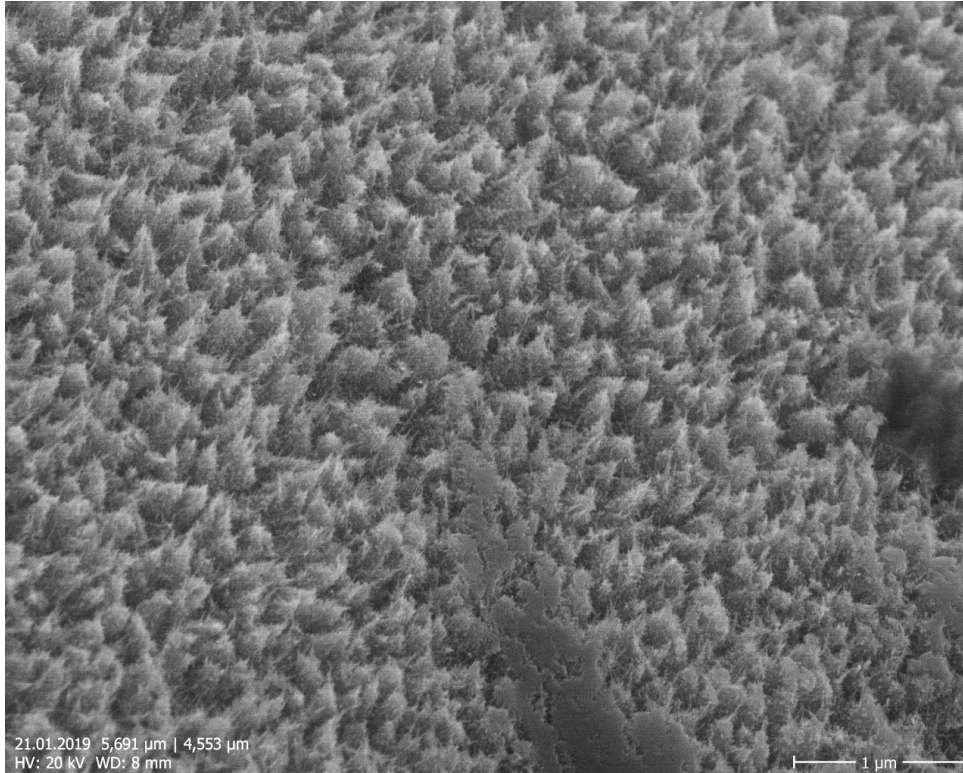


Figure 3.8: SEM image of the deposited Pd-black on a palladium wire (20 kV, size of depicted area:  $5,691 \mu\text{m} \times 4,553 \mu\text{m}$ ). It forms a dense forest-like structure, with very high surface area. This structure captures light, so that it appears dark. The structure is very delicate: In the lower middle of the image is a damaged part, where the needles were flattened because this part was slightly touched with pliers.



### 3.4.3 commercial ISFETs

ISFETs from Optoi Microelectronics (see Fig. 3.9) were used for some tests with ISFET-readout circuits. They use a  $\text{Si}_3\text{N}_4$ -membrane with 55 mV/pH sensitivity according to their datasheet [102]. An external reference electrode is required. ISFETs from Optoi Microelectronics are no longer available.

### 3.4.4 ISFET-Simulator

To simulate ISFETs to test readout-circuits standard discrete MOSFETs were used. The lead for the reference electrode was connected to the gate of the MOSFET. To imitate the  $V_{th}$  change of an ISFET a voltage source was placed in series to the gate (see Fig. 3.10). Voltage steps were created and could then be observed with the same magnitude in the output of the readout circuit provided it worked correctly. Using MOSFETs for testing of the circuitry is easier, as they usually work reliable and produce always the same result, unlike quite fragile electrochemical sensors. Also no complex and error prone fluidics is needed. For quick and repeatable tests this method is superior.

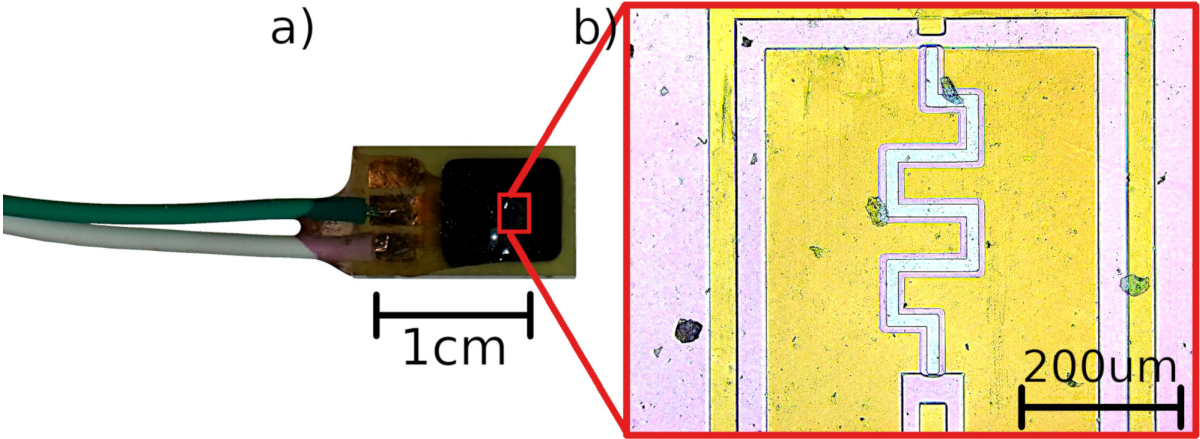



Figure 3.9: a) Optoi ISFET. The white and the green wire are drain and source+bulk respectively. The black patch is epoxy, which has an opening for the actual ISFET surface, here marked by the red box. b) shows a magnification of the ISFET die. The golden appearing structures are metal, left and right are source and drain and in the middle is the channel, forming a meander. Surrounding that structure is another wire for bulk connection, which is connected to source. 

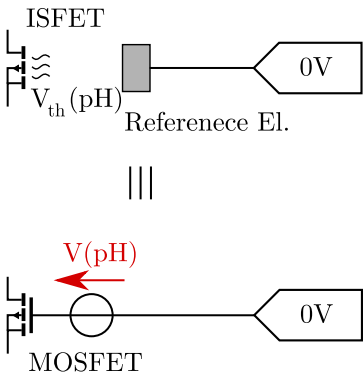



Figure 3.10: ISFET simulation: The behaviour of ISFETs, to change their  $V_{th}$  depending on pH (upper schematic) was simulated with an equivalent circuit of a MOSFET and a variable voltage source in series to the gate (lower schematic). 

## 3.5 Test Setups

Different test setups were built to characterize sensors and systems.

### 3.5.1 Automated Fluidic Package Test

To test packaged sensors a system was built to apply different fluids automatically and record the results. The system consists of multiple bottles with pH-buffer, DI-water and other sample fluids, a pump, a valve to select one of the bottles, a test fixture for the sensors, readout- and control-electronics and a waste bottle. There were different generations of this setup, which was constantly improved.

#### 3.5.1.1 Generation 1

The first system used four bottles with pH-buffers (4,7,9) and one with DI-water connected to a rotary valve with six input ports. Tygon tubing was used for all fluidics. The output of the valve was connected to a fluidic socket, which was placed in a fixture that was glued on top of the sensor. The sensor-chip was soldered to a PCB which broke out all pins to 2,54 mm headers. A discrete ISFET-electronic was used to constantly monitor one of the four ISFETs. The voltage was recorded with a potentiostat in open-circuit-voltage mode. To measure another ISFET a jumper wire needed to be switched. The outlet of the fluidic socket was then fed to a flow-through Ag/AgCl-reference electrode. Then a peristaltic pump followed, which pumped the liquid through the whole system into a waste bottle. The pump and valve were controlled with a microcontroller, which ran different buffer sequences. The whole setup was placed in an incubator for temperature control. This system was prone to errors through air-bubbles that got caught in the tubes and on top of the sensor, breaking the circuit. Also changing the sensor was tedious, as it needed to be soldered to the PCB and the fluidic adapter needed to be glued on top. Only one ISFET (or MOSFET) could be measured at a time. The flow of the pump was rather slow and the used tubes for it were subject to wear-out. The valve was old and clogged from time to time due to wear of the valve-element. These issues were improved with a new setup.

#### 3.5.1.2 Generation 2

This system is derived from Generation 1 and uses PTFE tubing with standard IDEX-fittings. The pump was omitted and the bottles with the fluids are pressurized with nitrogen to push them out of the bottles similar to spray cans. The rotary valve was replaced with a new modern one with USB-control. The two ports not connected to a bottle were sealed. By setting the valve to one of those the flow can be stopped. To read the sensor the DemoBoard (see Section 4.2) is used. This system is used to characterize ISFETs with different pH-buffers and O<sub>2</sub>FETs with PBS with different oxygen levels. A schematic of this setup is depicted in Fig. 3.11 and a photograph in Fig 3.12.

In this system was also a new socket for the ISFET chips used. It was built by TI and is based on a normal ZIF-socket<sup>1</sup> for the used CLCC28 packages. The lid was modified

---

<sup>1</sup>) zero-insertion-force



and a fluidic adapter was inserted with two IDEX-ports for fluidics. The two ports are connected to two small channels, which end in a one millimetre plate surrounded by an o-ring. This is pressed by the lid onto the opening of the sensor chip and allows a flow over the sensitive area without leakage (see Fig. 3.13). Changing a sensor is now a matter of seconds.

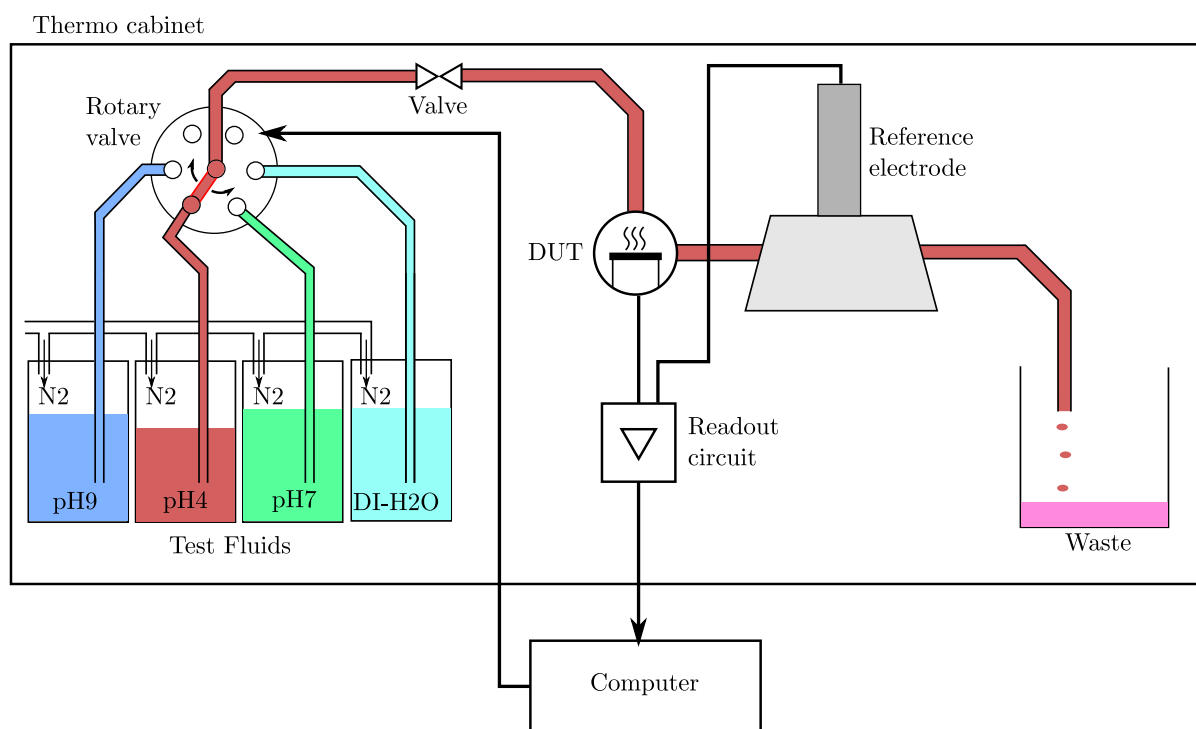


Figure 3.11: Schematic of the automatic fluidic test stand (Gen 2). Four bottles with different test liquids are pressurized with nitrogen. A rotary valve is used to chose one of these sources or one of the closed inputs for flow stop. A manual valve can also be used to interrupt the flow for maintenance. The liquid is fed through the DUT, which is an ISFET-chip in a special fluidic adapter socket. The fluid then passes an Ag/AgCl-reference electrode, before it is dumped in a waste container. A readout circuit, e.g. the DemoBoard or the integrated ISFET controller is used to control the ISFET and send results to a computer. This computer also controls the rotary valve and thus generates a fluidic test pattern.



### 3.5.2 Waferprober

A waferprober was modified to test ISFETs with liquids on wafer. This development was mainly done by TI and is mentioned here for completeness. The package tester and the wafer tester were developed and improved alternating. The advantage of the wafer prober is a drastic cost reduction for testing. Testing can be done before the ISFETs are packaged. Packaging is a quite expensive production step, especially for the ISFET with its non-standard housing which requires an opening. By testing the ISFETs still on the wafer defective units can be discarded before packaging. This will help reducing the cost of the sensor chips, which is essential to make the multi-well-plate affordable as it needs 24 sensor chips. The waferprober was very long time in development as it is very difficult to confine the liquid to the sensitive area while not spilling it to the surrounding contact pads. Another requirement is the change of the buffer during test to measure the sensitivity. For this purpose a sophisticated fluidics system needed to be developed. Earlier approaches in

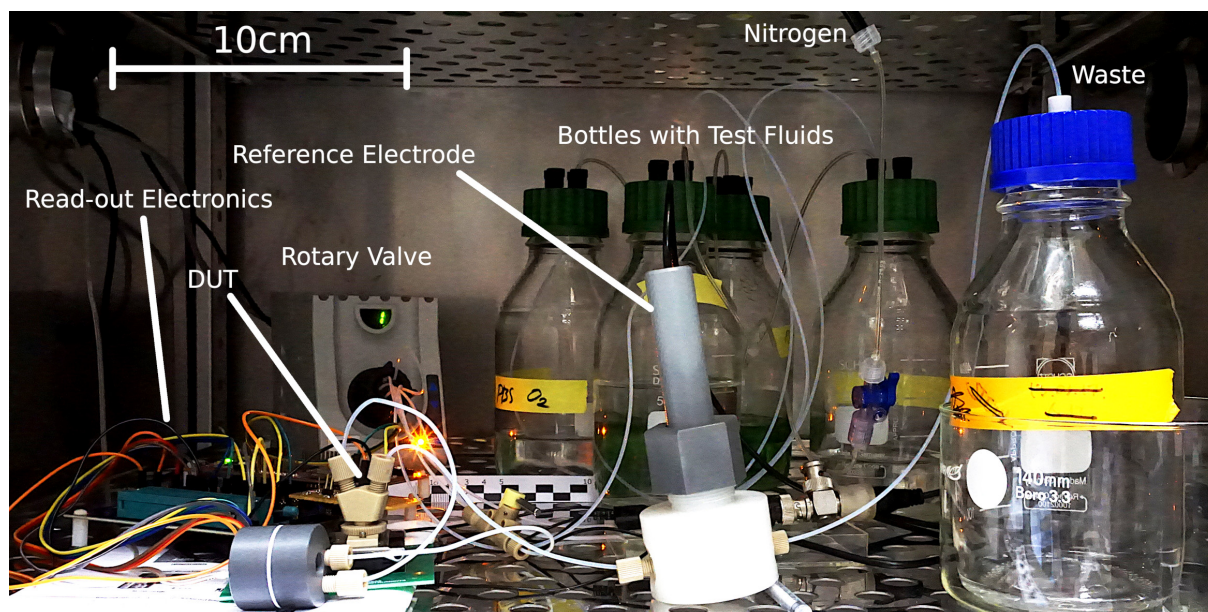



Figure 3.12: Image of the automatic fluidic test stand (Gen 2). Four pressurized glass bottles are in the background. Each is connected to a nitrogen supply and with a thinner tube to the rotary valve (white box on the left). In the foreground is from left to right the readout electronics, the fluidic device socket, a flow-trough reference electrode and the waste bottle. For a more comprehensible schematic of the setup see Fig. 3.11. 

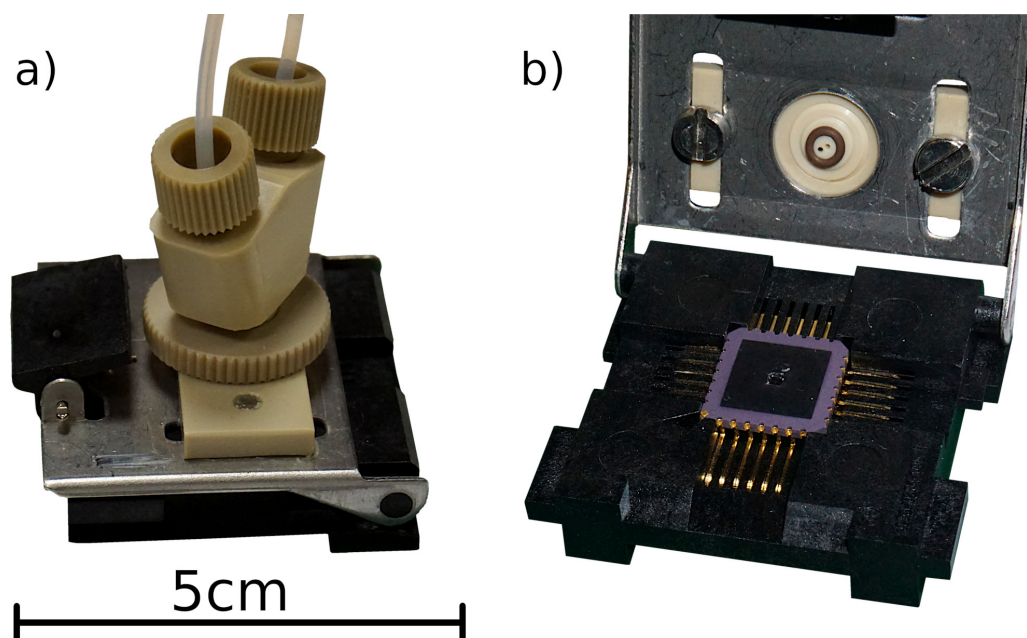



Figure 3.13: Picture of the fluidic chip socket. a) shows the closed socket. The socket has a custom PEEK-fluidic part mounted on top with two IDEX-connectors for tubes. b) shows the opened socket with a ceramic chip package inserted. The opened sensor area is clearly visible in the centre of the dark mould. In the metal lid there is a hole with the aforementioned PEEK-part. It has two very small holes in the middle that connect to the IDEX-ports. This opening is placed directly over the sensitive area when the lid is closed. A brown o-ring around those two holes is used to prevent leakage of fluids. 

literature use a lithographically structured PDMS-cell with two connectors for tubing for in and out flow. Unfortunately, such an assembly was too large for the new chips. There were experiments with a pneumatic dispenser, which could not control the amount of liquid precise enough. Also, the droplet evaporated very quickly or would spread too much and short the contacts. A wetted q-tip was also too large to fit between the probe needles. Catheters for medical applications were tested, as there are models with multiple internal channels, so called multi-lumen catheter. One lumen is used for the supply of buffer while the other is used to remove it. Catheters for toddlers are available in diameters below one millimeter and with two lumen. However, the handling was not easy and it was not possible to create a spill free flow over the wafer surface. With some improvements, it is now finally possible to test chips with fluids on wafer.

### 3.5.3 Thermo cabinets

Two different types of thermo cabinets were used for different experiments. One is an incubator, which can only heat. The Heraeus Function Line incubator can reach temperatures up to 70 °C. This system was used for most experiments that should be conducted at a constant temperature. It takes quite a while to reach the set temperature and to settle. Therefore it is suitable for static temperature experiments. It can also serve as a basic Faraday cage.

For experiments with temperature changes or temperatures lower than room temperature or very high temperatures a climate chamber from CTS was used. This specific model has a temperature range from  $-40\text{ °C}$  to  $180\text{ °C}$  with active cooling and can also control humidity. The built in fan ensures a fast homogeneous temperature distribution.

## 3.6 Sensor Chips

Sensor chips were designed and manufactured by Texas Instruments Deutschland (Freising). The process flow was specifically developed for this sensor type and features ISFETs and platinum metallization layer. Later generations are based on a standard flow and include basic parts of the readout electronics and multiplexers.

### 3.6.1 Layouts

#### 3.6.1.1 Generation 1 - DOE

This layout was intended to test different sizes and configurations of ISFETs as part of a Design of Experiments (DOE) and was designed by Sebastian Meier [151]. A single chip consists of four FETs pairs and is 2 mm x 2 mm. A pair is identical in geometry but one is an ISFET, the other a normal MOSFET. There are also variants with two ISFETs, O2FET-MOSFET or ISFET - O2FET. In total, there are 44 different sizes of FETs. For all sizes there are n- and p-channel variants. All FETs have a common source and bulk connection. The Gates for the MOSFETs are connected together as well as the cathodes for the O2FETs. The drains are separate. Drain and source also have kelvin

voltage sensing lines. That is also useful to check continuity. The MOSFETs are used to evaluate the CMOS process and probe for manufacturing problems. Microscope images of such a chip, already packaged, are displayed in Fig. 3.14 and 3.15.

The reticle for this layout also contains different sized interdigitated electrode structures (IDES) with and without nitride passivation. An image of such a chip is shown in Fig. 3.16.

The chips were electrically tested on wafer with an automated prober. Some of them with good results were also packaged (see Section 3.6.2).

### 3.6.1.2 Gen2 - improved process

The second generation is based on a standard CMOS process-flow. For the sensors two metal layers are used and an additional mask for PO-opening. Platinum is used for the top metal layer instead of aluminium. It is much less susceptible to corrosion than aluminium and therefore usable for fluid exposed electrodes. The ISFETs are built as extended gate ISFET with a  $\text{Si}_3\text{N}_4$  sensing layer. This is required due to the CMOS process during which it is not possible to create an opening down to the gate oxide without losing the advantages of the standardized process. Metal one is used to implement a resistive heater underneath the extended gate electrode to use the temperature rise for pH-referencing.

This physical effect and its usability to measure absolute pH can be described by the following equations. From [70] we get:

$$\Delta\Psi = -\ln(10)\frac{RT}{F}\alpha \cdot \Delta\text{pH} \quad (3.1)$$

for the change in the surface potential  $\Delta\Psi$  of the ISFET, which directly affects  $V_{th}$ . Derived after the temperature  $T$ , this yields:

$$\partial\Delta\Psi = -\ln(10)\frac{R}{F}\alpha \cdot \Delta\text{pH}\partial T \quad (3.2)$$

So a change  $\partial T$  in temperature causes a change in pH sensitivity of  $-\ln(10)\frac{R}{F}\alpha = -0,198\text{ mV} \cdot \alpha$ , where  $\alpha$  is close to 1, depending on chemical buffer capacity of the used gate insulator [70].  $\alpha$  has also some temperature dependence, which will cause a non-linear behaviour that should be considered for precise measurements. By applying a defined pulse to the heater the sensitive area on top will change temperature, too. The now slightly different sensitivity will change the voltage over the electrolyte-insulator stack, which can be detected by the ISFET. This difference is dependent on the temperature difference and the absolute pH. If the heat pulse is always the same the pH is the determining factor for the voltage step. Heating can be done in a few microseconds due to the close proximity of the heater to the surface, therefore pH measurement still works without a long-term stable reference electrode. A simple Pt electrode can be used, which is stable for at least a few seconds. The heat dissipation is also very fast, so that the system cools down in some hundred microseconds. This allows to apply repeated heater pulses and use a lock-in-amplifier to amplify the relatively small voltage variation. The chip also includes a programmable amplifier to boost the signal. Above some heater structures the sensing plate was replaced by a Pt wire to measure the temperature change via the resistance change.

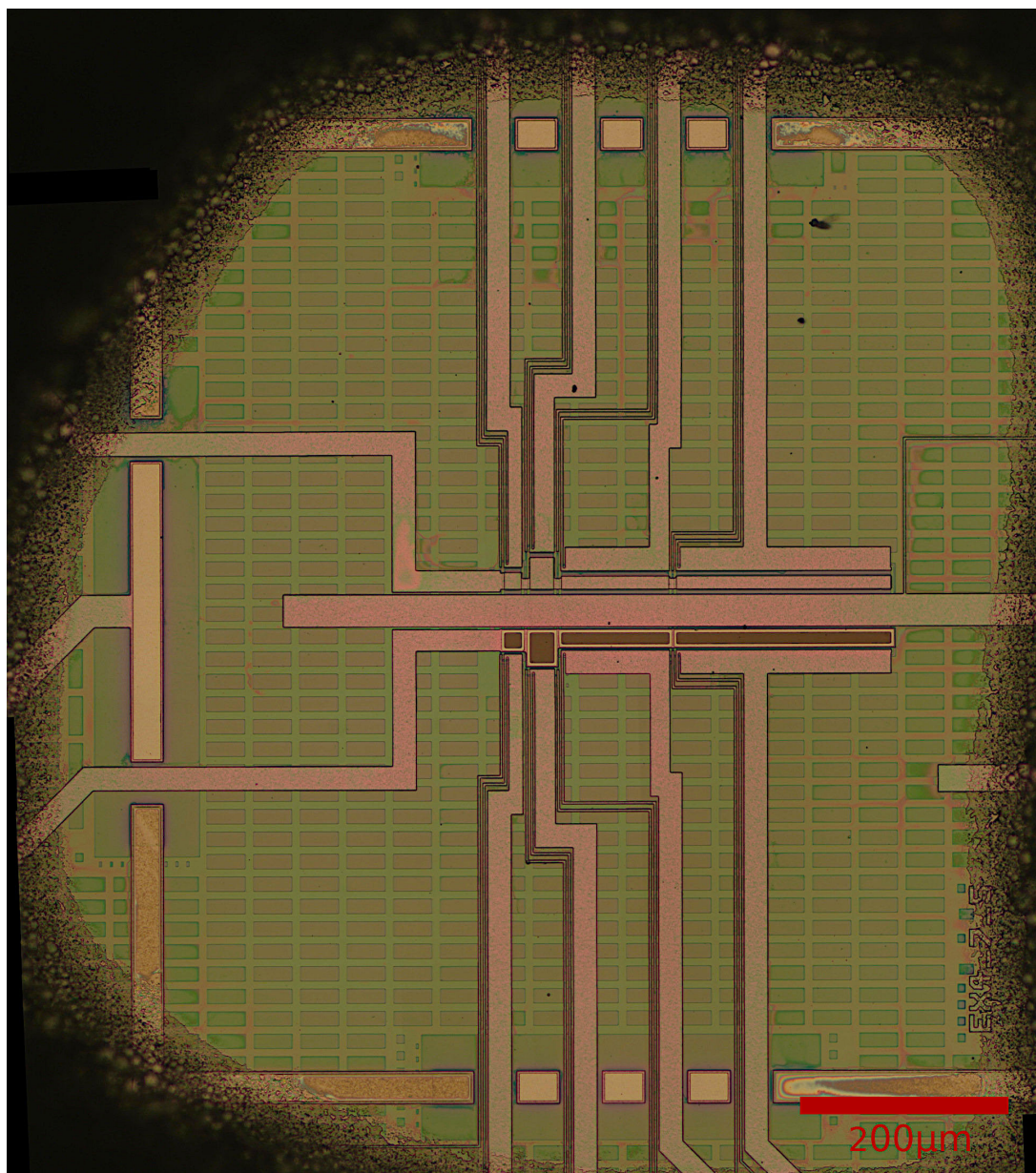



Figure 3.14: Stitched optical microscope image of a die of the first ISFET-layout generation. The chip is covered with a dark epoxy mould visible on the edges with the sensitive area left open. The biggest element in this area is a bare Pt-electrode that goes around the opening. In this example its edges are covered by some epoxy due to manufacturing tolerances. Several covered Pt-wires, which therefore appear light purple, go through feedthroughs into the centre. They connect four ISFETs on the lower and four MOSFETs on the upper half. The dimensions of the ISFETs and the MOSFETs are identical. Drain connections come from the top and bottom, gate connection is on the left and the source of all transistors are connected in the middle and lead to the right of the image. Each drain and the source are also connected via a thin Kelvin-wire. Wires of similar thickness are also used to connect the back-gate. The opened gates of the ISFETs appear brown. The gate openings are surrounded by a silvery shiny ring. This is an additional Pt-electrode, making this device not only an ISFET but an O<sub>2</sub>FET. The regular pattern of light pink rectangles is a dummy structure. A magnified image of the centre region is displayed in Fig. 3.15. 

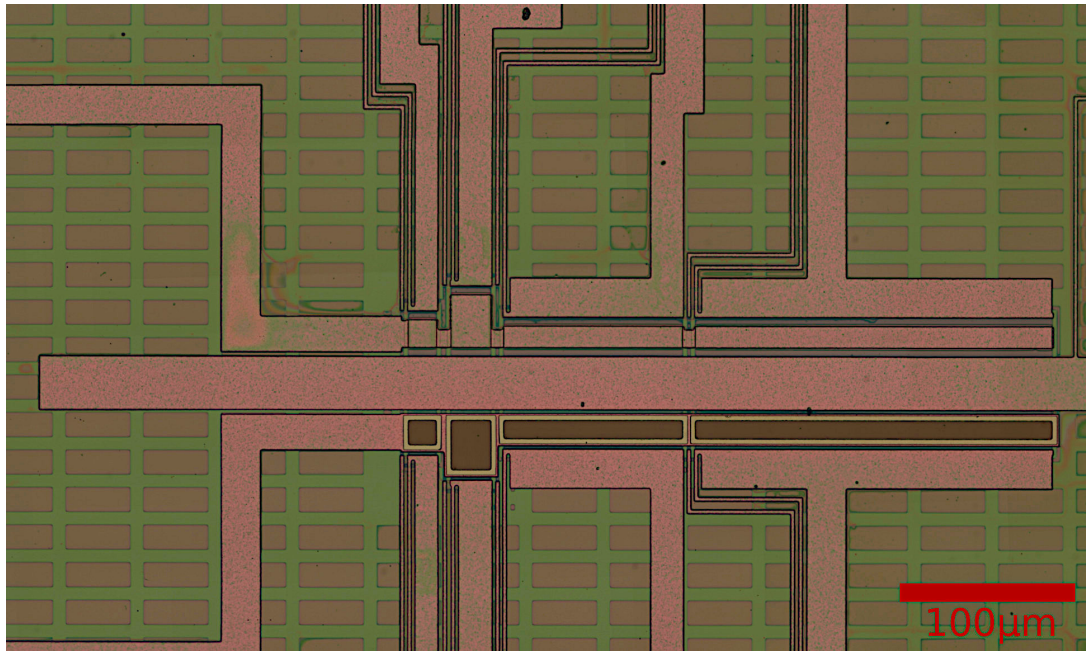



Figure 3.15: Optical microscope image of a die of the first ISFET-layout generation, magnification of Fig. 3.14. Several covered Pt-wires, which therefore appear light purple, lead into the centre of the die. They connect four ISFETs on the lower and four MOSFETs on the upper half. The dimensions of the ISFETs and the MOSFETs are identical. Drain connections come from the top and bottom, gate connection is on the left and the source connections of all transistors are combined in the middle and lead to the right of the image. Each drain and the source are also connected via a thin Kelvin-wire. Wires of similar thickness are also used to connect the back-gate. The opened gates of the ISFETs appear brown. The gate openings are surrounded by a silvery shiny ring. This is an additional Pt-electrode, making this device not only an ISFET but an O2FET. The regular pattern of light pink rectangles is a dummy structure. 

However, it should be noted that this concept of thermal reference is not yet thoroughly tested and validated. The idea seems simple but there might still be some pitfalls that need to be examined.

To avoid the problem with trapped charges on the floating node two variants of the chip are designed. One flavour has a transfer-gate to set the floating node to a defined level. The other uses tunnel-structure, similar to floating-gate memory devices to program the floating node to the desired level.

Another variant of the gen2-chip has two IDES structures and two O2FETs but no heater. It is intended for bio-sensing applications like the electronic multi-well-plate.

### 3.6.2 Packaging

A ceramic lead-less 28-pin chip carrier (CLCC28) with a side length of 11,4 mm and height of 1,8 mm was used as prototype package. The chip was glued into the carrier and bonded to the contact pads. In a special process called *dam-and-fill* the bondwires and contact pads were covered with epoxy while leaving the sensitive area in the middle of the chip open. This was done by an external company. First a dam of high-viscous epoxy is applied around the sensitive area. Then the rest is filled with a low-viscous epoxy, while the dam prevents it flowing onto the sensing area. The epoxy is then thermally cured. The ceramic

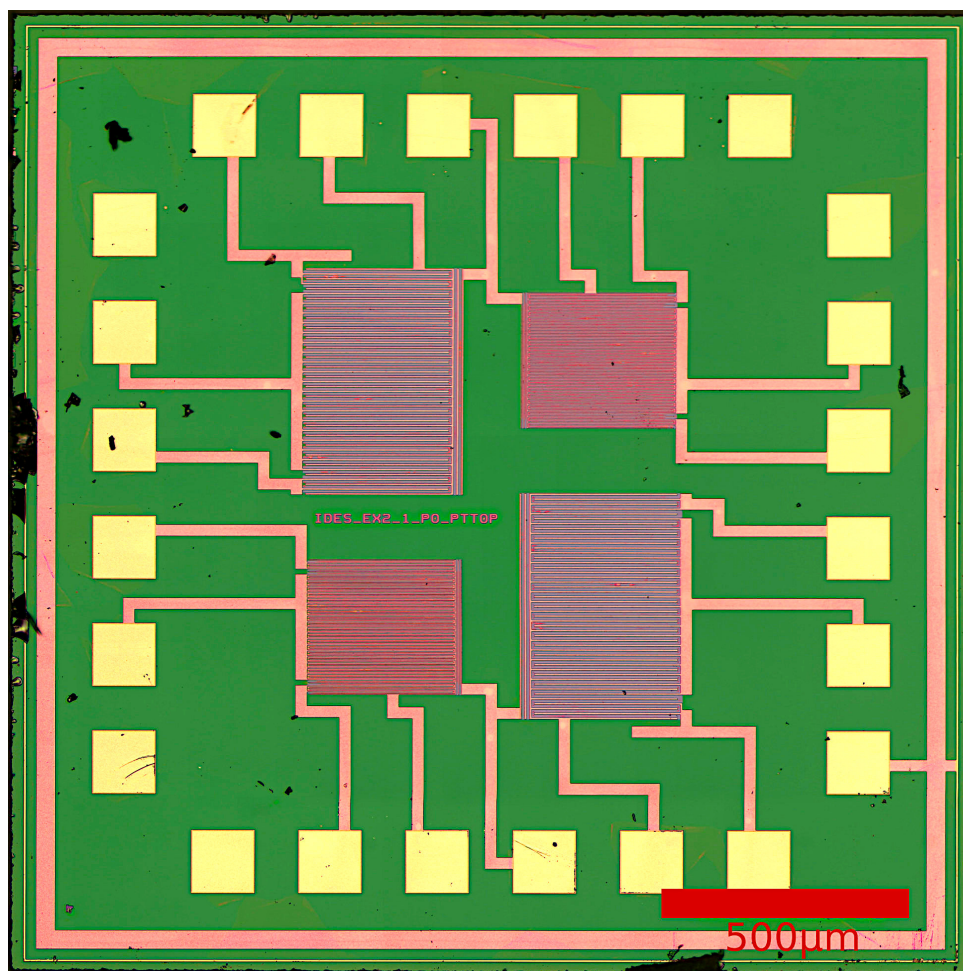



Figure 3.16: Stitched optical microscope image of a generation 1 bare die with IDES. In the middle are four IDES with two different sizes. Bondpads for connection are all around the 2x2 mm die. 

packages are depicted in Fig. 3.17. For easier handling of the prototypes an adapter board was built, which converts the package to a DIP-28. This adapter can be see in Fig. 4.1.

These packages are quite expensive and have turnaround times of more than a month. Therefore different packaging concepts were developed by TI and Niklas Fauth [152]. It is a flip chip approach: The silicon die is directly soldered to a PCB. The PCB has a hole underneath the active area that allows access to it. Then either an o-ring is placed on the area and compressed to achieve a water tight seal or an epoxy underfill is used to keep water away from the contacts.

### 3.6.3 Temperature Sensor

Different approaches were used to measure temperature with the sensor chips:

**MOSFETs** can be used to measure temperature by evaluating their shift in  $V_{th}$  and  $\mu$  which both have a negative temperature coefficient [153]. They are easily integrated in the process and well understood and characterized. The MOSFETs used for temperature

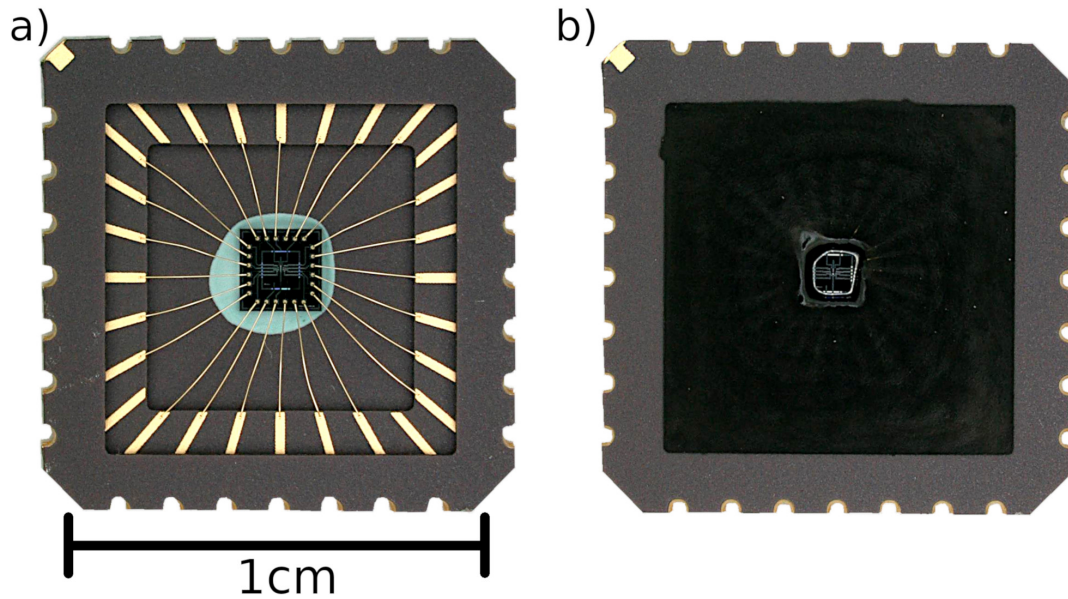


Figure 3.17: Packaged prototype ISFETs: a) is a mounted and bonded ISFET-die of the first generation without epoxy mold in a 28 pin ceramic chip carrier. b) is a fully packaged unit. It has an opening in the epoxy for the sensitive area. Photographs: Sebastian Meier, TI. Reproduced and modified (background removed) with permission.

measurement have the same dimensions as the ISFETs, so they can be used to compensate temperature effects of the ISFETs.

**A Thermistor** was built using the Pt metallization similar to a Pt1000 device. This is a widely used industry standard for temperature measurement. The built devices though did not adhere to the standard as they had a different nominal value and temperature coefficient. But those can be characterized and calibrated. Measurement can be done with a four-wire method for maximum precision or with a simpler two-wire method if not such high accuracy is required. This was used for the gen2-chip. On some parts a thermistor was placed directly over the heater to test the heat transfer and measure its characteristics. Then the same structure can be used to measure the temperature of the fluid, too.

### 3.6.4 TUM Sensor-Chip

TUM sensor-chips were used to test the impedance spectroscopy. The ISFETs on them were unusable, due to an error occurring during bonding that led the substrate contact unconnected. The die and the packaged chip are depicted in Fig. 3.18. The chip contains an IDES with 50  $\mu\text{m}$  spacing, a Clark electrode for oxygen measurement, four ISFETs and two O<sub>2</sub>FETs. There is also one reference MOSFET transistor and a diode for temperature measurement. The chips were manufactured at the LTE clean-room, now ZEITlab at TUM and use  $\text{Si}_3\text{N}_4$  as sensitive layer and platinum as metallization. They measure 7,5 mm  $\times$  7,5 mm and were encapsulated in ceramic packages similar to the gen1 TI-chips but bigger.



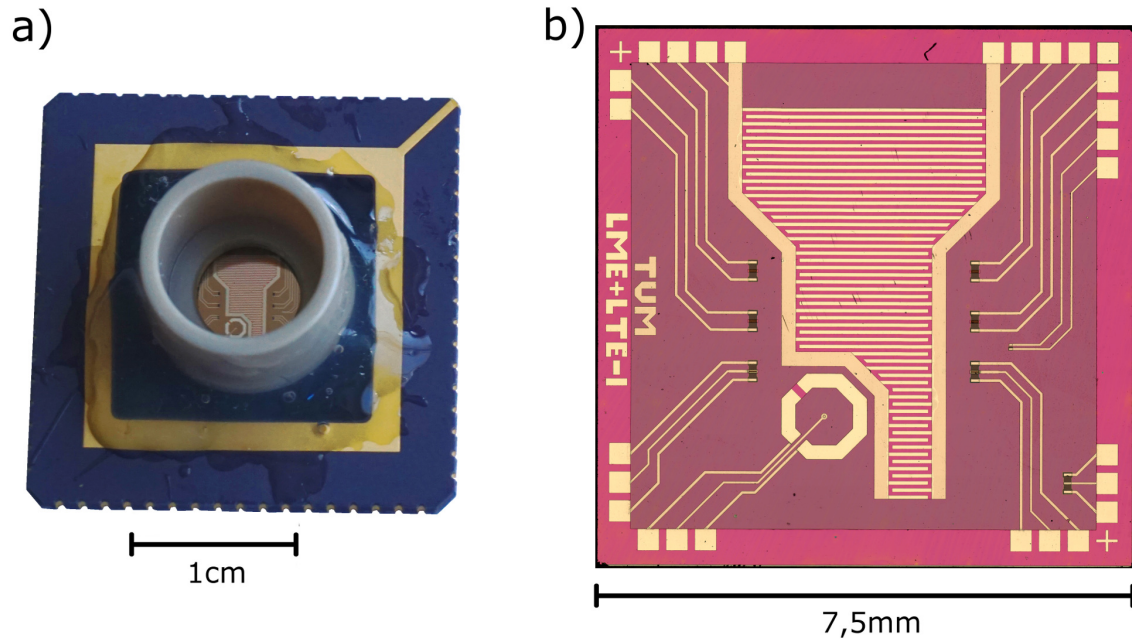



Figure 3.18: TUM ISFET chip. a) shows the encapsulated chip in a ceramic package with a well insert. b) is a die shot of the silicon chip. It contains a large IDES and a Clark sensor, which is the circular structure on the bottom left. Left and right of the IDES, there are each three O<sub>2</sub>/ISFETs, visible as small dark rectangular shapes with either two or three wires. In the right bottom edge there is a normal MOSFET for reference purposes. 

## 3.7 Conventions

### 3.7.1 ISFET voltages and currents: $V_{sg}$ , $V_{sd}$ and $I_{sd}$

In this thesis the voltage between the source of the ISFET and a (reference) electrode plays an important role. It is composed of the threshold voltage of the actual FET  $V_{th}$  and a pH dependent voltage created at the interface between liquid and sensitive layer. In traditional FET applications the term  $V_{gs}$  is used for this voltage, an abbreviation for gate-source-voltage. In this thesis however the gate is the (reference) electrode and often the reverse voltage  $V_{sg}$  is used in calculations and plots. The reason for using the reverse is that the first used source-drain-follower to read the ISFETs (see Section 4.1) sets the gate or (reference) electrode potential to zero or system ground. The source voltage is used as output. This can be easily measured by a voltmeter referenced to ground which then displays  $V_{sg}$ . As it happened the first working FETs were p-channel so this voltage was also positive. All subsequent developed circuits follow this convention and print  $V_{sg}$  as the result for the ISFET. For n-channel this value is therefore negative.

The first tested devices were p-channel devices so their  $I_{ds}$  and  $V_{ds}$  were negative. For them to also obtain positive values they were called  $I_{sd}$  and  $V_{sd}$  and recorded as such. This convention was kept for the later n-channel devices, too, in this case resulting in negative values.



## 4 Electronics

To read and characterize the sensors and create the electronic multi-well plate different electronics have been employed, developed and manufactured. These are described in this chapter. Table 4.1 gives an overview of the different sensors and the used measurement circuits or devices.

Table 4.1: Sensors and the used measurement devices

Sensor → Device ↓		ISFET		O2FET	IDES	RTD
		Gen1	Gen2			
B1500, p.39		x				
SMU/DMM, p.39		with SD-follower			x	x
Ivium, p.37		with SD-follower			x	
DemoBoard, p.56		x	x	x	(x)	x
Standalone Impedance, p.61					x	
MSP430, p.62	1x, p.71	x	(x)	x	x	x
	6x4, p.87	x	x	x	x	x

Commercial lab measurement equipment like the B1500, SMUs and the Ivium potentiostat were used to characterize the sensors and as benchmark for the self developed circuits. Some of the self developed electronics such as the DemoBoard were then used to perform more tests on the sensors. The DemoBoard can capture more different values in parallel and provides a more comprehensive data-format than the lab meters. A standalone impedance analyzer based on an older design was built to perform some early measurements with IDEs sensors. A new readout circuit for ISFETs and IDEs based on an MSP430 microcontroller was then developed to fit into the size constraints of the multi-well-plate. Finally, the sensor equipped multi-well-plate was designed to combine  $6 \times 4 = 24$  sensors with the required read-out on a PCB the size of a post-card.

### 4.1 Source-Drain-Follower

This SD-follower was based on the schematics by Optoi (see Fig. 2.11) without further additions. It was used to perform the first tests on ISFETs to check their functionality and to test the SD-follower principle as a starting point for a self developed circuit. A different Opamp and bandgap reference model was used and some resistors were replaced by potentiometers to make  $V_{ds}$  and  $I_{ds}$  adjustable. The output is an analog voltage. A digital multimeter was used to monitor it and later the Ivium in open-circuit-potential mode for recording. It was used for first tests with the new ISFETs with  $|I_{ds}| = 55 \mu\text{A}$  and  $|V_{ds}| = 800 \text{ mV}$ . To change the channel type the diode and the bias voltage needs to be reversed. The circuit works well and was therefore used for the DemoBoard, too.

## 4.2 DemoBoard

### 4.2.1 Specifications

The DemoBoard or EvalBoard was developed for the characterization of the new sensors for the multi-well-plate while they are still in development and for demonstration. It can read up to eight ISFETs because the first chips of gen1 have eight FETs. It is equipped with high-end ADCs and DACs to be able to characterize the sensors with a decent precision and accuracy. A domain specific programming language to control measurement sequences and data processing allows the flexible use and adaption of the board to new sensors and research questions. It is connected via USB to a computer and controlled with a Python-GUI and can log several measurement values in parallel.

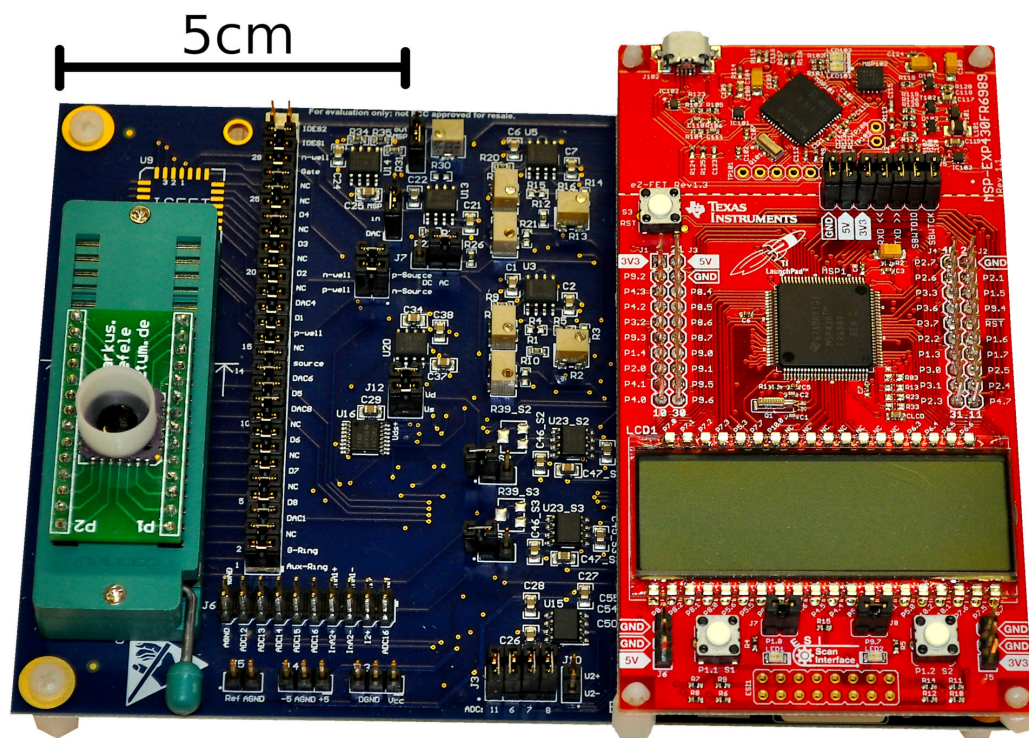



Figure 4.1: DemoBoard for electro-chemical sensors. It consists of a standard microcontroller evaluation board from TI (red PCB) and a custom analog front-end (blue PCB). Sensors can be connected on the left side, either on a DIL-adaptor (green PCB) or with jumper wires to the large pin header. 

### 4.2.2 Circuit Design

The DemoBoard is designed as extension for standard TI-microcontroller eval boards and equipped with a specific connector. This connector carries SPI and I2C interfaces, power and GPIO. A common MSP430FR6989 eval board is mounted as processing unit. It has a display and an USB-connector. A block diagram of all available components and connections is depicted in Fig. 4.2. The full schematic of the DemoBoard is attached in Appendix D.1.

The board generates 5 V and  $-5$  V from the supplied 3,3 V for its analog circuitry. The 3,3 V rail is used as digital supply. Care was taken to filter noise generated by the boost

converter in the analog supply. A star grounding scheme is used to minimize ground reference errors.

A discrete ISFET circuit based on the suggestion from Optoi [102] is used (see Fig. 2.11). It is extended with circuits to measure the drain-current and drain-source-voltage. The operating point defining resistors are replaced by potentiometers. Two instances are implemented: One for n- and one for p-channel devices. The schematic for the n-channel version is depicted in Fig. 4.3. A multiplexer is used to switch between these two. This multiplexer also allows to switch drain and source. The substrate connections are separate and also switchable by multiplexers. A second multiplexer is used to switch the drain-connection and connect up to eight FETs.

A 18-bit 8-channel ADC is used to digitize the measured voltages. A 8:1 multiplexer is used to extend the available channels. For different usages unity-gain and 10x instrumentation amps are available. They can be used in conjunction with two 200  $\mu$ A current sources to read Pt100 sensors or to monitor other interesting voltages.

Eight 12-Bit DACs can be used for biasing purposes. They can provide voltages between zero and 4 V with a current of 1 mA. One 4096 mV reference source (REF6041) is used for both the ADC and the DAC.

All relevant signals are routed to standard pin-headers. The connectors for the sensors are also pin-headers. This way new sensor layouts can be easily adapted with jumper-wires.

### 4.2.3 O2FET readout

To read O2FETs for oxygen measurements, the board was programmed to output different voltage patterns with its DACs to the chip's electrodes while monitoring the FETs. As the DACs cannot generate a negative voltage as needed for the reduction of oxygen the cathode is set to zero volt while the anode is set to a positive voltage. Care has to be taken about the reference electrode: If it is present it should be floating at least during reduction. Different voltage levels were tested. The reduction voltage was applied for about 10 s. Also the effect of the periodic application of a reversed voltage in between reduction cycles was tested.

### 4.2.4 Software

The firmware controls the low-level functions like ADC readout and initialization and was developed in large parts by Andreas Lösel during an internship at TI. An assembler-like domain specific language is implemented to configure the board and program measurement routines. This language also allows loops, conditionals, simple calculations as well as the selection, which data is sent back to the PC. It can be used to read data from different inputs and can be used to generate complex excitation voltages for electrochemical measurements. With GPIOs external devices can be controlled and synchronised with the measurements.

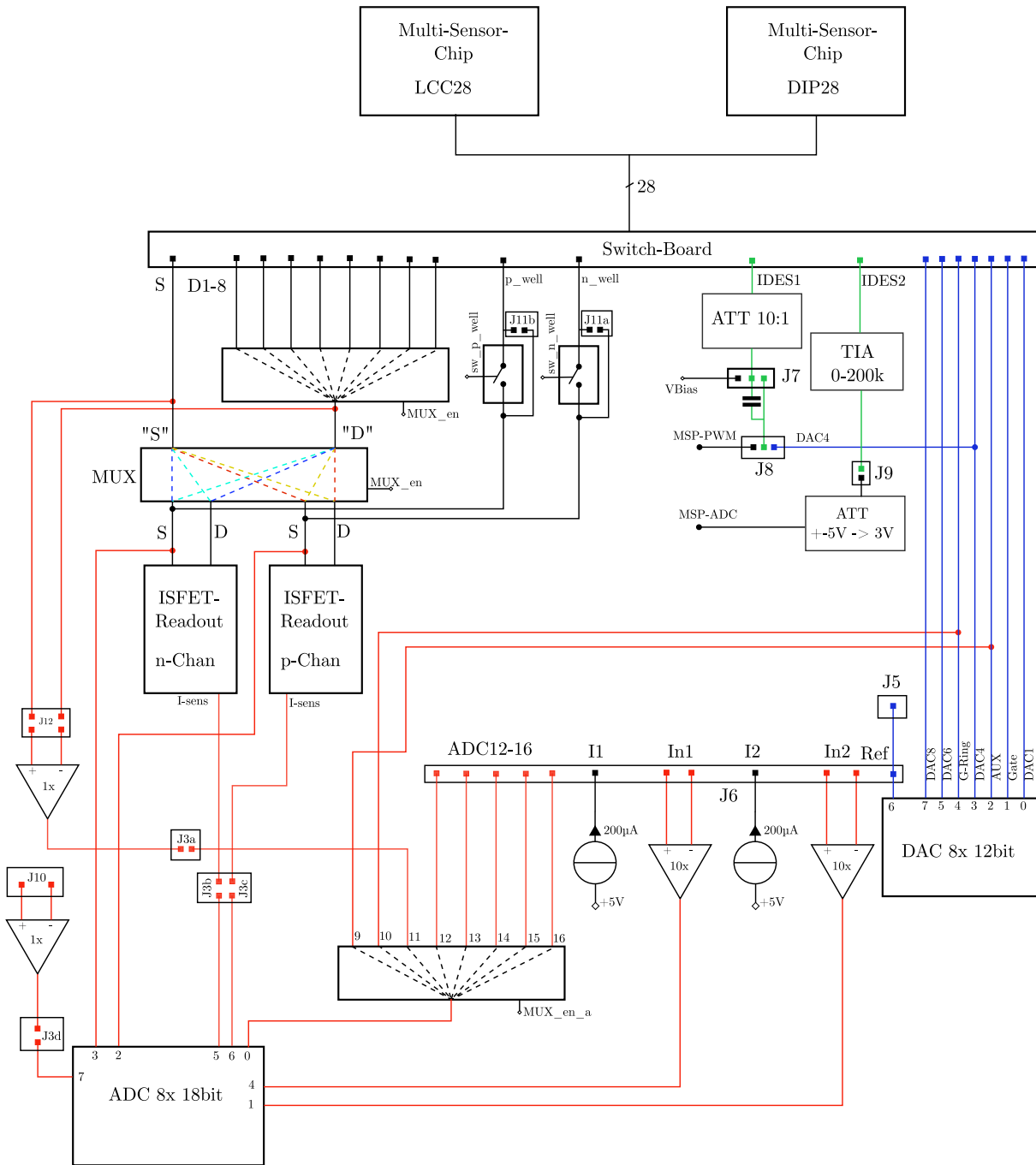



Figure 4.2: Block diagram of the ISFET eval board. The Sensor is connected via a switch matrix to the electronics to provide compatibility with newer sensor designs. Eight ISFETs can be connected via a multiplexer to an ISFET control circuit. A second multiplexer can switch between two of these circuits for n- and p-channel devices (see Fig. 4.3 for the inner details of such a block). Some buffer and 10x amplifiers can be switched in the signal path or connected to additional electrodes with jumper wires. An ADC is used to digitize the signals. A DAC is available to generate bias voltages. Two current sources can be used to read resistive sensors. For impedance measurements an attenuator (ATT) and a transimpedance amplifier (TIA) is available. 

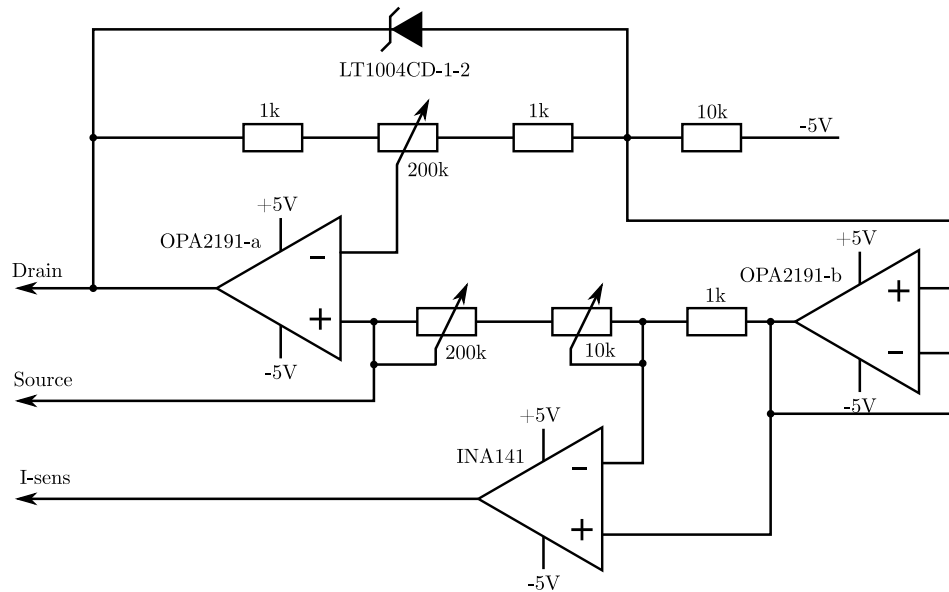



Figure 4.3: Circuit of the source-drain-follower of the DemoBoard for n-channel ISFETs. The Circuit is based on the Optoi-circuit (see. Fig. 2.11 p.24). Relevant resistors have been replaced by potentiometers to adjust  $I_{ds}$  and  $V_{ds}$ . Additionally, an instrumentation amplifier is used to monitor the current  $I_{ds}$  via an 1 k $\Omega$  resistor. Another instrumentation amplifier is used to monitor  $V_{ds}$ . This part is used for both p- and n-channel measurements and therefore not in this scope of the schematic. It is depicted in Fig. 4.2 The output of this circuit that corresponds to the  $V_{th}$  of the ISFET is the *source* signal. 

#### 4.2.4.1 Domain specific language

The structure of this language resembles assembler. Each command is placed in one code line and consists of a code word followed by two arguments separated by white spaces. Everything after the third white space in a line is a comment and ignored by the interpreter. The interpreter is integrated in the PC GUI software. Programs can be written there, uploaded and downloaded to and from the DemoBoard. The interpreter does basic syntax and argument checking and then converts the instructions to a bytecode which is then send to the DemoBoard and executed there by some form of virtual machine. The program starts from line 0 and continues sequentially. Conditionals are implemented by either jumping to the next line or skip this next line. There is an absolute jump instruction which will jump directly and unconditionally to the supplied line. For loops there is a repeat instruction that repeats a variable number of lines specified times. These repeat loops are not stackable!

Several registers are available. Their datatype (integer, long, float) is fixed. To save a float, a float register must be used otherwise an implicit cast is performed and undefined behaviour is possible. There are also pointer registers. Most instructions accept direct value, a register or a pointer as arguments but there are some exceptions.

An interactive help and function reference is available by executing the `manual.py` script. An example of a program to read ISFETs is shown in Listing 4.1.

#### 4.2.4.2 User GUI

A Python-GUI, also developed by Andreas Lösel, is used to program the board, plot the data and save logfiles. It is possible to hide and show different transmitted values of the board.

A set of status indicators, one for each ISFET, in the style of a traffic-light allow a quick overview of the operation of the FETs. A red indicator denotes a broken FET or dry ISFET. Green indicates a FET in the correct operating point and with plausible output. Yellow means: “not completely broken but not working properly either”. The decision is made by evaluating current and voltages of the FET and comparing them to user defined reference values. This feature allows the user to check the proper functioning of the chip at a glance.

All data from the board is permanently logged as CSV-files to disk to avoid the loss of valuable experiment data because of the user forgetting to save it. The files are rotated daily. The user can also manually specify a file to log data to. This file is not rotated.

```

0  sgate  0      0      Set Gate 0V
1  rall   4      1      Read VGS, IDS, VDS (avg. 16x, n-ch)
2  rt     F1     0      Read Temperature (save to F1)
3  movd   0      0      Move the collected data for UART transfer
4  json   1      0      Send the Data out (JSON for GUI)
5  lcd    0      0      Display Menu on LCD
6  dlms   640    0      Wait for 640 mseconds
7  jmp    1      0      Restart (jump to line 1)
8  end    0      0      end

```

Listing 4.1: Example Code for the Domain Specific Language of the DemoBoard. This programm reads all eighth FETs and sends the results back to the PC.

#### 4.2.5 Performance

To verify the performance of the developed board some tests and measurements were conducted. The same experiment was also done with the new integrated front-end (see Section 4.4) and then compared with the DemoBoard. The resulting graphs are therefore plotted in that Section 4.4.6 on page 72. Linearity was tested with a MOSFET (IRLML5203, p-channel) and a voltage source (Keithley 2401) in series to the gate. A stair function between  $-300\text{ mV}$  and  $500\text{ mV}$  was programmed. The actual voltage applied was also recorded. The output voltage of the ISFET-front-ends followed this disturbance (see Fig. 4.10 on page 73) with some minor deviations. There is a slight offset between the two circuits in the order of  $23\text{ mV}$  to  $31\text{ mV}$ . The DemoBoard experienced higher non-linearity than the design with the integrated front-end (see Fig. 4.11 on page 73).

The noise was tested with a similar setup. A MOSFET was measured in a temperature controlled environment while the output voltage was recorded. The standard deviation was around  $400\text{ }\mu\text{V}$ . To achieve this the ADC is sampled several times and the results are arithmetically averaged. The number of samples can be programmed to different powers of two, so the division is trivial for the controller. The  $400\text{ }\mu\text{V}$  are achieved with 16 times oversampling.



Another important metric of an ISFET circuit is the voltage range it supports. Usually,  $V_{gs}$  is the limiting parameter. It is dependent on the set operation point, the intrinsic  $V_{th}$ , the pH and the reference electrode. This voltage can easily add up to a couple of volts. The circuit needs to be able to deliver such large voltages which can be challenging for some low-voltage designs that operate on only 1,8 V. The maximum range of the demoboard for  $V_{gs}$  is around 4 V which is enough for most produced ISFETs thanks to its design with a symmetric  $\pm 5$  V supply. This might seem as a waste of resources but was necessary as the exact parameters of the newly manufactured ISFETs were not yet known. Therefore the design had a good amount of safety margin.

With these results the DemoBoard was a valuable test equipment for various tests on the new sensor chips. Especially the programming feature allowed an easy adaption on different measurement needs. It showed some glitches, though. It could be observed that  $V_{ds}$  changes with an applied gate bias. The cause could be identified as the used multiplexer to switch between the circuit for n- and p-channel devices. This multiplexer (MUX36D04) has according to its datasheet [154] a  $R_{on}$  of 200  $\Omega$  to 600  $\Omega$  depending on the voltage at the switch with respect to the chip ground. A shift in the absolute voltage of the ISFET drain and source therefore can cause a resistance change. Due to the current which flows through the ISFET and the MUX and which is kept constant by the circuitry this causes a voltage shift at the ISFET-terminals. The drain-source voltage is measured after the multiplexer at the FET-terminals. But the control-circuit acquires its feedback before the multiplexer and keeps this voltage constant. In practical measurements a voltage shift of around 40 mV was observed. This was probably the cause for the aforementioned deviation between the DemoBoard and the FR2355 circuit in the linearity test. The circuit with the FR2355 controller therefore uses better multiplexers with a maximum  $R_{on}$  of only 10  $\Omega$  and is therefore not susceptible to this error in such an extend.

The operating point of the ISFETs needs to be set by manual potentiometers. It cannot be adjusted by software. This is a disadvantage as experiments with the operating point with the DemoBoard cannot be automated. One could use electronic potentiometers instead of manual ones but they need to be capable of tolerating a symmetric power supply of  $\pm 5$  V. Many electronic potentiometers either do not allow negative voltages or up to 10 V supply or provide the required resolution or digital interface. If their ground is referenced to the negative rail then usually the control signal lines need to be level shifted. This additional circuit complexity was therefore avoided and manual potentiometers used. The integrated AFE with the MSP430FR2355 (see Section 4.4) has the ability to change the operating point in software and allows therefore some interesting experiments.

### 4.3 Stand-alone impedance analyser

For urgent experiments in a cooling facility with IDES-sensors to detect bacteria growth a small impedance analyser was constructed (see Fig. 4.4). Main reason for the new PCB were some size constraints: The whole circuit should be placed inside a water basin with a standard water pipe as enclosure. The existing impedance analyser, which also contained optical sensors, was too big for that. Therefore the impedance circuit was isolated and a new smaller PCB was designed. The microcontroller and parts of the analog front-end was replaced, which unfortunately caused some trouble. The analyser is based on the AD5933 IC [130] because the newer system based on the MSP430FR2355 was not ready

at that point of time. It comes with a RS-485 interface to allow data transmission over long distances. On board are two fixed resistors for calibration switchable by a multiplexer and the system can switch between three measurement ranges. Fig. 4.5 shows a simplified schematic, the full schematic is in Appendix D.2. The new microcontroller is too weak to perform the complex error correction routines for the AD5933 so this task was moved to a PC. The impedance analyser sends only raw data over the serial interface. The post-processing was implemented in python for easy portability and works with Windows and Linux. The data files are rotated daily to copy them from the PC without disturbing the data capture.

This system is capable of impedance spectroscopy from 1 to 100 kHz. Unfortunately, it is very expensive due to the used ICs, notably the AD5933 and the AD9834. Therefore the solution with the MSP430FR2355 was developed as described in the next chapter.

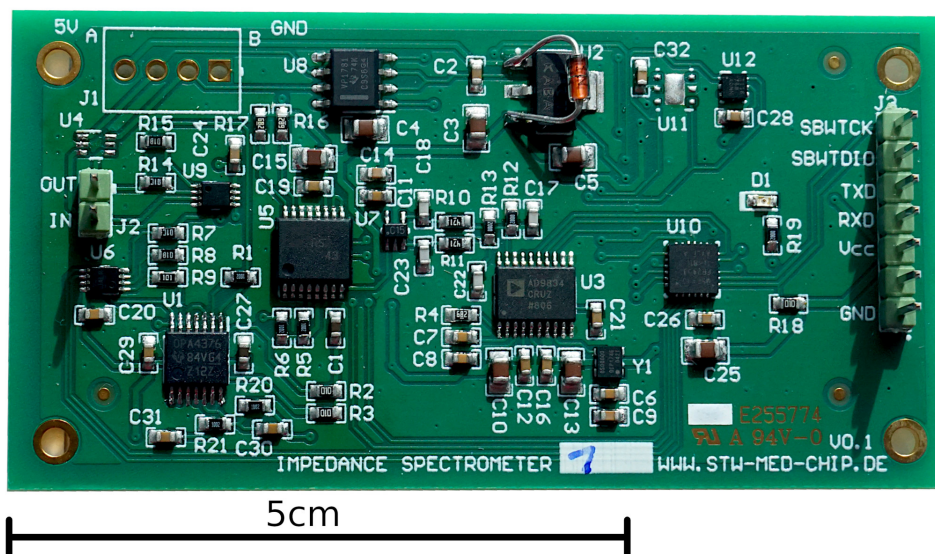



Figure 4.4: Stand-alone impedance spectrometer based on the AD5933 IC. On the left ist the connector for the impedance labelled with *IN* and *OUT*. Above it is the (unpopulated) connector for power and RS-485 Data. U5 is the AD5933. U3 is a DDS to generate a variable clock for the AD5933. U10 is a MSP430 microcontroller performing the measurements and sending the data back. The pin header on the right is for debug and programming. 

## 4.4 Integrated mixed-signal-frontend

### 4.4.1 Specifications

Main goal of this design is to use a single integrated chip to read ISFET and impedance sensors. This shall help to decrease the size of the whole circuit and allow to pack 24 of these front-ends on a multi-well-plate with sensors. Such an architecture of the plate has some advantages as discussed in Section 4.5.7. The package of the chip usually needs a lot of space compared to the naked silicon die, so the more packages are involved the more space is wasted. The package to silicon ratio is especially for devices such as opamps very unfavourable. But these are required for nearly all analog circuits. Therefore a fully integrated circuit allows the smallest size. Unfortunately, the development of a

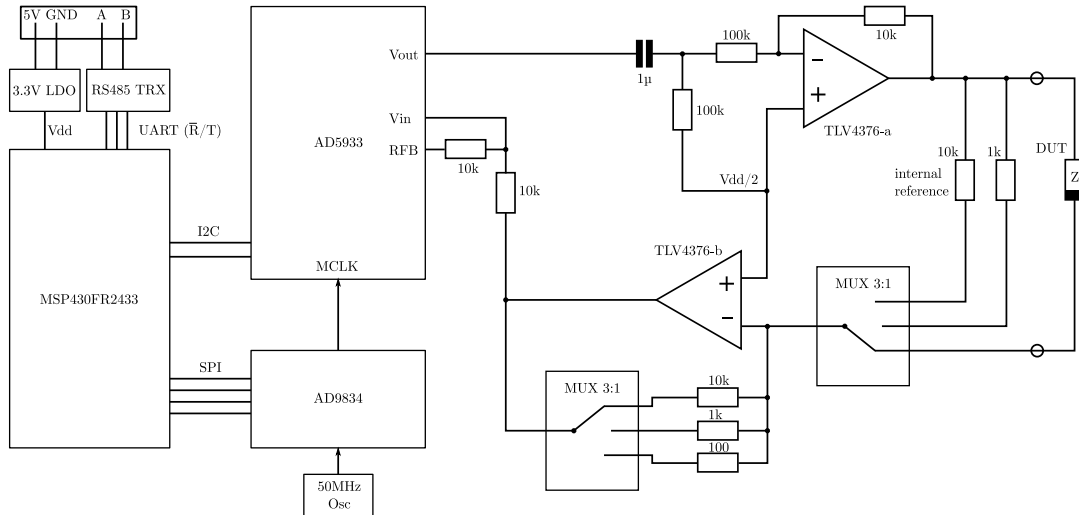



Figure 4.5: Simplified schematic for the stand-alone impedance spectrometer based on the AD5933 IC. The MSP430 controls the system and can communicate via a RS-485 interface. A LDO converts higher voltage from the connector to the operating voltage  $V_{dd}$  of 3,3 V. The AD9834 is a DDS and clocks the AD5933 impedance analyser chip. Its output is set to a DC-offset of  $V_{dd}/2$ , attenuated 10:1 and buffered. A multiplexer is used to connect either the unknown impedance  $Z$  or two internal reference resistors. The current is then detected by a TIA with a switchable feedback resistance and the signal is fed back to the AD5933. The DC-offset of  $V_{dd}/2$  is also cancelled in this step. 

custom integrated circuit can easily cost several millions. So, a solution with commercially available ICs needs to be found.

A mixed-signal microcontroller MSP430FR2355 from Texas Instruments is used to accomplish this task. It contains an ADC and several opamps. Each opamp has an accompanying DAC and a resistor network. With several analog switches different amplifier topologies and gains can be configured. It also has the usual microcontroller peripherals such as timers, a real-time-clock, digital communication interfaces and general purpose IOs. The smallest available package is VQFN-32 (4 mm x 4 mm).

With the processing capabilities diagnosis and calibration functionality can be realized. Through digital interfaces an easy connection to other systems is possible. The I2C interface provides the advantage to easily use multiple sensor interfaces in parallel.

This work was also published here on the IEEE NEWCAS 2019 conference [155].

## 4.4.2 Operating principle

The circuit of the analog front-end is depicted in Fig. 4.6. The different operating modes are described in the following sections.

### 4.4.2.1 ISFET readout

To read ISFETs with the controller up to four opamps and three DACs are used. The opamps are mainly used to buffer the DACs and the ADC input. The operating point is set via a servo loop implemented in software. The ISFET is kept at constant  $I_d$  and  $V_{ds}$ .  $\Delta V_{gs}$  is then proportional to  $\Delta pH$ . The circuit is depicted in Fig. 4.6.

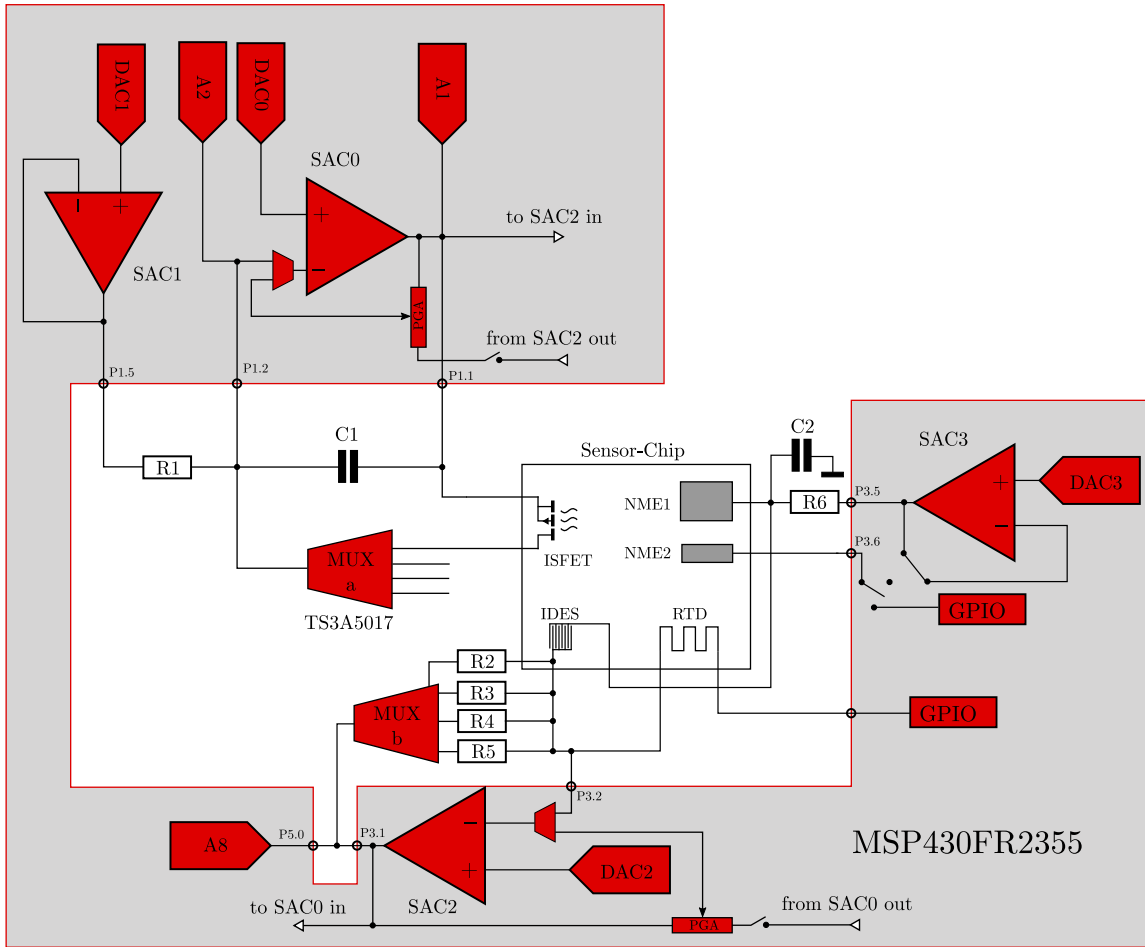


Figure 4.6: Schematic of the whole circuit for the integrated multi-purpose analog front-end. Core is the MSP430FR2355 which integrates most of the analog parts such as four opamps with DACs, so called SmartAnalogCombos (SAC), and an ADC with multiple inputs (A1, A2, A8). Only a multiplexer is external and two capacitors and six resistors. More is not needed to interface the multi-parametric sensor-chip. The principle for the ISFET read-out with this circuit is depicted in Fig. 4.7. (Adapted from [155] with permission, ©2019 IEEE.)

The opamp OA0 is used to set the voltage of the drain node. The output of one opamp is connected to the source, the inverting input is connected to the drain node. DAC0 is used to set the non-inverting input. DAC1 is used to control the current  $I_d$ . OA1 is used as buffer. The potential difference of DAC0 and DAC1 together with R1 sets the current  $I_d = \frac{DAC0 - DAC1}{R1}$  through the ISFET. A simplified version of the circuit parts to control the ISFET is described in Fig. 4.7. With the ADC inputs A1 and A2 the voltage can be measured at the source and the drain respectively. With this information  $V_{ds}$  can be calculated and the DACs can be adjusted till this voltage is in the desired range. If it is not possible to adjust the voltage and the current the gate bias voltage can be adjusted with DAC3. This DAC drives OA3 which in turn drives the electrolyte via an electrode. Negative feedback for the buffer can be either provided by the same or a separate (reference-) electrode to be able to set a precise potential. A flow diagram for the algorithm is depicted in Fig. 4.7. The result  $V_{gs}$  is the difference of A1 and the applied gate bias.

C1 (10nF) is required for stability. The internal 2,5 V reference is used to be independent of an external reference and unstable supply voltages. It has an accuracy of 1,5 % and a

temperature coefficient of 24 ppm/K.

The internal ADC only has a resolution of 12 bit which translates to 0,6 mV at the chosen reference. By using the controllers ability to cascade the opamps a higher resolution can be achieved. First the voltage is measured with the 12 bit resolution. Then the cascaded opamp is connected to the voltage to be measured, in this case the source voltage, and the feedback resistor for the inverting amplifier configuration is set to a gain of  $-32$ . This would result in many cases in the opamp going into saturation. Therefore the DAC is then used to bias the non-inverting input closely above the previously determined voltage level, in this implementation ca. 10 mV. Now the difference between these two voltages is amplified by  $-32$  and can be measured by the ADC. Assuming that the DAC voltage  $V_{bias}$  is relatively precise to its set value for the actual voltage following equation is true:

$$V_{17bit} = \frac{33V_{bias} - V_{ADC}}{32} \quad (4.1)$$

Where  $V_{ADC}$  is the amplified difference voltage the ADC reads. This introduces a little additional offset due to the second opamp but the resolution and noise is improved. The resolution gains about 5 bits and is now equivalent to 17 bit or about 20  $\mu$ V steps.

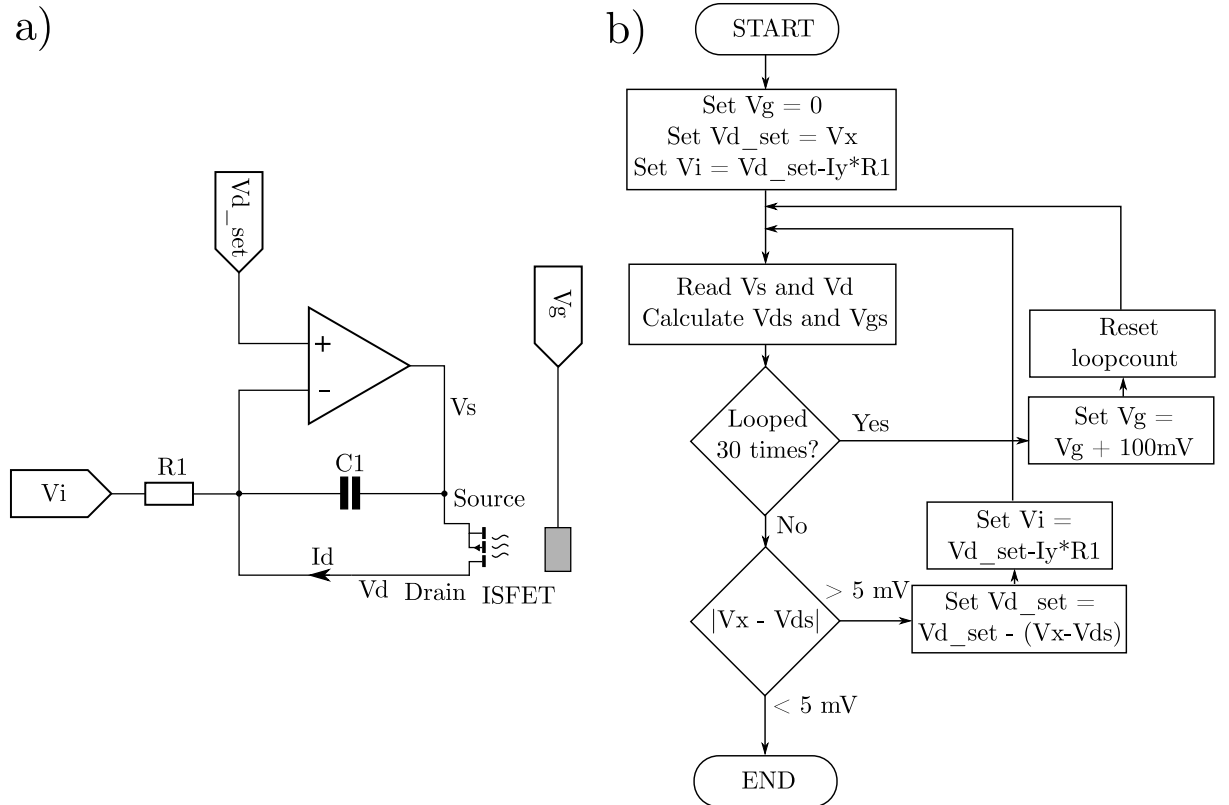


Figure 4.7: Simplified schematic a) and flow diagram of the ISFET readout algorithm b). The ISFET is connected as depicted in a) to the Opamp of the mixed-signal processor and three of its DACs,  $V_g$ ,  $V_i$  and  $V_{d\_set}$ . An external resistor  $R_1$  is used for current control and a capacitor  $C_1$  is needed for stability. The ISFET is brought to an operating point defined by  $V_{ds}$  and  $I_{ds}$  and the resulting  $V_{gs}$  is read. The algorithm in b) consists of two loops. If adjusting the source voltage is not successful the gate-bias is increased. Then the inner loop is called again. Therefore the execution time for this algorithm is not constant. The flow in the picture is for p-channel devices, for n-channel devices the polarity need to be reversed. (Adapted from [155] with permission, ©2019 IEEE.)

#### 4.4.2.2 Impedance spectroscopy

The DAC and OA for gate bias have a dual use to generate a sine voltage for impedance measurement. The voltages are calculated from a look-up-table with 32 entries to reduce code size and computation. This register and the program flow is depicted in Fig. 4.8. One of the internal timers is used to generate an interrupt to control the generation. An external first order low-pass filter is used to smoothen the sinus. OA2 is used as transimpedance amplifier with an external feedback resistor to measure the current. To cover a wider measurement range different resistors are selectable with a multiplexer. The feedback capacitor parallel to the resistor is important and needs to be matched to the resistor and the desired impedance range. The excitation amplitude and frequency is configurable. An ADC input is used to first synchronously sample the current signal and then the voltage over the DUT to account for voltage drops due to the low-pass. The ADC is not fast enough to directly sample the signal therefore the periodicity of the signal is exploited: Each period one sample is acquired each time shifted  $\frac{1}{32}$  of the period. This is all done by the same interrupt routine that also generates the excitation thus the relative phase shift between generation and sampling is always constant. Fig. 4.8 depicts this sampling from a software point of view.

The length of the timer interrupt routine is the limiting factor for the frequency. It was therefore programmed with great care to be as fast as possible. It has a minimum length of 14 assembler instructions. In case it triggers an ADC measurement two additional instructions are executed. When the ADC is switched from current to voltage measurement again two additional instructions are required. The 2110 cycles after which this switch occurs was chosen so that the ADC is not triggered in this cycle to prevent an overly long interrupt routine. With a 16 MHz clock the maximum frequency observed is nearly 5,5 kHz. This is with 32 samples per period an interrupt frequency of about 176 kHz or one interrupt every 5,68  $\mu$ s. With a processor clock of 16 MHz in this interval fit 91 clock cycles. Calculated from the disassembled code the cycle counts for the routine are at 74 for normal sample, 86 cycles when the ADC is triggered and 92 when the switch to voltage sensing is made. Therefore the absolute maximum frequency is 5,43 kHz which equals to 92 cycles. At higher frequencies the next interrupt would occur while the routine is not finished resulting in erroneous behaviour. It is probably possible save some cycles in the routine by using a different instruction set format<sup>1</sup> which executes in fewer cycles. I.e. reducing the maximum cycle count to 80 would give a maximum frequency of 6,25 kHz. However, this introduces other difficulties as the faster instruction set has a limited addressing capability and therefore cannot access the whole memory space. The effort to craft such code is in no relation to the gained frequency range. But there is a much easier way to extend the frequency range: A software switch was implemented that generates a sinus look-up table with two periods in 32 samples. This way, the same code can be used but the output frequency is doubled.

Care has to be taken for the oscillator frequency which directly affects the output. The internal DCO-clock-generator proved to be not stable enough due to the used frequency-locked-loop (FLL). The oscillator generates 16 MHz on *average* by switching between a higher and lower frequency. This can cause some distortion of the excitation signal resulting in more noisy impedance measurements. Better results can be achieved by using a quartz oscillator. But this will require an additional component. A work-around is to

---

<sup>1)</sup> There are different instruction sets for the MSP430 which allow different address bit lengths.

disable the modulation for the DCO during the impedance measurement. Then, however, the frequency will have a little deviation. But this usually not an issue for bio-impedance spectroscopy.

The frequency of the excitation sinus is determined by the value the timer generates an interrupt upon reaching. The timer has a special register where this value is programmed. The following equation can be used to calculate the frequency:

$$f_{sin} = \frac{f_{MCLK}}{32 \cdot (TCCR + 1)} \quad (4.2)$$

Where  $f_{MCLK}$  is the processor's main clock frequency and TCCR the value in the timer / counter compare register. +1 is required because the generation of the interrupt will need another clock cycle. The used method for frequency generation leads to a hyperbolic dependency of the actual frequency and the set timer period. Only discrete frequencies are available while the possible frequency steps increase with frequency. At the low end steps are sub Hertz while at the maximum they are 57 Hz.

After the acquisition the controller calculates in-phase and quadrature part of the current and the voltage by multiplying the acquired vectors with the sinus look-up table or its by 90° shifted copy. The code can also detect if the signal is clipping and then returns an invalid value. The impedance can then be calculated in post-processing by a complex division together with the right factor for the used feedback resistor. There are however some systematic errors generated by the front-end (see Section 4.4.6.4) which need to be compensated in post-processing. There is a phase offset of nearly 180°. Also the feedback gain and the phase shift is variable with frequency. Test measurements showed a roughly linear response so linear functions were used to approximate and compensate these errors to keep complexity low. There are also some highly non-linear error components which could also be compensated but increase the required complexity and memory usage. These non-linear components are also dependent on the unit so this calibration needs to be performed for each device. The simpler linear behaviour is common for different units.

The error correction uses five coefficients and three parameters.

$$Z_{corrected}(f, \sigma, \mu) = \frac{Z_{raw} \cdot R_{\sigma, \mu}}{(1 + A_{\sigma, \mu} \cdot (f - f_0)) \cdot e^{i(f-f_0)B_{\sigma, \mu}}} \cdot \frac{1}{O_{phase, \sigma, \mu}} + O_{amp, \sigma, \mu} \quad (4.3)$$

The three parameters are the frequency  $f$ , the used feedback resistor  $\sigma$  and the used frequency multiplier  $\mu$ . The coefficients are dependent on  $\sigma$  and  $\mu$ . For  $\sigma \in \{1, 2, 3, 4\}$  and  $\mu \in \{1, 2\}$  there are a total of eight values for each.  $R_{\sigma, \mu} \in \mathbb{R}$  represents the feedback resistance.  $A_{\sigma, \mu} \in \mathbb{R}$  is the frequency dependence of the gain.  $B_{\sigma, \mu} \in \mathbb{R}$  is the frequency dependence of the phase shift. Here  $f_0$  is the lowest used frequency as measurements at  $f = 0$  Hz are not possible.  $O_{phase, \sigma, \mu} \in \mathbb{C}$ ,  $|O_{phase, \sigma, \mu}| = 1$  is the constant phase error.  $O_{abs, \sigma, \mu} \in \mathbb{R}$  is the amplitude offset. Some coefficients could be combined but this can increase rounding errors in numeric evaluation. To generate the coefficients several known resistors were measured using all combinations of frequency, feedback resistor and frequency multiplier. All measurements were repeated ca. 100 times to average them and dampen the noise. Not all possible frequency steps were measured as this would take very long for low frequencies. Here only a few were considered, for higher frequencies all steps were measured.

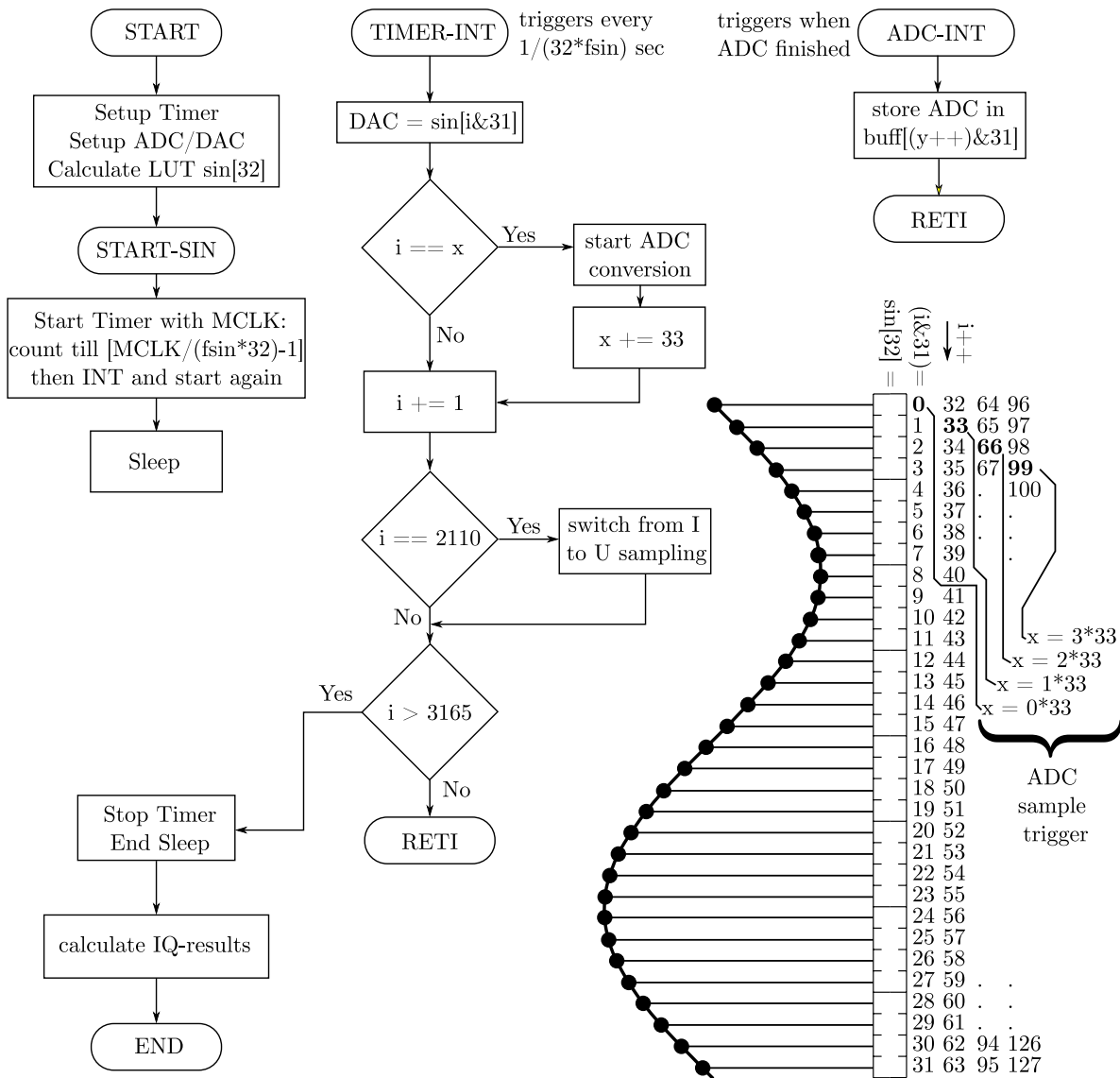



Figure 4.8: Flow diagram for the impedance measurement with the MSP430FR2355. The software first initializes the hardware and then waits for the measurement to start. When started the timer is set running and the CPU goes to sleep. When the timer reaches its programmed limit an interrupt occurs. In this interrupt routine the next sample from the sinus look-up-table (LUT) referenced by  $i$  is sent to the DAC. Every 33 output samples, equalling one full sinus period plus one sample, the ADC is sampled. On the lower-right the sinus LUT is symbolized with the indexes  $i$  highlighted where the ADC is sampled. When the ADC finishes conversion another interrupt routine writes the result in a ring buffer. After 2110 DAC samples ca. 64 excitation periods have passed. The DUT had 32 periods to settle and the ring buffer is filled with the latest 32 samples. At that point the ADC input is switched to measure the excitation voltage instead of the current. After again 32 periods a new ring buffer is full and the excitation stops. Finally the controller calculates IQ data from the ring buffers and ends the routine. 



The errors are highly dependent on the frequency step. A neighbouring frequency step can have much lower noise and absolute error. This should be considered when choosing frequencies to measure. Usually the application can tolerate a slightly shifted frequency for the benefit of better precision and accuracy. There is also the possibility to model the errors with an electrical circuit and use this model to calculate a compensation function. This approach was not considered as it adds unnecessary complexity, is also not able to compensate the high non-linear errors and any benefits of such an approach for higher precision are wasted for *just* a 12-bit ADC and medium precision opamps of the MSP430.

#### 4.4.2.3 RTD readout

The transimpedance amplifier is also used to read resistive temperature sensors. The other port of the resistor is connected to a GPIO-port of the controller. By setting it to Vcc the measurement is enabled. The non-inverting input of the amplifier is set via the DAC to 2,5 V to shift the output voltage in a suitable range for the ADC. By setting the IO-pin to high impedance measurement is disabled and the transimpedance amplifier can be used for impedance spectroscopy. The resolution of this measurement is however not that high. It was therefore abandoned in favour for a temperature measurement with MOSFETs and the ISFET readout circuit (see Section 5.1).

#### 4.4.2.4 Battery voltage measurement

The supply voltage to the chip, relevant during battery supply, can be measured by the controller without external parts using some tricks. The ADC can be used either with a quite precise internal 2,5 V reference or Vdd as reference. But the input voltage must be below the reference therefore direct measurement of Vdd is not possible. There is however a way to use one of the DACs and set its reference to 2,5 V. That way the internal reference can be fed to the input of the ADC. Here the SAC0 is used and set as buffer because its output pin is also an ADC input pin therefore no external connections are required. The ADC is configured to use Vdd as reference. When the DAC is set to maximum 2,5 V this yields:

$$V_{dd} = \frac{4096 \cdot 2,5 \text{ V}}{ADC_{code}} \quad (4.4)$$

To avoid the division the controller returns the ADC value to the user for further processing. Due to the hyperbolic function and the fact that the ADC has only 12 bit the resolution in the relevant voltage range around 3 V is between 1 and 0,6 mV. Using a lower DAC-output voltage will result in a better minimal resolution but only at much lower absolute voltages while the resolution around 3 V gets worse. Voltages below 2,6 V are not relevant although the controller is still working at such low supplies the internal reference of 2,5 V will stop working. There is also a 2 V and a 1,5 V reference but using them will only decrease the available voltage margin for ISFETs further. Therefore switching the reference was not implemented. Another problem is that this also needs to be considered for post-processing of the results. By measuring its supply voltage the controller can estimate the battery level, detect when it is too low to operate and it can compensate a varying Vdd in case it is used as reference. E.g. this is the case for the RTD measurement and if one wants to use higher voltages than 2,5 V for the ISFETs.

### 4.4.3 Software

The software for the microcontroller contains modules to read the sensors, provide an I2C-interface, several auxiliary functions to operate multiple controllers and a state-machine for sequence control. The ISFET sensor readout algorithm is depicted in Fig. 4.7, the algorithm for impedance in Fig. 4.8.

The auxiliary functions include methods to transfer the data via an UART-interface, e.g. via an LED. There is also a functionality to read other controllers and transfer their data via UART. These features are used for the multi-well-plate (see Section 4.5). The software for the multi-well-plate version and the stand-alone version are nearly identical, the application is defined by a different runtime configuration. Only the different pinouts are handled by preprocessor macros. These macros also set different default configurations which can be overwritten by the user.

#### 4.4.3.1 I2C-interface

The device is programmed to behave as I2C-slave and is organized in 128 8-bit addressable 16-bit wide registers, in total 256x8 bits. The lower 32 registers (64 bytes) are writeable and mainly used for configuration and status information. The following 96 registers (192 bytes) are read only and used for measurement data. The memory organization is little-endian. The meaning of these registers is described in Appendix B. They are mapped as global variables and used as such by the main program.

There is an internal pointer which is set to the first byte written by the master after a START. Subsequent writes or reads go to the byte addressed by the pointer. After each byte an offset to the pointer is incremented. The offset is reset to zero after a STOP sequence, the pointer is not. This behaviour is similar to most I2C-EEPROMs therefore I2C low-level library functions to read standard EEPROMs can also be reused here. In software this is implemented as one small interrupt routine and independent of the rest of the program. The I2C protocol is handled by the hardware peripheral. It can wake up the device upon reception of its address from the deepest sleep state helping with the power reduction of the plate. On the plate all but one devices are in this deep sleep with the lowest possible power consumption. Only one device is in a higher sleep state and has a low power oscillator running and clocking a timer. This requires significantly more power than the deep sleep. Upon a timer interrupt this master device can wake up all other devices via I2C. The other devices therefore do not need to run their own alarm clock and all measurements are synchronized.

Via I2C multiple of these devices can be easily managed requiring only four lines: Vdd, GND, SDA and SCL. All devices can be connected to the bus in parallel minimizing the wiring needed.

The address can be programmed freely. The current software has a preprocessor define to set the two highest bits. The remaining five bits are read from five GPIO-Pins that can be either connected to GND (1) or left floating (0). This allows up to 32 addresses, much more than usual I2C devices that often only allow eight different addresses. This is enough for the 24 well plate. The electrical encoding scheme was chosen because the centre pad of the VQFN-package used for the multi-well-plate is GND and therefore this connection can

be easily made in the layout. This way, the address can be defined by the layout while the programming is identical for all controllers. The stand-alone version of the software encodes a 1 with the pin connected to Vdd. Encoding one state as floating eases the layout. However, this requires a pull-down, respectively a pull-up, on the pin to set a defined state. For normal applications this is not an issue but for the plate this causes a significant current consumption as the resistances are not extremely high. Therefore, the resistors are only enabled at startup, the address is read and then the resistors are disabled and the pins that were detected floating are pulled to a defined potential to reduce current leakage.

For the multi-well-plate one controller needs to become an I2C-master to query the other devices and collect their measurement data. Only one of them may be configured in such a way otherwise collisions may occur which can lead to a dead-lock. In such a case the watchdog will eventually trigger and restart the device.

#### 4.4.4 Stand-alone front-end

A stand-alone version of this front-end based on the MSP430FR2355 was built for test and evaluation purpose and also for miscellaneous purposes (schematic in Appendix D.3). It is realized on a 5 cm × 5 cm two layer PCB (see Fig. 4.9). It has two 8-pin connectors

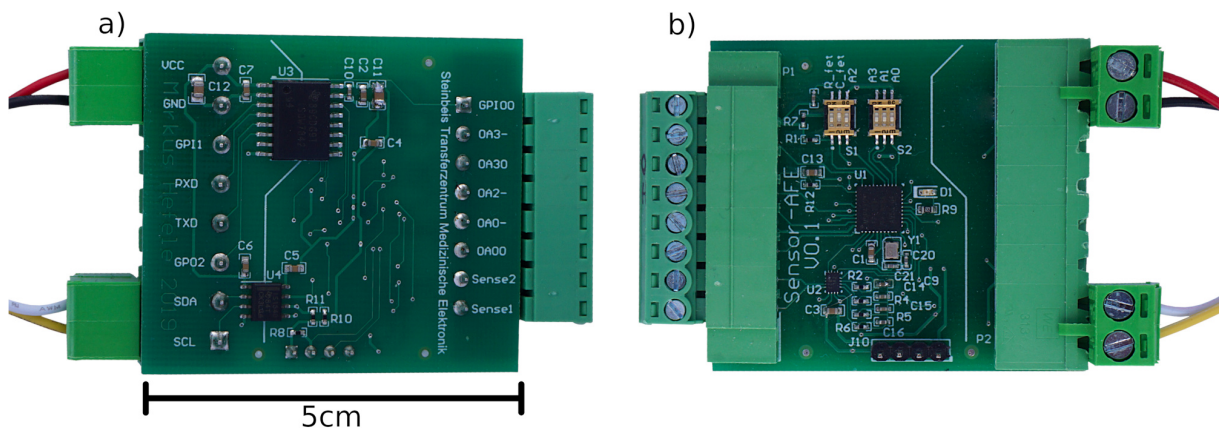



Figure 4.9: Stand-alone version of the integrated analog front-end based on the MSP430FR2355. a) is the bottom side of the PCB with two ICs for galvanic isolation: The large U3 on the bottom is for power and UART, the smaller U4 above for I2C. The white line symbolizes the isolation. b) is the top view. Here also a white line indicates the isolation barrier. The two largest parts are the green connectors on the left for the sensor and on the right for power and data. Terminal blocks are used to connect wires to them. On the output side power (red and black) and I2C (white and yellow) are connected. On the top are 6 DIP-switches for configuration. In the middle is the MSP430 (U1). On the bottom there is the multiplexer (U2) with the resistor array for the TIA and a pin header for programming. 

on both ends: One is the digital side for power supply and communication, the other is for sensor connection. It is fully galvanically isolated, power supply as well as all communications. The isolated power supply is an integrated chip, the ISOW7842F. The MSP430 can communicate with the outside world via I2C, UART, a digital input and a digital output pin. Internally the circuit operates on 3,3 V but it can be supplied with either 3,3 V or 5 V. The galvanic isolators can convert the voltages accordingly. Also the levels for the communication allow these values, even a mixed operation is in some

boundaries possible<sup>2</sup>, e.g. supply 5 V and I2C with 3,3 V. Four dip switches are available for configuration, currently used to select 16 different I2C addresses. Two further switches are used to select a different current measuring resistor and to connect the capacitor between source and drain for the ISFET measurements. A double 4:1 mux is used to select four different resistors for the TIA. The second mux is used to connect two sense lines to an ADC input. These are also on the 8-pin connector and can be used for voltage measurement. In the multi-well-version of the front-end this mux is used to select four ISFETs. This front-end also has a 16 MHz quartz oscillator to provide a stable clock especially for impedance measurement. Currently this hardware is tested for ISFET and impedance measurement. Due to the capabilities of the processor other sensors could also be read by modifying the software.

#### **4.4.5 Multi-Chip-Module integration with sensor**

To create a sensor with a digital interface in one package a so called multi-chip-module (MCM) was considered. In general, this means the combination of different silicon dies in a common package. The dies are connected to the lead-frame and to each other via bond wires. Discrete components like capacitors can also be added. This approach has the advantage to use for different circuit parts optimized process technologies, i.e. for the sensor the special sensor process and for the microcontroller a different digital optimized process with analog features with properties that are normally not easy to combine in one process flow.

To evaluate the possibility to combine the ISFET-sensor chip with the MSP430FR2355 together with the required resistor and capacitor their die pin-outs were compared. Unfortunately it was not possible to find a bond-wiring where no wires needed to cross. Bond-schemes without crossing needed the connection of external pins of the package to establish the internal connections. Also normal SMD components with tin-terminals are not suitable for bonding. Special very expensive components are required for this purpose. To create a viable MCM both dies and especially their pin-outs need to be designed for this purpose [private communication Ralf Brederlow, Ernst Müllner]. This was not possible at least for the microcontroller so this concept was abandoned. There is however still the possibility to use a PCB as re-routing layer and assemble the components with classical methods and then package the whole module similar to a hybrid module.

#### **4.4.6 Measurement Performance**

This following section describes the tests and measurements performed with the new AFE to determine its properties and performance.

##### **4.4.6.1 ISFET Measurements**

The performance of the new front-end was evaluated and compared to the DemoBoard as a reference for the ISFET measurements.

---

<sup>2)</sup> Not all combinations are possible!

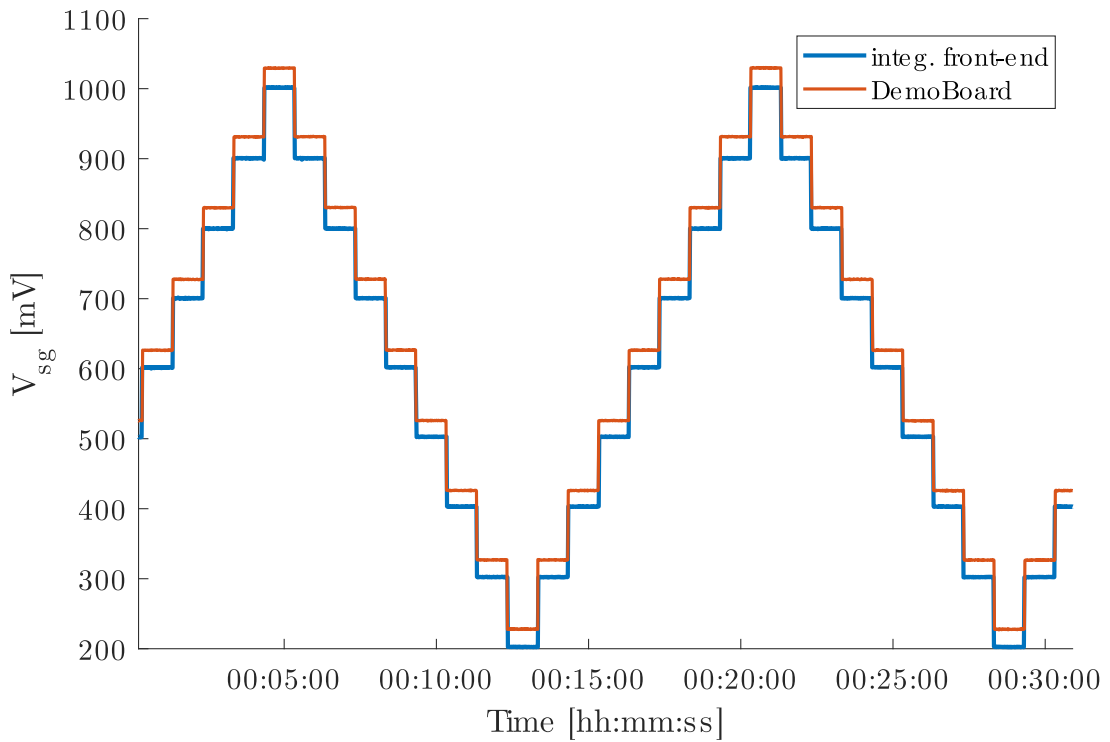


Figure 4.10: Output voltage of the two ISFET-front-ends when applying a change in bias voltage in series to the gate. The bias was set to steps of 100 mV with a SMU. The red and blue curve show the reaction of the two different front-ends. Ideally both curves should be the same. There is an offset between 23 mV and 31 mV and some difference in linearity. The later can be seen better in Fig. 4.11. Adapted from [155] with permission, ©2019 IEEE.

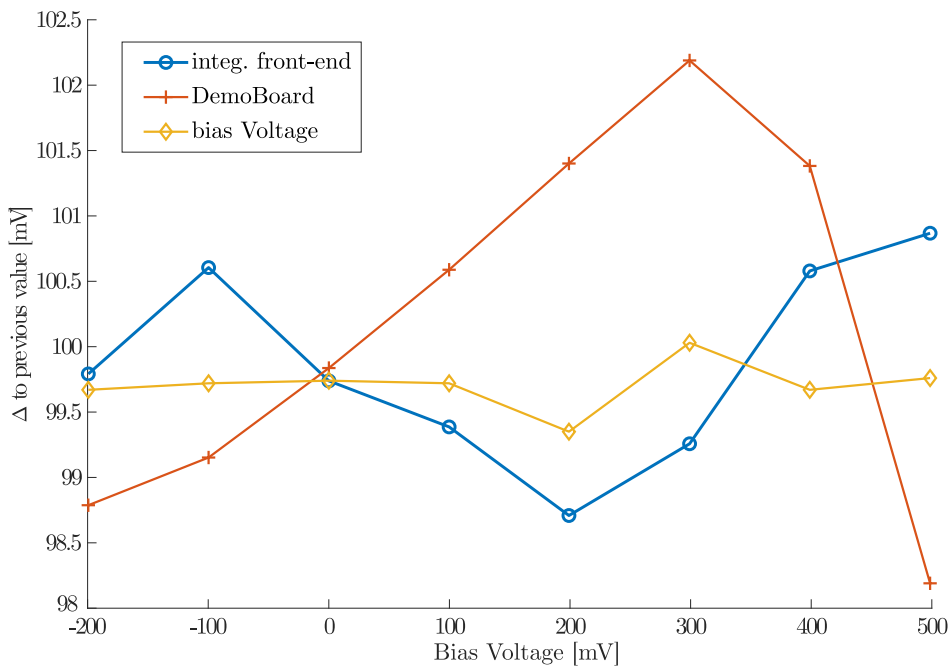


Figure 4.11: Change of the output voltage of the two ISFET-front-ends when applying a change in bias voltage in series to the gate. The yellow curve shows the actual change in bias voltage, set to steps of 100 mV with a SMU and measured with it. The red and blue curve show the reaction of the two different front-ends. Ideally all curves should be the same. (Because there are eight bias levels only seven differences exist and can be plotted.) Adapted from [155] with permission, ©2019 IEEE.

The range of the front-end, that is the voltage span for  $V_{th}$  it can cover, was tested with the ISFET simulator (see Section 3.4.4). The setup was the same as for the DemoBoard (see Section 4.2.5). The integrated front-end could also like the DemoBoard follow the simulated  $V_{th}$ -change. However, the maximum  $V_{gs}$  is only 2,5 V. Under certain circumstances this can be too low like when using a Pt-electrode to contact the electrolyte or when the intrinsic  $V_{th}$  of the transistor is quite high.

The software defined ISFET controller takes a variable amount of time to settle depending on the  $V_{th}$ . This is shown in the two oscillograms in Fig. 4.12. These are two extreme cases from about 10 ms to about 300 ms. For this experiment two different MOSFETs were connected which have a different  $V_{th}$ . This results in  $V_{sg} = -1$  V for the BSS138Q\_7\_F and  $V_{sg} = -1,9$  V for the SUB85N03-07P. The large difference in settling time can be explained by the structure of the algorithm (see Fig. 4.7). It starts at a very high gate voltage, thus very negative  $V_{sg}$ , and tries to find an operating point by changing the target drain voltage. If that is not possible within 30 loop cycles the gate voltage is decreased and the settling cycle starts again until either a operating point according to the preset is found or the gate voltage cannot be decreased further. The oscillogram on Fig. 4.12a shows that the gate voltage needed to be decreased by three steps till the operation point was found. The length of such a step consists of 30 attempts to adjust  $V_{sd}$  to the defined level. This takes some time to allow the opamps to settle and to sample the ADC multiple times to average the results. Therefore, the actual  $V_{th}$  of the ISFET can have a big influence on the settling time. But this can be compensated by the software. If the used sensors are known and especially their range of  $V_{th}$  the software can be changed in such a way that it tries favourable values for the gate voltage first. That way, it can set the correct operating point faster. Also the amount of loops till a gate voltage change can be reduced too and the size of the gate voltage steps can be optimized. The  $V_{sg}$ -range the circuit can settle for a certain set  $V_g$  is about one volt and also depends on the chosen  $V_{ds}$  and  $I_{ds}$ . This is described by the following inequations that must all apply (for n-channel):

$$0 < V_g < 2,5 \text{ V} \quad (4.5)$$

$$0 < V_g - V_{gs} < 2,5 \text{ V} \quad (4.6)$$

$$0 < V_{ds} - V_{gs} + V_g < 2,5 \text{ V} \quad (4.7)$$

$$0 < R \cdot I_{ds} + V_{ds} - V_{gs} + V_g < 2,5 \text{ V} \quad (4.8)$$

They emerge from the schematic and the voltage limits of the opamps and DACs which always need to be operated between zero and 2,5 V. The current software defaults are optimal for ISFETs with a  $V_{sg}$  of about  $-2$  V. Figure 4.13 illustrates these inequations for two different operation points.

#### 4.4.6.2 High resolution ADC mode

The integrated ADC of the MSP430 has 12-bit resolution. With the help of the integrated opamp 17-bit can be achieved in theory. In Fig. 4.14 both the pure 12-bit result and the 17-bit enhanced measurement are plotted together. The quantization steps for the 12-bit resolution are clearly visible while the 17-bit signal has more details. There is a little offset between the two signals of less than a mV. This is caused by the offset voltages of the internal opamps and can vary from unit to unit. However, as the ISFETs need to be

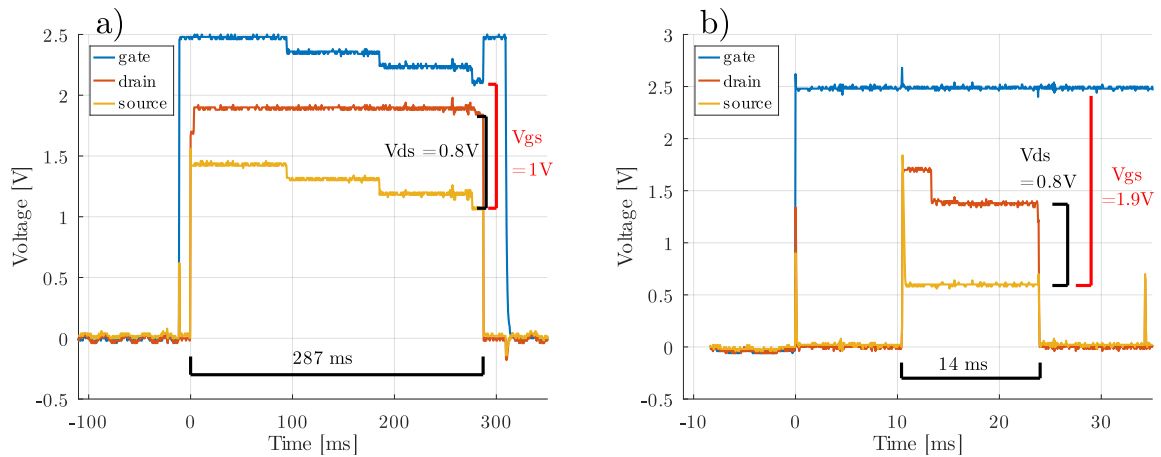



Figure 4.12: Oscilloscopes of the voltages  $V_g$ ,  $V_d$  and  $V_s$  that the integrated analog front-end applies to two different MOSFETs as ISFET replacement while the algorithm tries to find the correct operating point. In a) a BSS138Q\_7\_F MOSFET is used. This shows the worst case of about 300 ms settling time till the desired  $V_{ds}$  is reached.  $V_{gs}$  is here very low so that the  $V_g$  needs to be decreased to reach the operating point. This is done in an iterative way and takes some time. In b) a SUB85N03-07P MOSFET is used. In this case due to the much higher  $V_{gs}$  it settles in about 14 ms. 

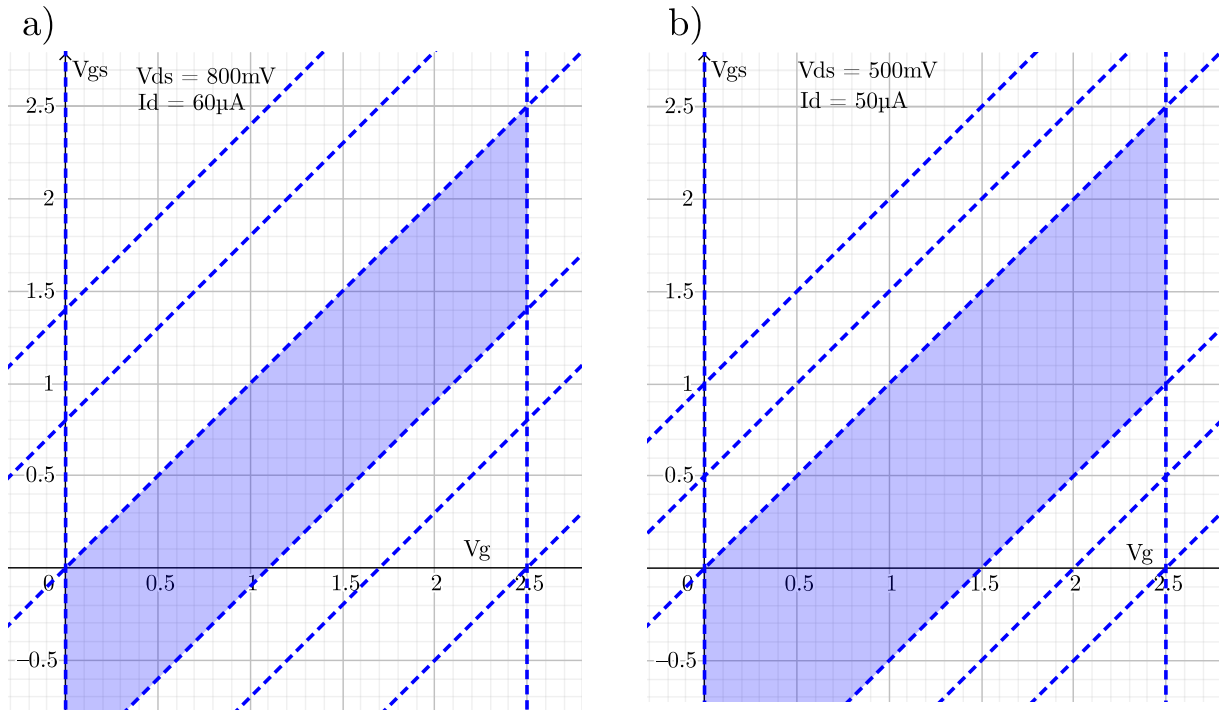



Figure 4.13: Voltage limits of the MSP430FR2355 based AFE. The x-axis is the current set voltage at the reference electrode  $V_g$  referenced to system ground. The y-axis shows the gate-source-voltage  $V_{gs}$ . The blue parallelogram is where all the inequations 4.5, 4.6, 4.7 and 4.8 are fulfilled. The dashed lines are the borders for the single inequations. a) and b) show this for two different operation points denoted on the top left. For each  $V_g$  which can be set with the DAC of the MSP the corresponding range for  $V_{gs}$  where the circuit can settle can be determined by the blue area. 

calibrated anyway and only the relative change in voltage is relevant this is not an issue for the actual measurement. The theoretical resolution in 12-bit mode is 0,6 mV while in 17-bit mode it is 20  $\mu\text{V}$  using a reference and upper limit of 2,5 V. The measured signal noise showed a normal distribution with  $\sigma = 600 \mu\text{V}$  for the 12-bit mode and  $\sigma = 40 \mu\text{V}$  for the 17-bit mode at a sample rate of about 10SPS. This is one or two LSBs respectively. The maximum achievable sample rate however is highly dependent on the  $V_{sg}$ . For practical applications these resolutions can be translated to pH or temperature. Assuming 40 mV/pH for ISFETs and 2 mV/K for MOSFETs this yields a theoretical resolutions of 0,015pH and 0,30 K for the 12-bit mode versus 0,0005pH and 0,01 K for the 17-bit mode. Considering the noise of the sensors the actual resolution is still more than enough for the intended measurements and the used sensors.

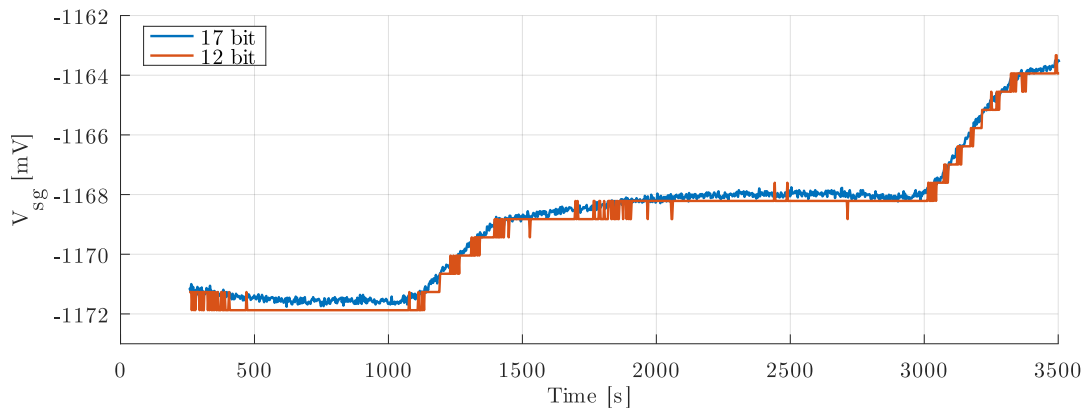



Figure 4.14: Comparison of the raw 12-bit measurement to the enhanced 17-bit mode with the help of the build-in PGA and DAC. The 12-bit signal shows quantization steps while the 17-bit signal has much more detail. There is however a slight offset of less than a mV. 

#### 4.4.6.3 Temperature stability

To test the temperature stability the circuit was placed inside a thermo cabinet. A MOSFET outside of the cabinet was measured for reference. It therefore was only subject to small room temperature changes. The cabinet was set to temperatures between  $-30^{\circ}\text{C}$  and  $35^{\circ}\text{C}$ . The actual temperature was monitored with a TMP275 sensor IC. Below  $0^{\circ}\text{C}$  the voltage signal is quite unstable. For higher temperatures the signal is stable and has a temperature dependence of 2 mV change at a 36 K change in temperature. This is around  $+55 \mu\text{V}/\text{K}$  (see Fig. 4.15).  $V_{sg}$  follows the temperature inside the cabinet instantly and then stays constant. Therefore it can be assumed that this effect is not caused by the thermo cabinet exhaust heating the room and thereby the dummy MOSFET that is placed there. In that case one would assume that at  $0^{\circ}\text{C}$  the heat exhaust is larger due to the active cooling which would result in a temperature increase for room and the MOSFET. Which cannot be observed. This temperature deviation of the signal is caused by the internal reference of the MSP430. According to the datasheet of the controller it has a temperature coefficient of 24 ppm/K. At 2500 mV set, a 36 K change would result in the reference to deviate by 2,16 mV. This change was observed in the deviation of the measured  $V_{sg}$ .

The instability at negative temperatures are for the intended application not relevant as the plate with the sensors and the electronics needs to be operated at around  $37^{\circ}\text{C}$  to



keep the cell cultures alive. Even without cell cultures the sensors need to be operated at temperatures above  $0^{\circ}\text{C}$  otherwise the water would freeze. ISFETs cannot measure ice. The front-end is in close proximity to the sensors to avoid noise through long cables and thereby seeing the same temperature. Hence there is no practical application where this circuit needs to work below  $0^{\circ}\text{C}$ .

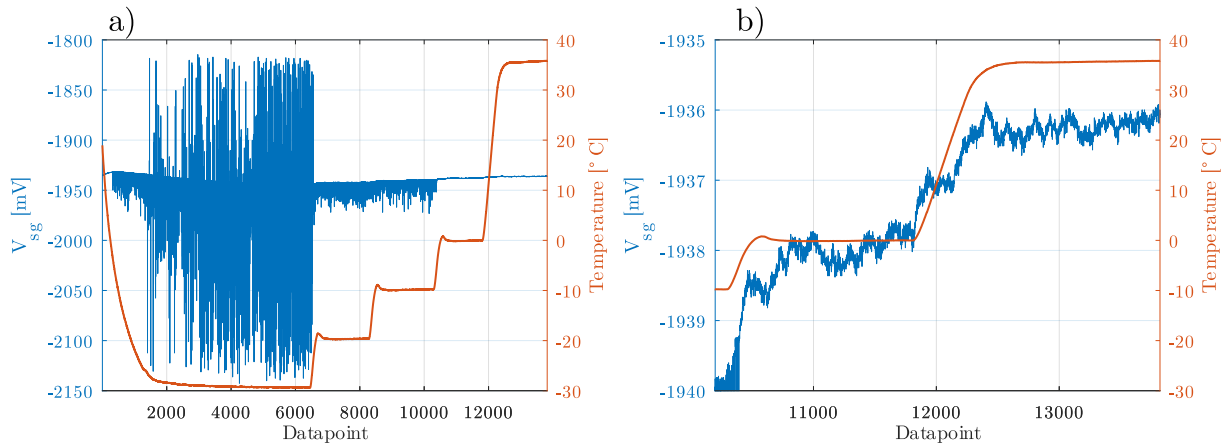



Figure 4.15: a) Temperature behaviour of the MSP430FR2355 based front-end. For temperatures below  $0^{\circ}\text{C}$  the voltage is quite unstable. For positive temperatures the signal is much more stable. b) shows a zoomed in Section of a). There is a slight temperature dependence of the signal, a  $36^{\circ}\text{C}$  increase leads to a 2 mV change. 

#### 4.4.6.4 Impedance Measurements

Impedance measurement was tested with RC-networks, e.g. Randles-circuit or plain ohmic resistors. The controller outputs the in-phase and quadrature values for current and voltage but also the raw ADC samples. The later were analysed and it was observed that these samples showed a little deviation from a perfect sinus (see Fig. 4.16). By averaging multiple samples for each phase step a much better sinus approximation could be achieved. These deviations cause a noise in the calculated impedance values. This can be reduced by either averaging the raw samples or averaging the in-phase and quadrature values calculated by the controller. The later is easier as less data needs to be transmitted and stored. A moving average of ten samples can then give acceptable results.

The sample rate is highly dependent on the measurement frequency as the controller always measures a certain amount of periods. So the measurement duration is indirect proportional to frequency.

It could also be observed that the noise is heavily dependent on the clock source for the controller. The internal digitally controlled oscillator (DCO) caused more noise than an external quartz or a lab frequency generator.

The measurement data shows that there is a linear error with raising frequency superimposed by a non-linear error. This non-linear pattern was consistent for several measurements at one device. Different units show a slightly different but similar pattern. To investigate this a sweep over all possible frequencies between 2 kHz and the maximum 5,5 kHz was performed. These are 159 frequencies as only discrete steps are possible due to the implementation. Several sweeps were recorded and averaged to filter random

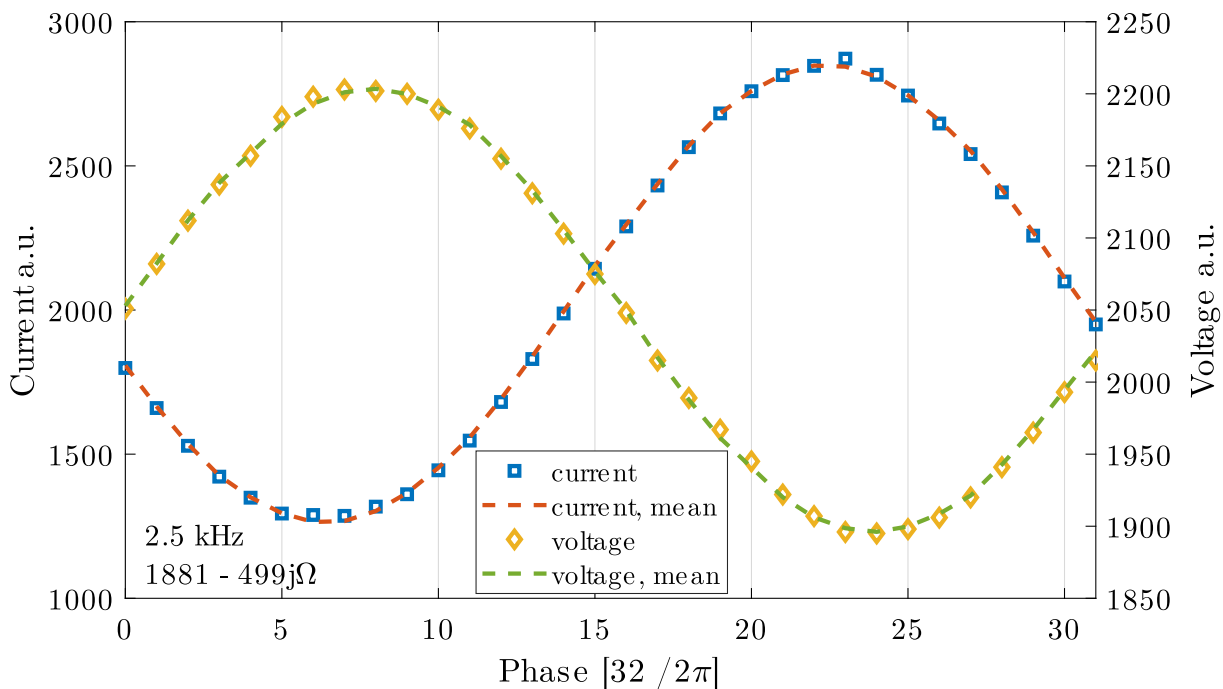



Figure 4.16: Raw ADC data for the impedance measurement. The blue square markers represent the ADC values measured for the current for each of the 32 phase steps during one period, the yellow diamond markers the corresponding voltage values. Their values are in arbitrary units. The dashed lines show the average of lots of superimposed single measurements. The single measurement usually has some deviations from an ideal sinus. The x-axis denotes the phase step. The real frequency was 2,5 kHz and the impedance about  $(1881 - 499i) \Omega$ . 

noise. Different settings for the front-end such as different feedback resistors, multipliers and test impedances were used. Compensated for that always a similar pattern in the results emerged for one device. An example is depicted in Fig. 4.17 and Fig 4.18a. Some frequencies always show higher noise than others. Especially a cluster of four neighbouring frequency steps around 3,8 kHz exhibit extremely high standard deviation (see Fig. 4.18b), this is also true for different devices. Often frequencies with high STD are at a distance of six but not always. Otherwise there is no regular pattern. No plausible explanation could be found for this behaviour.

Error correcting values were calculated with linear fits on averaged measurements of different known resistors for all configurations and a large set of frequencies. The used resistors were all 1 % rated and ranged from  $47 \Omega$  to  $180 \text{ k}\Omega$ . The exact values of the resistors were measured with a multimeter (3.5 digits). After applying the error corrections the results were compared with the known impedances and relative amplitude and absolute phase errors were calculated. The real phase was assumed to be zero as the measured impedances are ohmic. The mean of the relative errors over all frequencies are in a range of about 1-3 % with phase errors around  $2\text{-}4^\circ$ . Maximum error can be much higher (see Fig. 4.19 and 4.20). For some frequencies however the errors are in a reasonable range (see Fig. 4.21).

The Figures 4.19 and 4.20 also show that the range switching is effective to measure over a wider impedance range. With this feature an impedance range from  $50 \Omega$  to  $100 \text{ k}\Omega$  can be covered with errors always below 5 %, for over  $200 \Omega$  even below 1 %. The corrections were applied to the measurement data from the  $1 \text{ k}\Omega$  resistor and are plotted in Fig. 4.22. Compared to the original uncorrected values in Fig. 4.17 and 4.18 the linear error with

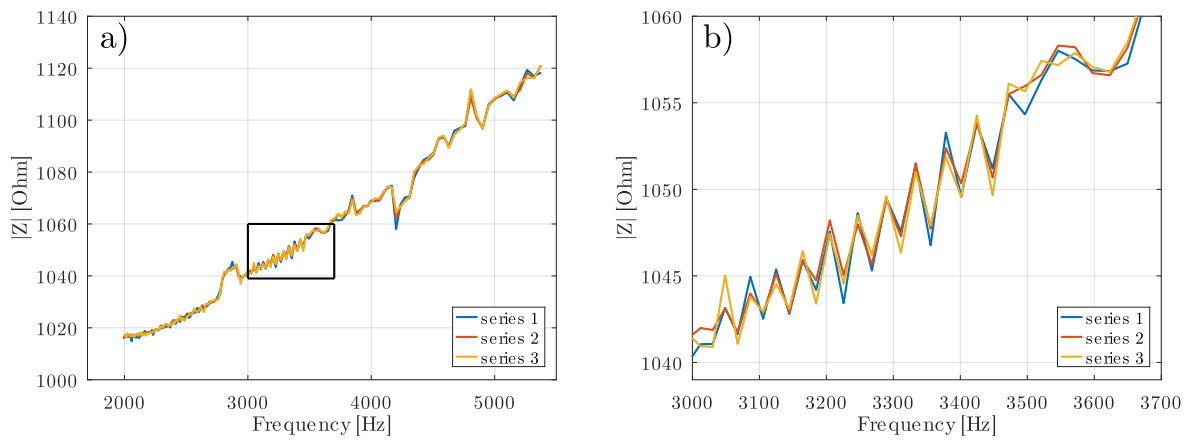



Figure 4.17: a) Absolute value of the impedance spectrum from the MSP430FR2355 front-end with 159 frequency steps. A  $1\text{ k}\Omega$  (1%) resistor was measured three times. The feedback resistance was assumed to be ideal. No calibration and correction was done yet. A linear error with rising frequency is visible. Also there is a smaller non-linear error visible. Each frequency point was measured multiple times and only the mean is plotted. b) shows a magnified plot marked by a black rectangle in a). The non-linear error aligns for all three measurement series. 

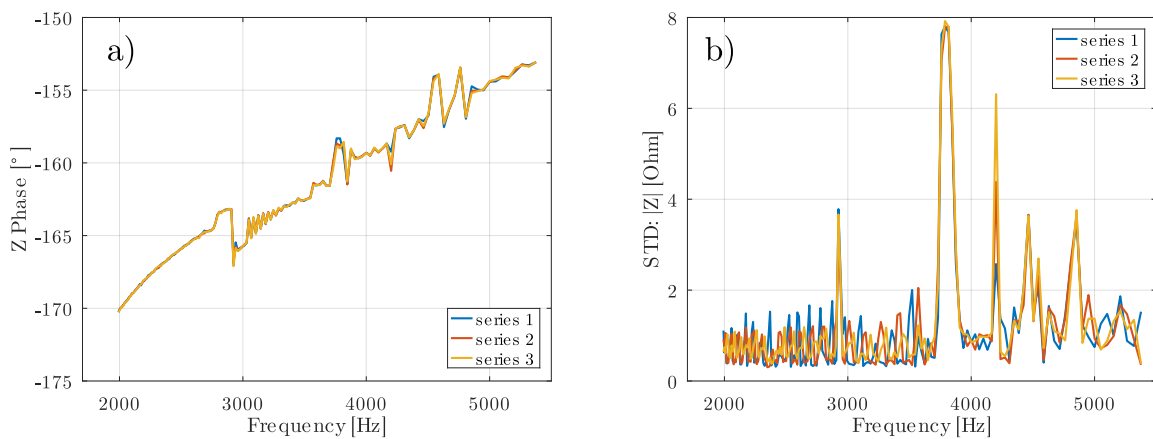



Figure 4.18: a) Phase of the impedance spectrum from the MSP430FR2355 front-end with 159 frequency steps. A  $1\text{ k}\Omega$  (1%) resistor was measured three times. A linear phase error with rising frequency is visible. Also there is a non-linear error visible. Each frequency point was measured multiple times and only the mean is plotted. b) shows the standard deviation of these multiple measurements for three series. Here the curves do not align that good except for four frequencies around 3,8 kHz and some of the high spikes. 

frequency is nearly gone. There is however a second order effect visible. The non-linear systematic error is still there.

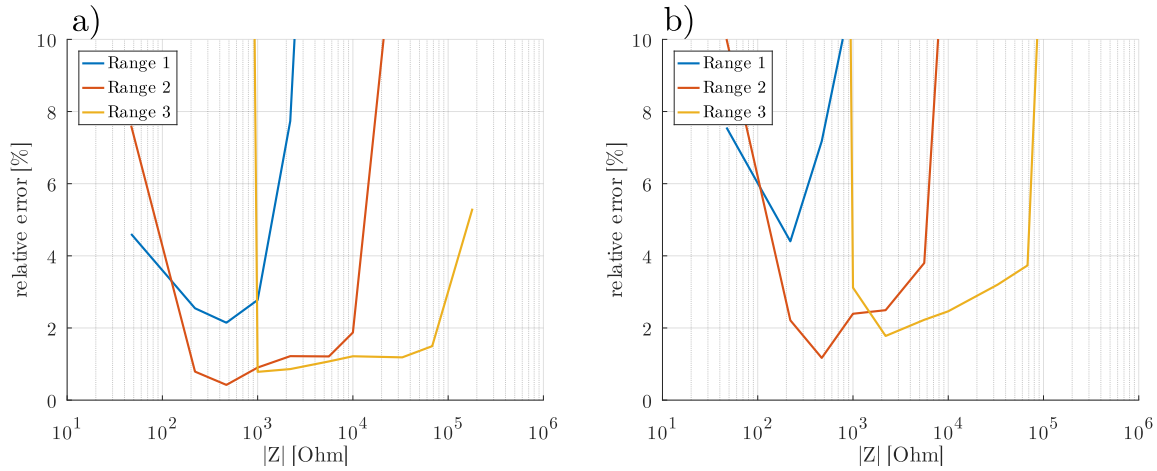



Figure 4.19: a) Mean of the relative error over all frequencies for the different ranges for different resistances. The ranges show their sweet spot for accurate measurement in a certain impedance range. Higher or lower impedances are measured with worse accuracy in the range. This is the point where to switch to another range. b) shows the maximum occurring error over all frequencies. 

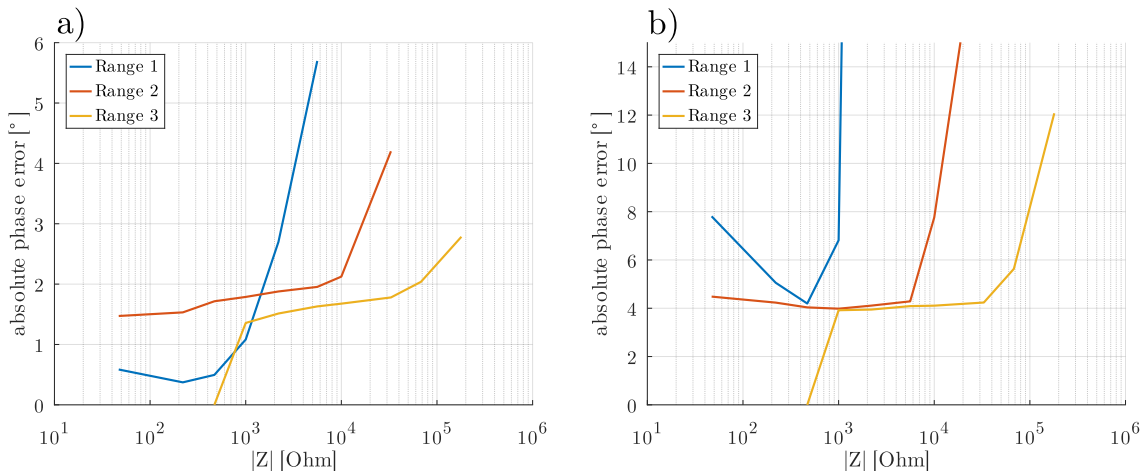



Figure 4.20: a) Mean of the absolute phase deviation over all frequencies for the different ranges for different resistances. The ranges show their sweet spot for accurate measurement in a certain impedance range. Higher or lower impedances are measured with worse accuracy in the range. This is the point where to switch to another range. b) shows the maximum occurring error over all frequencies. 

To simulate an IDES with cells and test the resolution of the circuitry a resistor decade switch box was used. According to [129] the change in magnitude is around 20% when cells are adhered compared to a cell free structure. This change was simulated using the switch-box. The used base resistances of 100 Ω and 1 kΩ represent two different sized IDES in cell culture medium. This implies two different measurement ranges to be used. For the low resistances the 100 Ω feedback resistor was used while 1 kΩ was used for the higher resistance. With the switch box the resistance of the simulated sensor was increased every two minutes by a tenth of the total change of 20%. Then it was set back to the base value. The results are plotted in Fig. 4.23. The changes can be observed for both base impedances even in the unfiltered raw results. By applying a moving average over 32 samples the change is even better visible. Therefore the front-end has enough resolution to detect the change cells would cause on an IDES.

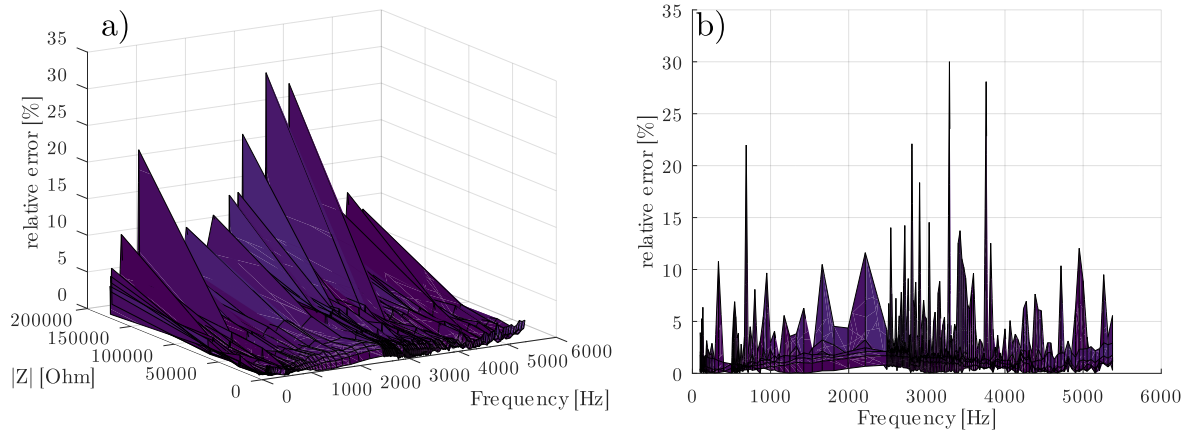



Figure 4.21: a) Relative error over all frequencies for different resistances in the Range 3 (highest range). The error level is higher for higher impedances but also the frequency is very important. There are some frequencies which have much lower total errors. This can be best seen in b) which shows rotated projection of the 3D-data from a). The impedance axis is perpendicular to the paper plane. Here the minimum and maximum relative error for each frequency can be easily seen. 

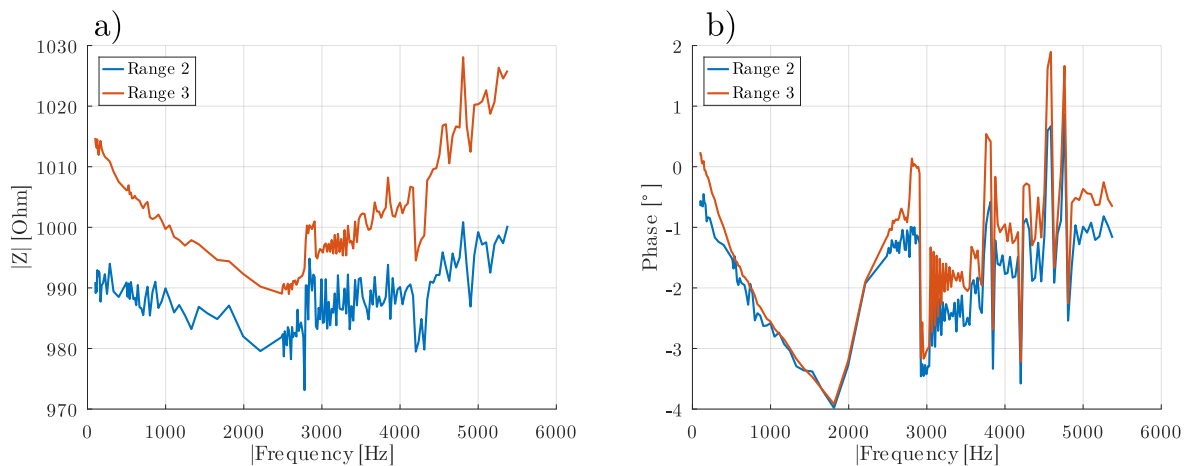



Figure 4.22: A  $1\text{ k}\Omega$  (1%) resistor was measured and the static errors of the front-end were corrected with the described function (Equation 4.3). a) shows the amplitude while b) shows the phase of the complex impedance over the frequency. Ideally both should be a flat line. 

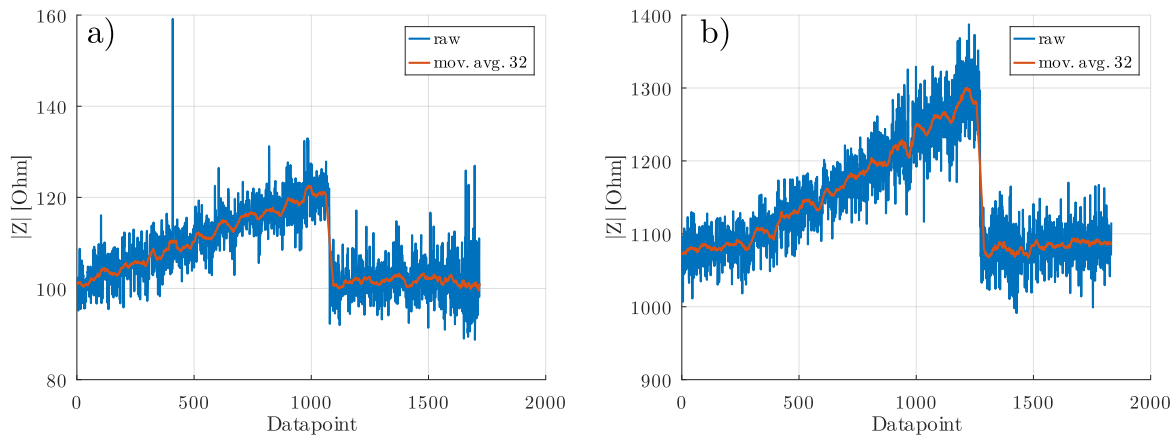



Figure 4.23: Effect of a changing impedance magnitude: A base resistance of a)  $100\ \Omega$  and b)  $1\ \text{k}\Omega$  was measured with the FR2355 front-end at  $9,6\ \text{kHz}$ . The impedance was increased every two minutes by 2% of the base impedance till 20% were reached. This simulates the impedance change an IDEs is experiencing during the growth of a cell culture [129]. After reaching this value it is reset to the original impedance. The blue curve shows the raw samples, the orange curve is a moving average of 32 samples. The measurement b) has an offset of around  $70\ \Omega$  but the relative change is accurate. 

#### 4.4.7 Discussion of MSP430FR2355 AFE

The MSP430FR2355 is a good solution to read an ISFET and provide a digital interface. It might not be the smallest, the most accurate, the most precise or the least energy hungry but compared to other approaches in literature for ISFET read-out it has many advantages relevant for *practical use*:

- very cheap, ca. 2-3 EUR bill of materials
- all parts available through common electronics distributors
- small size:  $4,5\ \text{mm} \times 4,5\ \text{mm}$
- flexible interface through the microcontroller: I2C, SPI, UART, etc.
- thus very easy parallelization
- n- and p-channel compatible
- software defined operating point for the ISFETs
- O2FET read out possible
- sensor diagnostics and post-processing with the help of the microcontroller
- additional sensors attachable (impedance, RTD, ...)
- microcontroller can also be used for other tasks
- approach can also be transferred to a similar controller in case the MSP430FR2355 is no longer available

Furthermore, its accuracy and precision are adequate for the application with a resolution of  $20\ \mu\text{V}$ . The power consumption is very low. The sleep current is in the order of  $1\ \mu\text{A}$  while measurement takes about  $4\ \text{mA}$  for 10 to 300 ms. More detailed measurements on the power consumption are provided for the whole multi-well-plate with 24 AFEs in Section 4.5.6.1.

The minimum requirements for a replacement controller are: Three (buffered) DACs, two ADC inputs, one integrated opamp and an integrated voltage reference. One example would be the STMicroelectronics STM32G473CB or the Cypress CY8C5888LTI-LP097 [156, 157]. For this project the MSP430 was more suitable as it comes with a smaller package and has FRAM which eases data storage and lowers power consumption. The STM32 and the Cypress PSoC are a bit overpowered for that application and about two to six times as expensive.

#### 4.4.7.1 ISFET readout

Chan et al. present an ISFET circuit with under  $80\ \mu\text{W}$  static power consumption (excluding digital core and IO) and 8-bit accuracy [83]. Thanapitak presents a design for an ISFET circuit that even achieves  $1\ \text{nW}$  consumption in the simulations [158]. The MSP430 has in the presented configuration at least a few  $\mu\text{W}$  permanent consumption depending on the sleep mode and some mA during measurement for a few hundred milliseconds. The advantage of the MSP430 over the previous solutions is that it is easily available. The other solutions require the very expensive manufacturing of a custom chip.

There is a little catch if the maximum  $V_{gs}$  is above  $2,5\ \text{V}$ . Depending on the used ISFET or the reference electrode is not always the case. E.g. when using a platinum electrode a higher voltage was observed resulting in the inability of the FR2355 to read the FET. A reason for this limitation is the use of the internal voltage reference of the controller of  $2,5\ \text{V}$ . This is used for all DACs and the ADC to provide a stable reference independent from the supply. The DACs therefore cannot output a higher voltage. It is however possible as a workaround to set the reference for the Gate-DAC to  $V_{dd}$ . Then this DAC can output a higher voltage and potentially bring the FET in the proper operating point. But this costs accuracy if  $V_{dd}$  is not sufficiently known and stable as i.e. on battery supply or by using a cheap regulator. There is however a method measuring  $V_{dd}$  and referencing it to the internal standard which will require some additional calculations. This gives a method to correct for an unknown  $V_{dd}$  in some boundaries. In the relevant range below  $3,3\ \text{V}$  the resolution is between  $0,6\ \text{mV}$  and  $1\ \text{mV}$ . This inaccuracy will add to the overall achievable accuracy and makes it a little worse compared to a precision voltage reference. However, some more voltage headroom for the ISFET is gained.

Obtaining even more voltage range is difficult. Modern circuits are designed for low-voltage operation to decrease power consumption. Most of them do not support voltage above  $3,6\ \text{V}$ . Also to generate higher voltages either more battery cells or boost converters are required. More battery cells require more space and boost converters can cause EMI. Therefore such high voltages for ISFETs are not desired. The ISFETs should be designed so that they can be operated with voltages below  $3\ \text{V}$ .

#### 4.4.7.2 Parameter Sweep

With the MSP430FR2355 AFE it is possible to automatically sweep the ISFET operation parameters  $V_{sd}$  and  $I_{sd}$ . This allows the detection of faulty FETs. Fig. 4.24 shows an example of such a measurement series. Three of the four devices show a MOSFET behaviour while one device is odd. This one is the same as the first device but was subjected to a high voltage prior to measurement to destroy it. The plot also shows that a change in  $V_{sd}$  does not change  $V_{sg}$  while  $I_{sd}$  has a square rooted influence. This means that the FET is operated in saturation where the following equation applies:  $V_{gs} = V_{th}(pH) + \sqrt{\frac{2I_{ds}}{K_n}}$ . This characteristic can be algorithmically checked to detect if the FET behaves correctly.

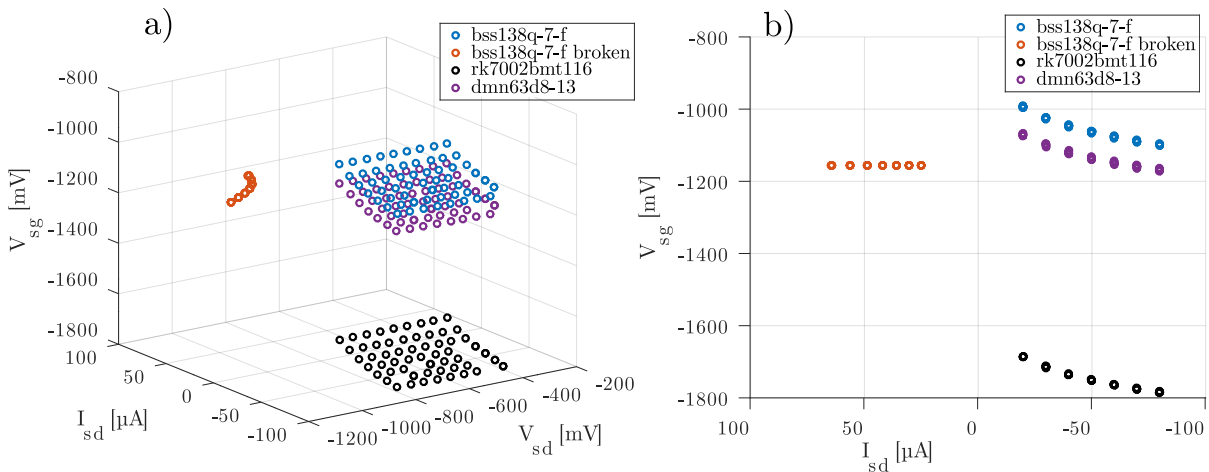



Figure 4.24: Example of a parameter sweep for different MOSFETs with the MSP430 based AFE. The circuit was programmed to automatically change  $V_{sd}$  and  $I_{sd}$  and record the resulting  $V_{sg}$ . This was done for four different devices and the results are plotted in a 3D coordinate system in different rotation angles a) and b). Two distinct patterns are visible: Three devices show a normal MOSFET behaviour while one device shows an odd behaviour. This one was deliberately destroyed prior to the measurement with a high voltage. Hence it is possible to distinguish faulty MOSFETs due to their characteristics. 

#### 4.4.7.3 Impedance spectroscopy

Impedance spectroscopy proved to be a challenging task. A major problem is the wide range of impedance to cover. This requires careful amplifier design and some tricks, i.e. the use of variable feedback resistors. But it is not enough to simply change the resistance as this also changes the dynamic behaviour. So a matched capacitor is also needed and some performance cuts need to be expected for higher frequencies at higher gains. Another problem is the generation of the sinus excitation. A step function is used to approximate the sinus here. The steps cause high frequency harmonics resulting in severe ringing of the transimpedance amplifier. This can be mitigated by using more steps. E.g. the AD9837 DDS chip uses a 10-bit DAC and can synthesize sin waves up to a few MHz. The datasheet denotes a THD<sup>3</sup> of 0,04%. The lower the THD the better. The THD of the sine generated by the FR2355 with 32 steps and with a dynamic range of ca. 7 bit<sup>4</sup> is in theory around 5,7%. Depending on the number of steps for the sinus and the available dynamic range better or worse values can be achieved. This has been plotted in Fig. 4.25 (see Appendix

<sup>3)</sup> total harmonic distortion

<sup>4)</sup> Based on a signal amplitude of 100 mV at the full range of 2,5 V with 12 bit:  $\log_2(100/2500 \cdot 2^{12}) = 7,4$



C for a script to calculate these values). The AD9837 costs around 3 EUR and uses  $4\text{ mm} \times 4\text{ mm}$  and  $8,5\text{ mW}$ . It requires a  $50\text{ MHz}$  clock and configuration via SPI. But by using a simple first order passive low-pass filter a significant reduction of harmonics for the FR2355 based solution can be achieved, enough for a ringing free operation of the TIA and at a cost of 0.02 EUR and a space of two SMD components.

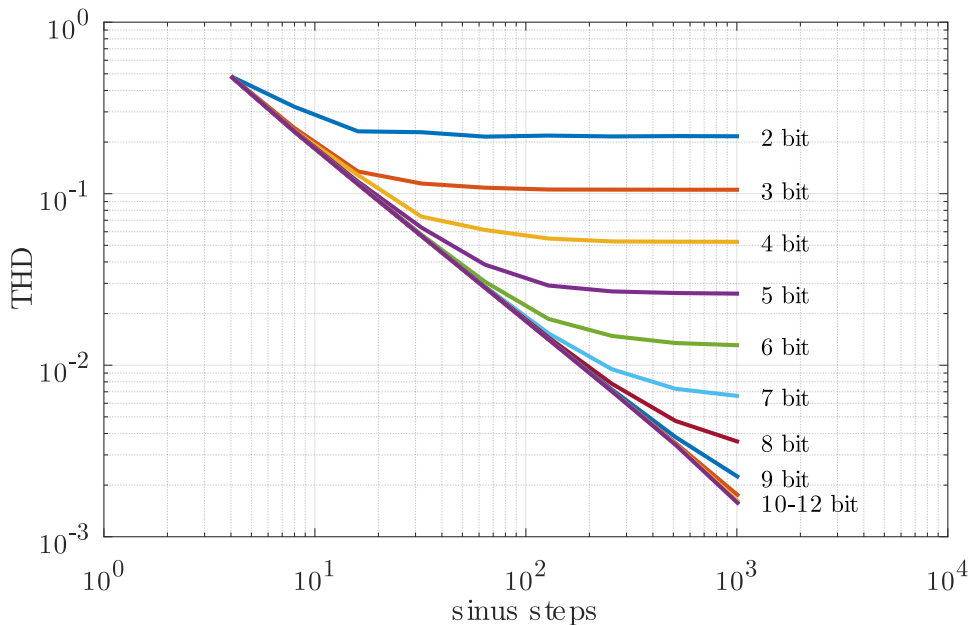



Figure 4.25: Plot of the expected Total Harmonic Distortion (THD) for a sinus function approximated with different amounts of steps and available dynamic range in bits. See Appendix C for a function to generate these values. 

Another often used technique is an impedance to frequency converter. Here the impedance is used as frequency determining element of an oscillator. The most well known device for that is the 555-IC. A modern example for that task is the LDC2114 from TI that is an inductance to digital converter IC. This approach is very simple and robust as only a frequency needs to be measured which can be done very precise with digital circuits. However, the frequency used to excite the DUT is now not constant. But the goal of bio-impedance spectroscopy is to measure at a certain frequency as the impedance is also variable with frequency, often in a non-linear way. These inductance or capacitance to digital converters usually assume a DUT with a linear behaviour. The operating frequency is usually in the MHz domain and therefore unsuitable for measurements around  $10\text{ kHz}$  as required for biological samples.

The main advantage of the implementation of the impedance spectroscopy with the MSP are size and cost. The MSP is available in packages down to VQFT-32 with a footprint of  $4\text{ mm} \times 4\text{ mm}$ . The required external low-pass filter and the feedback resistor & capacitor for the transimpedance amplifier are in total four SMD parts. If required 01005 form factor can be chosen for the resistors. There are no restrictions due to power loss. Only for the capacitor there is a size constraint, as e.g.  $100\text{ nF}$  are not available that small but in 0201. With double sided mounted PCBs this setup would require an area of less than  $20\text{ mm}^2$ . Even the more elaborated version with a quartz oscillator and a multiplexer for different measurement ranges can easily be built below  $200\text{ mm}^2$ . The total part cost for that is ca. 5 EUR in single quantities.

In contrast, the AD5933 costs around 20-30 EUR, more than 10 times as much as the MSP430FR2355 and then additional amplifiers are needed to perform bio impedance measurements. Also a microcontroller for control is required. The IMOLA (see Section 2.1.1.5) uses this approach. Its *IDES module* is 60 mm × 60 mm and includes a microcontroller, a multiplexer, the mentioned amplifier and a galvanic isolation for power and data. It only has a fixed measurement range and a fixed excitation voltage level. The frequency range for this module is up to 100 kHz. The DC-offset that this circuit generates over the DUT does not seem to be compensated.

It is comparable to the standalone version of the integrated analog front-end (see Section 4.4.4). This can only achieve up to 11 kHz but it is only 50 mm × 50 mm. It is also not susceptible to spectral leakage like the AD5933 without a variable clock [159, 130] due to its implementation. The excitation voltage is fully configurable and there is no DC-offset over the electrodes. There are four measurement ranges. Additionally this module can also read an ISFET and has software to either operate as peripheral device of a master controller or operate on its own.

Finally, there is a newer IC from AnalogDevices, the ADuCM355, that can also be used for impedance spectroscopy. This is discussed in Section 6.1.1 in detail.

Another possibility is the realization with discrete elements. Fig. 4.26 shows such a system based on a MSP430 for sinus generation. It controls a MDAC via a parallel interface to achieve the required sampling speeds. The signal is then low-pass filtered and attenuated. A buffer is used to drive the impedance. The current is amplified by a TIA and buffered. A fast ADC and a fast controller e.g. a DSP or an ARM-core is used to process the data. This master controller also controls the MSP. This concept was not realized as the parts required are together more expensive than the ADuCM355 let alone the MSP430FR2355.

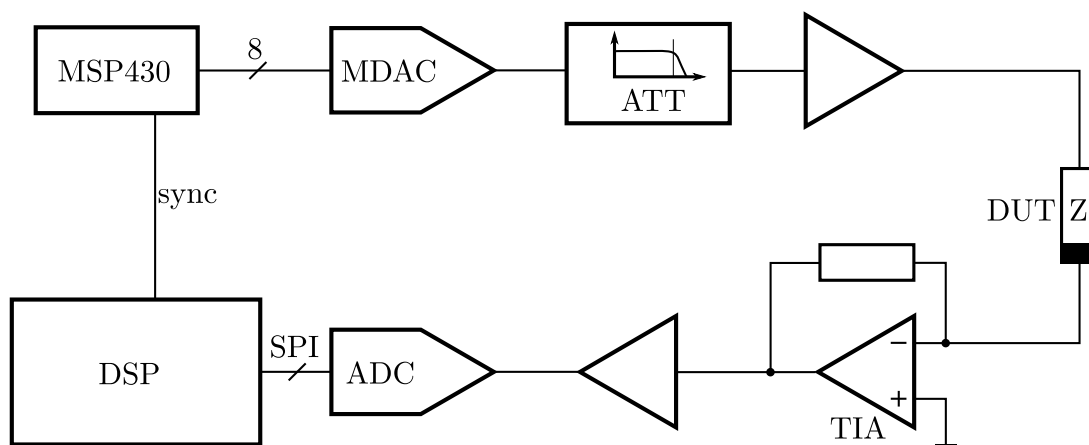


Figure 4.26: Impedance spectroscopy system with multiple ICs. The MSP430 generates a sinus signal with the MDAC. The parallel interface allows a high sample rate. The signal is conditioned: low-pass filtered, attenuated and buffered and then fed into the DUT. A transimpedance amplifier (TIA) detects the current. This signal is buffered again for the ADC and digitized. A digital signal processor (DSP) or an equivalent fast and powerful processor is controlling the system and calculating the impedance.

## 4.5 Electro-chemical multi-well-plate

The electrochemical multi-well-plate is intended to be a 24-well-plate with integrated sensors for pH, pO<sub>2</sub> and impedance for each well and the complete electronics for readout. It shall not need electrical connections as these are error prone and subject to corrosion.

The size of multi-well-plates is standardized as 127,76 mm by 85,48 mm. For a 24-well-plate this results in a well distance of approximately 18 mm. The top side of the PCB is kept free of parts to not obstruct the parts required to house the cell cultures. Only the sensors are placed on top. The rest of the electronics is placed on the bottom side. This side can be sealed with a transparent conformal coating to protect it against liquids.

For each well an analog front-end with the MSP430FR2355 is employed. For them the same layout cell can be used 24 times. The controllers are connected via a I2C bus therefore only four nets (Vcc, GND, SDA, SCL) need to be routed over the whole board. All other connections are local to the analog front-end cell. This simplifies the board layouting drastically. A schematic block diagram of this structure is depicted in Fig. 4.27.

Each controller has an individual I2C-address encoded by the layout. This is achieved through five GPIOs which are used to set the last five bits and are hard wired in a different configuration for each of the 24 controllers.

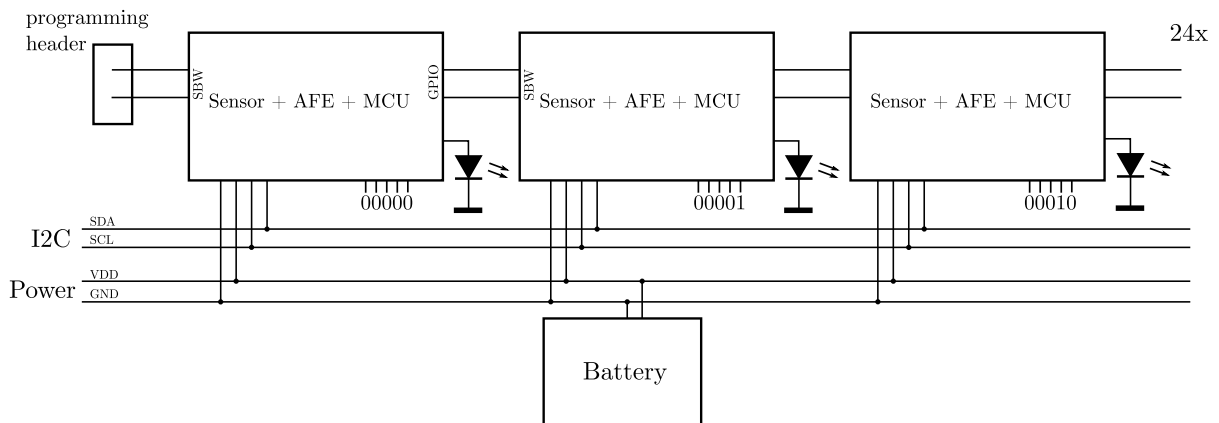



Figure 4.27: Block diagram of the electrochemical multi-well-plate. It consists of 24 identical blocks with the Sensor, the required AFE and a microcontroller. The inner details of the *Sensor + AFE + MCU* block is depicted in Fig. 4.6. These blocks communicate via an I2C bus. Five digital lines are used to encode an individual address for the blocks depending on their place on the board by either pulling them low or high. Each block has an LED which is used to transmit the data back to a base station. A battery is used to power the device. The programming interfaces (SBW) are chained: Only the first controller is programmed from outside and then programs its neighbour and so on. 

### 4.5.1 2x2 experimental module

A prototype of the multi-well-plate with four sensors was developed to test the concept and achieve the size constraints. It was the first layout for the proposed one controller-per-well and needed for debugging. Building only four wells was cheaper than 24 while it still allowed to test the interaction of the controllers on the bus and the programming concept. This prototype and the gained results were published here [155].

### 4.5.2 Contactless Electro-Chemical Multi-Well-Plate

To avoid problems with contacts in laboratory environments like corrosion a contactless version of the sensor-plate was developed. Data is transmitted unidirectionally from the plate via an optical link to a receiver. Power is provided via a Li coin-cell battery, e.g. CR1225 with 3 V and 48 mA h.

To achieve a long battery lifetime for several days the controllers spend most time in sleep mode. All peripherals are deactivated, only a low power oscillator and the real-time clock are running. The IOs are set to a defined level to avoid leakage due to floating nodes.

To transmit data from the plate an LED is used and connected to an IO with UART-peripheral. The normal UART functionality is used and sufficient to reliably transmit data over a few centimeters. A data-rate up to 19200 Baud is possible.

Other data transmission and power supply schemes were considered and tested like NFC<sup>5</sup> but were deemed unsuitable for the plate. The reasons are explained in the discussion in Section 4.5.6.2.

One controller on the plate acts as master which first triggers the measurement of the other controllers. This is required because the internal oscillators have too much deviation from each other. By using one as master clock all controllers collect their sample at roughly the same time. As the measurement has a rather huge power consumption the triggers are sent with a little delay for each chip so that there is not a huge spike in current drawn from battery. The master controller then collects the data from its slaves and transmits it via the optical link. This operation has a second advantage: Only one controller needs to run an oscillator to count a measurement delay. The other controllers can stay in a deeper sleep state and thus reduce the power consumption significantly. Fig. 4.28 shows a prototype of this multi-well-plate and Fig. 4.29 shows details.

### 4.5.3 Contactless Electro-Chemical Multi-Well-Plate, rev 2

The first layout revision uses a four-layer board and mounts the sensors on the top side while the rest of the electronic components is on the bottom side. In contrast, this improved revision only needs two layers and the sensors are mounted on the bottom side as flip-chip with a hole in the PCB for the fluid. This could be achieved by using a variant of the microcontroller with a smaller package. Instead of the 40-pin VQFN a 32-pin VQFN<sup>6</sup> is used. Also the sensor as flip-chip mount is now only as big as the die. Here the new gen2-chip is used so the die is approximately 4 mm × 4 mm therefore it fits on the underside of the PCB together with the MSP. A two-layer board is cheaper to manufacture. For programming and configuration Tag-Connect is used. This concept does not need to mount a part on the board and therefore saves valuable vertical space.

This board also includes a loop antenna and space for a rectifier and LDO to test wireless power supply for the plate. The antenna can be tuned to 13,56 MHz with a parallel capacitor. This is a standard frequency for NFC or RFID<sup>7</sup> and can be used licence free.

---

<sup>5</sup>) near field communication

<sup>6</sup>) This package option was released later by the manufacturer.

<sup>7</sup>) Radio Frequency IDentification

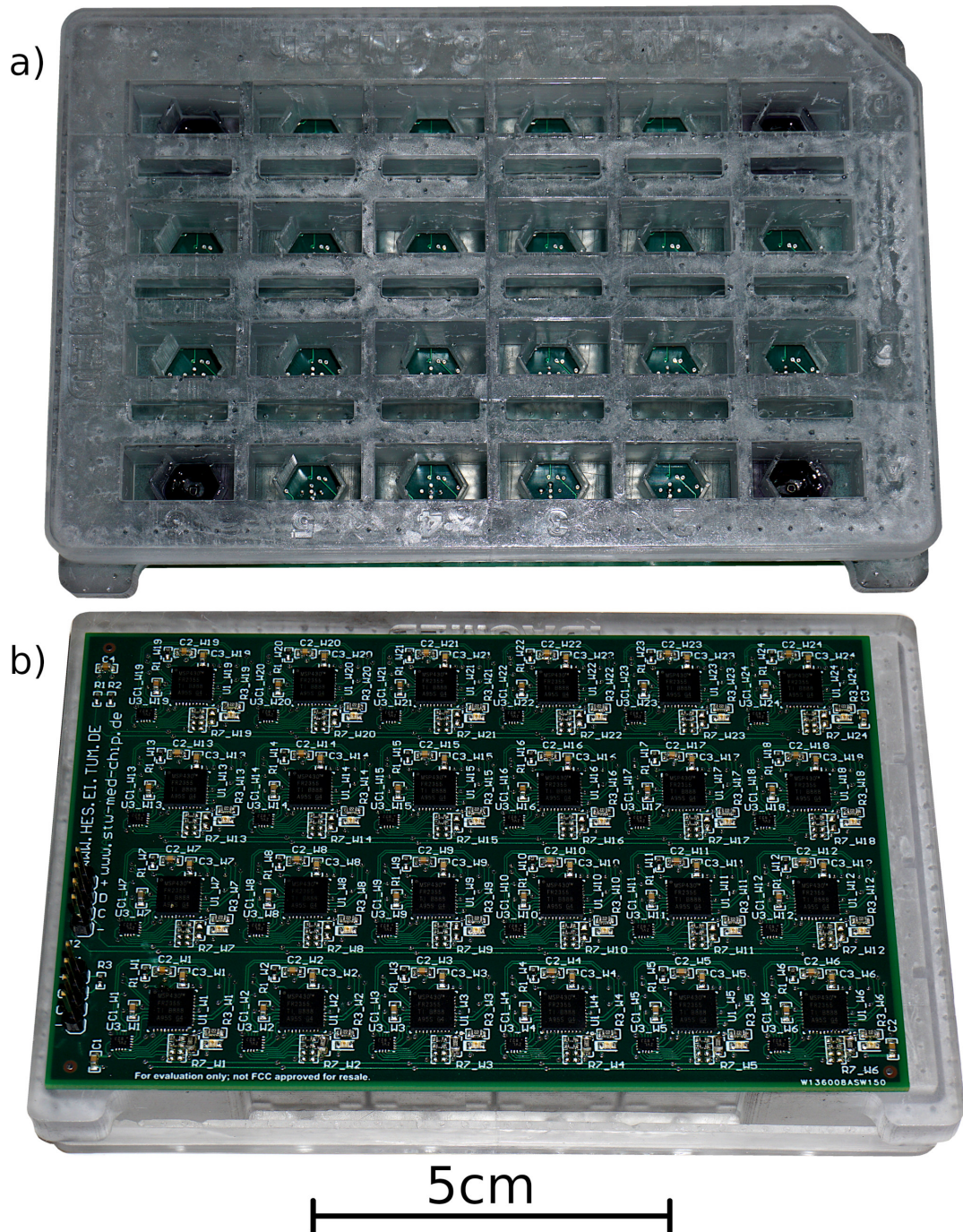



Figure 4.28: Contactless multi-well-plate, layout revision 1: a) shows the top side of the plate with the fluidics. Only the four sensors in the edges are populated due to a limited number of sensor samples. b) shows the underside with the electronics for sensor readout. There are 24 identical circuit parts, one for each well. The large IC is the mixed-signal-processor, the smaller one is a multiplexer. The two pin headers on the left are for programming and debugging. 

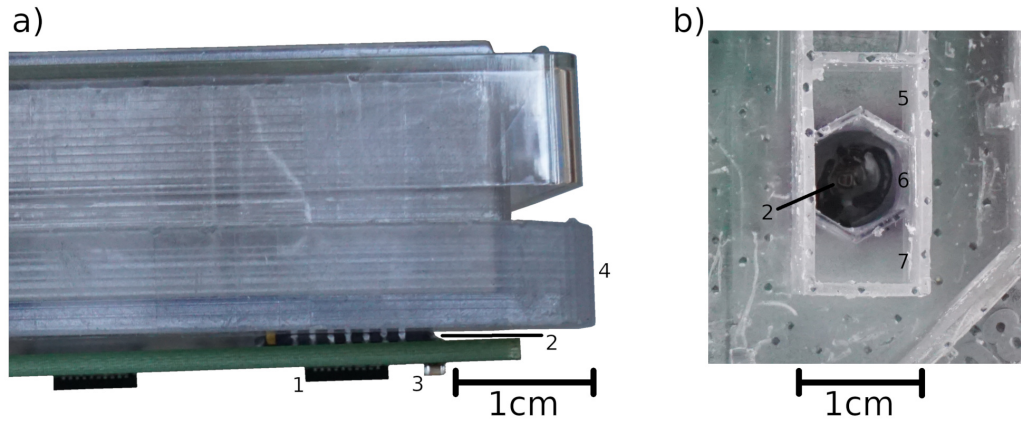



Figure 4.29: Detail photographs of the multi-well-plate. a) shows the plate from the side. 1 is the microcontroller, 2 is the sensor chip, 3 is a capacitor, 4 is the plastic vessel for the cell culture and medium. b) shows a top image of one well. It consists of three connected chambers: In the middle chamber (6) resides the sensor (2) and then the cell culture. The side chamber 5 is to pipet new medium in while chamber 7 is to pipet medium out. The chambers are separated by walls of different height. 

There are also commercial available transmitters for this application. It should be remarked though that most of these readers do not generate a continuous field thus may cause trouble powering the plate reliable. There is also the Qi wireless charging standard which can transmit several watts of power continuously. But they require larger, i.e. thicker antenna and the charger will only activate the charging field if it detects a proper client. So the client needs a suitable active chip that communicates with the charger and cannot simply draw power. There are Qi compliant receiver OEM modules that could be used for this purpose. They could be stacked directly on the back of the plate. However, it needs to be tested first if the EM-field will interfere with the measurement. This revision of the PCB has now also a proper battery mount included. The battery is placed on the top side and fits in a space of the multi-well-plate where no wells are. The schematics for it are attached in Appendix D.4. The PCB is depicted in Fig. 4.30. A with sensors half populated plate is depicted in Fig. 4.31. The sensors are equipped with solder balls and soldered to the PCB like a BGA-device. To increase the mechanical stability of the joint an underfill with epoxy is employed. The liquid epoxy is applied to the outline of the chip. Through capillary forces it is pulled under the chip. When carefully dispensed the epoxy does not flow in the center where it would obstruct the sensing area. It also acts as last barrier against liquid that might overcome other seals. This flip-chip packages can be assembled by standard pick-and-place machines and reflow soldered. The electronics of the plate can therefore be manufactured like any other PCB.

A specially designed multi-well part can then be glued on top of the PCB. O-rings are placed in the holes for the sensors. The multi-well part is in contact with the o-rings and compresses them thus forming a tight seal (see Fig. 1.4 for a cross-section). A glue is used to fix the plastic multi-well part to the PCB. This glue is not in contact with the cell culture medium.

**Data Transmission Protocol:** Data is sent from the plate to a computer in a modular format. The binary data from the microcontrollers is base64 encoded. After a comma a CRC16 (CRC-CCITT) checksum is appended in ASCII encoded hex to detect errors in

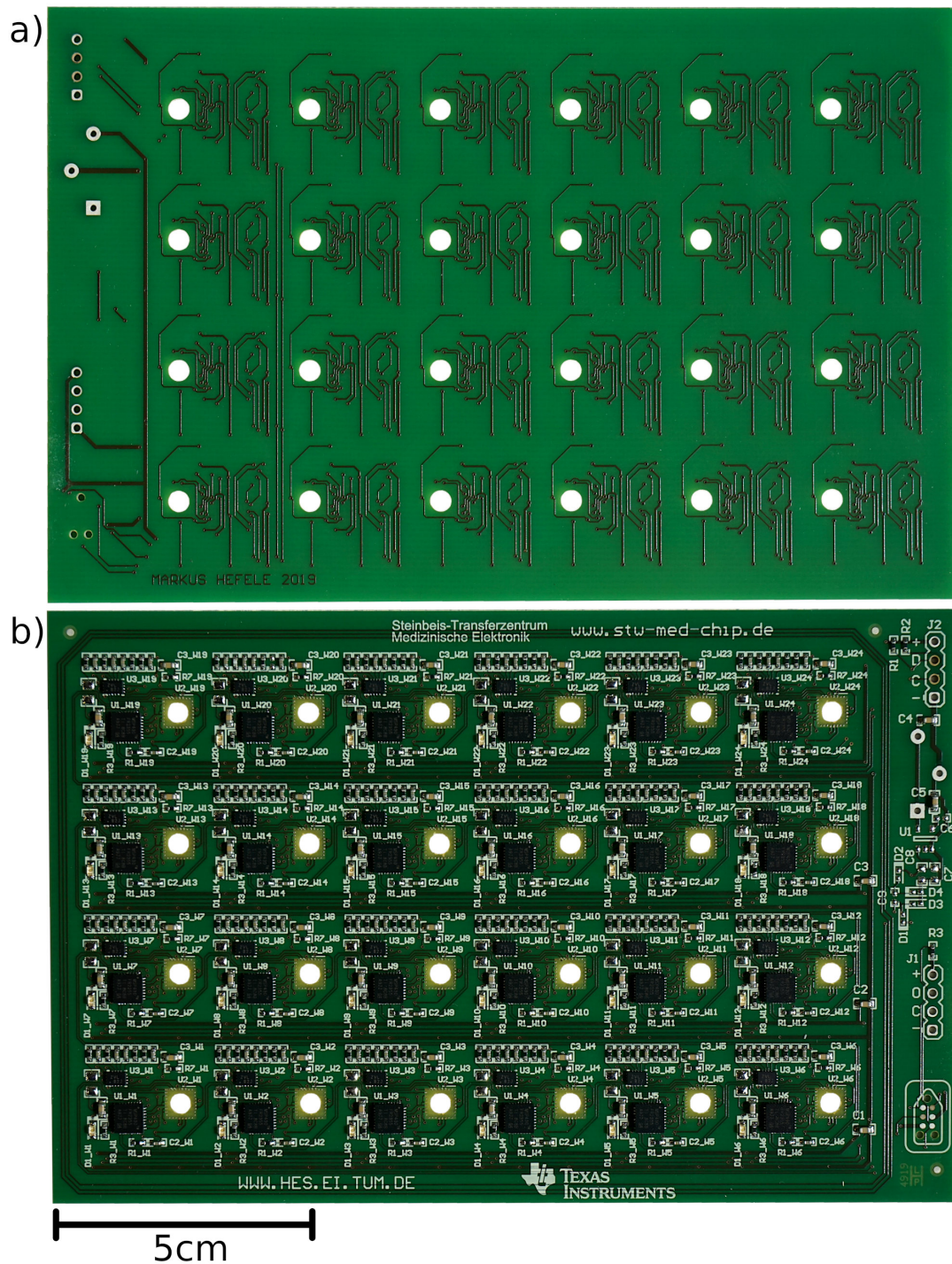



Figure 4.30: Contactless multi-well-plate, layout revision 2: a) shows the top side of the plate. No parts are located here. Only the battery holder can be soldered to the three vias on the top left edge. Through the holes the not yet mounted sensors have contact to the fluidic. b) shows the underside with the electronics for sensor readout. There are 24 identical circuit parts, one for each well. The square IC is the mixed-signal-processor, the smaller one is a multiplexer. In the lower right corner is a tag-connect footprint for programming. There are also two unpopulated legacy pin headers for programming. Around the PCB is a loop-antenna for wireless power experiments. The rectifier and regulator for that are on the right edge in the middle and unpopulated. 

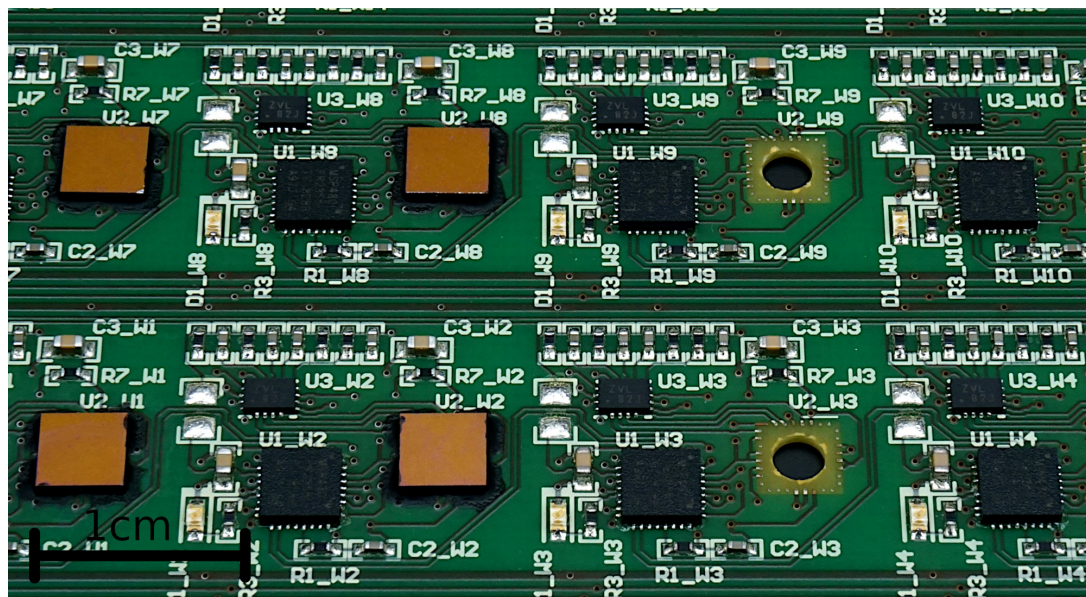



Figure 4.31: Close up of the second revision of the 24-well plate, partially populated with sensors. The gold-brown looking squares are the sensors. They are sealed with an epoxy underfill which is visible as black border. The right half is not populated. 

transmission. The CRC is calculated from the ASCII symbols of the base64 string. More complex methods of error detection and correction are not required: If the sender is in a good range to the receiver the transmission is relatively stable and causes nearly no errors. If the signal is too weak only garbage is received, if any, because the receiver will most likely not create an output pulse. During operation the plate is not moving and in a fixed and defined distance to the receiver ensured by a receptacle guaranteeing a good reception. Therefore a simple CRC is sufficient. Encryption and authentication of the data was omitted, too, because the link has only a limited range and is enclosed in an incubator. There is no real threat model to intercept or manipulate the traffic, also the microcontrollers only have limited processing power.

The described structure is the data block of one controller. Several of these blocks from all controllers of the plate are concatenated and separated by a semicolon. In the begin of the transmission 15 ASCII minus signs are sent to allow the receiver to lock on. The control and preamble characters were chosen to be printable ASCII that do not appear in base64 encoding to easily use string parsing functionality of Python. The raw data stream then also be printed in a terminal. A schematic representation of this format is depicted in Fig. A.1 in Appendix A. An extended version is available to also transmit configuration data (see Fig. A.2 in Appendix A). This is useful for impedance spectroscopy and parameter sweeps to correlate this information with the actual measurement data. The binary data blocks are read directly from the internal I2C registers of the controllers. Their structure is depicted in Fig. A.3 and A.4 in Appendix A.

#### 4.5.4 Receiver

The receiver is build into the base of the pipetting robot under the spot where the multi-well-plate lays. It converts the optical signal to a electrical signal again which can then be directly connected to an UART interface. The schematic of the receiver is depicted in Fig.



4.32, Fig. 4.33 shows a 3D-Model of the designed PCB. It detects fast intensity changes and uses them to reconstruct the original UART signal. A trans-impedance amplifier converts the current from a photodiode to a voltage. The signal is high-pass filtered with a capacitor to remove low frequency parts. Only the fast intensity changes will pass. When the light of the LED is turned on or off this results in a pulse after the high-pass. This signal is then shifted to a DC part of  $V_{dd}/2$  and amplified again. An inverting schmitt-trigger is then used for demodulation. A falling edge results in the output to jump to high, a rising edge to low. Due to the schmitt-trigger characteristic the level is kept till the next edge. The output is again the original UART signal that drives the LED with some minor jitter and delay. The receiver is able to detect data rates up to 57600 bit/s, however, sometimes the first byte is lost. For better link stability only 19200 bit/s are used.

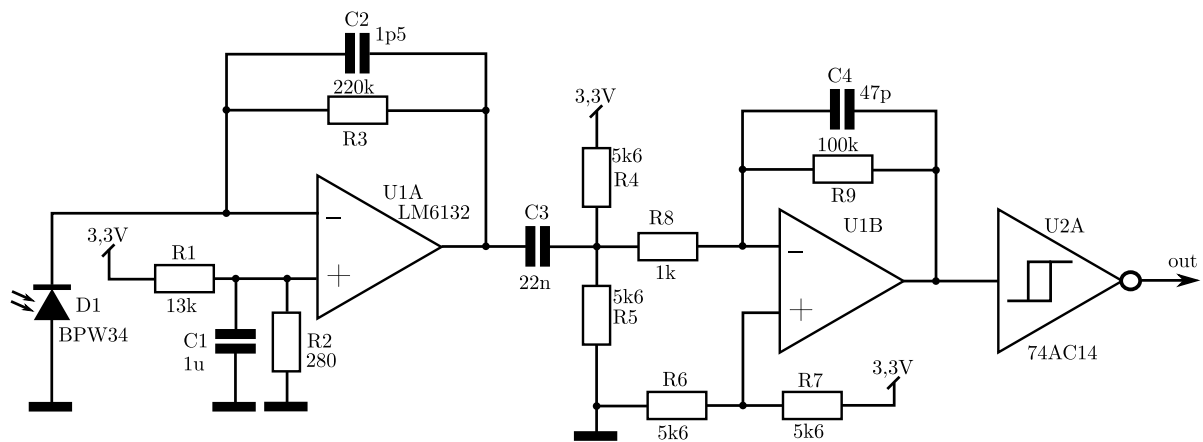


Figure 4.32: Schematic of the optical receiver for the contactless multi-well-plate. The photodiode D1 is connected to an transimpedance amplifier U1A. The signal is then high-pass filtered by C3 and amplified by U1B. A schmitt-trigger U2A is used to detect the either positive or negative edge and store the value.

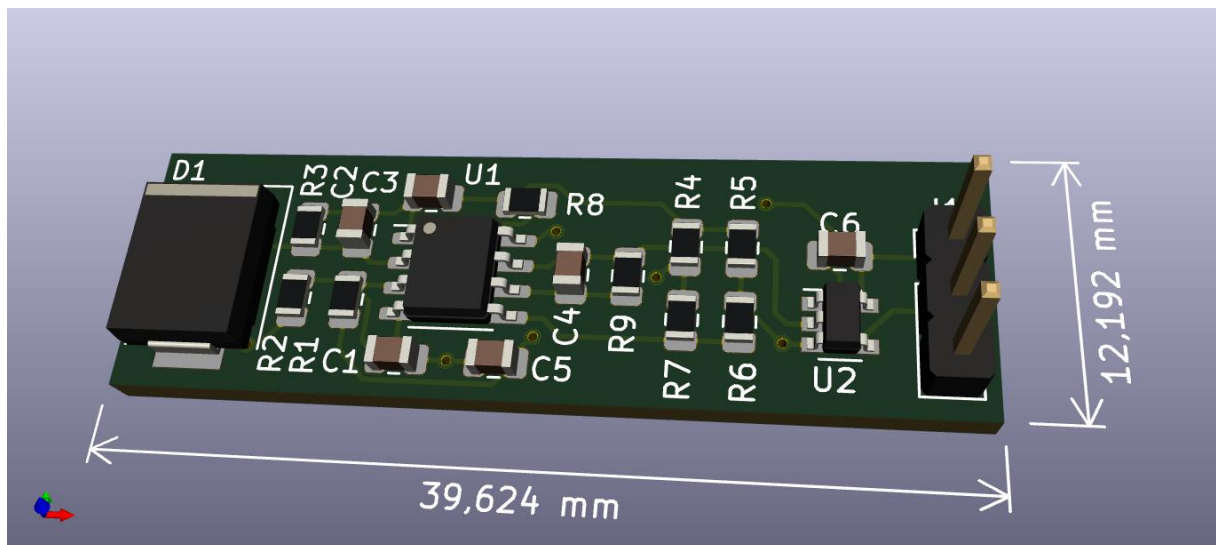


Figure 4.33: 3D rendering of the optical receiver for the contactless multi-well-plate. On the left side the photodiode D1 is placed. U1 is an opamp for amplification. U2 is a Schmitt-trigger for signal reconstruction. The pin header on the right is for supply and data output. Schematic in Fig. 4.32.



## 4.5.5 Software

A small program was written to parse the data stream from the plate and display it in a structured way. Only a ncurses-UI was programmed to have an overview of the current data and not a full fledged GUI with graph plotting. For further processing the data is logged in CSV format with a timestamp. There are already other programs that are much more suitable for this task so reinventing them would be a waste of resources.

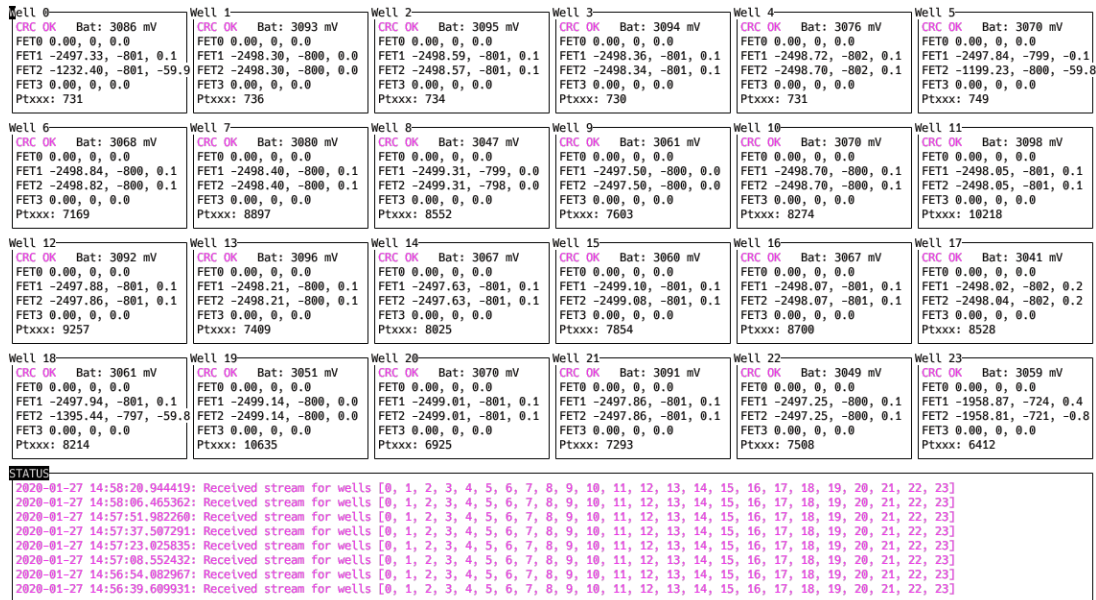



Figure 4.34: User interface for the 24-well-plate (colours inverted). The measurement data for each well is mapped to their respective location. Displayed are the measured battery voltage, the data for the four FETs ( $V_{sg}$ ,  $V_{sd}$ ,  $I_{sd}$ ) and the Pt resistor. The lower Section shows status information, e.g. the latest received data burst. 

## 4.5.6 Electrical tests

### 4.5.6.1 Battery Lifetime

The plate is operated by a battery supply and should be able to run a couple of days from a single coin cell battery. There should be no power connectors as they could corrode and fail in the possible wet lab environment. Therefore power-saving is an important issue for the electronics. The battery lifetime was first estimated by measuring the current consumption of the plate in its different operating states: Standby, measure and transmit. Current was measured with a bench multimeter. Standby current can be measured relatively easy as this state is held for a long time. Measurement and transmit states are more difficult to measure as these states only last a few seconds. To obtain accurate results the firmware was modified to be continuously in measurement mode. Transmit current consumption was measured in a similar fashion. This yielded the current consumption of the different modi. Their actual length was measured with a digital oscilloscope. With these data the charge consumption and thus the lifetime of a battery can be estimated. These results are shown in Table 4.2

Table 4.2: Power consumption of the contactless 24-well-plate during its different operating states used for battery lifetime estimation. Here with a measurement interval of 60 s.

state	current	duration	charge
measure	60 mA	0,1 s	6 mA s
transmit	2,9 mA	1,2 s	3,48 mA s
standby	60 $\mu$ A	58,7 s	3,5 mA s
<b>total</b>	N/A	60 s	13 mA s

The transmit and measurement time are fixed. The measurement interval and thus the standby time can be changed according to the application's requirements. This results in the following function for the battery lifetime depending on the interval:

$$t_{Bat}(t_{Interval}) = \frac{Q_{Bat} \cdot t_{Interval}}{t_{tx} \cdot i_{tx} + t_{meas} \cdot i_{meas} + (t_{Interval} - t_{meas} - t_{tx}) \cdot i_{stby}} \quad (4.9)$$

Together with the measured values from Table 4.2 this function can be plotted: see Figure 4.35.

With this estimation an experiment was conducted with a battery to verify the theoretical results. A CR2032 coin-cell with 200 mA h was connected to the plate and the plate set to a measurement interval of ca. 15 s. The recorded time-stamp for each measurement has a resolution of one second. The mean measurement interval was 14,58 s. The plate sent data back for 198,6 h. The measured battery voltage by the plate is plotted in Fig. 4.36. A few hours earlier when the battery voltage dropped below 2,69 V the plate failed to perform accurate measurements. At this supply voltage there is not enough headroom for the internal reference of 2,5 V. Equation 4.9 predicts with this values an expected lifetime of 291 h. However, the capacity of 200 mA h is stated with an end-voltage of 2 V according to the datasheet of the battery. As the circuit fails at around 2,7 V there is fewer capacity usable from the cell therefore the reduced operation time.

The reduction of current consumption is not only important for a longer battery lifetime but brings also other benefits for the system. The consumed power is eventually dissipated as heat. This will also increase the temperature of the cell culture which is in close proximity. Although the complete system is in a thermally regulated incubator this can cause the cell culture to be warmer than intended. Cells are very sensitive to temperature. Human cells need 37 °C, they may tolerate lower temperature, but will die above 42 °C. Even if the cells get not that hot the increased temperature can alter their metabolism and thus change the results of the assay. Therefore a reduced power consumption of the electronics is beneficial. The average power dissipation at an assumed voltage of 3 V and 60 s interval is for this plate 0,65 mW. For comparison, the handheld biosensor from Schmidhuber [43] has a maximum power consumption of 500 mW. The average power is probably lower but not described in the thesis nor are power saving functions. It can be assumed that the continuous power consumption is therefore in the range of a few hundred mW. And this is only a single measurement device and not 24. The optical reader presented in [130] consumes nearly 1 W merely due to the fact that it uses a lot of high performance opamps and has no circuitry to turn them off in standby. Such a high power consumption can cause trouble for the cells due to the heat. The new contactless

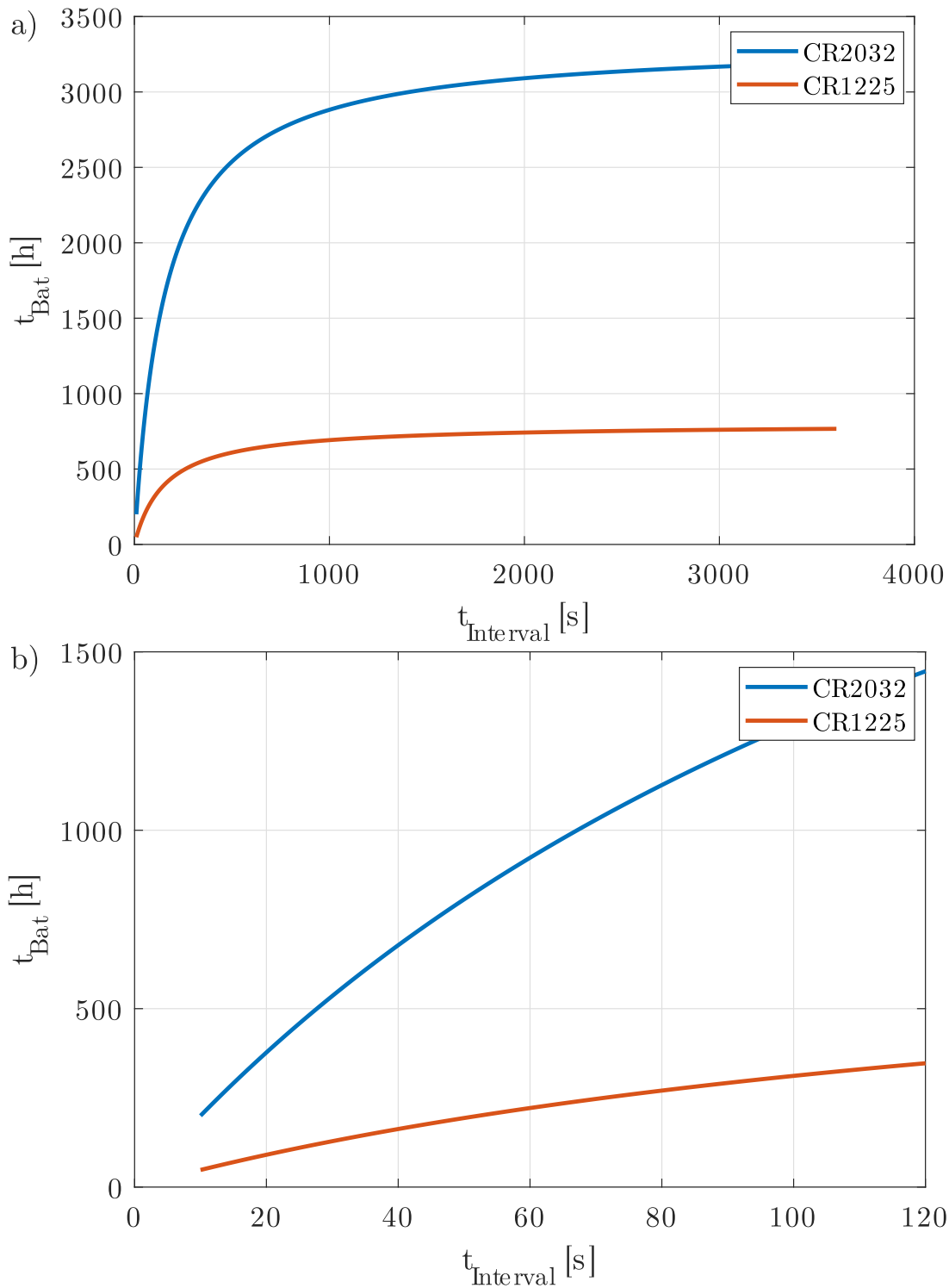



Figure 4.35: Plot of the expected lifetime of two different battery-types (CR2032 and CR1225) for the electronic multi-well-plate depending on the measurement interval according to equation 4.9 together with Table 4.2. b) shows a magnified plot of a). For long measurement intervals the lifetime has an upper bound of about 3200 and 800 hours as seen in a). 

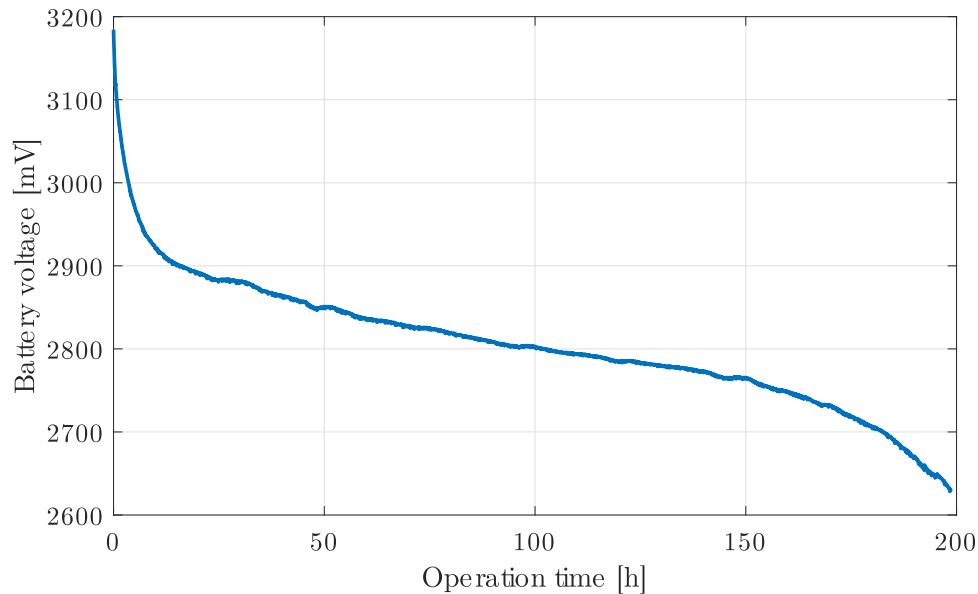



Figure 4.36: Plot of the measured battery voltage of a fresh CR2032 coin cell powering the electronic multi-well-plate which was set to 15 s measurement interval. The plate provided data for 198,6 h before the voltage dropped to low for reliable operation. 

electro-chemical multi-well-plate does not have this issue. Less than 1 mW spread over the size of a postcard will not increase the temperature locally for the cells significantly. For reference: The heated ISFET needs about 500 mW to increase the temperature by 10 °C at an area of less than a square millimeter. A key for this low-power operation is the fact that the controller can easily disable the integrated opamps by simply flipping a bit in a register (as all other peripherals). For external opamps models with a shutdown pin needed to be chosen or their supply pin would be needed to be connected to an IO of the controller. Both ways need an additional IO on the controller and a wire on the PCB, thus more complexity and space.

#### 4.5.6.2 NFC

NFC was evaluated for data transmission and power supply but eventually was not suitable. As stated previously, most NFC readers power the tag only periodically. This is not sufficient to keep the plate operational. Experiments with a self built continuous transmitter were made. But only currents of about 2 mA were achieved. Very large capacitances would be required to buffer the current during the actual measurement cycle. About 30 mF are needed to supply 9 mA s for one measurement and transmit cycle with a voltage drop of 0,3 V. Also, the software for the reader was inconvenient. Therefore this approach was abandoned in favour of a battery.

#### 4.5.6.3 Data Transmission

Data transmission was tested prior to the implementation on the plate. A normal USB-to-UART converter was used for this. The TX line was connected to an LED with a limiting resistor. The RX line was connected to the output of the receiver. A small Python

program was used to generate test patterns, send them via UART and then compare them with the received result. Three different patterns were used: all 0, all 1 and random. They had variable length up to 256 bytes. All 0 and all 1 represent the extreme cases which probably could lead to a receive errors due to their high DC-part. However, this was not observed. Either the connection was good and all patterns were received correctly without any bit errors or all patterns were distorted. There were nearly no random single bit flips detectable. Therefore only a simple CRC16 (CRC-CCITT) was used to detect errors and no sophisticated forward error correction. The connection was stable over a range of about 10 cm depending on the light conditions.

It was discovered that the MSP430 Launchpad which was used as USB-to-UART converter and power supply for the receiver has a quite noisy 3,3 V rail due to the DC/DC converter. This causes serious reception problems. Even a large electrolytic capacitor at the terminals of the receiver cannot filter this. Therefore a supply with a LDO is recommended.

### 4.5.7 Architecture

The architecture of the plate is a central design element of its realization. The main difficulty is the implementation of the readout electronics for multiple sensors for multiple wells at a given space and a reasonable complexity, price and of course accuracy. The chosen solution is to use multiple small, cheap and low-complexity analog front-ends with a microcontroller and connect them to a digital bus (see Fig. 4.27). The contrary approach would use one high performance analog front-end and a multiplexer cascade to switch between the wells and sensors (see Fig. 4.37). The later solution creates several difficulties. The routing of the PCB is more complex as lot's of signal lines need to be routed over the whole board to the multiplexers and the ADC. If the multiplexers are distributed over the whole board their control lines need to be routed, too. A possibility to ease the layout is to create a standard cell for each well which consists of the sensor and a multiplexer. There is one signal wire that runs over the whole board and the multiplexers are used to connect only one sensor at a time to the global signal line. This would require a lot of control-lines for the multiplexers that need to be routed over the whole board. So multiplexers with a digital addressable bus like I2C or One-Wire need to be used. Unfortunately, there is no such device available. Additionally, very few I2C-devices offer more than eight configurable addresses. So, for each well cell a microcontroller as interface between bus and multiplexer is required. A microcontroller can be programmed to interface such a bus and can be assigned addresses freely. Now we have a setup like in this thesis proposed: A microcontroller for each well and a multiplexer. But then the actual analog front-end is still missing. This needs space somewhere: Either it is placed in between the well-cells or at the border of the board. Between the well-cells is at maximum 18 mm space due to the well to well distance. This space is also needed for the routing of power and I2C and the global signal line, reducing it further. Of course, the mux and the controller can be chosen very small and they can be shifted in such a way that more room is available for the rather large chips of the analog front-end and main processor. But this would require the modification of some of the well-cells and therefore render their layout advantage useless. So another possibility is to place them at the border of the PCB. Here some space is available but not much (see Fig. 4.28 for comparison). To leverage the full potential of the *a single layout cell for all wells* approach it seems reasonable to mainly use this cell

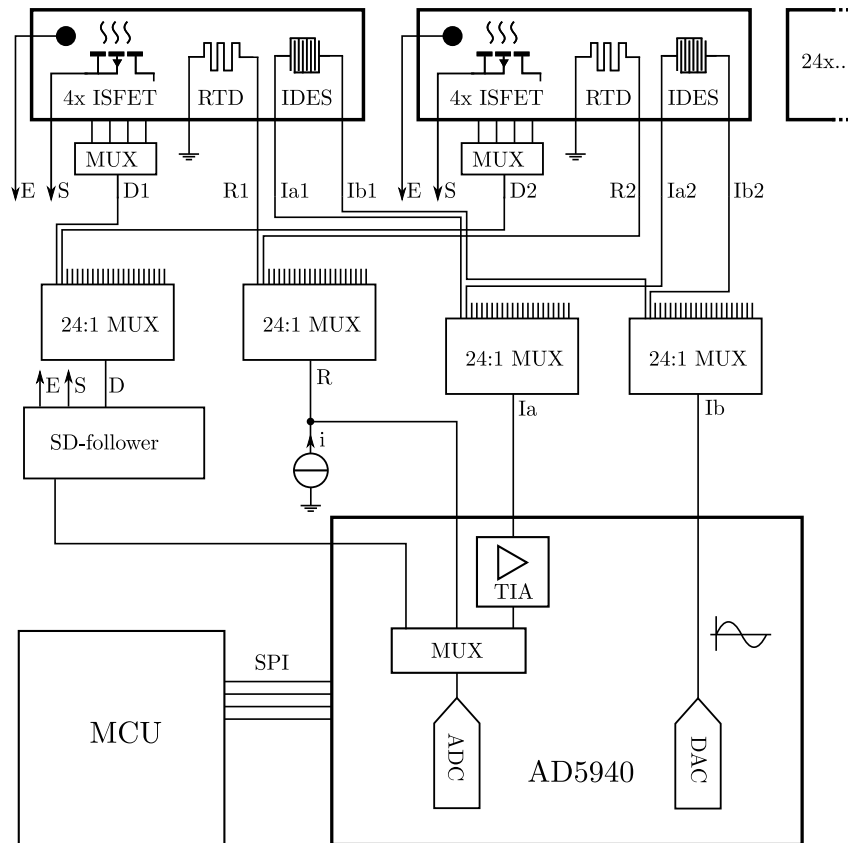



Figure 4.37: Alternative architecture for the 24 multi-well-plate with one high performance analog front-end and multiplexer to connect the sensors successively. In the top row are the 24 sensor chips, each with multiple ISFETs, a thermistor (RTD) and an IDEs structure for impedance measurement. A multiplexer is used to switch between the drains of one sensor chip. Each well is then connected to the read-out electronics. There are some global nets that are common for all sensors: E for all reference electrodes, S for all FET-sources and ground for the RTDs. The other signal lines are connected via four 24:1 multiplexers to the analog front-end: D1-24 for the aggregated drains, R1-24 for the RTDs and Ia1-24 and Ib1-24 for the impedance measurement. For the ISFETs a discrete source-drain-follower (SD-follower) with analog output is used. The RTDs are fed by one current source so a voltage drop can be measured. For the impedance measurement the AD5940 is used. It has a DDS to generate the excitation signal and a TIA to amplify the current from the IDEs. It can also measure the DC-voltages from the ISFETs and RTDs. A microcontroller reads the data via SPI interface and controls the multiplexers. 

and do as little as possible outside of it. So in the end the analog front-end needs to be in this layout cells which is the solution proposed in this thesis.

## 4.6 Auxiliary Software

### 4.6.1 MSP. elegans

MSP. elegans is a software tool to program a chain of MSP430-type microcontrollers.

#### 4.6.1.1 Problem

Microcontrollers need to be programmed: Initially and for updates. Therefore they come with in-system programming and debugging capabilities, usually based on JTAG. For JTAG usually six connections plus two for supply are required. To reduce the number of required connections and thus save space for a large connector there are also serial protocols which only require two data lines (and power supply). The MSP430 series also have a bootloader to download the firmware over a UART or I2C connection. To trigger this loader the two pins of the serial debug interface are also required, so there is no reduction in pin count.

Most applications only have one at most a hand full of controllers on a PCB. Therefore adding a separate header or even only needle test points for each controller's programming interface is not an issue. Furthermore JTAG supports daisy-chaining of devices so that one header can control several chips.

The electronic contactless multi-well-plate requires 24 controllers for a multi-well-plate, one for each sensor. They all need the same firmware. As they are FRAM devices their memory content might be deleted by high temperatures which are required for soldering. Also pre-programming needs to be done by the PCB manufacturer as the semiconductor manufacturer will only ship pre-programmed devices in very large quantities. This means the devices need to be unpacked, put in a socket, programmed and packed again for the pick-and-place machine. Using preprogrammed devices for assembly is therefore not an option. Last, to update the software and to solve program errors in-system-programming capabilities are absolutely necessary.

Programming 24 controllers by hand, i.e. connecting a cable, wait, unplug and connect the next controller is a painstaking process and not suitable for production. Additionally the 24 headers would require lots of space on the PCB. Unfortunately MSP430 does not fully support JTAG daisy-chain mode.

#### 4.6.1.2 Concept

To solve this problem MSP. elegans was developed. Its aim is to program a series of identical controllers with the same firmware using only one program header. The main idea is to use a microcontroller to program its neighbour. This requires only two GPIO-pins of the controller to be connected to its neighbouring controller's debug pins. The first controller in this chain is programmed with a PC-based programmer. Then the programmer is used to load MSP. elegans into the RAM. There this program is then started. It programs the next controller, making an exact copy of itself including the original firmware in FRAM and MSP. elegans in RAM. Afterwards it starts the new controller which then programs its neighbour and so on. An interaction with the PC-based programmer is no longer required.

MSP. elegans is based on the REPLICATOR (REP430F) [160] by TI. This device uses a MSP430 to program other MSP430s. Its firmware is distributed under a three clause MIT license. All non-essential functions were stripped to fit in 4KB, some additional functions were written to copy the FRAM and the RAM to the target. The parameters for the MSP430FR2355 and the multi-well-plate are currently hard coded in these functions, but



can also be parametrized to ease the adoption to new controllers. This also includes the LED which the controller turns on when it has finished programming its neighbour. This LEDs help the operator to check the process of the programming.

As the invocation of MSP. elegans still requires some manual tweaks with the programming software a way to integrate it into the firmware was created. MSP. elegans is compiled and the output binary is converted into a hexdump which is then placed in a constant of the target firmware. The firmware has a function that when triggered via an I2C-command will copy this binary blob in the RAM and executes it. That way a normal production programmer can be used to program the first controller. Then only a simple I2C-command is required to trigger MSP. elegans. This is easier to automatize than some special commands for the debugger required previously.

#### 4.6.1.3 Limitations of MSP. elegans

MSP. elegans requires a minimum of 4 kB RAM to implement all required functions. Some of them could be put into FRAM and then remain there but then this FRAM is no longer available for user code and MSP. elegans needed to be integrated into the user code. If it runs from RAM alone user code development and MSP. elegans development can be completely separated.

All controllers in the chain need to have the same firmware. This usually also requires that they are the same model. There is a limited possibility to individualize the controllers, e.g. by programming an increasing number at one memory address.

Also the programming takes some time. Copying the 32kB FRAM and 4kB RAM takes about 45s. The whole plate with 24 controllers take about 20 minutes. This might be annoying while development but is not an issue during production. After the process is initialized the plate only needs power and does the rest on its own. The programmer can then be used to initialize the next plate which takes about a minute and so on. For debugging it is advisable to do this with the first controller which has a direct debugger interface. Only when the software works there correctly MSP. elegans<sup>8</sup> should be invoked.

---

<sup>8)</sup> Yes, this is a reference to C. Elegans; They are both worms...



# 5 Results and Discussion

This chapter contains the results of the measurements of the sensors with the previously described electronics together with a discussion. First the pure sensor performance is shown, then in conjunction with the self developed analog front-ends and then the multi-well-system. Finally the first results for the thermally referenced ISFETs are presented.

## 5.1 Temperature Measurement

MOSFETs can be used as temperature sensors (see Section 3.6.3) when interfaced with the ISFET readout circuit. All ISFET sensor chips also have at least one MOSFET for test purposes which can then also be used to monitor the temperature on the chip. This is important because the cells will behave differently at different temperatures. It is a double check that the conditions for the cells were right and the incubator worked correctly. This MOSFET is also used to verify that the interface circuit is operating properly.

A multi-well-plate equipped with eight sensors (gen1) was placed in a thermo cabinet and subjected to different temperatures. The  $V_{sg}$  of the MOSFETs was recorded via I2C. The cabinet (CTS,  $-40\text{ }^{\circ}\text{C}$  -  $180\text{ }^{\circ}\text{C}$ ) was set to a staircase temperature profile. After each change it took several ten minutes to settle and  $V_{sg}$  to stabilize. The curve for one MOSFET is plotted in Fig. 5.1. The other MOSFETs showed a similar signal but each with a different offset. Fig. 5.2 shows the average  $V_{sg}$  versus the temperature together with a linear fit. There are also errorbars in this plot showing the standard deviation. But the deviation is only about  $100\text{ }\mu\text{V}$  so they are not visible at this zoom factor.

For each of the eight sensor chips on the plate the linear fit was calculated. One sensor was broken and returned data with very large noise. The noise for all other sensors was  $\sigma \approx 100\text{ }\mu\text{V}$ . A measurement was triggered every two seconds.

The results for the linear fit according to  $V_{sg} = m \cdot \theta + o$  for all seven sensors are shown in Table 5.1. Here  $\theta$  is the temperature in  $^{\circ}\text{C}$ ,  $m$  is a linear factor in  $\text{mV}/\text{K}$  and  $o$  is  $V_{sg}(\theta = 0\text{ }^{\circ}\text{C})$ . The average of the sensitivity is ca.  $2\text{ mV}/\text{K}$  which is a typical value for such a sensor. They are also nearly the same for all seven sensors. The offset  $o$  has a larger deviation. For an application the sensors need to be calibrated to compensate the offset. Then the precision of the temperature measurement is  $\sigma_{\theta} = \sigma_{V_{gs}}/m \approx 0,1\text{ mV}/(2\text{ mV}/\text{K}) = 0,05\text{ K}$ . The maximum error of the real  $V_{sg}$  values compared to the fit is ca.  $1\text{ mV}$  translating to an error of  $0,5\text{ K}$ . This error is for the lowest temperature of  $25\text{ }^{\circ}\text{C}$ , between  $30\text{ }^{\circ}\text{C}$  and  $40\text{ }^{\circ}\text{C}$  the error is only about  $0,1\text{ mV}$  or  $0,05\text{ K}$ .

This measurement data is by the design of the experiment not obstructed by errors or effects of the chemical system, only the pure electronic parts have an influence. These results show that the analog front-end for the ISFETs is fully operational and capable of delivering data with the required precision to accurately measure a  $V_{th}$  change of sub-mV.

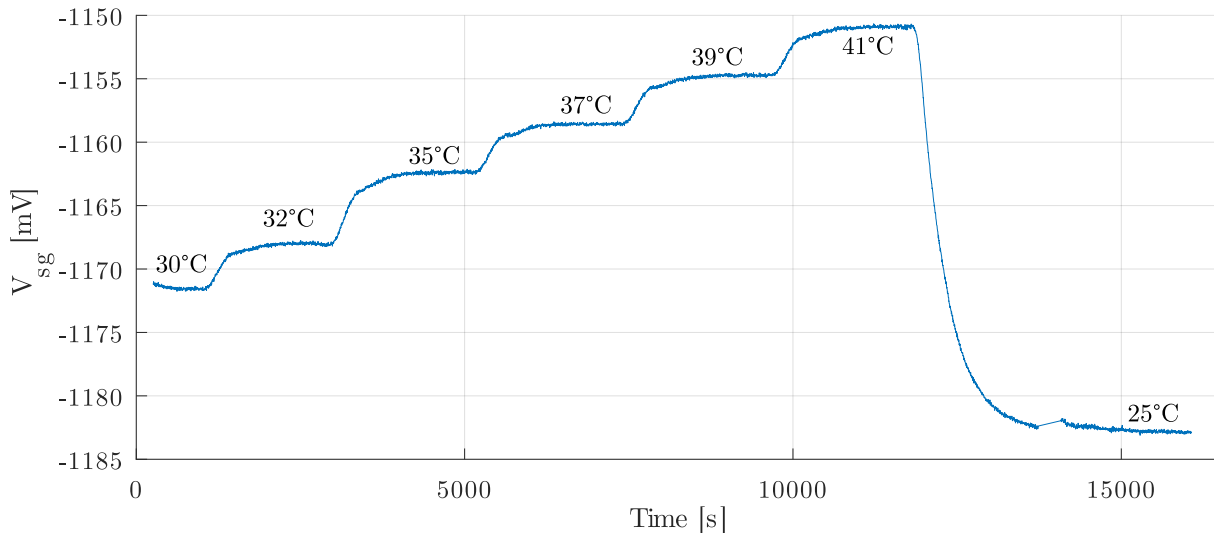



Figure 5.1:  $V_{sg}$  of a MOSFET connected on the multi-well-plate to an ISFET-readout and subjected to different ambient temperatures. The whole plate was placed in a thermo cabinet which took several minutes to adjust the temperature (fast change in curve). After the air temperature was stable the thermal mass of the plate needed some minutes to adopt the new temperature (slow change in the curve). When a stable point was reached around fifteen minutes of samples were used to calculate an average before programming a new temperature. 

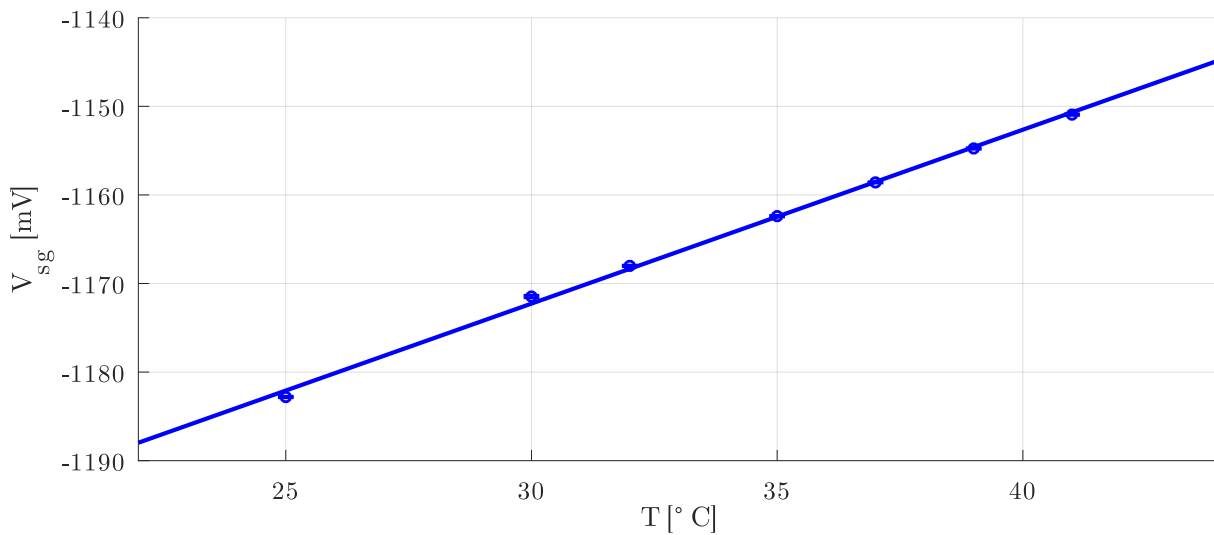



Figure 5.2: Temperature vs.  $V_{sg}$  of a MOSFET connected on the multi-well-plate to an ISFET-readout and subjected to different ambient temperatures. Data points are marked with a circle and a linear fit is applied. The datapoints do have errorbars which represent  $1\sigma$  of the raw signal but  $\sigma \approx 100 \mu\text{V}$  so they are not visible. 

Table 5.1: Results of the linear fit for the temperature dependence of  $V_{sg} = m \cdot \theta + o$  of MOSFETs integrated on seven sensor chips that were placed on an electronic multi-well-plate.

sensor	$m$	$o$
1	1,9874 mV/K	-1275,0 mV
2	1,9501 mV/K	-1498,3 mV
3	1,9707 mV/K	-1242,2 mV
4	1,9631 mV/K	-1231,2 mV
5	2,0234 mV/K	-1291,4 mV
6	1,9552 mV/K	-1436,1 mV
7	2,0166 mV/K	-1460,3 mV
mean	1,9809 mV/K	-1347,8 mV
std	0,0293 mV/K	112,79 mV

The pH dependence of the ISFETs is about 20 times higher than their temperature dependence, about 40 to 50 mV/pH. So in theory this allows a pH resolution of 0.0025 pH steps neglecting the additional noise of the ISFETs due to electro-chemical effects. It is also possible to monitor temperature in the physiological relevant range around 37 °C with high precision with this system and the manufactured MOSFETs.

## 5.2 PdH electrode

Different methods for the creation of a PdH electrode were tested by Daniel Kaindl [147] for his Master's Thesis. It was possible to charge the electrode with hydrogen by electrolysis and it was stable for some hours with one charge. Afterwards it could be recharged. It was also observed that dissolved oxygen in the electrolyte lead to unstable behaviour. This can be countered by either purging the electrolyte with nitrogen or by enlarging the surface area of the electrode through the deposition of Pd-black as described in literature [123]. Then the PdH electrode has a pH dependent potential with about 58,2 mV/pH. At high pH-levels around 11 there were some minor deviations from the ideal curve. Depending on the electrode geometry a lifetime up to 2 days was possible in continuous operation. The electrode was recharged every couple of hours which lead to some wear. Detailed results are reported by Daniel Kaindl in his Master's Thesis [147].

Due to the stated pH dependence the electrode is unsuitable as reference electrode for pH measurement. However, it is possible to use it for applications where a reference electrode is needed e.g. reduction potential measurements provided the pH was determined previously with a different sensor. Here the temperature referenced ISFET can be used. The integration of the Pd however still needs some engineering. Probably the easiest way is to use a Pd bond wire and attach a loop on the chip. This needs to be coated with Pd-black though which requires a galvanic process step then.

## 5.3 ISFETs

An Optoi ISFET was used to test if the developed circuits fulfil their intended use. It was sequentially dipped in beakers with different pH-Buffers together with an Ag/AgCl-reference electrode. While in transfer the circuit is open and therefore a spike occurs in the signal. The same procedure was performed with the integrated MSP430 AFE and the DemoBoard to compare them. The results shown in Fig. 5.3 look very similar. The absolute voltage values for the pH steps are very slightly different due to the drift of the sensor and the fact that the operation point set by the DemoBoard and the FR2355 were not exactly the same. Especially a different drain-source current can cause a different  $V_{gs}$ . The largest difference occurs for the pH4 buffer. The results are summarized in Table 5.2. The relative deviation in the sensitivity which are up to 7 mV/pH cannot be explained with different operation points and are probably caused by some parasitics in the front-end, e.g. the different multiplexers used.

However, both circuits work and are suitable to read ISFETs. In practical applications this difference between the two variants are no issue as every sensors needs to be calibrated separately. During this calibration possible deviations of the front-end can be cancelled too. The MSP430FR2355 variant however is much more cost effective and compact.

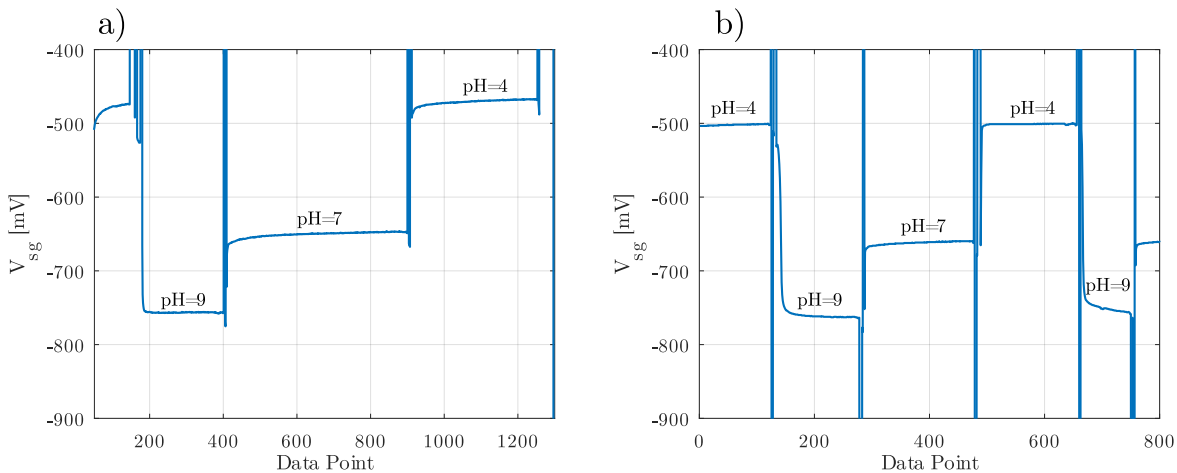


Figure 5.3: Direct comparison of the DemoBoard and the FR2355-based ISFET readout with an Optoi-ISFET and an Ag/AgCl reference electrode. a) is recorded with the DemoBoard and shows the reaction of the ISFET to three different pH-Buffers (9, 7, 4). Between buffers there is a positive spike because the ISFET was transferred between different beakers. b) shows the result for the FR2355 front-end with the same ISFET and the same buffers but slightly different timing. Here not only a positive spike but also a negative spike is visible. The absolute voltage levels for the pH levels are also slightly different due to drift and slightly different operating points although it was taken care to set them identical. b) adapted from [155] with permission, ©2019 IEEE.

TI ISFETs were tested with the automated test setup (gen 2) and with three pH-buffers: 4, 7, 9 in that order. The cycle time for each buffer was usually a couple of minutes to speed up testing. An example of such a measurement result is depicted in Fig. 5.4. The sensitivity is between 35 and 51 mV/pH as expected for  $\text{Si}_3\text{N}_4$ . The three different ISFETs on the chip all have a similar sensitivity. However, the relation between pH and voltage is not linear. The sensitivity from pH4 to pH7 is around 35 mV/pH compared to 43 mV/pH from pH7 to pH9. The drift between the cycles is in the range of 2 mV. In the beginning it is higher as the chip was dry before testing. This *soaking* behaviour was observed with

Table 5.2: Comparison of the two ISFET readouts (MSP430FR2355 and DemoBoard) with the same ISFET.

pH	$V_{sg}$ MSP430FR2355	$V_{sg}$ DemoBoard
pH4	-500,49 mV	-467,86 mV
pH7	-659,79 mV	-647,49 mV
pH9	-762,33 mV	-756,21 mV
pH4-pH7	159,3 mV	179,63 mV
pH7-pH9	102,54 mV	108,72 mV
pH4-pH9	261,84 mV	288,35 mV

all ISFETs. When first tested the drift was quite high and gradually decreased while the device was wet. When referenced against a Pt electrode (see Fig. 5.4b) the pH to voltage relation is no longer unambiguous. This is due to the changing potential of the Pt electrode that is added to the pH dependent ISFET voltage. Fig. 5.5b shows the Pt electrode vs. the Ag/AgCl-electrode.

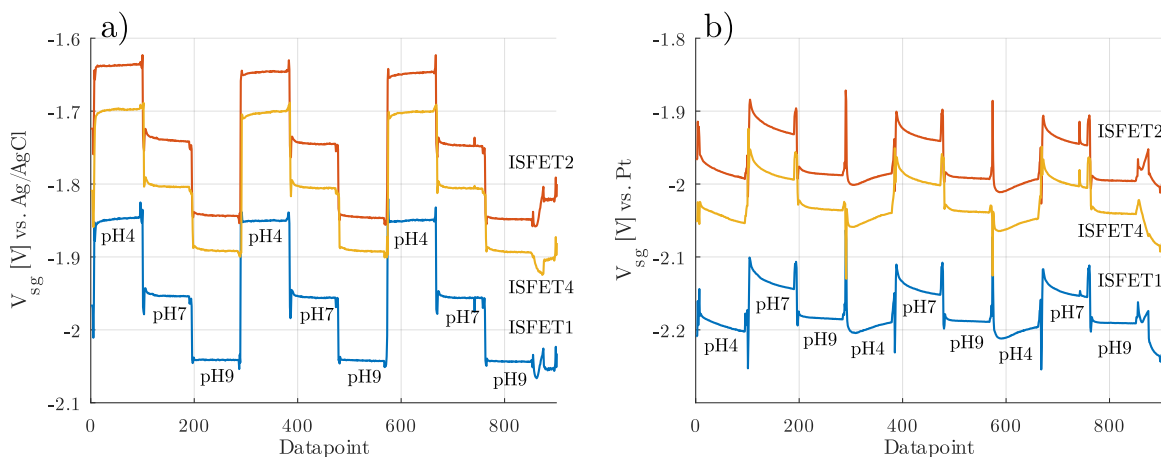



Figure 5.4: Exemplary measurement of a gen1 TI-ISFET sensor chip with the buffers pH4, pH7 and pH9 recorded with the DemoBoard. There are four ISFETs on the chip, one is affected by a punch through and therefore not usable. The three working ISFETs are plotted: in a) vs. the Ag/AgCl reference electrode and in b) vs. the Pt-electrode that is used to force the electrolyte. 

In total around 100 chips from different production lots were tested. Early samples had a systematic issue with their passivation that would break after about 20 minutes with voltage applied. This created leakage currents into the electrolyte. With a reference electrode this was not an issue as its potential could tolerate those little currents in the nA and even  $\mu$ A range. Therefore this issue was not detected for some time. However, the reference electrode was slowly damaged. In contrast, when using a Pt electrode the potential was severely affected. Later versions of the chip were manufactured with an improved process flow and are more stable. However, also from the latest gen1 batch there are some leaky chips. Around one third of these chips are either dead from the start or broke down shortly after testing.

To detect this leakage with the DemoBoard a program in the domain specific language was developed by Ernst Müllner to create a slow triangular signal to bias the FETs.

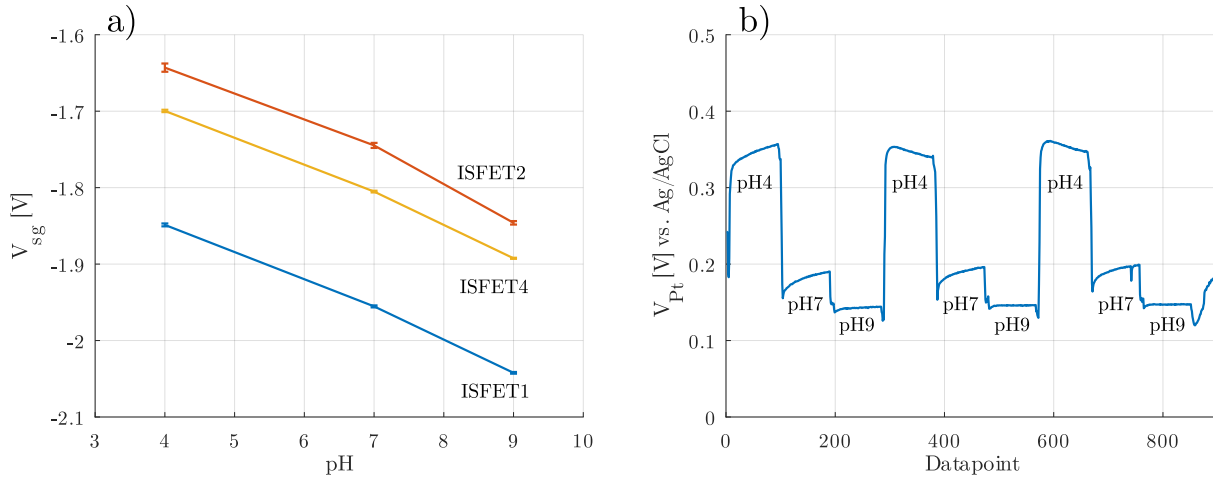


Figure 5.5: a) pH vs.  $V_{sg}$  of the ISFETs plotted in Fig. 5.4. The curve is slightly bent indicating a not perfect linear pH sensitivity. It is between 35 and 43 mV/pH. b) Potential of the Pt electrode vs. the Ag/AgCl reference electrode. Depending on the buffer a different voltage emerges. This voltage is then overlaid with the pH dependent voltage change of the ISFET resulting in the curve of Fig. 5.4b.



Two different frequencies were generated simultaneously, one was fed to the gate of the MOSFETs and the other to the ISFETs' reference electrode. This triangular signal then shows up in the  $V_{sg}$ -signal. If the chip is working properly, the MOSFETs' and the ISFETs'  $V_{sg}$  show their respective waveform. In case of some leakage through the passivation, the two waveforms are superimposed on the ISFETs' signal. This usecase again shows the versatility of the DemoBoard and its possibility to adapt to new requirements.

For systematic tests the automated waferprober was intended as it is able to quickly test a huge amount of sensors to yield statistical good results. Also, the very expensive and time consuming packaging with ceramic packages can be circumvented. The bad chips could be discarded before packaging. However, the construction of such a prober is very challenging and took now almost four years. First wet measurements with the prober started recently but there are still some issues preventing stable operation required for mass testing.

### 5.3.1 Parameter Sweep

The parameter sweep was also tested on the multi-well-plate with the sensor chips (gen1). All combinations for  $I_{sd} \in \{-20, -30, -40, -50, -60, -70, -80\} \mu\text{A}$  and  $V_{sd} \in \{-400, -450, -500, -550, -600, -650, -700, -750, -800\} \text{mV}$  were set and measured for all controllers on the plate. The MOSFETs showed the expected results (see Fig. 5.6). Working and defective devices are clearly distinguishable. The ISFETs however, did not give such a nice graph as their  $V_{sg}$  in conjunction with the Pt-electrode was at the limit of the AFE (see Fig. 5.7). Although, they also form distinct cluster. It is therefore possible to do basic functionality checks in-system to determine if the plate and single sensors are working. Non-functional plates can be discarded. If only some sensors are non-functional they can be excluded from the experiment to avoid spoiling the results and scraping the whole plate. This self-check is not only feasible for the manufacturer but also for the user. With the MOSFETs quick dry tests are possible before starting the more



elaborated wet test of the ISFETs. When the MOSFETs on a chip do not work this is usually a bad sign for the ISFETs too.

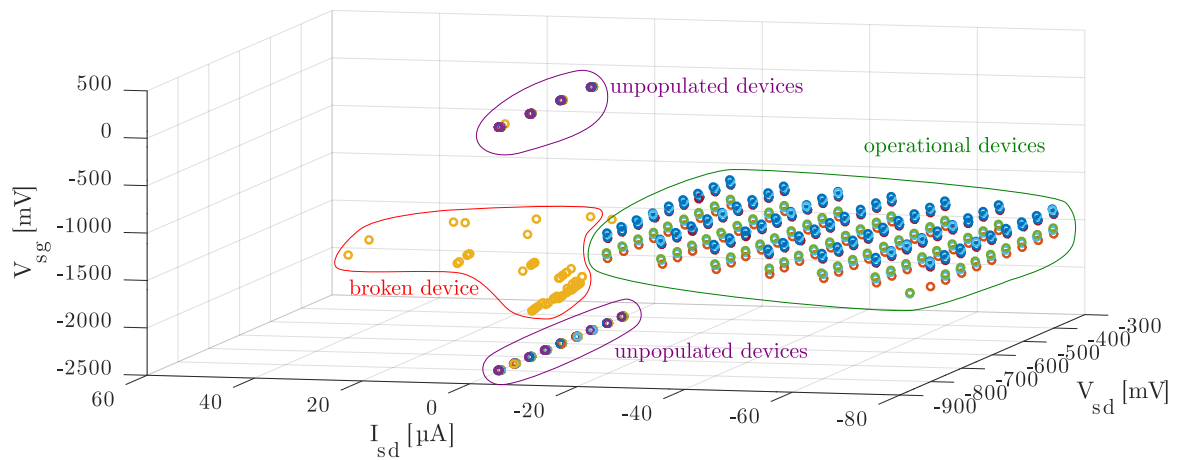



Figure 5.6: Parameter sweep of the MOSFETs of a partly assembled multi-well-plate. The different devices are marked with different colours. AFEs without a sensor chip assembled form two clusters at  $I_{sd} = 0$ . Functional devices form the large structured cluster on the right middle. One device is scattered all over the left half - it is broken. 

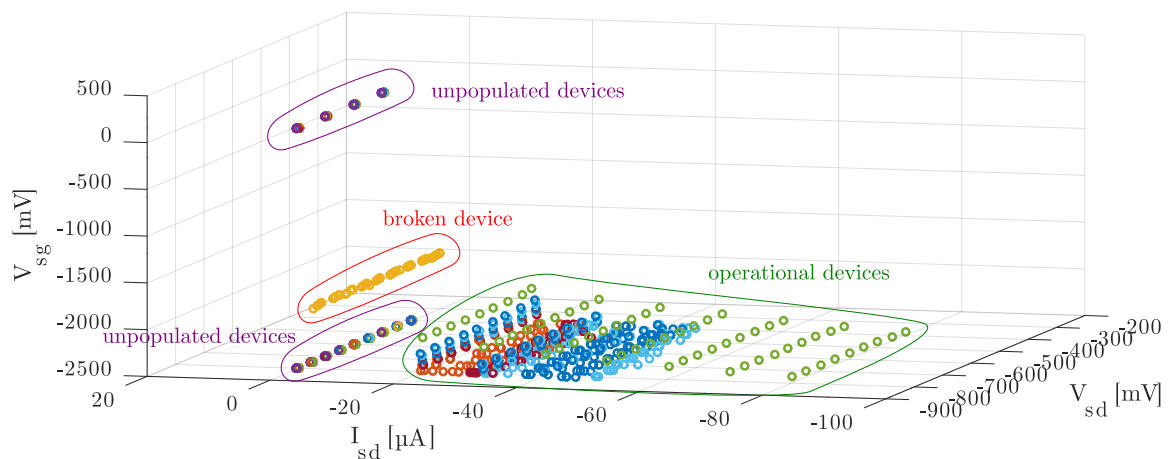



Figure 5.7: Parameter sweep of the ISFETs of a partly assembled multi-well-plate. The different devices are marked with different colours. Here again AFEs without a sensor chip assembled form two clusters at  $I_{sd} = 0$ . The broken device is this time a cluster at  $I_{sd} = 0$  and  $V_{sg} = -1,9$  V. The operational ISFETs again form a grid like cluster in the right half, however, their  $V_{sg}$  is a bit low so that the AFE cannot drive them properly. This can be caused by the Pt electrode that is used to drive the electrolyte. For at least one device the typical FET behaviour is visible, though. 

### 5.3.2 O2FET

O2FETs were tested with the automated fluidic test setup (gen 2). One part of the PBS (VWR Chemicals) was bubbled with nitrogen to remove all oxygen. The second part of the PBS was shaken in a bottle with air repeated times with the cap opened in between to obtain full air oxygen saturation. A third part was bubbled with oxygen from an oxygen concentrator to achieve about 400-500% saturation. These solutions were tested

with a Fibox 2 dissolved oxygen meter to verify the success of the preparation. It can be observed that due to the nitrogen atmosphere used to pressurize the bottles to pump the liquid the dissolved oxygen concentration of the samples will reach almost zero after some time. Therefore the solutions were prepared fresh before each experiment run. In longer experiments the gradual decrease of oxygen in the samples is visible in the data.

First measurements were conducted with the DemoBoard as it is easier to implement new auxiliary waveforms, has more independent voltage outputs, a wider range for the ISFETs and can monitor multiple of them. In case one of them does not react there are still others on the same chip that are monitored simultaneously.

The generated data shows a large change in  $V_{sg}$  when the reduction voltage is switched. To calculate a value corresponding to the oxygen concentration from this raw data the last  $V_{sg}$  before the start of the reduction and the last  $V_{sg}$  during reduction are subtracted. An example is plotted in Fig. 5.8 with markers showing these values. This gives the value  $\Delta V_{sg}$  that is used for further analysis. It is around 1 V. For higher oxygen concentrations the difference is larger.

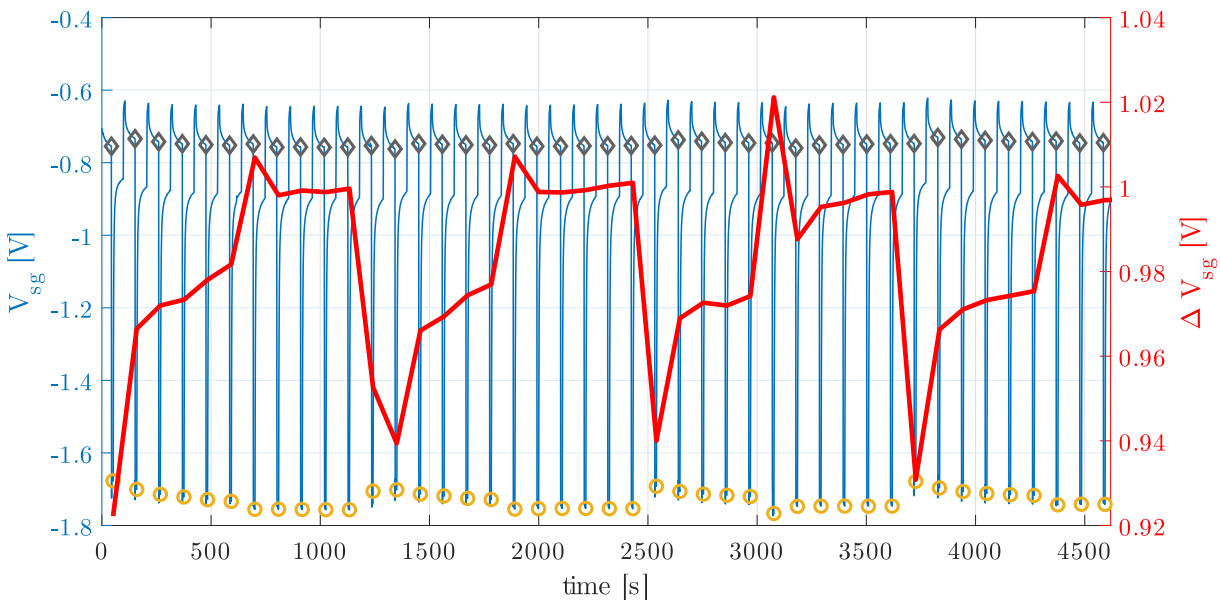



Figure 5.8: Raw and processed data from the O2FET. The blue line shows the raw output signal of the FET. The change due to the periodically applied reduction voltage is clearly visible as spikes. The last reading before the application of the bias and the last reading during it are used to calculate the oxygen content. These points are marked with a grey diamond and a yellow circle respectively. The difference of these values is plotted as the red overlaid curve. A higher difference corresponds to a higher oxygen concentration. 

Literature states that the required voltage for reduction is  $-600\text{ mV}$  at the platinum electrode [92]. But this is referenced to an  $\text{Ag}/\text{AgCl}$  electrode. When using two platinum electrodes a larger difference is needed to start the reaction due to a different electrode potential of the Pt. To find an appropriate voltage that starts the reduction but does not cause electrolysis of water or corrosion of the electrodes different voltages in  $100\text{ mV}$  steps were tested. Fig. 5.9 shows such a series in the range of  $1,1\text{ V}$  to  $1,6\text{ V}$ . One oxygen measurement was performed at the lowest voltage, the next oxygen measurement was then performed at the next higher voltage and so forth. The buffer on the sensor was changed between  $0\%$  and  $100\%$  oxygen concentration so that at each voltage step at least

two measurements were performed for the concentration. For the lowest voltage of 1,1 V no oxygen signal is visible. For higher voltages a square-wave pattern is visible. This pattern indicates that roughly 1,2 V are enough to reduce oxygen. For higher voltages the amplitude of this square-wave pattern is higher. For subsequent experiments 1,4 V were used to ensure that the potential is definitely over the threshold, a high sensitivity is achieved and the potential is not yet dangerously high to cause electrolysis or electrode corrosion. The critical voltage for electrolysis is around 2 V.

To bring the Pt-electrode in a defined state after the reduction a reverse potential of 900 mV is applied after the FET has been read. This helps reducing the drift of the Pt-Electrode which is used as reference for the TI sensor chips. The effect of this measure is depicted in Fig. 5.10a. Fig. 5.10b shows the difference voltage and the oxygen concentration have a linear relation.

The MSP430FR2355 can also be used to read an O2FET. Fig. 5.11 shows an exemplary oxygen measurement.

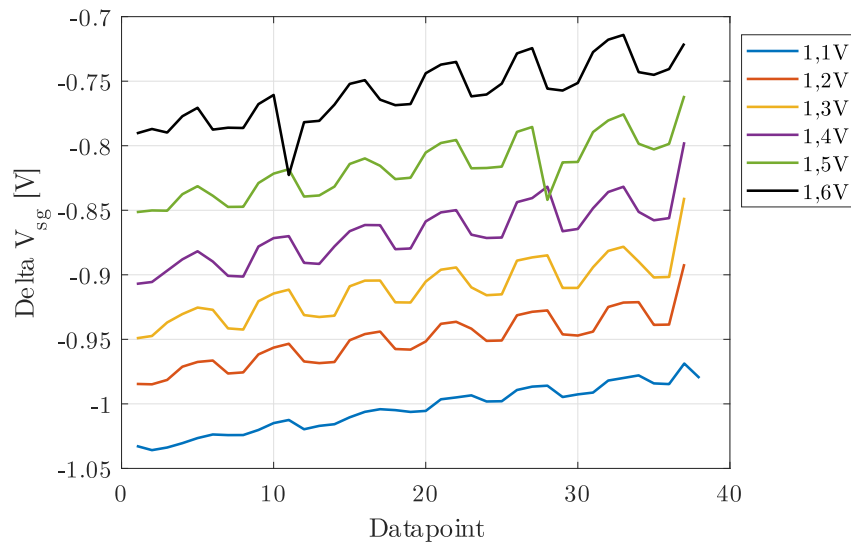



Figure 5.9: Effect of different reduction potentials on the sensitivity of the oxygen measurement. For a potential of 1,1 V or below there is now square-wave pattern visible in delta  $V_{sg}$  caused by a periodical change of the oxygen concentration between 0 and 100% in the liquid. The amplitude of the oxygen signal is slightly higher for higher reduction voltages. Higher voltages were not tested to avoid electrode corrosion. 

## 5.4 Cell Culture Measurements with the Plate

The first prototype of the plate (layout revision 1, see Section 4.5.2) was tested with L929 fibroblasts. The plate was cleaned with alcohol and then sterilized with UV-light under laminar flow.  $10^5$  cells were seeded in DMEM in each well that was equipped with a sensor. The cells were then incubated for 24 hours in a  $\text{CO}_2$ -incubator. After the incubation period the DMEM was replaced with an unbuffered medium (DMEM-base + glucose) so that the change in pH would not be compensated by the buffer. The plate was hooked up in a test fixture, the electronics activated and the measurement data recorded. The medium was refreshed every 10 to 20 minutes. After some cycles Triton-X-100 was added

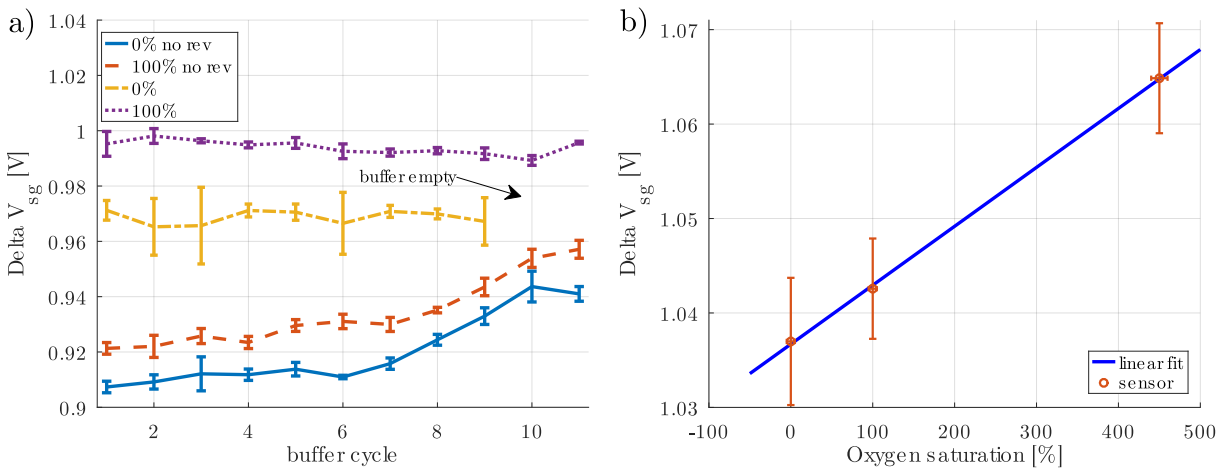



Figure 5.10: a) is a comparison of two O2FET measurements with alternating 0% and 100% oxygen saturated buffers. One experiment was conducted with, the other without the application of a reverse potential. Plotted is the delta of the source-gate-voltage before and after reduction. Without the reverse potential this difference is more unstable than with. b) shows the linearity of the O2FET tested with three buffers with 0%, 100% and 450% oxygen levels. Multiple values were collected for each concentration. The error-bars show the standard deviation. 

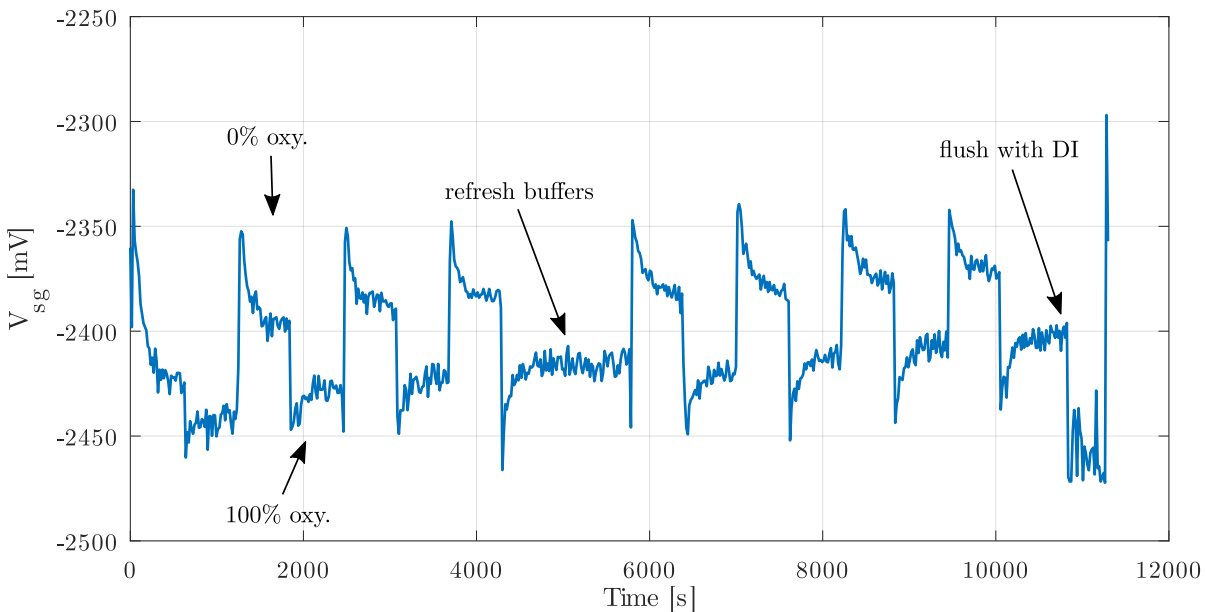



Figure 5.11: O2FET measurement with the MSP430FR2355 and a TI-Sensorchip gen1. With the automated teststand (gen2) PBS with 0 and 100% oxygen was applied to the sensor in alternation. After a few cycles the two PBS bottles were mixed, split again and prepared again with their oxygen concentrations (marked in the graph). Afterwards the measurement cycle was repeated. Plotted is  $V_{sg}$  shortly after the reduction voltage had been applied. The on-chip Pt electrode was used as pseudo-reference. 

to some wells and the cycling of the medium continued. The Triton-X-100 should destroy the cells changing the data pattern of the sensors. However, the expected signal could not be observed. It should look like a sawtooth: When fresh medium is added the pH and O<sub>2</sub> levels should be reset and then change in a more or less linear slope till the next medium change. No such pattern was measurable. Optical inspection after the experiment did not show evidence of a confluent cell layer growing on the sensors that were not treated with Triton-X-100. On sensors treated with Triton-X-100 there should be no more intact cells and none were observed. It is suspected that there is a cytotoxic component still in the plate, probably the epoxy that was used to seal the first generation of sensors. The experiment was repeated, this time with the plate being incubated with only DMEM+FCS before the cells were seeded to saturate toxic binding sites in the epoxy. However, this was not successful, the observations were the same.

The multi-well body and the glue used to attach it to the sensors are biocompatible. The only remaining component touching the cells are the sensors. The die itself should only expose Si<sub>3</sub>N<sub>4</sub> and Pt which should be biocompatible. The sensors were also thoroughly rinsed before use so there should be no residues from production. The only possible non-biocompatible material is the epoxy used to seal the packages. There is no statement from its supplier about its biocompatibility. However, there was also no alternative to this material as this process was done by an external contractor who was able to perform this process. It can be concluded that the used batch of sensors were not suitable for cell cultures. A different and better packaging is required. A very promising solution is the described flip chip approach with o-ring. In this package the liquid only touches the sensor surface, the o-ring and the multi-well body and probably an adapter. The adapter can be made from a biocompatible material such as PEEK or PS. There are also biocompatible o-rings made of EPDM, FKM or silicone.

## 5.5 IDES

An old TUM-biochip was tested with the MSP430 based analog front-end as the new chips with IDES were not yet available. To check if the impedance range of this structure is in the appropriate range for the AFE different diluted NaCl with concentrations from 0,001 to 1 mol/L were applied. Cell culture medium usually has a salt concentration of around 140 mmol/L. Two measurement ranges were recorded to get a larger dynamic range. The result is plotted in Fig. 5.12. When measuring a low impedance in the high range the signal clips resulting in wrong results. The controller can detect this issue and returns an error. The results show that the AFE is capable of resolving these different impedance values. Depending on the magnitude either the low or the high range yields better results.

Bio-impedance measurements were conducted on L929 cell line fibroblasts. Again the TUM-chip was used for this purpose as it is biocompatible and has an IDES with a suitable impedance range of about 150 Ω with cell culture medium. Two chips were used and each connected to a standalone version of the MSP430FR2355 AFE. These were connected to a microcontroller with an SD-card interface. The controller instructed the AFE to measure impedance at 9,6 kHz and about 100 mVpp. Three impedance ranges were used sequentially. Every 15 s such a measurement series was triggered on both wells. The system run autonomous and the results were stored on SD-card. About 10<sup>5</sup> cells were seeded on

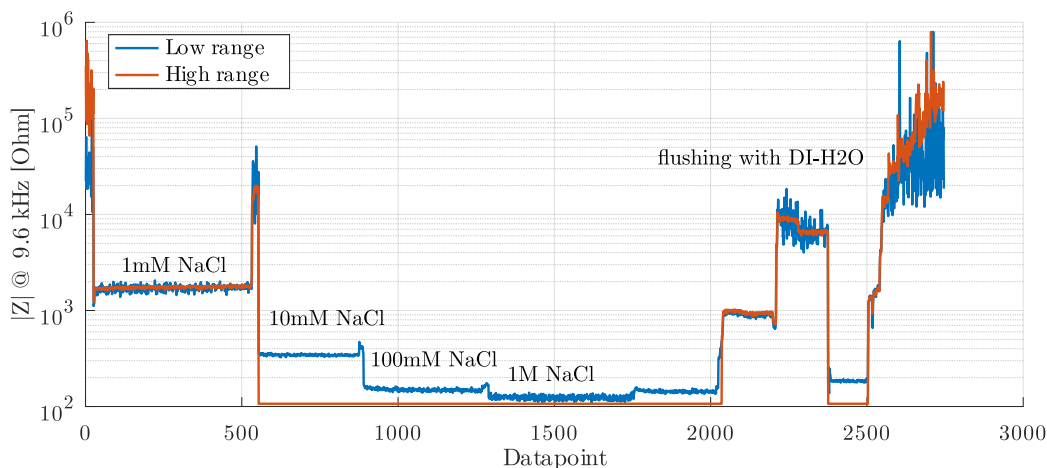



Figure 5.12: Impedance measurement with an IDES subjected to different concentrated NaCl solutions. Two measurement ranges were recorded, one suitable for high impedances and one for low impedances. They therefore show different levels of noise depending on the actual impedance. This way the dynamic range can be extended. In the high range the signal clips at low impedances which is detected by the electronics and an error is returned. After the four different NaCl solutions the IDES was flushed with DI-water several times to clean it but also to create some more impedance values. 

the chip and incubated in DMEM in a CO<sub>2</sub> incubator at 37 °C. The measurement was started shortly after seeding. After about 24 h 1% Triton-X100 was added to one of the wells, the other was untouched. The data acquisition was continued for another hour. Then the measurement was stopped and the chips were examined with a microscope.

The results are printed in Fig. 5.13. After seeding the cells will settle at the bottom, adhere to the sensor surface and form a confluent layer. This can be seen as an increase of impedance in the graph. The current can no longer pass freely through the electrolyte but is obstructed by the cells' walls. Therefore the impedance increases. When a confluent monolayer is established the value will stay constant. As soon as Triton-X100 is added the cells' walls will be destroyed and the obstruction cleared. The impedance first raises for a few minutes, probably due to the mixing involved in the addition, and then falls from previous 180 Ω to 150 Ω. This change can be easily measured with the circuit. Microscopy images confirm a confluent monolayer of cells on the sensor which was not subjected to Triton-X100 while the other does not show cells.

## 5.6 Thermally referenced ISFET

The thermally referenced ISFET is relatively new and currently under test at TI. First tests with flip-chip mounting on PCB had issues with their passivation and the solder connections. However, the heater could be tested dry. It is able to increase the temperature of the sensitive layer of the chip by 15 K. The temperature rise can be controlled by an analog voltage which regulates the heater current. A dynamic temperature measurement with a thermistor on the metal layer above the heater is depicted in Fig. 5.14. This measurement was done with a chip having an aluminium metallisation instead of platinum.

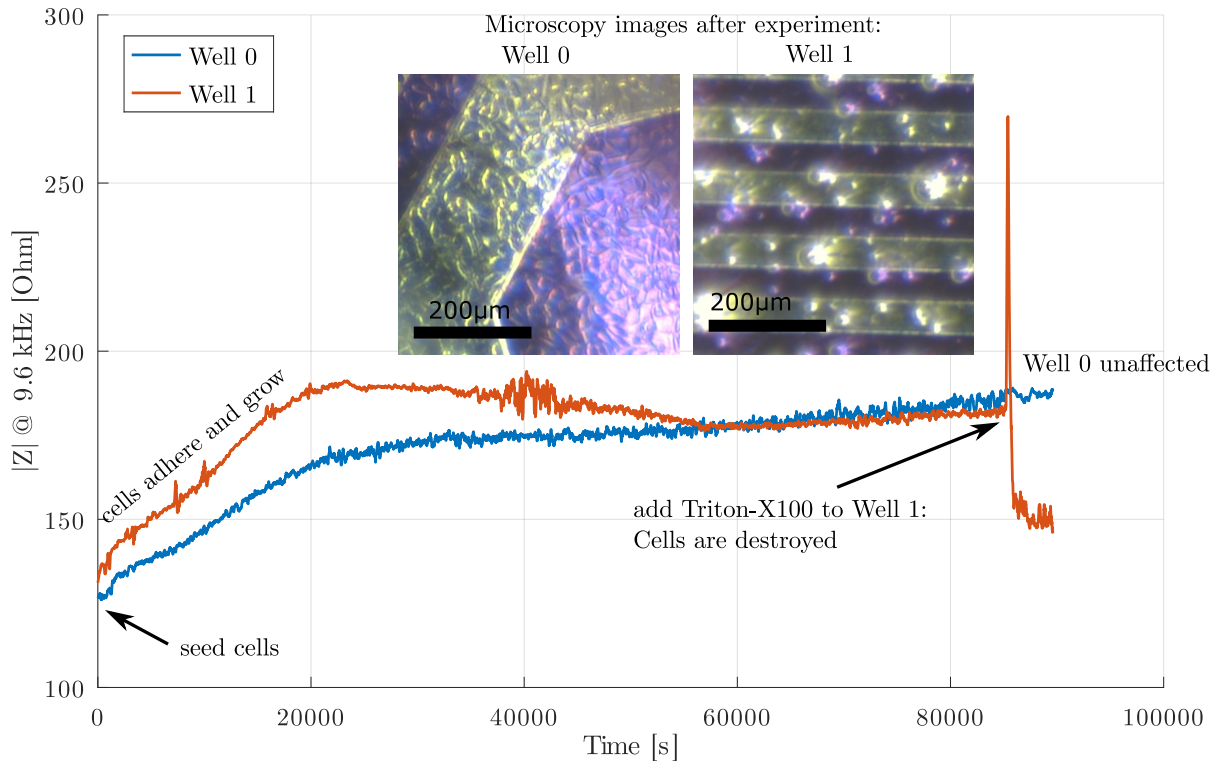



Figure 5.13: Impedance measurement with two IDES and cell cultures. Plotted is a moving average over ten samples of the absolute value of the impedance of two IDES with a cell culture on each in two different wells. In the first hours the cells will settle on the IDES and grow into a confluent monolayer thus increasing the impedance as the cells' walls obstruct the current flow. A stable is reached and the impedance stays more or less constant. After 24 h Triton-X100 is added to one well leading to the destruction of the cells and thus decreasing the impedance again. The two inserts show microscopy images of the two wells after the experiment. On Well 0 a confluent cell layer is visible. The golden structure is a platinum electrode while the purple is  $\text{Si}_3\text{N}_4$ . The cells can be seen as translucent shapes that fit tightly together. Compared to that, in the other Well 1 there are no such structures visible. There are only some spherical unconnected shapes visible but no closed cell layer. 

In this example the heater can heat the thermistor by 11,5 K with a 200  $\mu\text{s}$  pulse<sup>1</sup>.

The first actual working measurement with liquid was done with the wafer prober. This results are plotted in Fig. 5.15. They look promising but need to be considered with caution: This is the first test. Only one chip was tested with three thermally referenced ISFETs. Only two of them worked. However, a linear relation of the delta voltage is clearly visible.

Further tests with more devices confirmed the first results. They showed an linear increasing voltage delta for increasing pH and increasing heating power as predicted by equation 3.2 in Section 3.6.1.2. There is no effect visible when activating a heater of a different sensor structure on the same chip. As expected the heat effect only works on close proximity. This also means that the measured signal is not caused by electrical coupling from the fast switching of the relatively large heater current of a couple of hundred mA on the chip.

The overall sensitivity of the sensor is as expected in the range of about 1 mV/pH which is very low compared to a normal ISFET with 59 mV/pH. Larger sensitivity requires a

<sup>1</sup>) Base resistance:  $\sim 21 \Omega$ , TCR aluminium:  $\alpha = 0,00429/^{\circ}\text{C}$ , resistor current: 2,5 mA, voltage change over resistor: 2,6 mV.

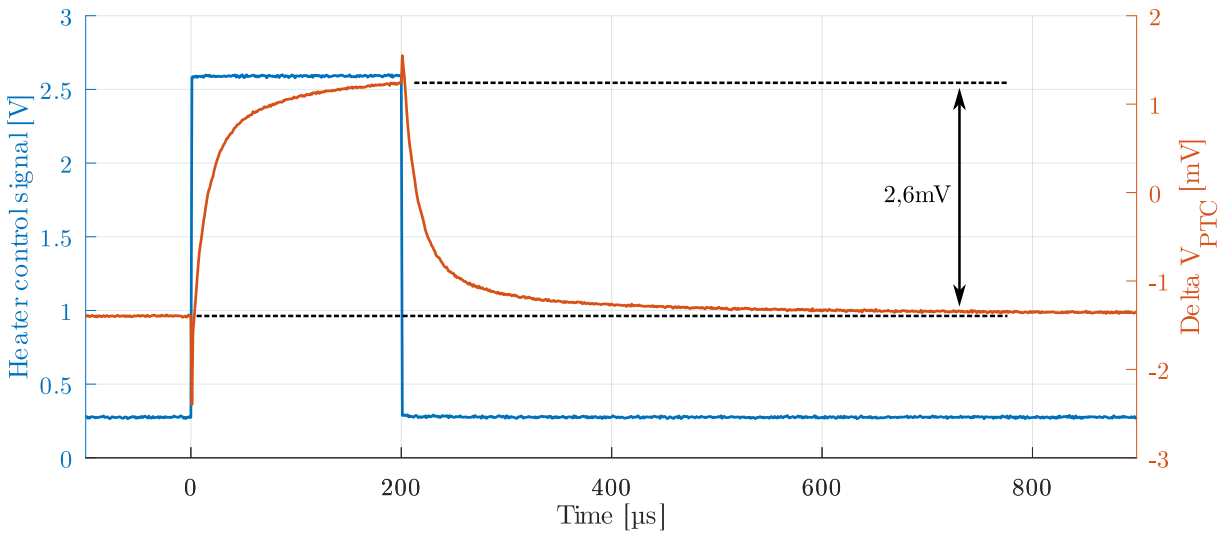



Figure 5.14: Effect of the heater of the thermally referenced ISFET. The blue curve shows the heater control signal which is a 200  $\mu\text{s}$  pulse. The orange curve shows the voltage change over an integrated aluminium resistor (Metal2) directly over the heater (Metal1) through which a (nearly) constant current flows. This difference voltage over the resistor is measured with a difference amplifier with AC-coupling therefore the signal is centred around 0. Through the heat the resistance of the aluminium increases resulting in an increase of the difference voltage of 2,6 mV which corresponds to about 11,5 K. 

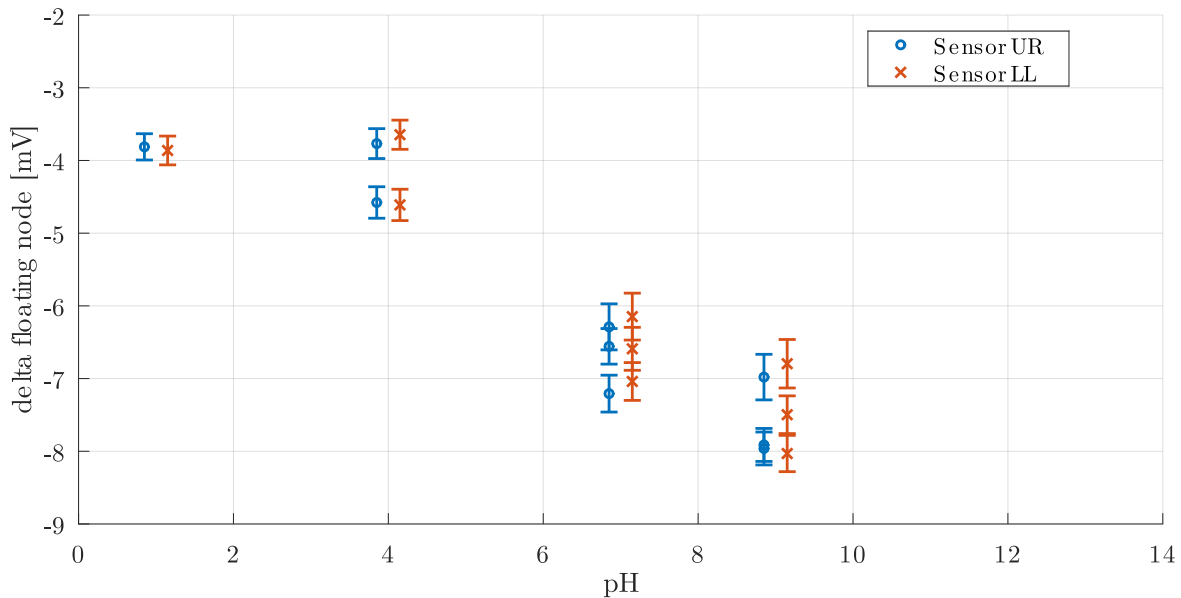



Figure 5.15: First measurement of the thermally referenced ISFET. Plotted is the voltage change of the floating gate when it is heated for five different pH. Two sensors (UR and LL) on one chip were tested. Some pH values were tested multiple times. There is a linear relation between pH and the voltage delta. 



greater temperature change and thus more power. However, this device does not need a large bulky reference electrode anymore which is hard to integrate and can potentially leak silver ions which are cytotoxic. It also has integrated amplifiers to boost the signal by factor 10 or 100 to provide an easier to process signal for a microcontroller with integrated ADC.



## 6 Conclusion and Outlook

In this work a demonstrator for a fully electronic and wireless multi-well-plate is presented. However, due to the lack of enough functional sensors due to manufacturing delays, no complete plate could be tested, yet. Therefore extensive tests were conducted to verify the newly developed read-out concept for ISFETs combined with impedance spectroscopy based on an off-the-shelf mixed-signal processor. Multiple of these cheap ICs were used to read 24 sensors. The electronics responded well and showed to be able to read ISFETs correctly under various condition and do impedance spectroscopy on cells. The accuracy and precision is not ground breaking, but the cost, size, form factor and versatility definitively is. Nevertheless, the circuit is still accurate and precise enough to accomplish its task. It also has the ability to perform diagnosis on the sensors. The plate is able to run on a small coin cell battery for several days and transmit data wirelessly. No electrical contacts to a base station are required, eliminating this error source.

The available sensor samples were tested and characterized with an automated fluidic test-stand that was developed for this purpose. The results were used by the manufacturing team to improve the sensor process further. The sensors were also tested with the various interface circuits to develop and adapt them. For this purpose an universal ISFET test board, the DemoBoard, was constructed. This is currently in use for further sensor tests.

A new type of pH sensor is proposed based on an ISFET. This device now does not require a classical reference electrode unlike all other available ISFET type pH sensors for absolute measurements. It uses a temperature variation to create a reference. A mere pseudo reference electrode, e.g. plain Pt, is sufficient allowing the manufacturing of such a sensor on a single die with standard CMOS processes. It can be also build much smaller, the sensing element itself is a normal Si-die with less than  $1\text{ mm}^2$ . The classical Ag/AgCl-reference electrode is usually the largest part of any commercial ISFET probe. Its only disadvantage is the relative large power consumption due to the heater and a low amplitude output signal. However, the power consumption can be reduced further with a different layout and the weak signal can be amplified by circuits integrated on the same die.

### 6.1 Future improvements and research opportunities

#### 6.1.1 AFE with ADuCM355

To achieve even better results for the impedance spectroscopy and perhaps ISFET-readout, the MSP430 can be replaced with the ADuCM355. This is a precision analog interface for electrochemical sensor combined with an ARM Cortex-M3 microcontroller. It has special analog circuitry for impedance analysis as well as for classical potentiometric procedures.

Internally, it is composed of two dies, one with the ARM-Cortex and one for the analog circuits. A comparison with the MSP430FR2355 is compiled in Table 6.1. Overall, the specs are much better than for the MSP but this reflects also in a five times higher price. Also the package, a LGA-type<sup>1</sup>, is much more difficult to handle and requires tighter PCB specs. It has in total five DACs: One high-speed 12-bit, two low-speed 12-bit and two 6-bit DACs. The low-speed DACs have a range from 0,2 to 2,4 V. While the high-speed DAC and its buffer-amp have a range from 0,2 to AVDD-0,6 V. The ADC has a sample rate of up to 400 kSPS at a resolution of 16 bit. A PGA for signal conditioning is available. A large internal MUX is used to connect around two dozen internal and external signals to the ADC.

Table 6.1: Comparison of the MSP430FR2355 and the ADuCM355.

	<b>MSP430FR2355</b>	<b>ADuCM355</b>
<b>ISFET</b>	Yes	possible [111]
max. $V_{gs}$	up to 2,5 V(3,3 V)	up to 2,5 V
Resolution	12/17 Bit	16 Bit
No. of FETs	4 with ext. mux	2
<b>Impedance</b>	100 Hz - 11 kHz	16 mHz - 200 kHz
Excitation	100 - 2500 mVpp external resistor required	30 or 600 mVpp TIA with integrated variable R
	12 bit ADC	16 bit ADC
	12 bit DAC	12 bit DAC
	50 $\Omega$ - 100 k $\Omega$	0,4 $\Omega$ - 10 M $\Omega$
<b>Core</b>	MSP430	ARM Cortex-M3
Memory	32kB FRAM, 4kB SRAM	128kb Flash, 64kB SRAM
Clock	16 MHz (max. 24 MHz)	digital 26 MHz, analog 32 MHz
Peripherals	I2C, SPI, UART	I2C, SPI, UART waveform ROM, DFT
<b>ext. components</b>	3x C, 5x R, MUX	ca. 10x C
<b>Size</b>	4 mm $\times$ 4 mm VQFN-32	6 mm $\times$ 5 mm LGA-72
<b>Price</b>	1,50€ @ 100 pc.	7,80€ @ 100 pc.

The ADuCM355 has two independent low-speed blocks with a 12- and 6-bit DAC, an opamp and a TIA. Each of these blocks can be used for a potentiometric measurement. The DAC provides the bias voltage, the 6-bit for the TIA-zero level and the 12-bit for the working electrode (labelled as SE) potential. The opamp is used to measure the potential with the reference electrode (RE) and adjust the counter electrode (CE) voltage so that  $RE = DAC(12\text{-bit})$ . The working electrode is connected to the input of the TIA. Its zero level can be adjusted independently from the bias voltage with the 6-bit DAC. The feedback resistance is integrated and can be adjusted from 1 k $\Omega$  to 512 k $\Omega$ .

The impedance functionality uses amplifiers and DACs with higher bandwidth and thus more power consumption. Up to 200 kHz are possible. The signal is generated by a waveform generator with a sin-ROM and then amplified by a driver with different gains.

<sup>1)</sup> Land Grid Array

An excitation voltage of 30 or 600 mVpp is choosable. Also a DC-bias can be applied. The current is measured by a high-speed TIA, also with variable feedback but not so much range as the low-speed TIA, and then digitized by the ADC. A hardware DFT-accelerator can then be used to calculate the real and imaginary part of the impedance.

This chip offers lot's of possibilities but is also very complex. It is therefore uncertain if it can be used to read ISFETs. Probably this is feasible but with a slightly different approach than with the MSP430. The ADuCM355 has at least three DACs as required for the ISFET algorithm. But the high-speed DAC can only be connected to a pin that is also used for the two other 12-bit DACs or to the calibration resistor pin. To overcome this, one of the TIA-inputs could be used in conjunction with the 6-bit DAC to set their bias potential. Then also the current through the ISFET could be monitored directly. An external multiplexer is still required to connect multiple ISFETs. Zimmer and Peacock offer a readout unit based on the ADuCM355. They claim to be able to read up to two sensors which can also be FETs [111]. But this product seems to be still in development, there is no information available on how it works.

Concluding, there is a possibility for the ADuCM355 to replace the MSP430FR2355 to achieve better measurement results if this is required. But there is still a significant engineering effort alone required to check if it is really possible, yet to realize it. Especially, if all sensors can be connected to the chip, i.e. if there are enough pins with the right functions available and the development of sophisticated methods to overcome possible limitations. The ISFET readout probably needs to be designed in a slightly different way. The already integrated TIAs could here be advantageous. Also the space constraints need to be considered. The PCB is a bit more complex to cope with the BGA-package; probably 4 layers are required, increasing cost. There is also the possibility of a hybrid setup maintaining the 24 MSP430s for the FETs and adding a single ADuCM355 for impedance spectroscopy (see Fig. 6.1) to combine their advantages of low cost and precise impedance spectroscopy.

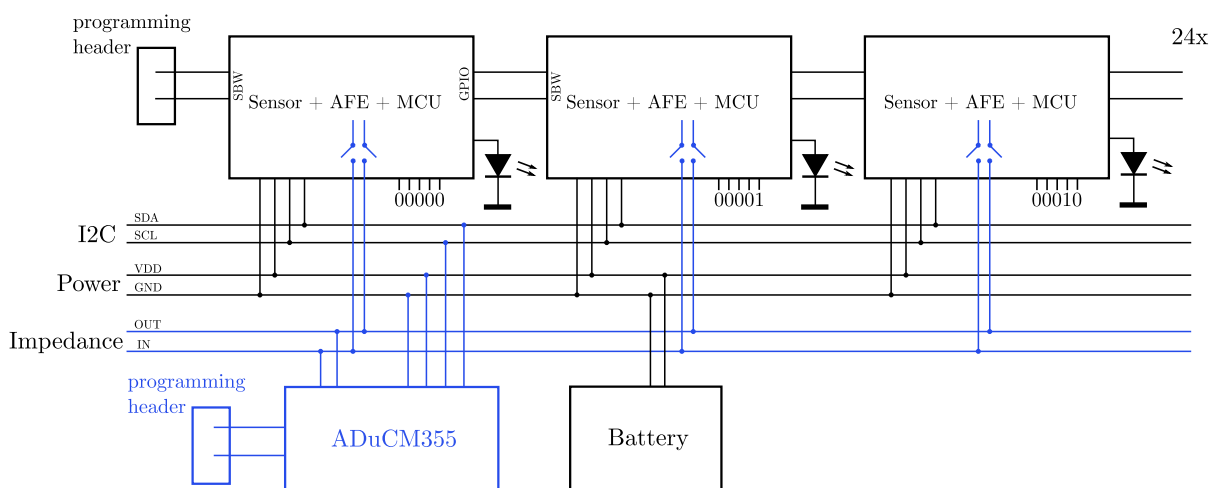



Figure 6.1: Concept for an improved fully electronic multi-well-plate. It is still based on the MSP430FR2355 for each well (see Fig. 4.27). New parts are marked blue: The ADuCM355 is added, one for the whole plate due to cost and size, as a better impedance analyser. Also two new global nets IN and OUT are introduced to connect each well to the ADuCM355. Inside the well-blocks two switches are placed to connect or disconnect the impedance structure of each well independently to the ADuCM355. 

### **6.1.2 Industrial and Consumer Applications for ISFETs**

The newly developed electronics is not restricted to medical and biological applications. ISFET sensors can be employed for many other uses, e.g. in household appliances to monitor the input water quality. Also for drinking water monitoring, process water applications and industrial process control pH or ion sensing with modified ISFETs is interesting. For such applications a reliable so called transmitter is required. This is an electronic circuit that controls the sensor and converts its output to a standardized format which the upstream process control unit can process. With the MSP430 based front-end such a transmitter for ISFETs can be easily realized in a compact and flexible format. The stand-alone front-end (see Section 4.4.4) can be considered as a prototype for such a transmitter. It was designed with wide margins so there is still a lot of potential to easily decrease its size. It is flexible in its operation parameters, such as FET polarity,  $V_{ds}$  and  $I_{ds}$  and therefore not bound to a specific ISFET type or manufacturer.

### **6.1.3 Sensor research**

The plate will be used in further research project to develop new ISFET-based sensors, i.e. with different functionalization. Either the ISFETs or the IDES can be used to detect the reaction of the functionalization layer. Which is better needs to be determined for the specific layer. Here the plate is ideal as it supports both principles. The plate will be modified to make the sensors exchangeable so that non-working or used-up sensors can be easily replaced and the development cost can be reduced. However, this makes the plate higher, more expensive and more susceptible to errors. Therefore this was not considered for the user-version of the plate in this thesis.

### **6.1.4 Recycling and Waste Management**

Another open issue of the fully electronic multi-well-plate is its disposal and possible recycling to reduce the pile of electronic waste. Electronic waste is a global problem, therefore the reduction of it is a key factor of the solution. The waste problem does not end with the electronic multi-well-plate. It needs to be solved on a global scale and there is still a lot of research to be done. A small contribution could be to make the electronics and the sensors detachable. The electronics could then be equipped with a new sensor PCB and reused. This could be done by the manufacturer of the plate in the form of a deposit system: If you buy a new plate and return a used one you get discount. The manufacturer separates sensors and electronics and builds a new plate with the used electronics and new sterile sensors. In this way it can be ensured that the user always receives a well tested diagnostic tool unlike if he had to replace the sensors himself.

# APPENDIX





# A MWP Communication Protocol

This is the dataformat that is transmitted by the contactless electro-chemical multi-well-plate. The Figures A.1, A.2, A.3 and A.4 show the structure of the data. First the overall structure is shown and then the format of the base64 encoded fields.

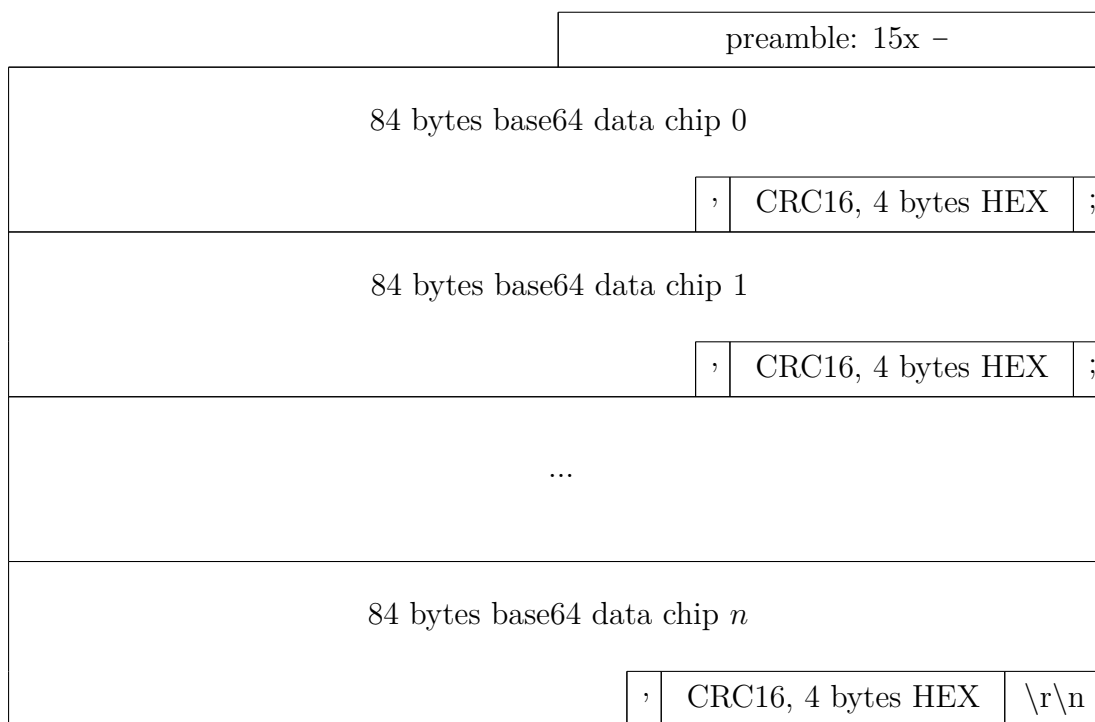


Figure A.1: Data format transmitted by the 24-well-plate. To allow the receiver to lock, 15 ASCII minus signs are sent as preamble. Then for each sensor chip, a string consisting of 84 bytes of base64 encoded data, followed by a CRC16 (CRC-CCITT) of the base64 string in ascii-hex separated by a comma, is sent. These segments are separated by a semicolon. The base64 data block contains the measurement data of the corresponding analog front end and is further described in Fig. A.3.

preamble: 15x -		
84 bytes base64 data chip 0		
	,	CRC16, 4 bytes HEX \$
80 bytes base64 config data chip 0		
	,	CRC16, 4 bytes HEX ;
84 bytes base64 data chip 1		
	,	CRC16, 4 bytes HEX \$
80 bytes base64 config data chip 1		
	,	CRC16, 4 bytes HEX ;
...		
84 bytes base64 data chip $n$		
	,	CRC16, 4 bytes HEX \$
80 bytes base64 config data chip $n$		
	,	CRC16, 4 bytes HEX \r\n

Figure A.2: Extended data format transmitted by the 24-well-plate. In addition to the short format described in Fig. A.1, there is also an extended format. After the base64 data block with CRC16 (CRC-CCITT) another base64 block with CRC is attached, separated by a \$ sign for each chip. The content of the config data block is described in Fig. A.4.

0	1	2	3	4	5	6	7	8	9	10	11	12	13	14	15	16	17	18	19	20	21	22	23	24	25	26	27	28	29	30	31	
$V_{gs}[0]$																$V_{gs}[1]$																} int16
$V_{gs}[2]$																$V_{gs}[3]$																
$V_{ds}[0]$																$V_{ds}[1]$																
$V_{ds}[2]$																$V_{ds}[3]$																
$I_{ds}[0]$																$I_{ds}[1]$																
$I_{ds}[2]$																$I_{ds}[3]$																
I2C-Address																PT1000																} uint16
$V_{gs}[0]$ 17-bit																																} int32
$V_{gs}[1]$ 17-bit																																
$V_{gs}[2]$ 17-bit																																
$V_{gs}[3]$ 17-bit																																
impedance current in-phase																																
impedance current quadrature																																
impedance voltage in-phase																																
impedance voltage quadrature																																
battery voltage																																} uint16

Figure A.3: Structure of the data block transmitted by the controller-chip after base64 decoding. The numbers in the top row denote bits. One row contains 32 bits. The data block is in total 496 bits long. All data is little encoded and encoded as the type declared on the right side. Negative values are encoded a twos complements.

0	1	2	3	4	5	6	7	8	9	10	11	12	13	14	15	16	17	18	19	20	21	22	23	24	25	26	27	28	29	30	31
status																control															
impedance frequency																impedance amplitude															
impedance offset																ISFET $V_{ds}$ set															
ISFET $I_{ds}$ set																ISFET polarity															
ISFET device type																measurement interval															
single shot control																impedance TIA range															
impedance frequency multiplier																reserved															
reboot counter MSB																															
number of frequencies																Battery voltage															
impedance spectroscopy frequencies to measure (16 bit per frequency, up to 7)																															
current impedance frequency																reserved															
start address of I2C slaves																number of I2C slaves															

Figure A.4: Structure of the config data block transmitted in extended data mode by the controller-chip after base64 decoding. The numbers in the top row denote bits. One row contains 32 bits. The data block is in total 512 bits long. All data is little endian and usually encoded as 16-bit unsigned integer, except for  $V_{ds}$  and  $I_{ds}$  set, which are signed integers. Negative values are encoded a twos complements.



## B MSP430FR2355 front-end register structure

Table B.1: MSP430FR2355 I2C exposed register structure, Addresses 0-63, all little-endian

Address	Type	Name	RW	Comment
0	uint16_t	status	R	see Table B.3
2	uint16_t	control	RW	see Table B.4
4	uint16_t	impedance frequency	RW	$\langle \text{val} \rangle = (16 \text{ MHz} / (32 \cdot f) - 1)$
6	uint16_t	impedance amplitude	RW	$\langle \text{val} \rangle = A / 2,5 \text{ V} \cdot 4096$
8	uint16_t	impedance offset	RW	$\langle \text{val} \rangle = O / 2,5 \text{ V} \cdot 4096$
10	int16_t	ISFET $V_{ds}$ set	RW	$\langle \text{val} \rangle = V_{ds} / 2,5 \text{ V} \cdot 4096$ (always positive)
12	int16_t	ISFET $I_{ds}$ set	RW	$\langle \text{val} \rangle = I_{ds} / 2,5 \text{ V} \cdot 4096 \cdot R$ (always positive)
14	uint16_t	ISFET polarity	RW	see Table B.5
16	uint16_t	ISFET device type	RW	see Table B.5
18	uint16_t	measurement interval	RW	$\langle \text{val} \rangle \cdot 0,1 \text{ s}$
20	uint16_t	single shot control	RW	trigger in $(\langle \text{val} \rangle - 1) \cdot 0,1 \text{ s}$
22	uint16_t	imp TIA range	RW	0-3
24	uint16_t	imp freq multiplier	RW	1 or 2
34	uint32_t	reboot counter	R	number of chip startups
38	uint16_t	Battery voltage	R	$V_{bat} = 4096 / \langle \text{val} \rangle \cdot 2,5 \text{ V}$
40	uint16_t	number of frequencies	RW	for auto sweep
42	uint16_t	imp spect freq 0	RW	see impedance frequency
44	uint16_t	imp spect freq 1	RW	
46	uint16_t	imp spect freq 2	RW	
48	uint16_t	imp spect freq 3	RW	
50	uint16_t	imp spect freq 4	RW	
52	uint16_t	imp spect freq 5	RW	
54	uint16_t	imp spect freq 6	RW	
56	uint16_t	current imp freq	RW	only if auto sweep active
60	uint16_t	start addr of I2C slaves	RW	
62	uint16_t	number of I2C slaves	RW	

Table B.2: MSP430FR2355 I2C exposed register structure, Addresses 64-255, all little-endian

Address	Type	Name	RW	Comment
64	int16_t	$V_{sg,12bit}[0]$	R	$V_{sg} = \langle \text{val} \rangle \cdot 2,5 \text{ V} / 4096$
66	int16_t	$V_{sg,12bit}[1]$	R	$V_{sg} = \langle \text{val} \rangle \cdot 2,5 \text{ V} / 4096$
68	int16_t	$V_{sg,12bit}[2]$	R	$V_{sg} = \langle \text{val} \rangle \cdot 2,5 \text{ V} / 4096$
70	int16_t	$V_{sg,12bit}[3]$	R	$V_{sg} = \langle \text{val} \rangle \cdot 2,5 \text{ V} / 4096$
72	int16_t	$V_{ds,12bit}[0]$	R	$V_{ds} = \langle \text{val} \rangle \cdot 2,5 \text{ V} / 4096$
74	int16_t	$V_{ds,12bit}[1]$	R	$V_{ds} = \langle \text{val} \rangle \cdot 2,5 \text{ V} / 4096$
76	int16_t	$V_{ds,12bit}[2]$	R	$V_{ds} = \langle \text{val} \rangle \cdot 2,5 \text{ V} / 4096$
78	int16_t	$V_{ds,12bit}[3]$	R	$V_{ds} = \langle \text{val} \rangle \cdot 2,5 \text{ V} / 4096$
80	int16_t	$I_{ds,12bit}[0]$	R	$I_{ds} = \langle \text{val} \rangle \cdot 2,5 \text{ V} \cdot R / 4096$
82	int16_t	$I_{ds,12bit}[1]$	R	$I_{ds} = \langle \text{val} \rangle \cdot 2,5 \text{ V} \cdot R / 4096$
84	int16_t	$I_{ds,12bit}[2]$	R	$I_{ds} = \langle \text{val} \rangle \cdot 2,5 \text{ V} \cdot R / 4096$
86	int16_t	$I_{ds,12bit}[3]$	R	$I_{ds} = \langle \text{val} \rangle \cdot 2,5 \text{ V} \cdot R / 4096$
88	uint16_t	I2C address	R	of this device
90	uint16_t	Pt1000	R	$R = \langle \text{val} \rangle \Omega$
92	int32_t	$V_{sg,17bit}[0]$	R	$V_{sg} = \langle \text{val} \rangle \cdot 2,5 \text{ V} / 131072$
96	int32_t	$V_{sg,17bit}[1]$	R	$V_{sg} = \langle \text{val} \rangle \cdot 2,5 \text{ V} / 131072$
100	int32_t	$V_{sg,17bit}[2]$	R	$V_{sg} = \langle \text{val} \rangle \cdot 2,5 \text{ V} / 131072$
104	int32_t	$V_{sg,17bit}[3]$	R	$V_{sg} = \langle \text{val} \rangle \cdot 2,5 \text{ V} / 131072$
108	int32_t	$\Re(I_{imp})$	R	Real part current
112	int32_t	$\Im(I_{imp})$	R	Imaginary part current
116	int32_t	$\Re(V_{imp})$	R	Real part voltage
120	int32_t	$\Im(V_{imp})$	R	Imaginary part voltage
124	uint16_t[32]	$I_{imp}[0..31]$	R	Raw current samples
188	uint16_t[32]	$V_{imp}[0..31]$	R	Raw voltage samples
252	uint16_t	Version	R	Software Version
254	uint16_t	Magic Number	R	= 1337, for identification

Table B.3: MSP430FR2355 I2C status register

bit set	in HEX	Meaning
15	0x8000	impedance measurement is running
14	0x4000	impedance measurement calculation pending
01	0x0002	O2FET was used
00	0x0001	any measurement is running



Table B.4: MSP430FR2355 I2C control register

bit set	in HEX	Meaning
15	0x8000	measure Pt1000
14	0x4000	measure impedance
13	0x2000	measure FETs
12	0x1000	measure battery
11	0x0800	send UART extended format
10	0x0400	sync slaves
09	0x0200	send data via UART (LED)
08	0x0100	enable status LED
02	0x0004	activate impedance sweep
01	0x0002	save current config
00	0x0001	Single shot measurement

Table B.5: MSP430FR2355 I2C polarity and device register

0b 00 00 00 00 44 33 22 11	Bitmask in register for FETs 1-4
0b00	p-channel
0b01	n-channel
0b00	RefFET
0b01	ISFET
0b10	O2FET
0b11	off
examples	
0b00000000 01 00 01 00	FET 4 and 2 n-, 3 and 1 p-channel
0b00000000 11 11 01 00	FET 4 and 3 off, 2 ISFET, 1 RefFET



# C Total harmonic distortion calculation

This is the OCTAVE/MATLAB function to calculate the THD for a step approximated sinus.

```
1 ## Copyright (C) 2020 markus hefele
2 ## Created: 2020-03-24
3
4 function thd = thd_calc (n,b)
5   % n = nr of steps
6   % b = bit depth
7
8   s=[];
9   pkg load communications
10  %quantisation table
11  minstep = 2/(2**b);
12  halfstep = minstep/2;
13  for i = [1:(2**b)]
14    qtab(i) = -1+minstep*i;
15  end
16  ctab = qtab-halfstep;
17
18  %%nr of steps
19  %n=32;
20  len = 2048/n;
21
22  for i =[0:(n*4)-1]
23    x = sin(i/n*2*pi);
24    frame = x*ones(1,len);
25    s = [s frame];
26  end
27
28  %%quantisation
29  [sidx, sq] = quantiz(s, qtab, ctab);
30
31  sq = sq.*hanning(length(sq))';
32  f = abs(fft(sq));
33
34  %main freq is always "4"(+1)
35  h0 = f(5);
36  %sum all harmonics
37  hx = 0;
38  for i = [1:ceil(length(f)/2/4)-1]
39    hx = hx + f(5+4*i)^2;
40  end
41  thd = sqrt(hx)/h0;
```

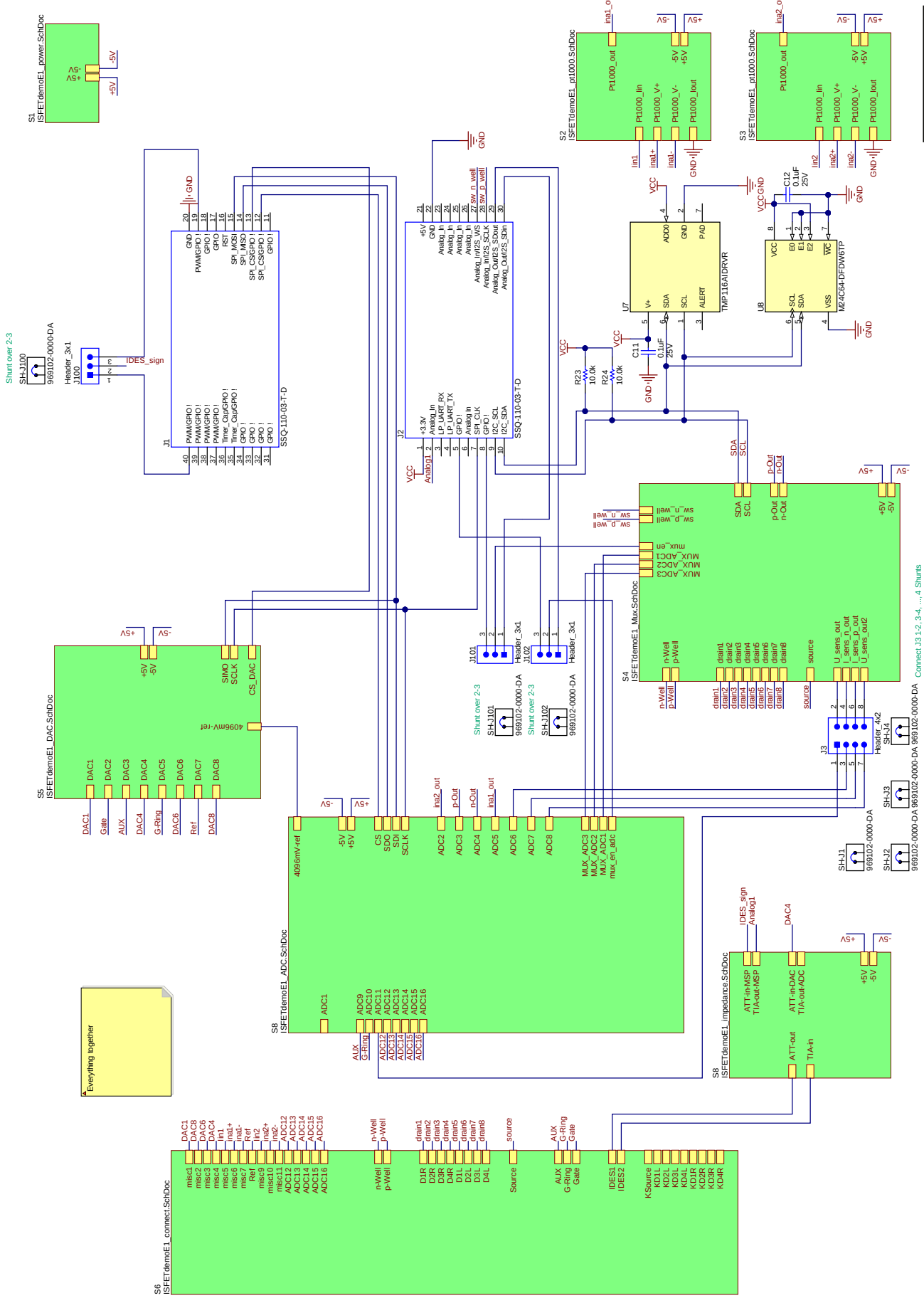
*Total harmonic distortion calculation*

42 **endfunction**

listings/thd\_calc.m

# D Schematics

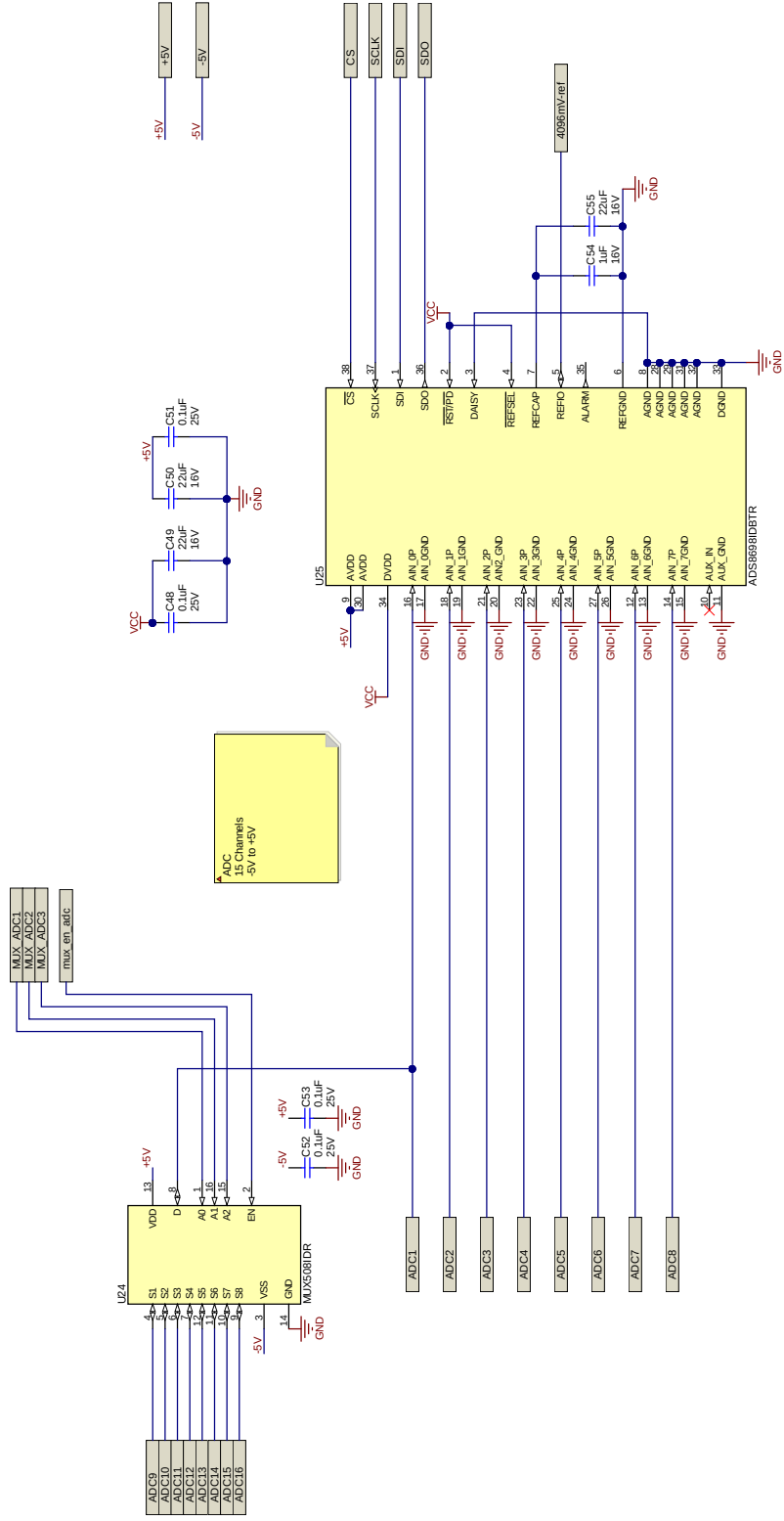
## D.1 DemoBoard

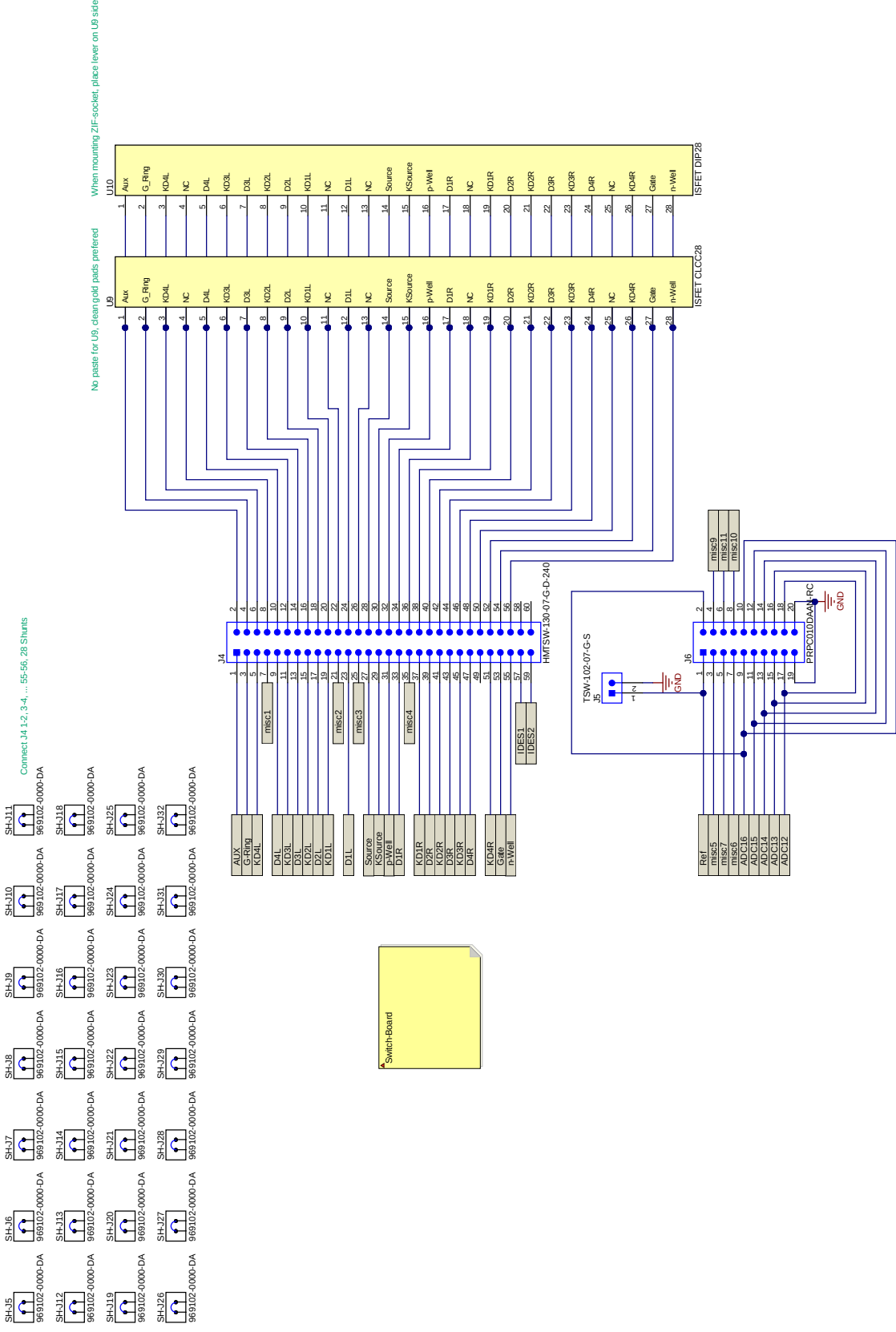


Everything together

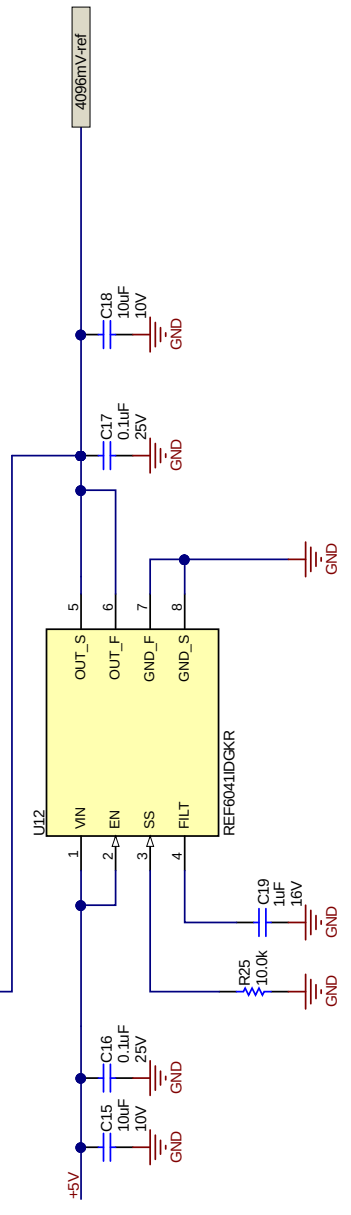
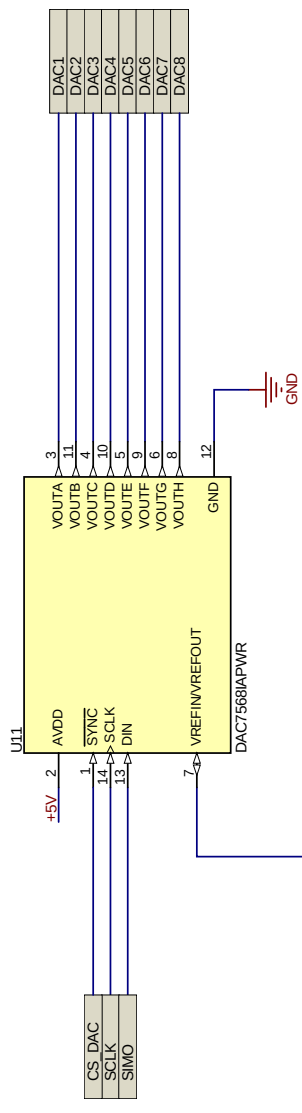
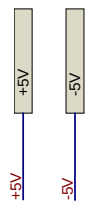
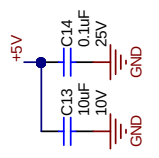
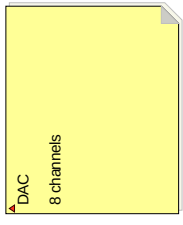
Connect: J3.1, 2, 3, 4, ..., 4 Shunts



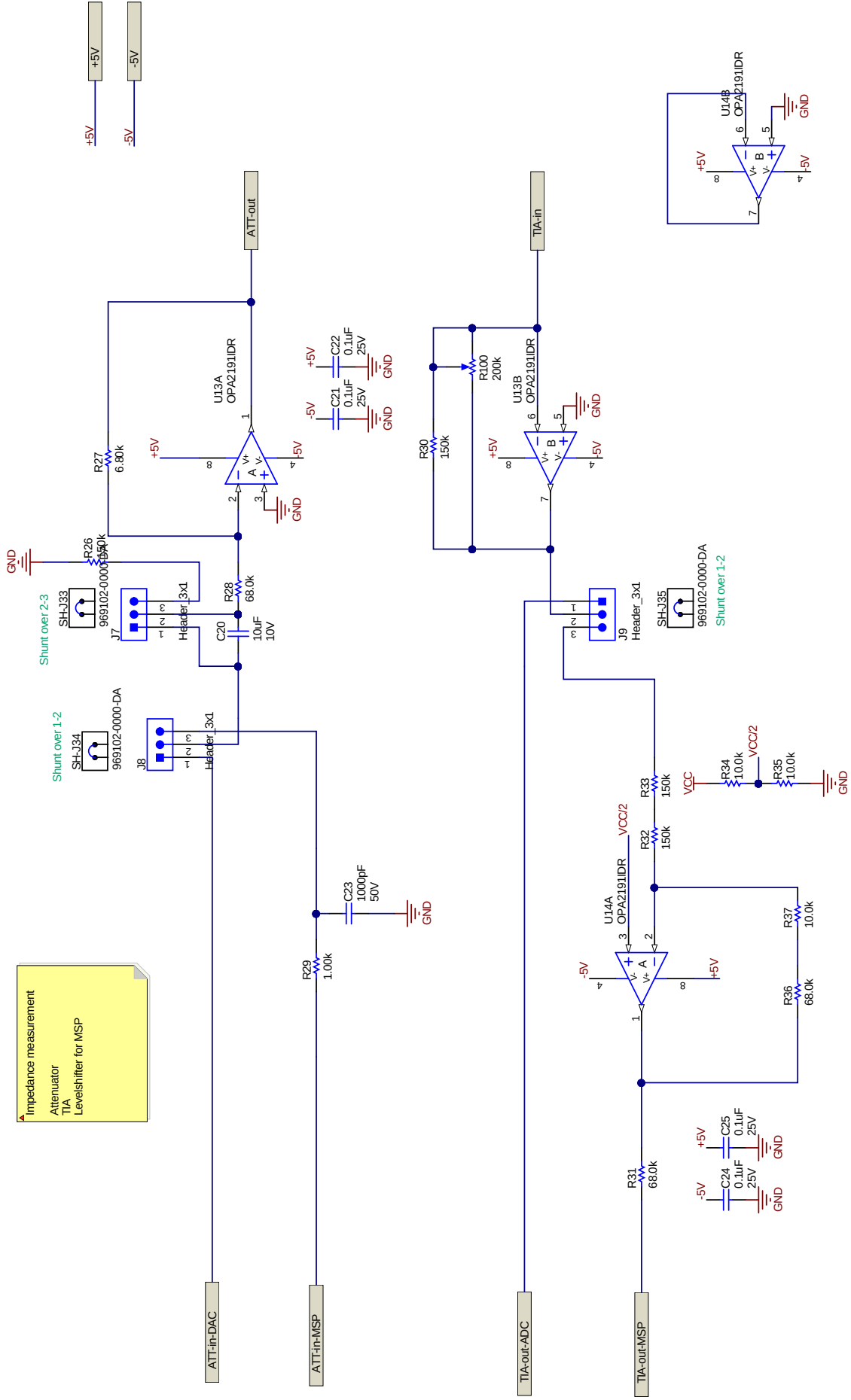


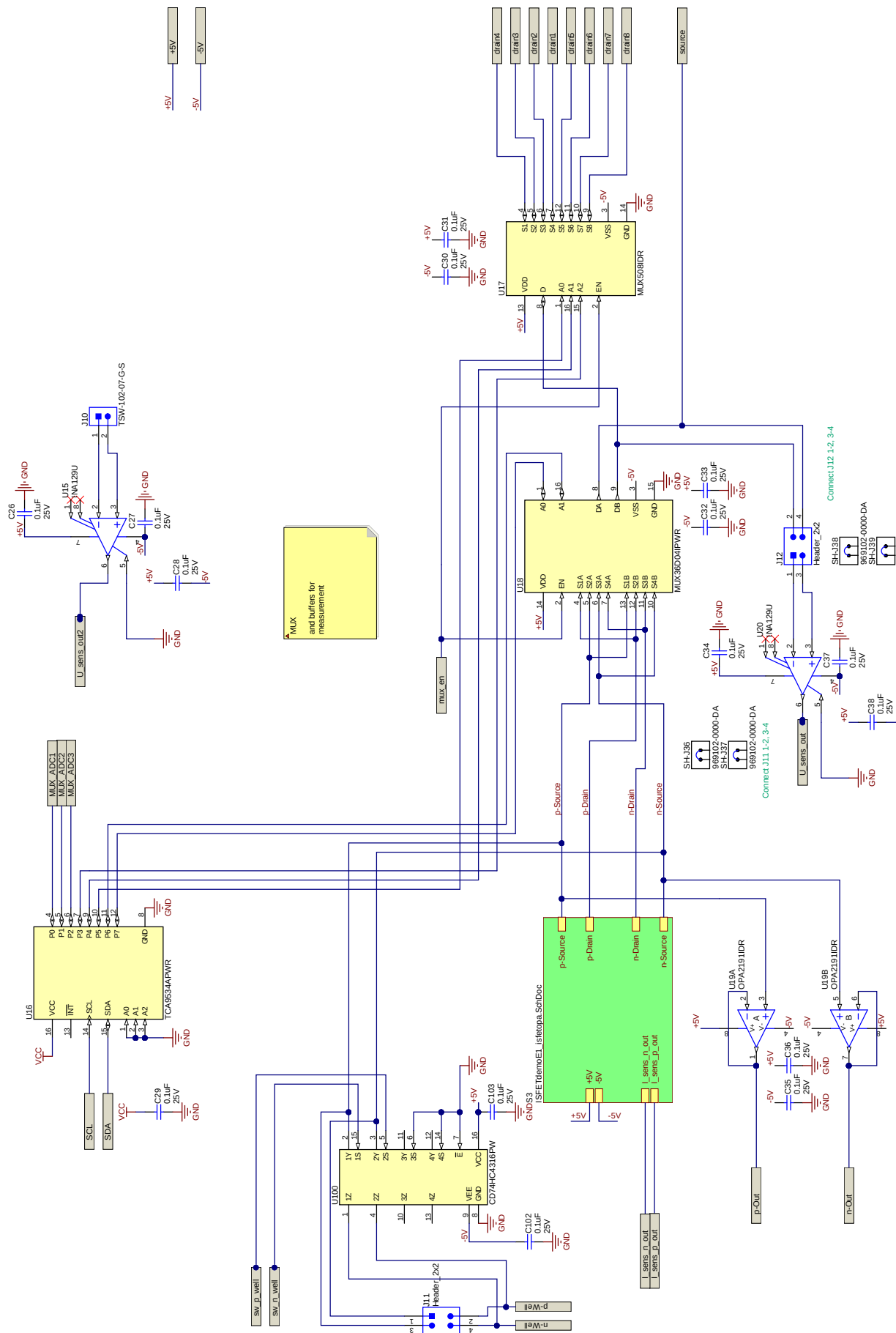


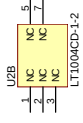
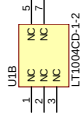
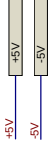




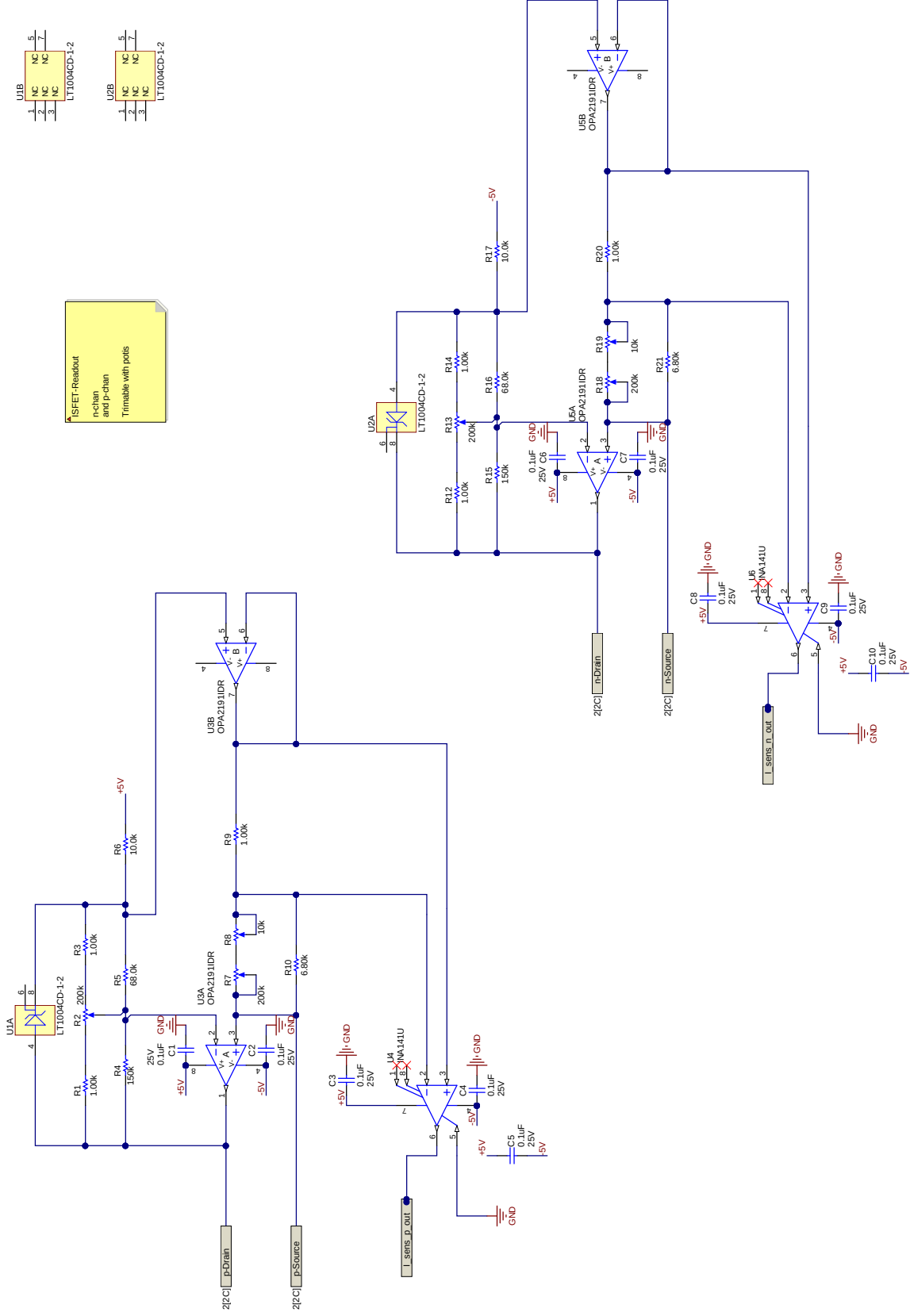
Impedance measurement  
Attenuator  
TIA  
Levelshifter for MSP



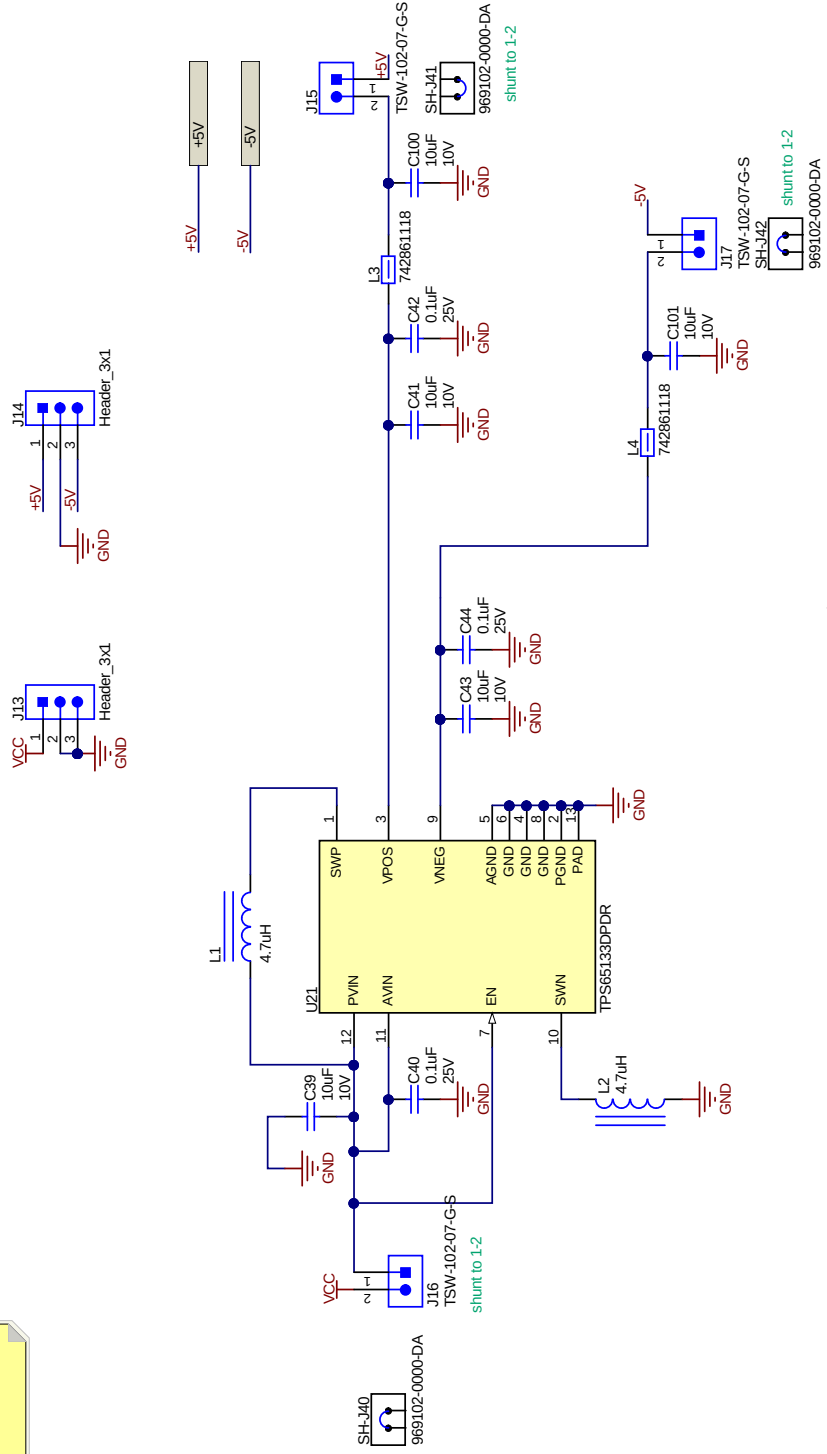


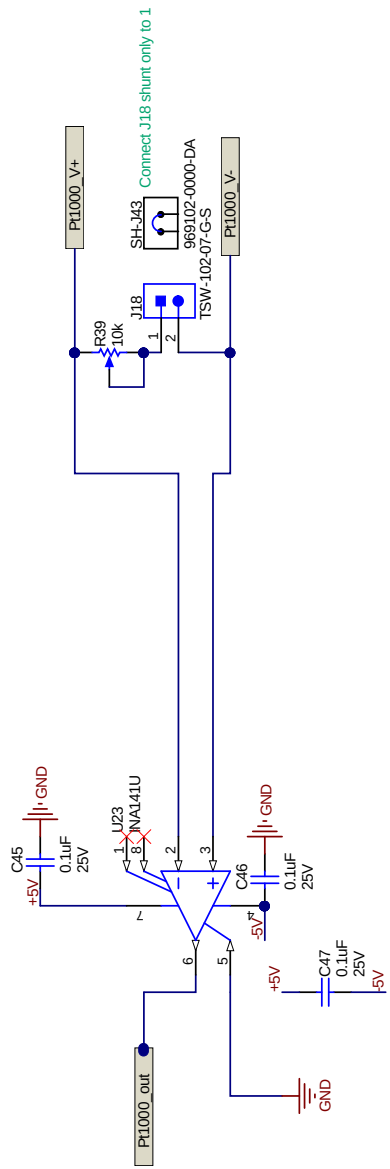
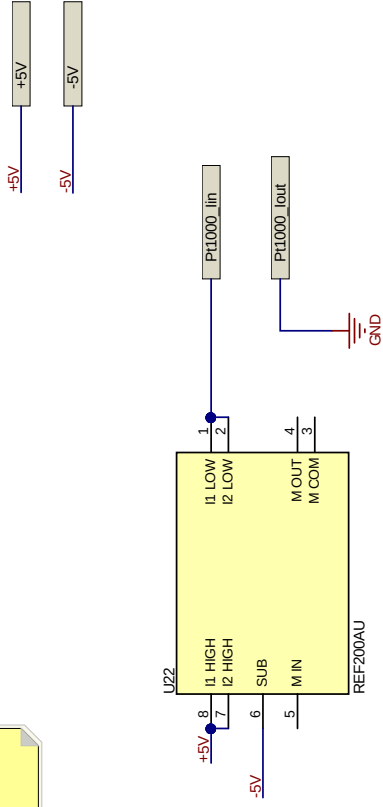
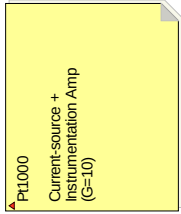


ISFET - Readout  
n-chan  
and p-chan  
Trimable with pins

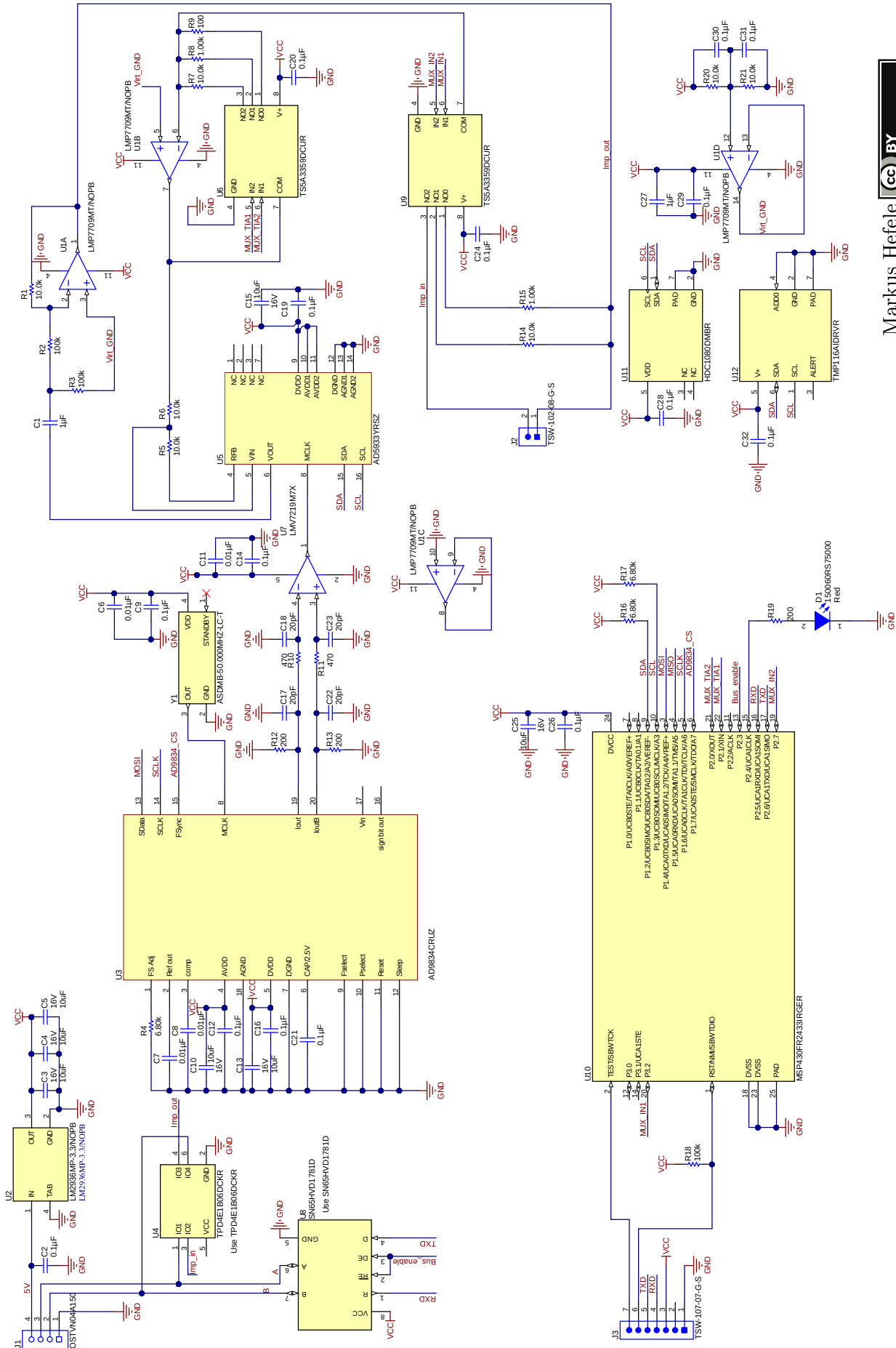


Powersupply:  
3.3V to +5V and -5V





## **D.2 Standalone Impedance Analyzer**



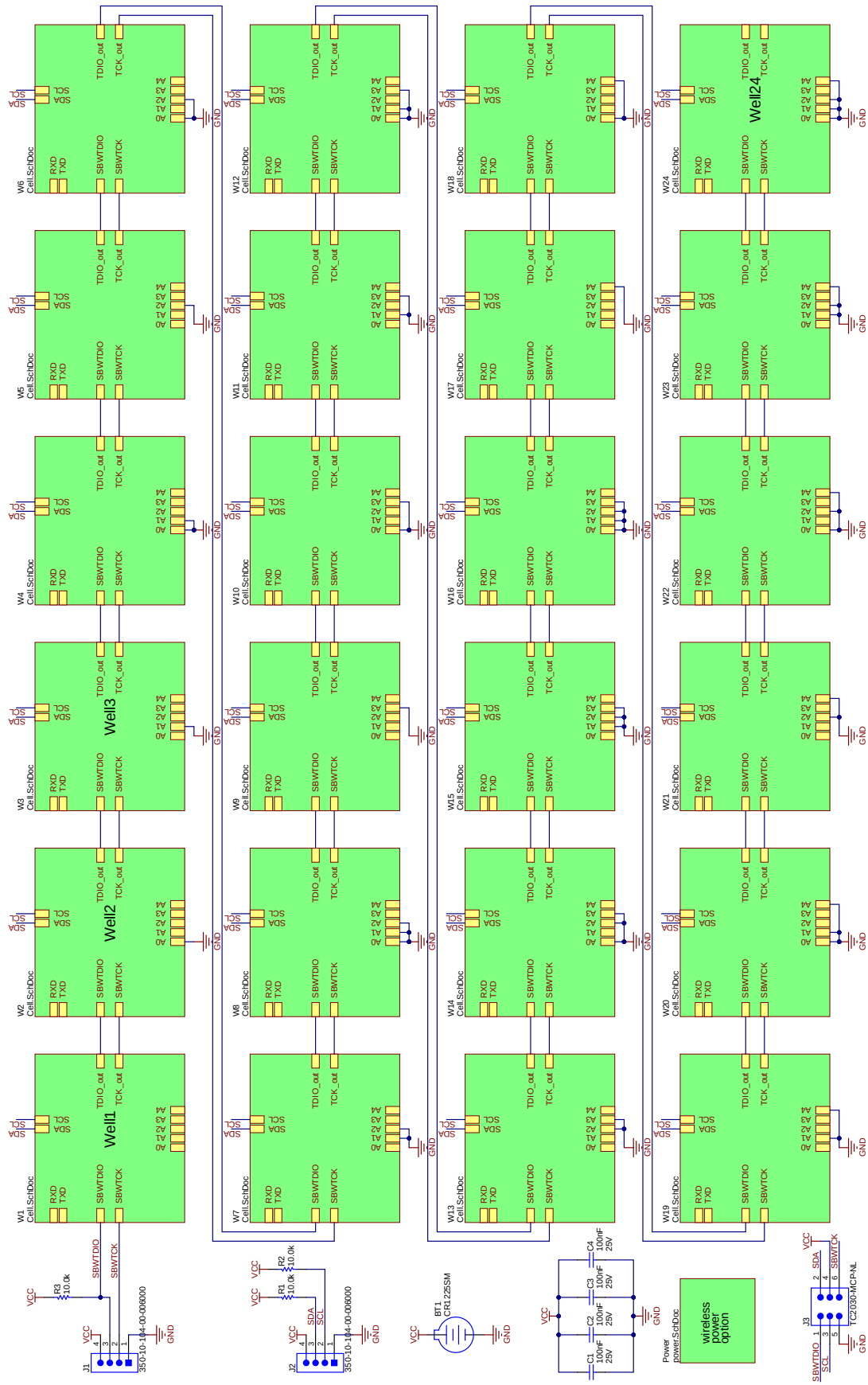


## **D.3 Integrated Front-end**

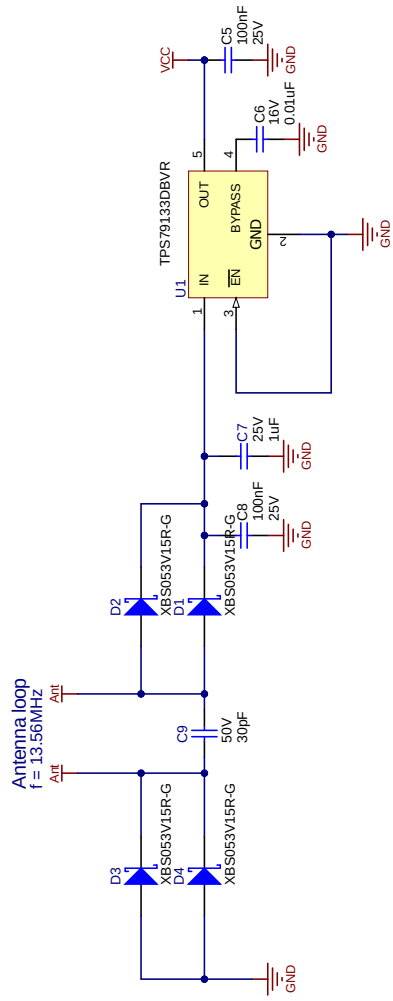


## **D.4 Contactless Multi-well-plate**

24well, revision 2 with smaller controller and gen2-sensor-chip.







B

C

# **E Eurosenors 2020 conference entry**

Abstract submitted for Eurosenors2020 Conference. The conference was postponed due to the SARS-CoV2 pandemic.

Abstract

# Dissolved oxygen detection with ISFETs without reference electrode †

Markus Hefele <sup>1,\*</sup>, Ernst Muellner <sup>2</sup>, Sebastian Meier <sup>1,2</sup>, Helmut Rinck <sup>2</sup>, Christian Pfeffer <sup>1</sup>, Ralf Brederlow <sup>1</sup>, Franz Kreupl <sup>1</sup> and Bernhard Wolf <sup>3</sup>

<sup>1</sup> Technical University of Munich, 80333 Munich, Germany

<sup>2</sup> Texas Instruments Deutschland GmbH, 85356 Freising, Germany

<sup>3</sup> Steinbeistransferzentrum für Medizinische Elektronik und Lab-on-Chip Systeme, 80802 Munich, Germany

Emails: markus.hefele@tum.de, e-muellner@ti.com, s-meier@ti.com, h-rinck@ti.com, christian.pfeffer@tum.de, r.brederlow@tum.de, franz.kreupl@tum.de, wolf@tum.de

\* Correspondence: markus.hefele@tum.de; Tel.: +49-89-289-22910

† Presented at the Eurosensors XXXIV, Lecce, Italy, 6-9 September 2020.

**Abstract** ISFET sensors can be used in conjunction with auxiliary electrodes to measure dissolved oxygen [1]. We present a method to do this without an Ag/AgCl-reference electrode. We achieve this by using a reverse potential to periodically recover the electrodes and improve sensitivity.

**Keywords:** ISFET, O2FET, dissolved oxygen, reference electrode

## 1. Introduction

Oxygen detection with ISFETs has been described first by Sohn and Kim in 1996 [1]. Here two auxiliary electrodes are used to reduce oxygen to hydroxide-ions. The negative electrode is a noble metal electrode in the vicinity of the ISFET, which detects the pH-increase. This is dependent on the available oxygen in the solution. The second electrode used is an Ag/AgCl-reference electrode and placed away from the ISFET. We present a similar concept that omits the reference electrode and uses two platinum electrodes for the reduction potential and also applies a reverse potential for electrode regeneration [2]. This decreases size and allows easy integration of both electrodes on a single chip. Such systems can be used for biomedical assays [3].

## 2. Materials and Methods

Custom made ISFETs with additional platinum electrodes are used (see Fig. 1). The sensing layer is silicon nitride. A custom electronic circuit reads the ISFET and controls the potential of the platinum electrodes. All measurement runs are conducted over the course of several days.

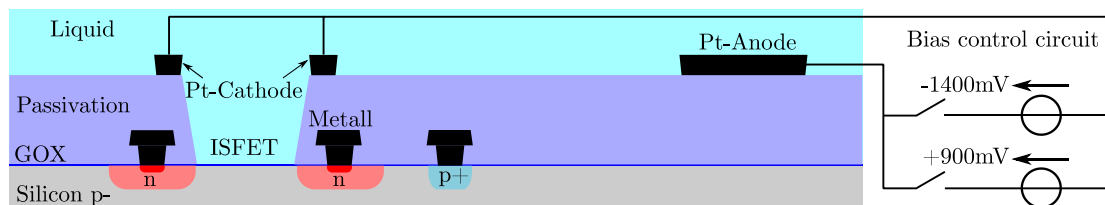


**Figure 1.** Schematic drawing of the sensor setup. The ISFET has two Pt-electrodes, the cathode near the sensitive gate area and the anode ca. 0.5mm away. The Pt-electrodes are set to a potential difference of -1.4V for 8 seconds. After that the second electrode is disconnected and left floating for 100 sec and the cycle repeats. Every second cycle a reverse potential of 0.9V is applied for 8 sec.

Different bias voltages were tested. Finally, 1.4V was used as below the sensitivity is very low. PBS (VWR chemicals) is deaerated with nitrogen, aerated or bubbled with pure oxygen to generate



solutions with 0%, 100% and ca. 450% air-oxygen saturation respectively. This is done immediately before each experiment. The fluid on the chip is switched computer controlled every 600 sec.

### 3. Results

A chip is tested repeatedly with the described buffer sequence. The last source-gate-voltage ( $V_{sg}$ ) reading before and during reduction are subtracted to form a measure for oxygen, delta  $V_{sg}$ . One experiment is conducted with, the other without reverse potential. Results are shown in Fig. 2.

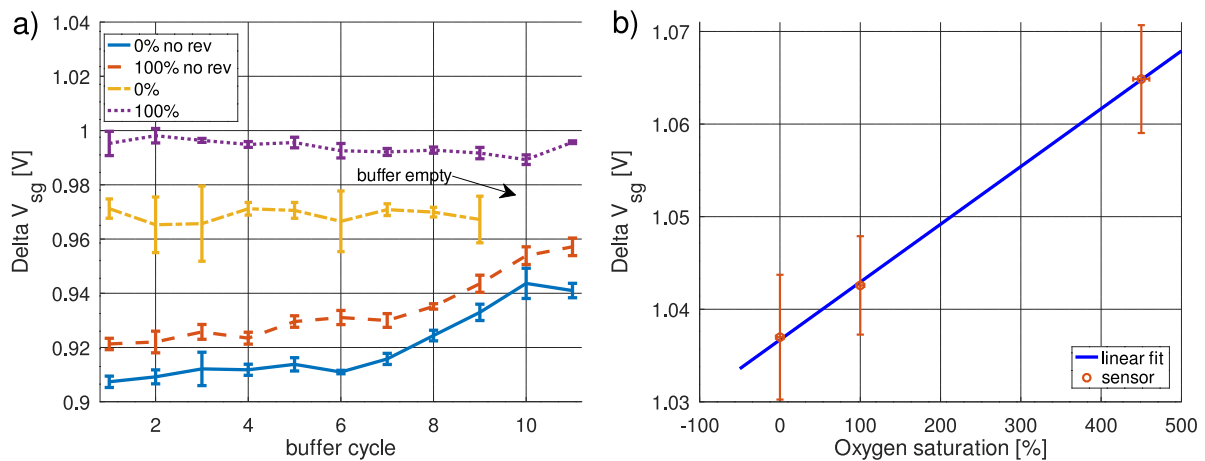


**Figure 2.** (a) Delta  $V_{sg}$  for different oxygen levels from two runs of the sensor, with and without reverse potential over multiple buffer changes. (b) Cumulated results of an experiment with three different oxygenated buffers on another chip. Mean and STD for the corresponding oxygen level was calculated and plotted. The first 120s after buffer change was omitted to remove settling effects.

The experiment without reverse potential shows a sensitivity of only 14mV difference between 0% and 100%, compared to 27mV with reverse potential in these runs. The drift which can be seen i.e. after the 5<sup>th</sup> cycle for the standard case is almost not visible with reverse potential. The sensor behaves linear over the full range of oxygen concentrations. The shown errors are even smaller than  $\pm 5$ mV when just looking at cycle to cycle difference or relative oxygen concentration.

### 4. Discussion

Applying a reverse potential to the electrodes in between measurements increased sensitivity, most likely because of reversing the drift of  $H^+$ -Ions in  $Si_3N_4$ , and improves stability for short-term measurement. However, there is still some long-term drift, as can be seen for the two runs in figure 2(a). The main benefit of this technique is higher sensitivity and easy integration. Compared to [1] the sensitivity is still low but no large and complex liquid or gel based reference electrode is needed. The chip can be manufactured with standard semiconductor processes without any special processing step except for the Pt electrode. For long-term stability an auto-calibration scheme [4] can be employed. The readout and control circuit can be built very small and cheap as shown in [5].

### References

1. Sohn, Byung-Ki, and Chang-Soo Kim. *Sensors and Actuators B: Chemical* 34.1-3, 1996, 435-440.
2. Weltin, Andreas, et al. *Lab on a Chip* 14.1, 2014, 138-146.
3. Wolf, Bernhard, et al. *Biomedizinische Technik* 52.1, 2007, 164-168.
4. Eminaga, Yazay, et al. *Sensors and Actuators B: Chemical* 177, 2013, 785-791.
5. Hefele, Markus, et al. *2019 17th IEEE International New Circuits and Systems Conference (NEWCAS)*.





# Publications

Parts of this work were published in the following media:

## Paper

- **Markus Hefe**le, Walter Wirths, Martin Brischwein, Helmut Grothe, Franz Kreupl, Bernhard Wolf. “Measuring fluorescence-lifetime and bio-impedance sensors for cell based assays using a network analyzer integrated circuit”. In: *Biosensors and Bioelectronics* 129 (2019), pp. 292–297. issn: 0956-5663.  
DOI: 10.1016/j.bios.2018.09.053  
URL: <http://www.sciencedirect.com/science/article/pii/S0956566318307449>
- **Markus Hefe**le, Ernst Müllner, Ralf Brederlow, Andreas Lösel, Sebastian Meier, Christian Pfeffer, Franz Kreupl, Bernhard Wolf. “Integrated multipurpose analog front-end for electrochemical ISFET sensors”. In: *2019 17th IEEE International New Circuits and Systems Conference (NEWCAS)* (2019). pp. 1-4.  
DOI: 10.1109/NEWCAS44328.2019.8961291  
URL: <https://ieeexplore.ieee.org/document/8961291>
- Robert Drehmel, Markus Hefele. “Increasing Autonomy of I/O Cores in Heterogenous FPGA-SoCs for Data Acquisition Applications”. 2020 IEEE International IOT, Electronics and Mechatronics Conference (IEMTRONICS), 9-12 September 2020, Virtual Conference  
DOI: 10.1109/IEMTRONICS51293.2020.9216335  
URL: <https://ieeexplore.ieee.org/document/9216335>

## Conference

- **Markus Hefe**le, Ernst Mueller, Sebastian Meier, Helmut Rinck, Christian Pfeffer, Ralf Brederlow, Franz Kreupl and Bernhard Wolf. “Dissolved oxygen detection with ISFETs without reference electrode”. Eurosenors 2020, Lecce Italy  
URL: <https://www.eurosenors2020.eu>, **submitted**, conference is postponed due to SARS-CoV2 pandemic, submitted abstract in appendix E.

## Conference Presentations

- **Markus Hefe**le, Petra Friedrich, Bernhard Wolf. “The bathroom as a healthcare location”. *52nd DGBMT annual conference, German Society for Biomedical Engineering*. 26-28 September 2018. Aachen
- **Markus Hefe**le, Ernst Müllner, Ralf Brederlow, Andreas Lösel, Sebastian Meier, Christian Pfeffer, Franz Kreupl, Bernhard Wolf. “Integrated multipurpose analog front-end for electrochemical ISFET sensors”. *2019 17th IEEE International New Circuits and Systems Conference (NEWCAS)*. 23-26 June 2019, Munich

## Patents

- U.S. Patent Application No. 63/030,062, Unpublished (filing date 26.5.2020) “pH SENSOR”, Scott Summerfelt, Ernst Müllner, Sebastian Meier, Markus Hefe

## Conference Poster

- **Markus Hefe**le, Walter Wirths, Martin Brischwein, Helmut Grothe, Bernhard Wolf. “Measuring fluorescence-lifetime and bio-impedance sensors for cell based assays using a network analyzer integrated circuit”. *Biosensors 2018, 28th Anniversary World Congress on Biosensors*. 12-15 June 2018. Miami, FL, USA

## Supervised student works

- Sargam Sharma, “Test setup for high throughput wafer level characterization of electrochemical sensors”, Master’s Thesis, 2018
- Syed Muhammad Ibad Ur Rahman Bukhari, “Comparison of Glass-Electrode and ISFET”, Master’s Thesis, 2018
- Daniel Kaindl, “Palladium Reference Electrode”, Master’s Thesis, 2019
- Stefan Dirr, “Implementierung eines Impedanzspektrometers mit Hilfe eines Mixed-Signal-Prozessors”, Bachelor’s Thesis, 2020
- Mohamed Amine Kthiri, “ISFET readout interface using Mixed-Signal-Controller”, Bachelor’s Thesis, 2020

# Bibliography

- [1] Wolfgang Schneider. *Lexikon zur Arzneimittellgeschichte: Sachwörterbuch zur Geschichte der pharmazeutischen Botanik, Chemie, Mineralogie, Pharmakologie, Zoologie*. Govi-Verlag, 1968.
- [2] Harry Eagle and George E. Foley. ‘The cytotoxic action of carcinolytic agents in tissue culture’. In: *The American Journal of Medicine* 21.5 (1956), pp. 739–749. ISSN: 0002-9343. DOI: 10.1016/0002-9343(56)90090-0. URL: <http://www.sciencedirect.com/science/article/pii/0002934356900900>.
- [3] Harry Eagle and George E. Foley. ‘Cytotoxicity in Human Cell Cultures as a Primary Screen for the Detection of Anti-Tumor Agents’. In: *Cancer Research* 18.9 (1958), pp. 1017–1025. ISSN: 0008-5472. eprint: <https://cancerres.aacrjournals.org/content/18/9/1017.full.pdf>. URL: <https://cancerres.aacrjournals.org/content/18/9/1017>.
- [4] Simon Festing and Robin Wilkinson. ‘The ethics of animal research’. In: *EMBO reports* 8.6 (2007), pp. 526–530. DOI: 10.1038/sj.embor.7400993. eprint: <https://www.embopress.org/doi/pdf/10.1038/sj.embor.7400993>. URL: <https://www.embopress.org/doi/abs/10.1038/sj.embor.7400993>.
- [5] Megha S. Even, Chad B. Sandusky and Neal D. Barnard. ‘Serum-free hybridoma culture: ethical, scientific and safety considerations’. In: *Trends in Biotechnology* 24.3 (2006), pp. 105–108. ISSN: 0167-7799. DOI: 10.1016/j.tibtech.2006.01.001. URL: <http://www.sciencedirect.com/science/article/pii/S0167779906000023>.
- [6] R. E. Wilsnack, F. J. Meyer and J. G. Smith. ‘Human Cell Culture Toxicity Testing of Medical Devices and Correlation to Animal Tests’. In: *Biomaterials, Medical Devices, and Artificial Organs* 1.3 (1973), pp. 543–562. DOI: 10.3109/10731197309118562. eprint: <https://doi.org/10.3109/10731197309118562>. URL: <https://doi.org/10.3109/10731197309118562>.
- [7] P. Wolf et al. ‘Automated platform for sensor-based monitoring and controlled assays of living cells and tissues’. In: *Biosensors and Bioelectronics* 50 (2013), pp. 111–117. ISSN: 0956-5663. DOI: 10.1016/j.bios.2013.06.031. URL: <http://www.sciencedirect.com/science/article/pii/S0956566313004284>.
- [8] R Schindler. ‘Use of cell culture in pharmacology’. In: *Annual review of pharmacology* 9.1 (1969), pp. 393–406. DOI: 10.1146/annurev.pa.09.040169.002141. URL: <https://doi.org/10.1146/annurev.pa.09.040169.002141>.

- [9] W.H Baumann et al. ‘Microelectronic sensor system for microphysiological application on living cells’. In: *Sensors and Actuators B: Chemical* 55.1 (1999), pp. 77–89. ISSN: 0925-4005. DOI: 10.1016/S0925-4005(99)00116-1. URL: <http://www.sciencedirect.com/science/article/pii/S0925400599001161>.
- [10] Regina Kleinhans et al. ‘Sensor-based cell and tissue screening for personalized cancer chemotherapy’. In: *Medical & biological engineering & computing* 50.2 (2012), pp. 117–126. DOI: 10.1007/s11517-011-0855-7. URL: <https://link.springer.com/article/10.1007/s11517-011-0855-7>.
- [11] Liang Ma et al. ‘Towards personalized medicine with a three-dimensional micro-scale perfusion-based two-chamber tissue model system’. In: *Biomaterials* 33.17 (2012), pp. 4353–4361. ISSN: 0142-9612. DOI: 10.1016/j.biomaterials.2012.02.054. URL: <http://www.sciencedirect.com/science/article/pii/S0142961212002591>.
- [12] Hongmei Mou, Karissa Brazauskas and Jayaraj Rajagopal. ‘Personalized medicine for cystic fibrosis: Establishing human model systems’. In: *Pediatric Pulmonology* 50.S40 (2015), S14–S23. DOI: 10.1002/ppul.23233. eprint: <https://onlinelibrary.wiley.com/doi/pdf/10.1002/ppul.23233>. URL: <https://onlinelibrary.wiley.com/doi/abs/10.1002/ppul.23233>.
- [13] J. Wiest et al. ‘Intelligent Mobile Lab for Metabolics in Environmental Monitoring’. In: *Analytical Letters* 39.8 (2006), pp. 1759–1771. DOI: 10.1080/00032710600714089. eprint: <https://doi.org/10.1080/00032710600714089>. URL: <https://doi.org/10.1080/00032710600714089>.
- [14] Geonsoo Jin et al. ‘Lens-free shadow image based high-throughput continuous cell monitoring technique’. In: *Biosensors and Bioelectronics* 38.1 (2012), pp. 126–131. ISSN: 0956-5663. DOI: 10.1016/j.bios.2012.05.022. URL: <http://www.sciencedirect.com/science/article/pii/S095656631200317X>.
- [15] Bernhard Wolf et al. ‘Lab-on-a-chip systems for cellular assays’. In: *BioMEMS*. Springer, 2006, pp. 269–307. DOI: 10.1007/978-0-387-28732-4\_9. URL: [https://doi.org/10.1007/978-0-387-28732-4\\_9](https://doi.org/10.1007/978-0-387-28732-4_9).
- [16] Bernhard Wolf et al. ‘Monitoring of cellular signalling and metabolism with modular sensor-technique: The PhysioControl-Microsystem (PCM®)’. In: *Biosensors and Bioelectronics* 13.5 (1998), pp. 501–509. ISSN: 0956-5663. DOI: 10.1016/S0956-5663(97)00136-X. URL: <http://www.sciencedirect.com/science/article/pii/S095656639700136X>.
- [17] Sigma-Aldrich. URL: <https://www.sigmaaldrich.com/MSDS/MSDS/DisplayMSDSPage.do?country=DE&language=de&productNumber=M2128&brand=SIGMA> (visited on 05/08/2020).
- [18] Magdalena Wodnicka et al. ‘Novel Fluorescent Technology Platform for High Throughput Cytotoxicity and Proliferation Assays’. In: *Journal of Biomolecular Screening* 5.3 (2000). PMID: 10894757, pp. 141–152. DOI: 10.1177/108705710000500306. eprint: <https://doi.org/10.1177/108705710000500306>. URL: <https://doi.org/10.1177/108705710000500306>.

- [19] Mirko Lehmann et al. ‘Non-invasive measurement of cell membrane associated proton gradients by ion-sensitive field effect transistor arrays for microphysiological and bioelectronic applications’. In: *Biosensors and Bioelectronics* 15.3 (2000), pp. 117–124. ISSN: 0956-5663. DOI: 10.1016/S0956-5663(00)00065-8. URL: <http://www.sciencedirect.com/science/article/pii/S0956566300000658>.
- [20] Angela M. Otto. ‘Cell Cultivation and Sensor-Based Assays for Dynamic Measurements of Cell Vitality’. In: *BetaSys: Systems Biology of Regulated Exocytosis in Pancreatic  $\beta$ -Cells*. Ed. by Bernhelm Booß-Bavnbek et al. New York, NY: Springer New York, 2011, pp. 221–240. ISBN: 978-1-4419-6956-9. DOI: 10.1007/978-1-4419-6956-9\_10. URL: [https://doi.org/10.1007/978-1-4419-6956-9\\_10](https://doi.org/10.1007/978-1-4419-6956-9_10).
- [21] Olivier Braissant et al. ‘Biomedical Use of Isothermal Microcalorimeters’. In: *Sensors* 10.10 (10/2010), pp. 9369–9383. ISSN: 1424-8220. DOI: 10.3390/s101009369. URL: <http://dx.doi.org/10.3390/s101009369>.
- [22] Ingemar Wadsö et al. ‘A well-plate format isothermal multi-channel microcalorimeter for monitoring the activity of living cells and tissues’. In: *Thermochimica Acta* 652 (2017), pp. 141–149. ISSN: 0040-6031. DOI: 10.1016/j.tca.2017.03.010. URL: <http://www.sciencedirect.com/science/article/pii/S0040603117300680>.
- [23] T. Geisler et al. ‘Automated multiparametric platform for high-content and high-Throughput Analytical screening on living cells’. In: *IEEE Transactions on Automation Science and Engineering* 3.2 (2006), pp. 169–176.
- [24] Víctor de Lorenzo. ‘From the selfish gene to selfish metabolism: revisiting the central dogma’. In: *Bioessays* 36.3 (2014), pp. 226–235. DOI: 10.1002/bies.201300153. URL: <https://doi.org/10.1002/bies.201300153>.
- [25] Frieder W. Scheller et al. ‘Biosensors: trends and commercialization’. In: *Biosensors* 1.2 (1985), pp. 135–160. ISSN: 0265-928X. DOI: 10.1016/0265-928X(85)80001-8. URL: <http://www.sciencedirect.com/science/article/pii/0265928X85800018>.
- [26] Klaus Riedel et al. ‘Microbial sensors: Fundamentals and application for process control’. In: *Journal of Chemical Technology & Biotechnology* 44.2 (1989), pp. 85–106. DOI: 10.1002/jctb.280440202. eprint: <https://onlinelibrary.wiley.com/doi/pdf/10.1002/jctb.280440202>. URL: <https://onlinelibrary.wiley.com/doi/abs/10.1002/jctb.280440202>.
- [27] Guenter W. Gross et al. ‘The use of neuronal networks on multielectrode arrays as biosensors’. In: *Biosensors and Bioelectronics* 10.6 (1995), pp. 553–567. ISSN: 0956-5663. DOI: 10.1016/0956-5663(95)96931-N. URL: <http://www.sciencedirect.com/science/article/pii/095656639596931N>.
- [28] Bernhard Wolf et al. ‘Biofunctional hybrid structures—cell–silicon hybrids for applications in biomedicine and bioinformatics’. In: *Bioelectrochemistry and Bioenergetics* 46.2 (1998), pp. 215–225. ISSN: 0302-4598. DOI: 10.1016/S0302-4598(98)00169-X. URL: <http://www.sciencedirect.com/science/article/pii/S030245989800169X>.

- [29] Motohiko Hikuma et al. ‘Amperometric estimation of BOD by using living immobilized yeasts’. In: *European journal of applied microbiology and biotechnology* 8.4 (1979), pp. 289–297. DOI: 10.1007/BF00508793. URL: <https://link.springer.com/article/10.1007/BF00508793>.
- [30] L. Umar, F. A. Alexander and J. Wiest. ‘Application of algae-biosensor for environmental monitoring’. In: *2015 37th Annual International Conference of the IEEE Engineering in Medicine and Biology Society (EMBC)*. 2015, pp. 7099–7102. DOI: 10.1109/EMBC.2015.7320028. URL: <https://ieeexplore.ieee.org/abstract/document/7320028>.
- [31] M. Schmidhuber, J. Wiest and B. Wolf. ‘A mobile biosensor using living cells for water quality analysis’. In: *World Congress on Medical Physics and Biomedical Engineering, September 7 - 12, 2009, Munich, Germany*. Ed. by Olaf Dössel and Wolfgang C. Schlegel. Berlin, Heidelberg: Springer Berlin Heidelberg, 2009, pp. 24–26. ISBN: 978-3-642-03893-8. DOI: 10.1007/978-3-642-03893-8\_7. URL: [https://link.springer.com/chapter/10.1007/978-3-642-03893-8\\_7](https://link.springer.com/chapter/10.1007/978-3-642-03893-8_7).
- [32] Inc. Corning. URL: <https://www.corning.com/emea/en/products/life-sciences/products/label-free-detection.html> (visited on 06/09/2019).
- [33] New Life Scientific Inc. URL: <https://www.youtube.com/watch?v=tY4S9x04aW8> (visited on 23/03/2020).
- [34] Inc. ACEA Biosciences. URL: <https://www.aceabio.com/products/xcelligence-rtca/> (visited on 06/09/2019).
- [35] Inc. Agilent Technologies. URL: <https://www.agilent.com/en/products/cell-analysis/seahorse-analyzers> (visited on 06/09/2019).
- [36] Symcel. URL: <https://symcel.com/calscreener> (visited on 04/09/2019).
- [37] Cellasys GmbH. URL: <https://www.cellasys.com> (visited on 01/04/2020).
- [38] Frank Alexander, Sebastian Eggert and Joachim Wiest. ‘A novel lab-on-a-chip platform for spheroid metabolism monitoring’. In: *Cytotechnology* 70.1 (2018), pp. 375–386. DOI: 10.1007/s10616-017-0152-x. URL: <https://doi.org/10.1007/s10616-017-0152-x>.
- [39] innoME GmbH. URL: <https://zencellowl.com/> (visited on 30/07/2020).
- [40] Ning Hu et al. ‘A novel microphysiometer based on high sensitivity LAPS and microfluidic system for cellular metabolism study and rapid drug screening’. In: *Biosensors and Bioelectronics* 40.1 (2013). Selected Papers from the World Congress on Biosensors, pp. 167–173. ISSN: 0956-5663. DOI: 10.1016/j.bios.2012.07.010. URL: <http://www.sciencedirect.com/science/article/pii/S0956566312004307>.
- [41] Eléonore Cabala. ‘Monitoring multiparametrischer komplexer Mikrosensorarrays für zelluläre Analytik’. Dissertation. München: Technische Universität München, 2007. URL: <http://mediatum.ub.tum.de/?id=620614>.



- [42] Joachim Wiest et al. ‘Cellular Assays with Multiparametric Bioelectronic Sensor Chips’. In: *CHIMIA International Journal for Chemistry* 59.5 (2005), pp. 243–246. ISSN: 0009-4293. DOI: 10.2533/000942905777676623. URL: <https://www.ingentaconnect.com/content/scs/chimia/2005/00000059/0000005/art00008>.
- [43] Michael Schmidhuber. ‘Konzeption und Erprobung eines biohybriden nanoanalytischen Handheld Systems’. Dissertation. München: Technische Universität München, 2011. URL: <http://mediatum.ub.tum.de/?id=1071806>.
- [44] F Demmel et al. ‘Nutrient depletion and metabolic profiles in breast carcinoma cell lines measured with a label-free platform’. In: *Physiological measurement* 36.7 (2015), p. 1367. DOI: 10.1088/0967-3334/36/7/1367. URL: <https://doi.org/10.1088/0967-3334/36/7/1367>.
- [45] Martin Brischwein and Joachim Wiest. ‘Microphysiometry’. In: *Bioanalytical Reviews* (2018). DOI: 10.1007/11663\_2018\_2. URL: [https://doi.org/10.1007/11663\\_2018\\_2](https://doi.org/10.1007/11663_2018_2).
- [46] Leland C Clark JR et al. ‘Continuous recording of blood oxygen tensions by polarography’. In: *Journal of applied physiology* 6.3 (1953), pp. 189–193. DOI: 10.1152/jappl.1953.6.3.189. URL: <https://doi.org/10.1152/jappl.1953.6.3.189>.
- [47] Dmitri B. Papkovsky. ‘Methods in Optical Oxygen Sensing: Protocols and Critical Analyses’. In: *Oxygen Sensing*. Vol. 381. Methods in Enzymology. Academic Press, 2004, pp. 715–735. DOI: 10.1016/S0076-6879(04)81046-2. URL: <http://www.sciencedirect.com/science/article/pii/S0076687904810462>.
- [48] Xu-dong Wang and Otto S. Wolfbeis. ‘Optical methods for sensing and imaging oxygen: materials, spectroscopies and applications’. In: *Chem. Soc. Rev.* 43 (10 2014), pp. 3666–3761. DOI: 10.1039/C4CS00039K. URL: <http://dx.doi.org/10.1039/C4CS00039K>.
- [49] PreSens GmbH. URL: <https://www.presens.de/> (visited on 20/09/2019).
- [50] Max Cremer. *Über die Ursache der elektromotorischen Eigenschaften der Gewebe, zugleich ein Beitrag zur Lehre von den polyphasischen Elektrolytketten*. R. Oldenbourg, 1906.
- [51] Fritz Haber and Z Hlomensiewicz. ‘Über elektrische Phasengrenzkkräfte’. In: *Zeitschrift für physikalische Chemie* 67.1 (1909), pp. 385–431. DOI: 10.1515/zpch-1909-6720. URL: <https://doi.org/10.1515/zpch-1909-6720>.
- [52] Phyllis Tookey Kerridge. ‘The use of the glass electrode in biochemistry’. In: *Biochemical Journal* 19.4 (1925), p. 611. DOI: 10.1042/bj0190611. URL: <https://doi.org/10.1042/bj0190611>.
- [53] Thermo Fisher Scientific Inc. URL: <https://www.thermofisher.com/order/catalog/product/9810BN> (visited on 19/09/2019).
- [54] Unisense A/S. URL: <https://www.unisense.com/pH> (visited on 19/09/2019).

- [55] I. Klimant et al. ‘Dual Lifetime Referencing (DLR) — a New Scheme for Converting Fluorescence Intensity into a Frequency-Domain or Time-Domain Information’. English. In: *New Trends in Fluorescence Spectroscopy*. Ed. by Bernard Valeur and Jean-Claude Brochon. Vol. 1. Springer Series on Fluorescence. Springer Berlin Heidelberg, 2001, pp. 257–274. ISBN: 978-3-642-63214-3. DOI: 10.1007/978-3-642-56853-4\_13. URL: [http://dx.doi.org/10.1007/978-3-642-56853-4\\_13](http://dx.doi.org/10.1007/978-3-642-56853-4_13).
- [56] Stanisław Głab et al. ‘Metal-Metal Oxide and Metal Oxide Electrodes as pH Sensors’. In: *Critical Reviews in Analytical Chemistry* 21.1 (1989). PMID: 28135819, pp. 29–47. DOI: 10.1080/10408348908048815. eprint: <https://doi.org/10.1080/10408348908048815>. URL: <https://doi.org/10.1080/10408348908048815>.
- [57] Agner Fog and Richard P Buck. ‘Electronic semiconducting oxides as pH sensors’. In: *Sensors and Actuators* 5.2 (1984), pp. 137–146.
- [58] Kenneth G. Kreider, Michael J. Tarlov and James P. Cline. ‘Sputtered thin-film pH electrodes of platinum, palladium, ruthenium, and iridium oxides’. In: *Sensors and Actuators B: Chemical* 28.3 (1995), pp. 167–172. ISSN: 0925-4005. DOI: 10.1016/0925-4005(95)01655-4. URL: <http://www.sciencedirect.com/science/article/pii/0925400595016554>.
- [59] NF De Rooij and P Bergveld. ‘Iridium/anodic iridium oxide film electrode as a pH sensor’. In: *Monitoring of Vital Parameters during Extracorporeal Circulation*. Karger Publishers, 1981, pp. 156–165.
- [60] J Hendrikse, Wouter Olthuis and Piet Bergveld. ‘A method of reducing oxygen induced drift in iridium oxide pH sensors’. In: *Sensors and Actuators B: Chemical* 53.1-2 (1998), pp. 97–103.
- [61] Tae Yong Kim and Sung Yang. ‘Fabrication method and characterization of electrodeposited and heat-treated iridium oxide films for pH sensing’. In: *Sensors and Actuators B: Chemical* 196 (2014), pp. 31–38. ISSN: 0925-4005. DOI: 10.1016/j.snb.2014.02.004. URL: <http://www.sciencedirect.com/science/article/pii/S0925400514001439>.
- [62] X. Kang et al. ‘Fabrication and electrochemical comparison of SIROF-AIROF-EIROF microelectrodes for neural interfaces’. In: *2014 36th Annual International Conference of the IEEE Engineering in Medicine and Biology Society*. 2014, pp. 478–481. DOI: 10.1109/EMBC.2014.6943632.
- [63] Wiley Analytical Science. *World’s first calibration-free pH meter: pHit scanner*. URL: <https://analyticalscience.wiley.com/do/10.1002/gitlab.10132/full/> (visited on 03/07/2020).
- [64] Xiaobo Ji et al. ‘Palladium Sub-Nanoparticle Decorated ‘Bamboo’ Multi-Walled Carbon Nanotubes Exhibit Electrochemical Metastability: Voltammetric Sensing in Otherwise Inaccessible pH Ranges’. In: *Electroanalysis: An International Journal Devoted to Fundamental and Practical Aspects of Electroanalysis* 18.24 (2006), pp. 2481–2485. DOI: 10.1002/elan.200603681. URL: <https://onlinelibrary.wiley.com/doi/pdf/10.1002/elan.200603681>.

- [65] Henry C Leventis et al. ‘Derivatised carbon powder electrodes: reagentless pH sensors’. In: *Talanta* 63.4 (2004), pp. 1039–1051. ISSN: 0039-9140. DOI: 10.1016/j.talanta.2004.01.017. URL: <http://www.sciencedirect.com/science/article/pii/S0039914004000426>.
- [66] Gregory G Wildgoose et al. ‘Anthraquinone-derivatised carbon powder: reagentless voltammetric pH electrodes’. In: *Talanta* 60.5 (2003), pp. 887–893. ISSN: 0039-9140. DOI: 10.1016/S0039-9140(03)00150-4. URL: <http://www.sciencedirect.com/science/article/pii/S0039914003001504>.
- [67] Dean G Hafeman, J Wallace Parce and Harden M McConnell. ‘Light-addressable potentiometric sensor for biochemical systems’. In: *Science* 240.4856 (1988), pp. 1182–1185. DOI: 10.1126/science.3375810. URL: <https://doi.org/10.1126/science.3375810>.
- [68] *Contaminant Detection Assays*. Molecular Devices, LLC. 2020. URL: <https://www.moleculardevices.com/products/assay-kits/contaminants/contaminant-detection-assays#Technology> (visited on 10/03/2020).
- [69] P. Bergveld. ‘Short Communications: Development of an Ion-Sensitive Solid-State Device for Neurophysiological Measurements’. In: *IEEE Transactions on Biomedical Engineering* BME-17.1 (1970), pp. 70–71. ISSN: 15582531. DOI: 10.1109/TBME.1970.4502688. arXiv: TBME.1970.4502688 [10.1109]. URL: <https://doi.org/10.1109/TBME.1970.4502688>.
- [70] P. Bergveld. ‘Thirty years of ISFETOLOGY’. In: *Sensors and Actuators B: Chemical* 88.1 (2003), pp. 1–20. ISSN: 09254005. DOI: 10.1016/S0925-4005(02)00301-5. URL: [https://doi.org/10.1016/S0925-4005\(02\)00301-5](https://doi.org/10.1016/S0925-4005(02)00301-5).
- [71] P V Bobrov et al. ‘Chemical sensitivity of an ISFET with Ta<sub>2</sub>O<sub>5</sub> membrane in strong acid and alkaline solutions’. In: *Sensors and Actuators B: Chemical* 3.1 (1991), pp. 75–81. ISSN: 0925-4005. DOI: 10.1016/0925-4005(91)85010-G. URL: <http://www.sciencedirect.com/science/article/pii/092540059185010G>.
- [72] Kokab B. Parizi et al. ‘ISFET pH Sensitivity: Counter-Ions Play a Key Role’. In: *Scientific Reports* 7.3 (2017), p. 41305. ISSN: 2045-2322. DOI: 10.1038/srep41305. URL: <http://www.nature.com/articles/srep41305>.
- [73] Manfred Klein. ‘Time effects of ion-sensitive field-effect transistors’. In: *Sensors and Actuators* 17.1-2 (1989), pp. 203–208. ISSN: 02506874. DOI: 10.1016/0250-6874(89)80081-2.
- [74] Hirokazu Hara and Tatsuya Ohta. ‘Dynamic response of a Ta<sub>2</sub>O<sub>5</sub>-gate pH-sensitive field-effect transistor’. In: *Sensors and Actuators B: Chemical* 32.2 (1996), pp. 115–119. ISSN: 0925-4005. DOI: 10.1016/0925-4005(96)80119-5. URL: <http://www.sciencedirect.com/science/article/pii/0925400596801195>.
- [75] A. S. Poghossian. ‘The super-Nernstian pH sensitivity of Ta<sub>2</sub>O<sub>5</sub>-gate ISFETs’. In: *Sensors and Actuators: B. Chemical* 7.1-3 (1992), pp. 367–370. ISSN: 09254005. DOI: 10.1016/0925-4005(92)80326-S.

- [76] Piet Bergveld. ‘Development, operation, and application of the ion-sensitive field-effect transistor as a tool for electrophysiology’. In: *IEEE Transactions on Biomedical Engineering* 5 (1972), pp. 342–351. DOI: 10.1109/TBME.1972.324137. URL: <https://doi.org/10.1109/TBME.1972.324137>.
- [77] Tadayuki Matsuo and Kensall D. Wise. ‘An Integrated Field-Effect Electrode for Biopotential Recording’. In: *IEEE Transactions on Biomedical Engineering* BME-21.6 (11/1974), pp. 485–487. ISSN: 0018-9294. DOI: 10.1109/TBME.1974.324338. URL: <http://ieeexplore.ieee.org/document/4120831/>.
- [78] Luc Bousse, H.H. van den Vlekkert and N.F. de Rooij. ‘Hysteresis in Al<sub>2</sub>O<sub>3</sub>-gate ISFETs’. In: *Sensors and Actuators B: Chemical* 2.2 (05/1990), pp. 103–110. ISSN: 09254005. DOI: 10.1016/0925-4005(90)80018-U. URL: <http://linkinghub.elsevier.com/retrieve/pii/092540059080018U>.
- [79] Sara Rigante et al. ‘Sensing with Advanced Computing Technology: Fin Field-Effect Transistors with High-k Gate Stack on Bulk Silicon’. In: *ACS Nano* 9.5 (05/2015), pp. 4872–4881. ISSN: 1936-0851. DOI: 10.1021/nn5064216. URL: <http://pubs.acs.org/doi/abs/10.1021/nn5064216>.
- [80] Jung Chuan Chou and Jung Lung Chiang. ‘Ion sensitive field effect transistor with amorphous tungsten trioxide gate for pH sensing’. In: *Sensors and Actuators, B: Chemical* 62.2 (2000), pp. 81–87. ISSN: 09254005. DOI: 10.1016/S0925-4005(99)00363-9.
- [81] Jung Lung Chiang et al. ‘Study on the temperature effect, hysteresis and drift of pH-ISFET devices based on amorphous tungsten oxide’. In: *Sensors and Actuators, B: Chemical* 76.1-3 (2001), pp. 624–628. ISSN: 09254005. DOI: 10.1016/S0925-4005(01)00657-8.
- [82] J. Bausells et al. ‘Ion-sensitive field-effect transistors fabricated in a commercial CMOS technology’. In: *Sensors and Actuators, B: Chemical* 57.1-3 (1999), pp. 56–62. ISSN: 09254005. DOI: 10.1016/S0925-4005(99)00135-5.
- [83] Wai Pan Chan, Bhusana Premanode and Christofer Toumazou. ‘An integrated ISFETs instrumentation system in standard CMOS technology’. In: *IEEE Journal of Solid-State Circuits* 45.9 (2010), pp. 1923–1934. ISSN: 00189200. DOI: 10.1109/JSSC.2010.2053863.
- [84] P. A. Hammond and D. R S Cumming. ‘Performance and system-on-chip integration of an unmodified CMOS ISFET’. In: *Sensors and Actuators, B: Chemical* 111-112.SUPPL. (2005), pp. 254–258. ISSN: 09254005. DOI: 10.1016/j.snb.2004.12.065.
- [85] Mark J. Milgrew and D. R S Cumming. ‘Matching the transconductance characteristics of CMOS ISFET arrays by removing trapped charge’. In: *IEEE Transactions on Electron Devices* 55.4 (2008), pp. 1074–1079. ISSN: 00189383. DOI: 10.1109/TED.2008.916680.
- [86] Y. Hu and P. Georgiou. ‘A direct-capacitive feedback ISFET interface for pH reaction monitoring’. In: *2013 IEEE International Symposium on Circuits and Systems (ISCAS)*. 2013, pp. 189–192. DOI: 10.1109/ISCAS.2013.6571814. URL: <https://ieeexplore.ieee.org/abstract/document/6571814>.

- [87] A Errachid, J Bausells and N Jaffrezic-Renault. ‘A simple REFET for pH detection in differential mode’. In: *Sensors and Actuators B: Chemical* 60.1 (1999), pp. 43–48. ISSN: 0925-4005. DOI: 10.1016/S0925-4005(99)00242-7. URL: <http://www.sciencedirect.com/science/article/pii/S0925400599002427>.
- [88] Ruixue Zeng et al. ‘A reference-less semiconductor ion sensor’. In: *Sensors and Actuators, B: Chemical* 254 (2018), pp. 102–109. ISSN: 09254005. DOI: 10.1016/j.snb.2017.06.152. URL: <https://doi.org/10.1016/j.snb.2017.06.152>.
- [89] Mst Shamim Ara Shawkat and Nicole McFarlane. ‘A single-chip ISFET based pH sensor’. In: *Proceedings of IEEE Sensors 1* (2017), pp. 2–4. ISSN: 21689229. DOI: 10.1109/ICSENS.2016.7808833.
- [90] Byung-Ki Sohn and Chang-Soo Kim. ‘A new pH-ISFET based dissolved oxygen sensor by employing electrolysis of oxygen’. In: *Sensors and Actuators B: Chemical* 34.1-3 (1996), pp. 435–440. URL: [https://doi.org/10.1016/S0925-4005\(97\)80017-2](https://doi.org/10.1016/S0925-4005(97)80017-2).
- [91] Mirko Lehmann et al. ‘Simultaneous measurement of cellular respiration and acidification with a single CMOS ISFET’. In: *Biosensors and Bioelectronics* 16.3 (2001), pp. 195–203. ISSN: 09565663. DOI: 10.1016/S0956-5663(01)00123-3.
- [92] Joachim Wiest et al. ‘Measurement and simulation of the dissolved oxygen concentration and the pH value at the O 2-FET’. In: *World Congress on Medical Physics and Biomedical Engineering 2006*. Springer, 2007, pp. 645–647. DOI: 10.1007/978-3-540-36841-0\_149.
- [93] Y Eminaga et al. ‘3.5.4 Multiparametric Microsensors on Labonchip Systems for the Detection of Dissolved Substances’. In: *Proceedings IMCS 2012* (2012), pp. 316–318. DOI: 10.5162/IMCS2012/3.5.4. URL: <https://doi.org/10.5162/IMCS2012/3.5.4>.
- [94] Stanley D Moss, Jiri Janata and Curtis C Johnson. ‘Potassium ion-sensitive field effect transistor’. In: *Analytical Chemistry* 47.13 (1975), pp. 2238–2243. DOI: 10.1021/ac60363a005. URL: <https://doi.org/10.1021/ac60363a005>.
- [95] T Akiyama and E Niki. ‘Ion-sensitive field-effect transistor for pK and pNa sensing’. In: *Pure and applied chemistry* 59.4 (1987), pp. 535–538. DOI: 10.1351/pac198759040535. URL: <https://doi.org/10.1351/pac198759040535>.
- [96] Andrey Bratov et al. ‘Ion-selective field effect transistor (ISFET)-based calcium ion sensor with photocured polyurethane membrane suitable for ionised calcium determination in milk’. In: *Analytica Chimica Acta* 408 (03/2000), pp. 57–64. DOI: 10.1016/S0003-2670(99)00871-5.
- [97] Keun-Yong Park et al. ‘ISFET glucose sensor system with fast recovery characteristics by employing electrolysis’. In: *Sensors and Actuators B: Chemical* 83.1-3 (2002), pp. 90–97. DOI: 10.1016/S0925-4005(01)01049-8.
- [98] Bart H van der Schoot and Piet Bergveld. ‘ISFET based enzyme sensors’. In: *Biosensors* 3.3 (1987), pp. 161–186. DOI: 10.1016/0265-928X(87)80025-1.
- [99] Christofer Toumazou et al. ‘Simultaneous DNA amplification and detection using a pH-sensing semiconductor system’. In: *Nature methods* 10.7 (2013), p. 641. DOI: 10.1038/nmeth.2520. URL: <https://www.nature.com/articles/nmeth.2520>.

- [100] L. L. Visch et al. ‘pH measurements with an ion sensitive field effect transistor in the mouth of patients with xerostomia’. In: *IEEE Transactions on Biomedical Engineering* 38.4 (1991), pp. 353–356. DOI: 10.1109/10.133230. URL: <https://ieeexplore.ieee.org/abstract/document/133230>.
- [101] Nicolas Moser et al. ‘ISFETs in CMOS and emergent trends in instrumentation: A review’. In: *IEEE Sensors Journal* 16.17 (2016), pp. 6496–6514. DOI: 10.1109/JSEN.2016.2585920.
- [102] Optoi Microelectronics. *OIII ISFET SENSOR of pH measurement (datasheet)*. 2011.
- [103] Y Liu et al. ‘Minimal readout scheme for ISFET sensing arrays based on pulse width modulation’. In: *Electronics letters* 48.10 (2012), pp. 548–549. DOI: 10.1049/elel.2011.3847.
- [104] Nicolas Moser, Tor Sverre Lande and Pantelis Georgiou. ‘A novel pH-to-time ISFET pixel architecture with offset compensation’. In: *2015 IEEE International Symposium on Circuits and Systems (ISCAS)*. IEEE. 2015, pp. 481–484. DOI: 10.1109/ISCAS.2015.7168675.
- [105] B. Palán et al. ‘New ISFET sensor interface circuit for biomedical applications’. In: *Sensors and Actuators B: Chemical* 57.1 (1999), pp. 63–68. ISSN: 0925-4005. DOI: 10.1016/S0925-4005(99)00136-7. URL: <http://www.sciencedirect.com/science/article/pii/S0925400599001367>.
- [106] *Senstron*. URL: <https://www.sentron.nl/> (visited on 28/06/2019).
- [107] *Honeywell, Durafet product page*. URL: <https://www.honeywellprocess.com/en-US/explore/products/instrumentation/analytical-instruments-and-sensors/ph-orp/Pages/durafet-non-glass-ph-sensor.aspx> (visited on 28/06/2019).
- [108] *WINSENSE*. URL: <http://www.winsense.co.th/index.html> (visited on 28/06/2019).
- [109] Microsens SA. *Micorsens SA - Sensing Systems*. URL: <http://microsens.ch/products/systems.htm> (visited on 03/07/2020).
- [110] *Mettler-Toledo, ISFET product page*. URL: <https://www.mt.com/de/en/home/products/Process-Analytics/pH-probe/non-glass-ISFET-electrode.html> (visited on 28/06/2019).
- [111] Zimmer and Peacock. URL: <https://www.zimmerpeacocktech.com/products/gfet/> (visited on 23/05/2020).
- [112] M. Waleed Shinwari et al. ‘Microfabricated reference electrodes and their biosensing applications’. In: *Sensors* 10.3 (2010), pp. 1679–1715. ISSN: 14248220. DOI: 10.3390/s100301679.
- [113] M. A.G. Zevenbergen et al. ‘Solid state pH and chloride sensor with microfluidic reference electrode’. In: *Technical Digest - International Electron Devices Meeting, IEDM 1* (2017), pp. 26.1.1–26.1.4. ISSN: 01631918. DOI: 10.1109/IEDM.2016.7838482.

- [114] Pierre A. Comte and Jiří Janata. ‘A field effect transistor as a solid-state reference electrode’. In: *Analytica Chimica Acta* 101.2 (1978), pp. 247–252. ISSN: 0003-2670. DOI: 10.1016/S0003-2670(01)93361-6. URL: <http://www.sciencedirect.com/science/article/pii/S0003267001933616>.
- [115] Daiki Kaneko and Kazuyoshi Tsuchiya. ‘Development of the micro region pH sensor using Ag/AgIO<sub>3</sub> electrode method’. In: *Mhs2013* 2 (2013), pp. 1–4. DOI: 10.1109/MHS.2013.6710436. URL: <http://ieeexplore.ieee.org/lpdocs/epic03/wrapper.htm?arnumber=6710436>.
- [116] Ganesh Kumar Mani et al. ‘A novel electrolyte free solid state pH sensor for Bio-MEMS applications’. In: *2016 International Symposium on Micro-NanoMechatronics and Human Science, MHS 2016* (2017), pp. 2–5. DOI: 10.1109/MHS.2016.7824244.
- [117] James W. Ross Jr. ‘Temperature insensitive potentiometric electrode system’. U.S. pat. 4495050. 22/01/1985.
- [118] Jochen Kieninger. ‘Electrochemical microsensors for cell culture monitoring’. PhD thesis. Freiburg: Universität Freiburg, 2011. URL: <https://www.freidok.uni-freiburg.de/fedora/objects/freidok:8711/datastreams/FILE1/content>.
- [119] Espen V. Fanavoll et al. ‘A microfluidic electrochemical cell with integrated PdH reference electrode for high current experiments’. In: *Electrochimica Acta* 225 (2017), pp. 69–77. ISSN: 00134686. DOI: 10.1016/j.electacta.2016.11.147.
- [120] Thaddaeus A. Webster and Edgar D. Goluch. ‘Electrochemical detection of pyocyanin in nanochannels with integrated palladium hydride reference electrodes’. In: *Lab on a Chip* 12.24 (2012), pp. 5195–5201. ISSN: 14730189. DOI: 10.1039/c2lc40650k.
- [121] R. A. Goffe and A. C. Tseung. ‘Internally charged palladium hydride reference electrode - Part 1: The effect of charging current density on long-term stability’. In: *Medical & Biological Engineering & Computing* 16.6 (1978), pp. 670–676. ISSN: 01400118. DOI: 10.1007/BF02442446.
- [122] Mara Serrapede et al. ‘Nanostructured Pd hydride microelectrodes: In situ monitoring of pH variations in a porous medium’. In: *Analytical Chemistry* 86.12 (2014), pp. 5758–5765. ISSN: 15206882. DOI: 10.1021/ac500310j.
- [123] Ryan C. Wolfe et al. ‘Measurement of pH gradients in the crevice corrosion of iron using a palladium hydride microelectrode’. In: *Journal of the Electrochemical Society* 152.2 (2005), pp. 82–88. ISSN: 00134651. DOI: 10.1149/1.1851053. URL: <https://doi.org/10.1149/1.1851053>.
- [124] Digby D. Macdonald. ‘The Measurement of pH in Aqueous Systems at Elevated Temperatures Using Palladium Hydride Electrodes’. In: *Journal of The Electrochemical Society* 127.8 (1980), p. 1745. DOI: 10.1149/1.2129992. URL: <https://doi.org/10.1149%2F1.2129992>.
- [125] B Sanchez et al. ‘Basics of broadband impedance spectroscopy measurements using periodic excitations’. In: *Measurement Science and Technology* 23.10 (08/2012), p. 105501. DOI: 10.1088/0957-0233/23/10/105501. URL: <https://doi.org/10.1088%2F0957-0233%2F23%2F10%2F105501>.

- [126] J Ross Macdonald and E Barsoukov. ‘Impedance spectroscopy: theory, experiment, and applications’. In: *History* 1.8 (2005), pp. 1–13.
- [127] Uwe Tröltzsch, Olfa Kanoun and Hans-Rolf Tränkler. ‘Characterizing aging effects of lithium ion batteries by impedance spectroscopy’. In: *Electrochimica Acta* 51.8-9 (2006), pp. 1664–1672.
- [128] Ivar Giaever and Charles R Keese. ‘A morphological biosensor for mammalian cells.’ In: *Nature* 366.6455 (1993), pp. 591–592.
- [129] T Schwarzenberger et al. ‘Impedance sensor technology for cell-based assays in the framework of a high-content screening system’. In: *Physiological Measurement* 32.7 (06/2011), pp. 977–993. DOI: 10.1088/0967-3334/32/7/s18. URL: <https://doi.org/10.1088%2F0967-3334%2F32%2F7%2Fs18>.
- [130] Markus Hefele et al. ‘Measuring fluorescence-lifetime and bio-impedance sensors for cell based assays using a network analyzer integrated circuit’. In: *Biosensors and Bioelectronics* 129 (2019), pp. 292–297. ISSN: 0956-5663. DOI: 10.1016/j.bios.2018.09.053. URL: <http://www.sciencedirect.com/science/article/pii/S0956566318307449>.
- [131] S. B. Prakash and P. Abshire. ‘On-Chip Capacitance Sensing for Cell Monitoring Applications’. In: *IEEE Sensors Journal* 7.3 (2007), pp. 440–447. DOI: 10.1109/JSEN.2006.889213. URL: <https://ieeexplore.ieee.org/abstract/document/4099356>.
- [132] B. Senevirathna et al. ‘Lab-on-CMOS capacitance sensor array for real-time cell viability measurements with I2C readout’. In: *2016 IEEE International Symposium on Circuits and Systems (ISCAS)*. 2016, pp. 2863–2866. DOI: 10.1109/ISCAS.2016.7539190. URL: <https://ieeexplore.ieee.org/abstract/document/7539190>.
- [133] Sciospec Scientific Instruments GmbH. URL: <https://www.sciospec.de/> (visited on 17/09/2019).
- [134] Ivium Technologies B.V. URL: <https://www.ivium.com> (visited on 17/09/2019).
- [135] *CompactStat.h*. Ivium Technologies B.V. 2020. URL: [https://www.ivium.com/product/compactstat\\_h/](https://www.ivium.com/product/compactstat_h/) (visited on 17/02/2020).
- [136] ELIKO. URL: <https://www.eliko.ee/products/quadra-impedance-spectroscopy/> (visited on 06/08/2019).
- [137] J. Ojarand and M. Min. ‘Efficient Excitation Signals for the Fast Impedance Spectroscopy’. In: *Elektronika ir Elektrotechnika* 20.5 (05/2014), pp. 144–149. DOI: 10.5755/j01.eee.20.5.7115. URL: <http://eejournal.ktu.lt/index.php/elt/article/view/7115>.
- [138] PalmSens BV. URL: <https://www.palmsens.com> (visited on 17/09/2019).
- [139] *PalmSens4*. PalmSens BV. 2020. URL: <https://www.palmsens.com/product/palmsens4/> (visited on 17/02/2020).
- [140] Ametek Inc. URL: <https://www.ameteks.com/products/frequency-response-analyzers/1260a-impedance-analyzer> (visited on 06/08/2019).
- [141] Jean Rintoul. URL: <https://openeit.github.io/docs/html/index.html> (visited on 17/09/2019).



- [142] S. Grassini et al. ‘Low-Cost Impedance Spectroscopy System Based on a Logarithmic Amplifier’. In: *IEEE Transactions on Instrumentation and Measurement* 64.5 (2015), pp. 1110–1117. DOI: 10.1109/TIM.2014.2371191. URL: <https://ieeexplore.ieee.org/abstract/document/6975158>.
- [143] José Santos and Pedro M Ramos. ‘Impedance Measuring System based on a dsPIC’. In: (). URL: <https://www.imeko.org/publications/tc4-2010/IMEKO-TC4-2010-052.pdf> (visited on 21/07/2020).
- [144] Ian B Butler, Martin AA Schoonen and David T Rickard. ‘Removal of dissolved oxygen from water: a comparison of four common techniques’. In: *Talanta* 41.2 (1994), pp. 211–215. DOI: 10.1016/0039-9140(94)80110-X.
- [145] *Keysight Technologies, E4980A Precision LCR Meter, 20 Hz to 2 MHz*. E4980A. Keysight. 2018. URL: <https://www.keysight.com/de/pd-715495-pn-E4980A/precision-lcr-meter-20-hz-to-2-mhz?nid=-34124.536908436&cc=DE&lc=ger> (visited on 31/01/2020).
- [146] *Series 2400 SourceMeter SMU Instruments*. 2401. Tektronix. 2019. URL: [https://download.tek.com/datasheet/2400\\_SMU\\_Datasheet\\_1KW-2798-1\\_011719.pdf](https://download.tek.com/datasheet/2400_SMU_Datasheet_1KW-2798-1_011719.pdf) (visited on 01/02/2020).
- [147] Daniel Kaindl. ‘Palladium Reference Electrode’. Masterarbeit. Technische Universität München, 2019.
- [148] Y Sakamoto et al. ‘Electrical resistance measurements as a function of composition of palladium - hydrogen(deuterium) systems by a gas phase method’. In: *Journal of Physics: Condensed Matter* 8.19 (05/1996), pp. 3399–3411. DOI: 10.1088/0953-8984/8/19/015. URL: <https://doi.org/10.1088%2F0953-8984%2F8%2F19%2F015>.
- [149] W. T. Lindsay and F. W. Pement. ‘Electrical Resistance of Alpha Hydrogen-Palladium’. In: *The Journal of Chemical Physics* 36.5 (1962), pp. 1229–1234. DOI: 10.1063/1.1732718. eprint: <https://doi.org/10.1063/1.1732718>. URL: <https://doi.org/10.1063/1.1732718>.
- [150] W. J. Hamer and S. F. Acree. ‘A comparison of platinum and palladium hydrogen-electrodes in aqueous solutions of acid potassium phthalate’. In: *Journal of Research of the National Bureau of Standards* 33.2 (1944), pp. 87–103. URL: <https://archive.org/details/jresv33n2p87>.
- [151] Sebastian Meier. ‘Process and design of ISFET-based electrochemical sensor’. Masterarbeit. Technische Universität München, 2017.
- [152] Niklas Fauth. ‘Development of a Sensor-Implant for Cancer Research’. Bachelorarbeit. Karlsruher Institut für Technologie, 2019. URL: <https://github.com/NiklasFauth/sensor-implant>.
- [153] Ferran Reverter and Josep Altet. ‘MOSFET temperature sensors for on-chip thermal testing’. In: *Sensors and Actuators A: Physical* 203 (2013), pp. 234–240. ISSN: 0924-4247. DOI: 10.1016/j.sna.2013.08.026. URL: <http://www.sciencedirect.com/science/article/pii/S092442471300410X>.
- [154] *36-V, low-capacitance, low-leakage-current, precision, analog multiplexers*. MUX36D04. Version SBOS705D–JANUARY 2016 – REVISED FEBURARY 2019. Texas Instruments. 2019. URL: <https://www.ti.com/lit/gpn/MUX36D04>.

## Bibliography

- [155] M. Hefele et al. ‘Integrated multipurpose analog front-end for electrochemical ISFET sensors’. In: *2019 17th IEEE International New Circuits and Systems Conference (NEWCAS)*. 06/2019, pp. 1–4. DOI: 10.1109/NEWCAS44328.2019.8961291.
- [156] Mohamed Amine Kthiri. ‘ISFET readout interface using Mixed-Signal-Controller’. Bachelorarbeit. Technische Universität München, 2020.
- [157] Implementierung eines Impedanzspektrometers mit Hilfe eines Mixed-Signal-Prozessors. ‘Stefan Dirr’. Bachelorarbeit. Technische Universität München, 2020.
- [158] Surachoke Thanapitak. ‘An 1 V–1 nW source follower ISFET readout circuit for biomedical applications’. In: *2015 Science and Information Conference (SAI)*. IEEE. 2015, pp. 1118–1121. DOI: 10.1109/SAI.2015.7237284. URL: <https://ieeexplore.ieee.org/abstract/document/7237284>.
- [159] Markus Hefele. ‘Design eines hybrid optisch-elektrochemischen Detektors für zellbasierte Hochdurchsatz-Analytik’. Masterarbeit. Technische Universität München, 2016.
- [160] Texas Instruments. URL: <https://www.ti.com/tool/REP430F> (visited on 23/06/2020).